Investigations of chiral symmetry breaking and topological aspects of lattice QCD

D I S S E R T A T I O N

zur Erlangung des akademischen Grades

doctor rerum naturalium
Dr. rer. nat.
im Fach Physik

eingereicht an der
Mathematisch-Naturwissenschaftlichen Fakultät I
Humboldt-Universität zu Berlin

von

Elena García Ramos

Präsident der Humboldt-Universität zu Berlin:
Prof. Dr. Jan-Hendrik Olbertz

Dekan der Mathematisch-Naturwissenschaftlichen Fakultät I:
Prof. Stefan Hecht Ph.D.

Gutachter:

1. Dr. Karl Jansen
2. Prof. Dr. Michael Müller-Preußker
3. Prof. Dr. Giancarlo Rossi

eingereicht am: 01.10.2013
Tag der mündlichen Prüfung: 16.12.2013

To my parents,
for their constant support
and encouragement.

A mis padres,
por siempre animarme
y apoyarme en todo.

La vida cobra sentido cuando se hace de ella
una aspiración a no renunciar a nada

José Ortega y Gasset

Abstract

The spontaneous breaking of chiral symmetry is a fascinating phenomenon of QCD whose mechanism is still not well understood. It has fundamental phenomenological implications. It is, for instance, responsible for the low mass of the pions which are effectively Goldstone bosons of the spontaneously broken symmetry.In addition, the topological fluctuations of the underlying gauge fields are directly related to the $U(1)_A$ chiral anomaly and therefore linked to the unexpected large mass of the η' meson.

Since these phenomena belong to the low energy regime of QCD, non-perturbative techniques have to be applied in order to study them. Lattice regularization, through the path integral quantization of the theory, is such a non-perturbative method and it enables us to apply both analytical and numerical techniques from statistical mechanics to the study of QCD.

In this work we use the twisted mass lattice QCD regularization to compute the chiral condensate, the order parameter of spontaneous chiral symmetry breaking. To this end we apply the recently introduced method of spectral projectors which allows us to perform calculations in large volumes due to its inherently low computational cost. This approach, moreover, enables a direct calculation of the chiral condensate based on a theoretically clean definition of the observable via density chains.

We present a continuum limit determination of the chirally extrapolated condensate for $N_f = 2$ and $N_f = 2 + 1 + 1$ flavours of twisted mass fermions at maximal twist. We comprehensively investigate the systematic uncertainties arising in this calculation which allows us to present a reliable result for the chiral condensate. A good agreement with other lattice determinations is found.

In addition to computing the condensate, we study the chiral behavior of the topological susceptibility, a measure of the topological fluctuations of the gauge fields. We again apply the spectral projector method for this calculation, which is based on a definition of the topological susceptibility free of short distance singularities. In this case one of the biggest advantages is that it avoids the necessity for computationally expensive lattice chiral fermion formulations, and therefore allows us to perform large volume simulations. We comment on the difficulties which appear in the calculation of this observable due to the large autocorrelations involved.

When dynamical fermions are present, chiral perturbation theory establishes a relation between the chiral behavior of the topological susceptibility and the chiral condensate. Through this indirect method we extract an alternative determination of the chiral condensate which is in agreement with the previous one.

Finally we present the continuum limit result of the topological susceptibility in the pure gluonic theory which allows us to perform a test of the Witten-Veneziano relation. We found that this relation is well satisfied. Our results support the validity of the Witten-Veneziano formula which relates the topological fluctuations of the gauge fields with the unexpectedly large value of the η' mass.

Zusammenfassung

Die spontane Brechung der chiralen Symmetrie ist ein faszinierendes Phenomän der QCD mit fundamentalen phänomenologischen Implikationen, dessen Mechanismen aber nicht vollständig verstanden sind. Die Brechung der chiral Symmetrie ist beispielsweise verantwortlich für die niedrige Masse der Pionen, welche die effektiven Goldstone Boson der spontan gebrochene Symmetrie sind. In der QCD sind die topologischen Fluktuationen der zugrundeliegenden Eichfelder direkt mit der $U(1)_A$ chiralen Anomalie und damit auch der unerwartet hohen Masse des η' Meson verknüpft.

Die spontane Brechung der chiral Symmetrie und die chirale Anomalie sind niedrig Energie-Phenomäne der QCD, weshalb nichtperturbative Methoden nötig sind um sie zu studieren. Die Gitterregularisierung der QCD, mit Hilfe der Pfadintegral-Quantisierung der Theorie, ist die bislang erfolgreichste nichtstörungstheoretische Methode, um solche nichtperturbativen Fragestellungen anzugehen. Sie ermöglicht es uns, analytische und numerische Techniken des statistischen Mechanik anzuwenden.

In der vorliegenden Arbeit verwenden wir die Gitterregularisierung der QCD, um das chirale Kondensat, den Ordnungsparameter der spontanen Brechung der chiralen Symmetrie zu bestimen. Dazu wendeten wir die Definition der in dieser Arbeit studierten Observablen über Dichteketten an, die eine theoretisch wohldefinierte Bahndlung der Observablen zulässt. Für die praktische Berechnung wurde die kürzlich entwickelte Methode der spektralen Projektoren angewandt, die es ermöglicht, diese Berechnung einem vetretbar numerischen Aufwand durchzuführen.

In dieser Weise berchnen wir den Kontinuumlimes des chiralen Kondensates, das im chiralen Limes gewonnen, sowohl für $N_f = 2$ als auch für $N_f = 2+1+1$ Flavour von so genannten "twisted mass" Fermionen. Ein besonderes Augenmerk wurde auf die Untersuchung der systematischen Unsicherheiten gelegt, wodurch wir zuverlässige Ergebnisse für das chirale Kondensat gewinnen koennten, die kompatibel mit anderen Gittererrechnungen sind.

Des Weiteren untersuchen wir das chirale Verhalten der topologischen Suszeptibilität, woraus wir einen weiteren Wert für das chirale Kondensat erhalten, der mit der direkten Bestimmung übereinstimmt. Wir verwenden hier wieder die Methode der spektralen Projektoren, anstelle aufwendigerer Verfahren, die chirale Symmetrie erhalten, aber zu numerisch sehr aufwändigen Simulationen führen. Schließlich kommentieren wir die sich aus den starken Autokorrelationen ergebenden Schwierigkeiten dieser Rechnung.

Abschließend stellen wir die Kontinuumlimes-Ergebnisse der topologischen Suszeptibilität in der rein gluonischen Theorie vor, die es uns erlauben, die Witten-Veneziano-Formel zu testen. Unseren Untersuchung zufolge ist diese Formel gut erfüllt. Diese Tatsache stützt die Gültigkeit der Formel, die die topologischen Fluktuationen der Eichfelder mit der unerwartet großen Masse des η' Mesons in Verbindung setzt.

Contents

CHAPTER 1

Chiral symmetry in QCD

Contents

The fundamental forces in nature are gravitational, electromagnetic, weak and strong. All forces, except gravitational, are described by quantum gauge field theories. The standard model (SM) of particle physics is the current theory which describes the interaction of the constituents of matter. It is a remarkable and outstandingly successful theory which includes the electroweak and the strong interaction. The gravitational force is not considered since, on the experimental side for processes at present particle colliders it is insignificant, and on the theoretical side a consistent quantization of gravity is still missing.

Symmetries strongly influence the construction of the standard model and guide the understanding of numerous natural phenomena. Therefore they play a fundamental role in nature. In fact, as it was remarkably stated by Emmy Noether, for each continuous symmetry of the action there is a corresponding conservation law. In some cases, symmetries such as chiral symmetry are spontaneously broken leading to very important physical phenomena such as the appearance of a chiral condensate.

Within the standard model Quantum Chromodynamics (QCD) is the theory that describes the strong interaction between quarks and gluons. We dedicate this chapter to the introduction of QCD, its fundamental properties, its action and its symmetries. We then focus on one central phenomenon: the already mentioned spontaneous breaking of chiral symmetry.

Chiral symmetry and its spontaneous breaking have strong phenomenological implications that are profoundly interesting and still not well understood. This thesis is devoted to the study of chiral symmetry and, in particular, to the calculation of quantities which are directly related to it. The non-perturbative investigation of chiral symmetry breaking in this thesis offers a better understanding of the mechanism behind spontaneous chiral symmetry breaking.

Another focus of the thesis is the study of topological properties of QCD. We will introduce the concept of a topological charge and determine its fluctuations which will lead to the topological susceptibility. One goal of the thesis is to use the relation of the topological susceptibility with chiral symmetry breaking to determine the chiral condensate. An additional goal is to quantitatively test the Witten-Veneziano relation which provides an explanation for the surprisingly large mass of the η' meson by relating this mass to the topological susceptibility in the pure gluon theory.

This chapter is presented as a theoretical motivation for the study carried out in this thesis. Thus, it aims to introduce the fundamental concepts which are necessary to understand the phenomena of spontaneous chiral symmetry breaking and topology that inspired this work. For a more comprehensive discussion on QCD, chiral symmetry and topology we refer to specialized texts, e.g. Refs. [1, 2].

1.1. Introduction to Quantum Chromodynamics

Quantum chromodynamics (QCD) is the theory which describes the strong interactions. In the present chapter we introduce this theory starting from the quark model, which first described the hadrons found in nature. We will also comment on some particularities

of the QCD mass spectrum which will be relevant in the the next chapters. We then present some remarkable features of QCD at high and low energies and discuss the different approaches to the study of both regimes. We finally introduce the QCD action, the essential building block. We will then develop further the concepts of chiral symmetry and topology which are the crucial elements of QCD to be discussed in this thesis.

1.1.1. Quark model

The quark model, introduced in 1963 by Gell-Mann [3] and Zweig [4], and the addition of a quantum number called *flavor* led to describe particles as compound systems of quarks, elements of the fundamental representation of a global $SU(3)$ symmetry. Quarks, so far, are represented in nature in six different flavors. In the quark model, which originally only included three flavors (up, down and strange), quarks transform under the transformation $\mathbf{3}$ and antiquarks under $\bar{\mathbf{3}}$, both fundamental representations of $SU(3)$.

The bound states of quarks, called *hadrons* must be invariant under $SU(3)$ transformations, and are therefore color singlets. The only possible combinations of the lightest up, down and strange quarks are given by

$$\bar{q}^i q_i, \quad \text{mesons} \tag{1.1a}$$

$$\epsilon_{ijk} q_i q_j q_k, \quad \text{baryons} \tag{1.1b}$$

$$\epsilon_{ijk} \bar{q}_i \bar{q}_j \bar{q}_k, \quad \text{antibaryons} \tag{1.1c}$$

where the subindices represent the color index. Eq. (1.1) corresponds to *mesons*, *baryons* and *antibaryons* respectively as indicated. Mesons are then bound states of a quark-antiquark pair whose product $\mathbf{3} \otimes \mathbf{3}$ is invariant under $SU(3)$ and which can be decomposed into irreducible representations $\mathbf{3} \otimes \mathbf{3} = \mathbf{1} \otimes \mathbf{8}$. Both, the octet and the singlet, are represented in Fig. 1.1. Tab. 1.1 shows the masses and the quark content of the nine light pseudoscalar mesons represented in Fig. 1.1 and additionally the vector mesons

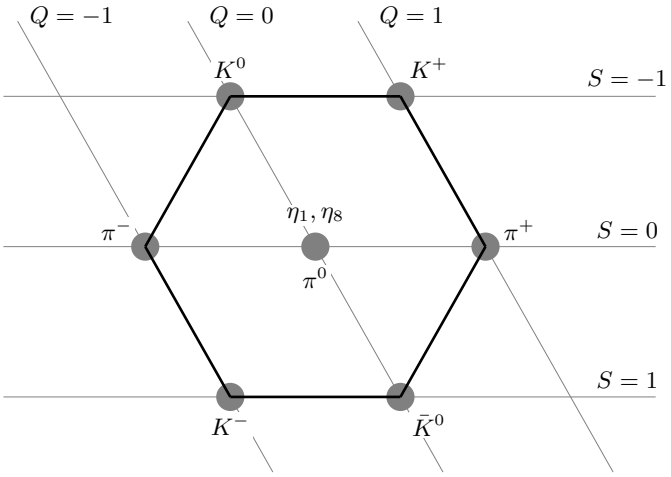

Figure 1.1.: Octet and singlet of pseudoscalar mesons.

meson	quark content	mass [MeV]
π^0	$(d\bar{d} - u\bar{u})/\sqrt{2}$	134.98
π^+	$u\bar{d}$	139.57
π^+	$d\bar{u}$	139.57
K^+	$u\bar{s}$	493.68
K^+	$s\bar{u}$	493.68
K^0	$d\bar{s}$	497.61
$\bar{K}^0$	$s\bar{d}$	497.61
η_1	$(d\bar{d} + u\bar{u} + s\bar{s})/\sqrt{3}$	-
η_8	$(d\bar{d} + u\bar{u} - 2s\bar{s})/\sqrt{6}$	-
η	$\approx \eta_8$	547.85
η'	$\approx \eta_1$	957.78
ρ^0	$(u\bar{u} - d\bar{d})/\sqrt{2}$	775.49
ρ^+	$u\bar{d}/\sqrt{2}$	775.40

Table 1.1.: Quark content and masses of mesons relevant for this thesis.

ρ^0, ρ^+. One can see that the pions have unexpectedly low masses in comparison with the ρ mesons, whose quark content is identical. Moreover η and η' mesons, with a similar quark content present a large difference in their masses. This intriguing pattern of the meson masses has been a major motivation of this thesis with the goal to understand theoretically this pattern from QCD.

Notice that η_1 and η_8 are the particles which belong to the singlet and the octet respectively whereas the particles which are actually observed experimentally, η and η', are linear combinations of them. The reason is that the electroweak force causes a mixing of eigenstates. However the mixing in this case is not very significant and the quark content of η is similar to the η_8 whereas η' is close to η_1. For more details we refer to any specialized text, e.g. Ref. [5].

Following the same strategy one can decompose the tensor product that represents the baryons $\mathbf{3} \otimes \mathbf{3} \otimes \mathbf{3}$, composed by three quarks, in $\mathbf{10} \otimes \mathbf{8} \otimes \mathbf{8} \otimes \mathbf{1}$ or equivalently the antibaryons $\bar{\mathbf{3}} \otimes \bar{\mathbf{3}} \otimes \bar{\mathbf{3}}$. Nevertheless we do not develop this line of thought further here.

1.1.2. Asymptotic freedom and confinement

QCD was introduced as the model which describes the strong interactions through a non-Abelian gauge theory with gauge group $SU(3)$ which is coupled to fermions in the fundamental representation. The reason to describe the strong nuclear interactions through a non-Abelian gauge group is that non-Abelian gauge theories were found to be asymptotically free [6]. This is a fundamental property of the strong interactions which states that for small distances (large energies) the quarks behave as free particles.

Consequently the interaction of quarks was described using a $SU(3)$ gauge group. This group represents the gauge fields through which the strong interactions are mediated. The $SU(3)$ gauge fields are referred to as *gluons*. Gluons belong to the Lie algebra of $SU(3)$

and also carry a color index. The non-Abelian nature of the gauge group implies that the gauge fileds also interact among themselves. The self-interacting property of gluons has strong consequences, such as the confinement of quarks, which explains why experimentally only compound systems of quarks (hadrons) are found and isolated quarks have never been observed. Confinement [7] becomes relevant at low energies, corresponding to large distances. This is in contrast to high energies, where the theory is asymptotically free [8, 9].

The strong coupling α_s determines how the fields in QCD interact with each other. The coupling constant in QCD depends directly on the energy and it is, therefore, usually known as the *running* coupling. The coupling becomes very large at low energies and decreases at high energies. This behavior of α_s, in contrast with other theories like QED, is directly related to the phenomena of confinement and asymptotic freedom.

QCD, remarkably, is expected to describe both phenomena, confinement at low energy and asymptotic freedom at high energies. In order to study the high energy regime of QCD one can make an approximation through a perturbative expansion in terms of the coupling constant. This method provides a very good description of the high energy phenomena and its theoretical predictions have been proven to be in very good agreement with experimental results.

However, to study low energy phenomena such as the hadron spectrum or chiral symmetry, the coupling constant becomes too large, preventing the use of perturbation theory. The only non-perturbative method proposed from first principles is based on the path integral representation of Greens functions. Moving to Euclidean space and introducing a 4-dimensional Euclidean finite lattice first of all regularizes the theory completely. In addition, it enables the application of numerical techniques to provide quantitative predictions avoiding the use of perturbative expansions. The concept of formulating the theory on a discretized Euclidean space-time lattice is referred to as lattice QCD and it provides nowadays the most successful non-perturbative evaluation of QCD. Moreover it offers a link between the high energy and the low energy regime since some high energy phenomena can also be addressed on the lattice, either by applying lattice perturbation theory or through numerical techniques.

1.1.3. QCD action

Quarks and antiquarks are massive fermions in the fundamental representation of $SU(3)$ gauge group and are represented by Dirac spinors

$$\psi(x), \qquad \overline{\psi}(x). \tag{1.2}$$

In principle the elements described in Eq. (1.2) carry a Dirac index, generally denoted by a greek letter, a flavor index f and a color index a

$$\psi(x) = \left(\psi_f^a(x)\right)_\alpha . \tag{1.3}$$

However, for clarity of notation, we usually omit the Dirac, color and flavor indices.

On the other hand gluons are massless gauge fields represented by traceless anti-hermitian 3×3 matrices which live in the adjoint representation of $SU(3)$ and are defined at each space-time x and for a given Lorentz index μ

$$A_\mu(x). \tag{1.4}$$

We are interested in the continuum QCD action which consists of three terms: one represents the quark fields, another one the propagation and self-interaction of the gluon fields and an additional interaction term which describes the interaction between quarks and gluons. Since all the phenomena we are interested in belong to the low energy regime of QCD, we ultimately require a non-perturbative method to analyze the theory. In particular we adopt lattice QCD as the regulator of our theory. Before we discuss lattice QCD, we introduce the continuum QCD action in Euclidean space-time.

The fermionic part of the action includes the interacting term and it is written as

$$S_F[\psi,\overline{\psi},A] = \sum_{f=1}^{N_f}\int d^4x\overline{\psi}^f(x)(\gamma^\mu D_\mu + m^f)\psi^f(x), \tag{1.5}$$

where D_μ represents the covariant derivative which is given by

$$D_\mu = \partial_\mu + A_\mu. \tag{1.6}$$

In Eq. (1.5) and in the following, the Einstein summation convention is assumed. In particular the sum over Lorentz indices accounts for the Lorentz invariance of the action.

On the other hand the gluonic part of the action is

$$S_G[A] = \frac{1}{2g^2}\int d^4x \text{ tr } [F_{\mu\nu}(x)F_{\mu\nu}(x)] \tag{1.7}$$

where the trace is over color indices in order to guarantee gauge invariance and $F_{\mu\nu}$ is the field strength tensor given by

$$F_{\mu\nu} = [D_\mu, D_\nu] = \partial_\mu A_\nu(x) - \partial_\nu A_\mu(x) + [A_\mu(x), A_\nu(x)]. \tag{1.8}$$

In Eq. (1.8) the term $[A_\mu(x), A_\nu(x)] \neq 0$ implies the self-interaction property of the gauge fields, which is, as said above, a remarkable feature of QCD leading to confinement.

The QCD action is then given by

$$S_{QCD}[\psi,\overline{\psi},A] = S_F[\psi,\overline{\psi},A] + S_G[A] \tag{1.9}$$

which is gauge and Lorentz invariant, both being fundamental symmetries of QCD. However we are particularly interested in another symmetry which has fundamental implications on the spectrum of QCD: chiral symmetry. In the next section chiral symmetry will be defined and its consequences will be discussed.

1.2. Chiral Symmetry

Once the QCD action has been introduced it can be analyzed with respect to the transformations which leave the Lagrangian invariant. In the following we focus on the two flavor theory where only the lightest quarks are considered. As it was previously mentioned, Eq. (1.9) remains invariant under Lorentz transformations and has a $SU(3)$ color gauge symmetry. In addition, the QCD action has an approximate global $U(2) \times U(2)$ flavor symmetry [1].

To study in detail this flavor symmetry we introduce the chiral projector operators $P_L,\ P_R$ which transform the spinor fields $\psi(x)$ into its chiral components $\psi_L,\ \psi_R$ in the following way

$$\psi_L = P_L\ \psi = \left(\frac{1-\gamma_5}{2}\right)\psi, \quad \psi_R = P_R\ \psi = \left(\frac{1+\gamma_5}{2}\right)\psi. \tag{1.10}$$

where $\psi = \psi_L + \psi_R$. If we apply these transformations to the fermionic part of the QCD action

$$\mathcal{L} = \overline{\psi}\gamma^\mu D_\mu \psi + m\overline{\psi}\psi \tag{1.11}$$

one can see that the mass term transforms differently from the interaction term. In particular in the first term of Eq. (1.11)

$$\overline{\psi}\gamma^\mu D_\mu \psi = (\overline{\psi}_L + \overline{\psi}_R)\gamma^\mu D_\mu(\psi_L + \psi_R) = \overline{\psi}_L\gamma^\mu D_\mu \psi_L + \overline{\psi}_R\gamma^\mu D_\mu \psi_R, \tag{1.12}$$

one can rotate the left- and right-handed parts of the Dirac fields independently, whereas the mass term

$$m\overline{\psi}\psi = m(\overline{\psi}_L + \overline{\psi}_R)(\psi_L + \psi_R) = m\overline{\psi}_L\psi_R + m\overline{\psi}_R\psi_L \tag{1.13}$$

mixes both chiral components.

All transformations which treat left-handed and right-handed fields separately are chiral transformations. We can then conclude that the global $U(2)\times U(2)$ flavor symmetry is an exact symmetry of *only* the massless theory, since the mass term breaks chiral symmetry explicitly. However, if we consider the two flavor theory with the up and down quark, $U(2) \times U(2)$ is a good approximation to a symmetry due to the low values of the quark masses which correspond to few MeV. Even three flavors would be an acceptable, nevertheless worse, approximation, since the mass of the strange quark introduced in the theory is comparable to the typical QCD scale Λ_{QCD}.

Due to the fact that the chiral transformations in the massless QCD Lagrangian treat left- and right-handed parts of the Dirac fields separately, our global $U(2)$ flavor symmetry can be decomposed in the following way

$$U(2)_L \times U(2)_R. \tag{1.14}$$

[1] For a more comprehensive discussion about chiral symmetry from a latticist perspective, the author recommends Refs. [10, 11].

For convenience we can rewrite Eq. (1.14) into its $SU(2)$ and $U(1)$ parts

$$SU(2)_L \times SU(2)_R \times U(1)_L \times U(1)_R. \tag{1.15}$$

The associated currents of the symmetries given in Eq. (1.15) are

$$L_\mu = \overline{\psi}_L \gamma_\mu \psi_L, \quad R_\mu = \overline{\psi}_R \gamma_\mu \psi_R \tag{1.16}$$

in the singlet case, for $U(1)_L$ and $U(1)_R$ respectively. And for the non-singlet case, $SU(2)_L \times SU(2)_R$, the currents would take the following form

$$L^a_\mu = \overline{\psi}_L \gamma_\mu \tau_a \psi_L, \quad R^a_\mu = \overline{\psi}_R \gamma_\mu \tau_a \psi_R, \tag{1.17}$$

where $\tau_a = \sigma_a/2$ are the generators of the $SU(2)$ group.

Let us analyze Eq. (1.15) in more detail. To do so we first focus on $U(1)_L \times U(1)_R$.

The associated transformations to $U(1)_L \times U(1)_R$ are given by

$$U(1)_L: \quad \psi'_L \to e^{i\theta_L}\psi_L, \tag{1.18}$$

$$U(1)_R: \quad \psi'_R \to e^{i\theta_R}\psi_R, \tag{1.19}$$

which corresponds to a rotation in flavor space.

For our original Dirac field

$$\psi' = \left[\frac{1}{2}(e^{i\theta_L} + e^{i\theta_R}) + \frac{1}{2}(e^{i\theta_L} - e^{i\theta_R})\gamma_5\right]\psi = (e^{i\theta_L}P_L + e^{i\theta_R}P_R)\psi \tag{1.20}$$

where $e^{i\theta_L}, e^{i\theta_R}$ are unitary matrices and $P_L,\ P_R$ are the chiral projectors introduced in Eq. (1.10).

We can now define the vector subgroup $U(1)_V \subset U(1)_L \times U(1)_R$ which corresponds to setting $\theta_L = \theta_R = \theta$ and whose transformations are

$$\psi' \to (e^{i\theta}P_L + e^{i\theta}P_R)\psi = e^{i\theta}\psi. \tag{1.21}$$

On the other hand the axial subgroup $U(1)_A$ is given by

$$\psi \to \left[e^{-i\theta_5}\left(\frac{1-\gamma_5}{2}\right) + e^{i\theta_5}\left(\frac{1+\gamma_5}{2}\right)\right]\psi = e^{i\theta_5\gamma_5}\psi \tag{1.22}$$

where $\theta_5 = \theta_R = -\theta_L$.

We finally obtain the following symmetry group

$$SU(2)_L \times SU(2)_R \times U(1)_V \times U(1)_A \tag{1.23}$$

where $U(1)_V \times U(1)_A$ is associated with the following transformations

$$U(1)_V: \quad \psi' \to e^{i\theta}\psi, \quad \overline{\psi}' \to e^{-i\theta} \tag{1.24}$$

$$U(1)_A: \quad \psi' \to e^{i\theta_5\gamma_5}\psi, \quad \overline{\psi}' \to e^{i\theta_5\gamma_5} \tag{1.25}$$

In principle the massless QCD Lagrangian is invariant under both transformations given in Eq. (1.24) and Eq. (1.25), however in the axial case (Eq. (1.25)) there is a most interesting subtlety. Noether's theorem states that global symmetries lead to conserved currents, therefore the vector and the axial current should be conserved. In the case of the axial current, however, it is only classically conserved, but the symmetry is broken at the quantum level by the chiral anomaly and therefore an extra term appears in the divergence of the current which takes the following form in the massless theory in four dimensions

$$\partial_\mu A_\mu(x) = -\frac{g^2}{16\pi^2}\epsilon_{\mu\nu\rho\sigma}F_{\mu\nu}F_{\rho\sigma}. \tag{1.26}$$

where $A_\mu = R_\mu - L_\mu = \overline{\psi}(x)\gamma_\mu\gamma_5\psi(x)$ is the singlet axial vector current which corresponds to the difference of the left and right-handed currents introduced in Eq. (1.16). Therefore, the axial $U(1)_A$ symmetry is explicitly broken by the chiral anomaly. We will come back to this observation in the coming sections.

In contrast, the $U(1)_V$ symmetry is indeed an exact symmetry of the massless theory and therefore it has an associated conservation law of the baryon number and, correspondingly, has an exactly conserved Noether current

$$\partial_\mu V_\mu = 0. \tag{1.27}$$

where $V_\mu = R_\mu + L_\mu = \overline{\psi}(x)\gamma_\mu\psi(x)$ is the singlet vector current given by the sum of the left- and the right-handed currents of Eq. (1.16).

So far, we have considered the massless theory. However, let us for a moment extend the discussion to the massive theory. To this end, we will look at the axial and vector currents of $U(1)$ and $SU(2)$, which are constructed through the difference and sum of the left- and right-handed currents introduced in Eq. (1.16) and Eq. (1.17) respectively for the axial and vector case

$$\partial_\mu V_\mu = 0 \tag{1.28}$$

$$\partial_\mu A_\mu = \overline{\psi}\gamma_5 M\psi - \frac{\alpha_s}{4\pi}\epsilon_{\mu\nu\rho\sigma}G_{\mu\nu}G_{\rho\sigma} \tag{1.29}$$

$$\partial_\mu V^a_\mu = \overline{\psi}\left[M, \tau^a\right]\psi \tag{1.30}$$

$$\partial_\mu A^a_\mu = \overline{\psi}\gamma_5\left\{M, \tau^a\right\}\psi. \tag{1.31}$$

In Eq. (1.30) and Eq. (1.31) $\tau_a = \sigma_a/2$ corresponds again to the generators of the $SU(2)$ group. M represents the diagonal mass matrix whose non-zero elements are given by the quark masses.

The singlet vector current is always conserved, even for finite quark massess and it is directly related to the baryon number conservation. The vector currents are conserved for degenerate quark masses. Thus, due to the small difference in the masses of the lightest quarks, up and down, $SU(2)$ is known as the isospin symmetry.

We have completed the basic analysis of the $U(1)_L \times U(1)_R$ part of Eq. (1.15) where

we have found the exact $U(1)_V$ symmetry related to the baryon number conservation. We have also touched upon the $U(1)_A$ symmetry and its breaking through the chiral anomaly which will be discussed in detail in further sections.

To summarize, we found the following global symmetry for the QCD Lagrangian

$$SU(2)_L \times SU(2)_R \times U(1)_V. \tag{1.32}$$

In the massless theory Eq. (1.32) should, in principle, be an exact symmetry. However this would imply that the nucleon N and its parity counterpart $N^\star$ would be degenerate in mass, which does not correspond with observations. The mass of the nucleon is around 940 MeV, whereas the $N^\star$ mass is of 1535 MeV. Such a large difference cannot be explained by the explicit isospin breaking of the up and down quark masses, since this effect is supposed to be small and at most at the order of a few MeV. Consequently there must be another reason for the mass difference of nucleon mass and the $N^\star$ mass.

The basic and fundamental mechanism is that the axial part of the $SU(2)_L \times SU(2)_R$ symmetry is *spontaneously* broken. A symmetry is said to be spontaneously broken when the Lagrangian remains invariant under the given transformations whereas the ground state of the system does not. The spontaneous chiral symmetry breaking leads to the formation of a non-vanishing fermion condensate, $\langle \overline{\psi}\, \psi \rangle$, which is not invariant under axial transformations, and which takes a non-vanishing value even in the chiral limit. It can be proven that the transformations of $SU(2)_V$ leaves the condensate invariant whereas the axial transformations mixes the left- and right-handed parts, very similar to our discussion of the mass term in the Lagrangian above. In fact, the chiral condensate acts as a mass term breaking the symmetry spontaneously. This implies the existence of massless Goldstone bosons which will be introduced in the next section.

The spontaneous breaking of chiral symmetry explains the observation that the nucleon and its parity counterpart $N^\star$ are not degenerate in mass, as one would naively expect studying the symmetries at the Lagrangian level.

The final expression of the global flavor symmetry takes therefore the reduced form

$$SU(2)_V \times U(1)_V \tag{1.33}$$

for degenerate quark masses.

In conclusion in QCD there are three sources of chiral symmetry breaking: the non-zero mass of the quarks which breaks chiral symmetry explicitly, the spontaneous breaking given by a non-vanishing value of the chiral condensate and the $U(1)_A$ chiral anomaly.

In the next sections we will study in detail the phenomena spontaneous chiral symmetry breaking and the chiral anomaly as well as their phenomenological implications which serve as the principal motivation for this thesis.

Renormalizable quark mass

As a side remark, we mention that chiral symmetry ensures that quark masses are only multiplicatively renormalized. Thus it avoids fine tuning if one is to find light fermion in the spectrum. This is an important fact, since there exist lattice QCD formulations which

break chiral symmetry explicitly even at zero quark mass. In such a situation, a additive renormalization of the quark mass is necessary leading to a fine tuning of parameters in the action. A prominent example for such a lattice action are Wilson fermions where the so-called Wilson term breaks chiral symmetry explicitly.

1.2.1. Spontaneous breaking of chiral symmetry

It is one of the most important properties of QCD that the strong interaction between quarks results in a non-zero quark condensate $\langle\overline{\psi}\psi\rangle$. If the axial transformations are applied to the vacuum expectation value of the condensate it leads to the mixing of left- and right-handed fields

$$\langle\overline{\psi}\psi\rangle = \langle\overline{\psi}_L\psi_R + \overline{\psi}_R\psi_L\rangle \neq 0. \tag{1.34}$$

Since this mixing is closely related to chiral symmetry, the expectation value in Eq. (1.34) is usually referred to as the chiral condensate and we will adopt this notation in the following. A rough estimate for the size of chiral condensate is that it should be around Λ^3_{QCD}, with $\Lambda_{QCD} \approx (250\text{GeV})^3$ the typical QCD scale.

A non-vanishing chiral condensate directly implies that the axial part of the $SU(2)_R \times SU(2)_L$ symmetry is spontaneously broken, since the Lagrangian of the system remains invariant under the given transformations, whereas the ground state given by the chiral condensate does not. Consequently the chiral condensate becomes an order parameter of the spontaneous breaking of chiral symmetry.

Notice that the chiral condensate is a non-perturbative quantity which vanishes at tree level of perturbation theory and whose perturbative corrections also vanish due to the symmetries of the Lagrangian. Consequently this observable is not accesible in perturbation theory. It is only the non-perturbative lattice QCD methods which, in principle, are able to test spontaneous chiral symmetry breaking and to determine quantitatively the size of the chiral condensate which is exactly one of the major goals of this thesis.

In the next section the consequences of the spontaneous chiral symmetry breaking will be introduced and discussed.

Goldstone theorem

The Goldstone theorem states that when a continuous global symmetry is spontaneously broken massless particles appear in the spectrum. Such a situation corresponds to a Lagrangian of the system which is invariant under this symmetry and the Noether currents are conserved whereas the ground state of the system is not invariant. Moreover, the Goldstone theorem states that the number of massless particles is equal to the number of generators of the spontaneously broken symmetry.

In the last section we have studied that $SU(2)_L \times SU(2)_R$ breaks spontaneously to $SU(2)_V$. The $SU(2)$ group has three generators and therefore we expected to find three Goldstone bosons in the spectrum which are identified with the pions. This explains the unexpectedly low masses of the pions that we observed in Tab. 1.1, since the pions are effectively Goldstone bosons. The reason why the pions do not appear massless in nature

is due to the explicit breaking induced by the small, but non-zero, quark masses. Of course, the masses of the lightest quarks are very low and therefore the explicit breaking is certainly mild giving the pions a light mass.

In the $N_f = 3$ case there would be eight Goldstone bosons corresponding to the eight generators of the group $SU(3)$. The Goldstone bosons are then given by the octet of pseudo-scalar mesons, which includes the pions, the kaons and the η.

1.2.2. $U(1)_A$ anomaly

The transformations associated to the $U(1)_A$ symmetry leave the QCD Lagrangian invariant, whereas the condensate again mixes left- and right-handed fields. In principle we could suspect that the $U(1)_A$ symmetry is spontaneously broken and therefore we would expect a Goldstone boson corresponding to the generator of the group. However the η' meson, which would be the corresponding massless particle in the spectrum, is too heavy to be considered a Goldstone boson, i.e. the explicit breaking given by the low quark masses does not justify a mass of η' of around 960 MeV. The reason for this large mass is that $U(1)_A$ is not a continuous symmetry of the quantum field theory, since it is explicitly broken by the chiral anomaly to a discrete symmetry, and therefore the η' cannot be considered a Goldstone boson.

In the previous section we discussed, without entering into details, that the divergence of the singlet axial current corresponding to the $U(1)_A$ symmetry is classically conserved

$$\partial A_\mu = 0 \tag{1.35}$$

in the theory with massless fermions.

However, $U(1)_A$ is not a symmetry of the quantum field theory and the radiative corrections give an additional term to Eq. (1.35), as it was introduced in Eq. (1.26). The non-vanishing divergence of the singlet axial current at the quantum level is called *the chiral anomaly*. In fact, it can be shown that the conservation of the singlet axial current is not compatible with gauge invariance [1].

There are several approaches that can be followed to compute the chiral anomaly. It can be shown perturbatively, originally for the case of Abelian theories like QED [12, 13], that the divergence of the axial current has a non-zero matrix element that create two photons. This can be extended to QCD through the coupling of massless fermions to non-Abelian gauge fields.

Alternatively [14] one can perform the following chiral transformations

$$\begin{aligned} \psi(x) &\to \psi'(x) = (1 + i\alpha(x)\gamma_5)\psi(x) \\ \overline{\psi}(x) &\to \overline{\psi}'(x) = \overline{\psi}(1 + i\alpha(x)\gamma_5), \end{aligned} \tag{1.36}$$

to the fermionic functional integral given by

$$Z = \int D\psi D\overline{\psi} \exp\left[\int d^4x \, \overline{\psi} \not{D} \psi\right], \tag{1.37}$$

and compute the contribution given by the fact that the measure of the integral does change with the change of variables due to the non-trivial Jacobian $\mathcal{J}$ which is given by

$$\mathcal{J} = \exp\left[-\frac{g^2}{16\pi^2}\epsilon_{\mu\nu\sigma\rho}F^{\mu\nu}F^{\sigma\rho}\right]. \tag{1.38}$$

In either case the conclusion is that the divergence of the singlet axial current has the following form with an additional term

$$\partial_\mu A_\mu = M\overline{\psi}\gamma_5\psi + \frac{g^2}{16\pi^2}\epsilon_{\mu\nu\sigma\rho}F^{\mu\nu}F^{\sigma\rho}. \tag{1.39}$$

Notice that in Eq. (1.39) we consider a theory with massive fermions.

Index Theorem

One remarkable result, directly linked to the $U(1)_A$ anomaly, is the index theorem [15], which relates the zero modes of the Dirac operator to the topological charge density represented by the anomalous term which appears in the divergence of the axial current (Eq. (1.39)). Due to its relevance for the work presented in this thesis and following Ref. [10] we attempt to sketch the derivation below for degenerate quarks.

The information about the topology of the gauge fields is contained in the winding number, also known as topological charge, an integer number associated to each gauge field and which, importantly, remains unchanged under continuous deformations of the configuration. The winding number can be defined as

$$\nu = \frac{g^2}{32\pi^2}\int d^4x\ \epsilon_{\mu\nu\sigma\rho}\mathrm{tr}\ F^{\mu\nu}F^{\sigma\rho}. \tag{1.40}$$

If we integrate Eq. (1.39) the divergence of the current vanishes, since it is a pure divergence, and one is left with the following expression

$$\int d^4x\ m\left\langle\overline{\psi}\gamma_5\psi\right\rangle_F = -\nu, \tag{1.41}$$

where we have applied the definition of the winding number and $\langle\rangle_F$ refers to the fermionic expectation value.

If we write $\left\langle\overline{\psi}\gamma_5\psi\right\rangle_F$ in terms of the path integral is given by

$$\left\langle\overline{\psi}\gamma_5\psi\right\rangle_F = \frac{1}{\mathcal{Z}}\int D\psi D\overline{\psi}e_F^S(m\overline{\psi}\psi), \quad \mathcal{Z} = \int D\psi D\overline{\psi}e_F^S \tag{1.42}$$

where S_F is the massive Euclidean fermionic action.

We expand the fermion fields in terms of eigenstates of the Dirac operator after a few

steps of algebra, one finds

$$\int d^4x \, m \left\langle \overline{\psi}\gamma_5\psi \right\rangle_F = m \sum_n \int d^4x \, \frac{\psi_n^\dagger \gamma_5 \psi_n}{i\lambda + m} \tag{1.43}$$

Since $\left\{\gamma_5, \not{D}\right\} = 0$, the eigenstates of ψ and $\gamma_5\psi$ for $\lambda_n \neq 0$ are orthogonal and therefore $\psi\gamma_5\psi$ cancels. Consequently the only terms which contribute to the sum are those for $\lambda_n = 0$, i.e. the zero modes, which are eigenstates of γ_5 and $\not{D}$ simultaneously.

We are thus led to main result of the index theorem

$$n_- - n_+ = \nu \tag{1.44}$$

which relates the number of zero modes of negative (n_-) and positive (n_+) chirality of the Dirac operator to the winding number ν and therefore the topological charge of the gauge fields.

A related quantity which is of high relevance for the study of topology is the topological susceptibility χ_{top} which is defined as

$$\chi_{\text{top}} = \frac{\langle Q^2 \rangle}{V} \tag{1.45}$$

and accounts for the fluctuations of the topological charge Q, or equivalently, the winding number ν.

Witten-Veneziano Formula

The Witten-Veneziano formula [16, 17] relates the mass of the η' meson with the topological susceptibility in the pure gluonic theory in the following way

$$\frac{F_\pi^2}{2N_f}\left(m_\eta^2 + m_{\eta'}^2 - 2m_K^2\right) = \chi_\infty \tag{1.46}$$

where $N_f = 3$ is the number of light flavors and where F_π is the pion decay constant.

This is an extraordinary result which aims to give an explanation to the unexpectedly large mass of the η' meson, which, through this formula, is directly related to the fluctuations of the topological charge of the gauge fields. The $U_A(1)$ problem is then explained by the appearance of topologically non trivial gauge configurations in QCD.

This remarkable result can be obtained by taking the large N_c limit, where simplifications of the theory allow us to address a variety of problems otherwise not reachable. In particular, in Ref. [16], the 't Hooft limit ($N_c \to \infty$, while $g^2 N_c$ and N_f are kept fixed) is taken. Alternatively, an expansion in $u = N_f/N_c$ around $u = 0$ can be used if it is assumed that it remains valid at all orders [17].

In the chiral limit the Witten-Veneziano formula takes the following form

$$\frac{F_\pi^2}{2N_f} m_{\eta'}^2 = \chi_\infty, \tag{1.47}$$

since η and the kaon mesons are Goldstone Bosons. This expression can be obtained in an intuitive way through the study of anomalous flavor-singlet Ward-Takahashi identities in limit $u \to 0$[18, 19].

In the large N_c limit, the fermionic determinant becomes negligible and can be ignored, therefore, the topological susceptibility which appears on the right-hand side of Eq.(1.47) must be computed in the pure Yang-Mills theory. If this approximation is valid only when N_c goes to infinity, then Eq.(1.47) is valid up to $\mathcal{O}(1/N_c)$ corrections.

To fully understand Eq.(1.47) is not an easy matter. However, an important claim is the fact that the $m_{\eta'} \sim 1/N_c$ and therefore vanishes at $N_c = \infty$. In such limit the anomaly does not appear and $m_{\eta'}$ becomes a Goldstone Boson whose mass vanishes in the chiral limit.

1.2.3. Conclusions

After the discussion given above we can then conclude that the peculiarities found in the spectrum of the pseudo-scalar mesons have their origin in the breaking of chiral symmetry. On the one hand a non-vanishing value of the chiral condensate leads to the spontaneous breaking of chiral symmetry and therefore to the appearance of Goldstone bosons in the spectrum, which for $N_f = 2$ correspond to the pions.

On the other hand the chiral anomaly breaks the $U(1)_A$ symmetry explicitly which leads to unexpectedly large mass of the η' meson. Moreover the large mass of the η' meson emphasizes the importance of the topology of the gauge fields since it appears to be responsible of the mechanism described by the Witten-Veneziano formula which relates the η' mass to the topological susceptibility in the pure gluon theory.

In this thesis we present a study of the relevant quantities directly related to the phenomena explained above. We perform a precise and reliable calculation of the chiral condensate, which, as expected, takes a value of $\mathcal{O}(\Lambda^3_{\mathrm{QCD}}) \approx 250\mathrm{GeV}$ in the chiral limit. In addition we study the chiral behavior of the topological susceptibility in the case of dynamical fermions and we attempt a first test of the Witten-Veneziano formula through the calculation of the topological susceptibility in the pure gluon theory. As already stressed, since the involved observables, i.e. the masses, the chiral condensate and the topological susceptibility belong to the low energy regime of QCD, a non-perturbative method has to be applied for their computation. To this end, we will employ in this thesis the lattice formulation of quantum chromodynamics. In the next section, we will provide an introduction to lattice QCD and explain, how this discretized version of QCD can be used to address the quantities of interest here.

CHAPTER 2

Lattice regularization

Contents

In the previous chapter we discussed the importance of chiral symmetry, a fundamental property of QCD, and its implications. Chiral symmetry requires a non-perturbative treatment of QCD. It is for this reason that we need to present lattice QCD, a formulation first introduced in 1974 by K. Wilson [7], which allows to study non-perturbative phenomena such as the hadron spectrum or chiral symmetry breaking among others.

In this chapter we first introduce the path integral representation in Euclidean space, which is the basic ingredient of lattice QCD. We also discuss different discretizations of the action including twisted mass fermions which is the discretization we chose for our calculations due the advantages that it offers. At the end we address the challenging implementation of chiral symmetry on the lattice and the progress that have been made over the years in that area.

The main aim of the present chapter is to briefly introduce the generalities of the field which are needed to understand the present work. Thus we refer to specialized books and lectures notes where lattice QCD has been discussed in detail for a deeper understanding of the topic, e.g. Refs. [20, 21, 22].

2.1. Path integral formalism

The path integral representation of the Green functions is the basis of the non perturbative quantization in lattice field theory. The reason is that going to imaginary time ($t \to -i\tau$) the Green function takes the same form of a correlation function in a statistical mechanics system defined by a partition function. This enables us to work with analytical and, more important, numerical techniques of (Euclidean) field theory and statistical mechanics.

The Euclidean correlators in the path integral formalism are described by the following expression

$$\langle \mathcal{O} \rangle = \frac{1}{Z} \int \mathcal{D}\psi \mathcal{D}\overline{\psi} \mathcal{D}A_\mu \, \mathrm{e}^{-\mathrm{S_F}[\psi,\overline{\psi},A_\mu]-\mathrm{S_G}[A_\mu]} \mathcal{O}[\psi,\overline{\psi},A_\mu], \tag{2.1}$$

where Z is the partition function which is given by

$$Z = \int \mathcal{D}\psi \mathcal{D}\overline{\psi} \mathcal{D}A_\mu \, \mathrm{e}^{-\mathrm{S_F}[\psi,\overline{\psi},A_\mu]-\mathrm{S_G}[A_\mu]}, \tag{2.2}$$

and $\mathrm{S_F}$ and $\mathrm{S_G}$ are the Euclidean fermionic and gluonic action respectively, which were already introduced in the previous chapter.

These integrals only have a rigorous meaning if we work with a finite number of degrees of freedom. We need to introduce a regularization which includes an ultraviolet and an infrared cutoff . One possibility is to discretize the continuous space-time. We thus introduce a 4D Euclidean space-time lattice of extend L, whose spacing between points we will denote by a, see Fig. 2.1. This regularization provides, by the inverse of a, an ultraviolet cutoff, whereas a finite extend L serves as an infrared regularization. The lattice spacing a will act as a regulator of the Feynman integrals and therefore of QCD. The advantage of this regularization is that it allows us to study quantum systems through numerical evaluation, a fundamental tool to provide quantitative predictions

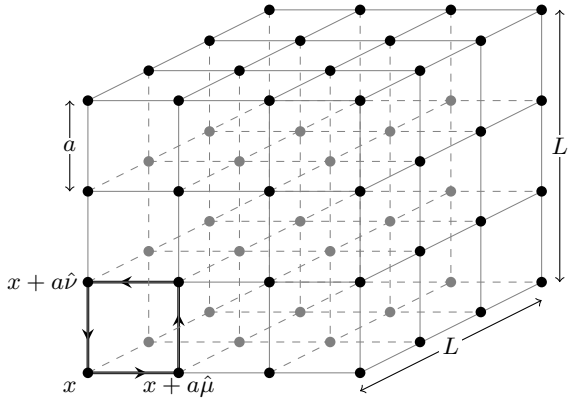

Figure 2.1.: 3-dimensional lattice

without using perturbative expansions. This fundamental feature opens the possibility to study low energy regimes, where perturbative methods cannot be applied due to the large value of the coupling constant, and therefore study problems that otherwise are not available to us like chiral symmetry.

Another crucial aspect to complete the quantization of the system is the discretization of the action. This task seems no to be too difficult when we treat the gluonic action. However, to discretize the fermionic action happened to be a more complex problem, as it will be explained in the following sections.

2.2. Gluons on the lattice

As we have already mentioned we regularize our theory by inserting a 4 dimensional lattice which will discretize our space-time by replacing our continuum variable x_μ with the discrete coordinate n_μ in all the four directions μ. We also need to substitute the integrals by sums in the following way

$$\int d^4x \to a^4 \sum_{n_\mu}. \tag{2.3}$$

In order to discretize the QCD action there are several restrictions we have to respect. The most important one is that we must recover the continuum expression of the action when we take the continuum limit $a \to 0$.

Another crucial issue that we need to consider are the symmetries that have to be preserved. When we discretize the theory by introducing a 4 dimensional Euclidean lattice there are, obviously, several symmetries that we loose, like Lorentz or rotation invariance. However we do need to preserve the gauge invariance, since physical observables are gauge invariant and moreover non-gauge invariant objects vanish under the path integral [23].

Before starting the discretization of the gluonic action, taking into account all the

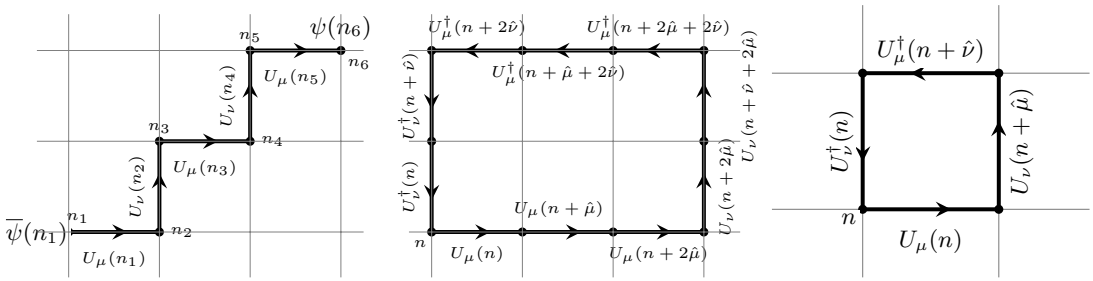

Figure 2.2.: Gauge invariant objects on the lattice. a.) corresponds to Eq. (2.10, b.) corresponds to a closed loop of gauge fields Eq. (2.6) and c.) corresponds to a plaquette Eq. (2.11)

properties we just mentioned, it is important to introduce one of the basic components of the theory: the gauge field $U_\mu(n)$. This element is crucial to keep the gauge invariance of the lattice action as it will be explained in the following lines.

We briefly comment on the properties of $U_\mu(n)$ and the differences with its continuum counterpart A_μ. $U_\mu(n)$ are elements of the $SU(3)$ gauge group, whereas A_μ is an element of the algebra of $SU(3)$. Both elements are related by the following expression

$$U_\mu(n) = \mathrm{e}^{iaA_\mu(n)}. \tag{2.4}$$

The gauge fields U_μ are attached to the link that connect the lattice sites n and $n+\hat{\mu}$[1]. It is for this reason that they are usually called links variables. They transform under gauge transformations as follows

$$U_\mu(n) \to U'_\mu(n) = \Omega(n)U_\mu(n)\Omega(n+\hat{\mu})^\dagger, \tag{2.5}$$

where $\Omega(n)$ denotes an element of the non-Abelian group $SU(3)$ which is unitary, $\Omega(n)^\dagger = \Omega(n)^{-1}$, and whose det[$\Omega(n)$]=1. Thus they represent local rotations among color indices.

We can make use of the gauge fields and its properties to construct gauge invariant objects on the lattice (Fig. 2.2).

An ordered product of link variables which describes a close loop on the lattice and where the trace has been taken is gauge invariant (see Fig. 2.2.c)

$$L[U] = \mathrm{tr}\left[\prod_{(n,\mu)\in \text{ loop}} U_\mu(n)\right]. \tag{2.6}$$

A particular case is the so-called Wilson loop $W[U]$ which consist on a closed loop but with a very specific shape. For a pedagogic understanding we illustrate an example of a non-planar and a planar Wilson loop in Fig. 2.3.a. and Fig. 2.3.b. respectively.

[1]Note that $U_{-\mu}(n) = U_\mu(n-\hat{\mu})^\dagger$ would connect the same sites as $U_\mu(n)$ but in the oposite direction

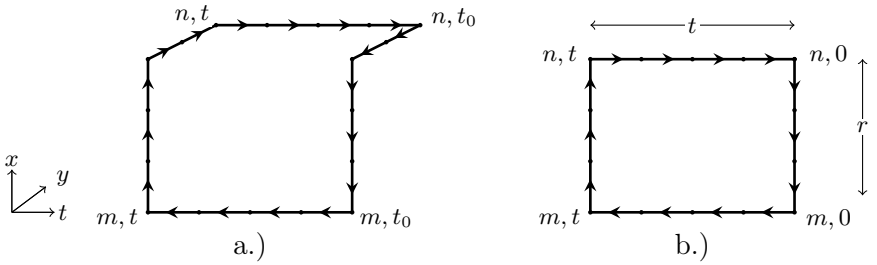

Figure 2.3.: Example of a non-planar (a.) and a planar (b.) Wilson loop on a 3 dimensional lattice.

To construct a Wilson loop we first connect the lattice point (m,t) to (n,t) where m and n are different spatial coordinate of the lattice and t corresponds to the temporal point which is kept fixed. We then keep the spatial coordinates constant and connect two different times (n,t) and $(n,0)$. We apply the inverse of the first step to return to the original space point $(m,0)$ but at a different time, and finally close the loop by connecting back again the time t and 0 keeping the space coordinates m fixed.

This observable is directly related to the quark-antiquark potential and can be used to determine the, a priori unknown, lattice spacing a through the Sommer parameter r_0 [24]. The strategy to set the scale using this method is briefly summarized in App. D.2.2.

We can construct another general gauge invariant object if we introduced the spinors, which represent the fermionic degrees of freedom, and that are now only defined at the lattice points

$$\psi(x) \to \psi(n), \qquad \overline{\psi}(x) \to \overline{\psi}(n), \tag{2.7}$$

and under gauge transformations behaves as follows

$$\psi(n) \to \psi'(n) = \Omega(n)\psi(n), \tag{2.8}$$

$$\overline{\psi}(n) \to \overline{\psi}'(n) = \overline{\psi}(n)\Omega(n)^\dagger. \tag{2.9}$$

Thus we can take an ordered product of links which this time connects two different points n, m of the lattice and insert a spinor at the lattice points n, m to recover gauge invariance. This gauge invariant object takes the following form

$$\overline{\psi}(n)\left[\prod_{(n,\mu)\in \text{ path}} U_\mu(n)\right]\psi(m). \tag{2.10}$$

and it is sketched in Fig. 2.2.a.

To discretize the gluonic action we use the shortest non trivial closed loop, called *plaquette* defined as

$$U_{\mu\nu}(n) = U_\mu(n)U_\nu(n+\hat{\mu})U_\mu(n+\hat{\nu})^\dagger U_\nu(n)^\dagger, \tag{2.11}$$

which is illustrated in Fig. 2.2.c.

We can write the discretized gluon action as a sum over all *plaquettes* where each plaquette is counted only once, independently from the orientation.

$$S_G[U] = \frac{2}{g^2} \sum_{n\in\Lambda} \sum_{\mu<\nu} \text{Re tr}[\mathbb{1} - U_{\mu\nu}(n)]. \tag{2.12}$$

This action is gauge invariant and assumes the continuum form after taking the continuum limit up to $\mathcal{O}(a^2)$ effects

$$S_G[U] = \frac{2}{g^2} \sum_{n\in\Lambda} \sum_{\mu<\nu} \text{Re tr}[\mathbb{1} - U_{\mu\nu}(n)] = \frac{a^4}{2g^2} \sum_{n\in\Lambda} \sum_{\mu<\nu} \text{tr}[F_{\mu\nu}(n)^2] + \mathcal{O}(a^2). \tag{2.13}$$

Nevertheless there are improved versions of this discretized gluonic action that cancel at least some of the $\mathcal{O}(a^2)$ terms and therefore in practice are more suitable, since they approach the continuum limit faster. Thus we introduce the following expression

$$S_G[U] = \frac{\beta}{3} \sum_x \left(b_0 \sum_{1\leq\mu<\nu} \text{Re tr}\left[\mathbb{1} - U_{\mu\nu}(x)\right] + b_1 \sum_{\mu\neq\nu} \text{Re tr}\left[\mathbb{1} - U^{\text{rect}}_{\mu\nu}(x)\right] \right) \tag{2.14}$$

where $U^{\text{rect}}_{\mu\nu}$ is the rectangular Wilson loop, the bare coupling g is written in terms of $\beta = 6/g^2$ and $b_0,\ b_1$ are coefficients that have to be computed to reach the improvement. In order to recover the continuum expression we need the condition $b_0 = 1 - 8b_1$ to be satisfied. In this way the tree-level Symanzik improved action [25, 26] is given by setting $b_1 = -\frac{1}{12}$. On the other hand we obtain the Iwasaki improved action [27, 28] by specifying $b_1 = -0.331$.

2.3. Fermions on the lattice. Doubling problem

Discretizing the gluon action was unproblematic, once it was realized by Wilson that the parallel transporter is the fundamental object to be used. However discretize the Euclidean fermionic action, whose continuous expression was given in Eq. (1.5), is more problematic.

First of all we need to introduce the fermion fields which follow the Fermi statistics and therefore anti-commute $\{\psi_\alpha(x), \psi_\beta(y)\} = 0$. Thus they are represented by Grassman variables. Due to the properties of the Grassman variables and to the fact that in the standard model the fermionic action is always bilinear in quark fields, we can rewrite the functional integral in the following way if we assume suitable conditions for the Dirac operator such that the integration can be performed,

$$\int D[\psi]D[\overline{\psi}]e^{-\int d^4x \overline{\psi}(x)D\psi(x)} = \det D, \tag{2.15}$$

where D is the Dirac operator. We can integrate out exactly the fermion fields and, in the end, we just need to compute the determinant of the Dirac operator.

Even though this task is highly not trivial due to the large dimensionality of the matrix D, it simplifies remarkably the calculation when we evaluate the integral numerically.

The fermion fields can be contracted through the Wick's theorem which, applied to the path integral in the case of a free Dirac field, relates the fermionic propagator to the inverse of the Dirac operator in the following way

$$D^{-1}_{\alpha\beta}(x,y) = \frac{\int D[\psi]D[\overline{\psi}]\psi_\alpha(x)\overline{\psi}_\beta(y)e^{S_F[\psi,\overline{\psi}]}}{\int D[\psi]D[\overline{\psi}]e^{S_F[\psi,\overline{\psi}]}}. \tag{2.16}$$

The fermion propagator is relevant because is the basic building block of many physical correlation functions.

If we naively discretize the fermion action as we did in the gluonic case, the transition from the continuum to the lattice is given by few substitutions. First we define the discretized version of the partial derivative as follows

$$\partial_\mu\psi(x) \to \frac{1}{2a}(\psi(n+\hat{\mu}) - \psi(n-\hat{\mu})). \tag{2.17}$$

However, if after these substitutions we now examine the obtained action we observe that, whereas the mass term remains gauge invariant, the discretized derivative is not. As we previously discussed, it is a crucial requirement that the action remains invariant under local rotations of the color of the quarks, also known as gauge invariance.

Thus we need to insert the gauge field $U_\mu(n)$, which were already introduced, in the derivative to ensure its gauge invariance. It is after this step that we obtain the lattice symmetric covariant derivative

$$\frac{1}{2}(\nabla_\mu + \nabla^\star_\mu)\psi(n) = \frac{1}{2a}(U_\mu(n)\psi(n+\hat{\mu}) - U_\mu(n-\hat{\mu})^\dagger\psi(n-\hat{\mu})), \tag{2.18}$$

which we insert in the action obtaining the *naive* discretization of the fermionic action

$$S_F[\psi,\overline{\psi},U] = a^4\sum_x \overline{\psi}(x)\left(\sum_\mu \frac{1}{2}\gamma_\mu(\nabla_\mu + \nabla^\star_\mu) + m_0\right)\psi(x). \tag{2.19}$$

It is straightforward to show that we recover the continuum action by expanding the link variables in terms of a

$$U_\mu(n) = \mathbb{1} + iaA_\mu(n) + \mathcal{O}(a^2). \tag{2.20}$$

This discretized action differs from the continuum action by $\mathcal{O}(a^2)$ terms and also respects chiral symmetry in the massless theory. However, when we analyze the poles of the quark propagator of massless fermions, a crucial problem appears that can not be ignored.

In the continuum, which is in the end what we are interested in, we find only one

pole which corresponds to the fermion we want to describe. In contrast, if we analyze the lattice propagator for a free fermion using the action given in Eq. (2.19), we find 16 poles, 15 of which are the so-called *doublers* which describe spurious fermions that do not appear in the continuum theory and therefore have to be removed.

In the next sections we introduce a new type of fermions which is free of doublers but, on the other had, introduces another problems like the loss of the $\mathcal{O}(a^2)$ scaling towards the continuum limit and chiral symmetry. We will discuss different proposals to address and partly solve these problems and motivate the choice for our calculations.

2.3.1. Wilson Fermions

In order to solve the problem of the *doublers*, Wilson proposed a new action

$$S_f^W = a^4 \sum_x \overline{\psi}(x)(D_W + m_0)\psi(x), \tag{2.21}$$

where D_W is the Wilson Dirac operator defined as

$$D_W = \sum_{\mu=0}^{3} \left[\frac{1}{2}(\nabla_\mu + \nabla_\mu^\star)\gamma_\mu - ar\nabla_\mu^\star \nabla_\mu \right]. \tag{2.22}$$

which includes an extra term, the so-called Wilson term [29], which contains a second derivative.

In Eq. (2.22) a represents the lattice spacing and r the Wilson parameter that can take values between $0 \leq r \leq 1$. Notice that if we specify $r = 0$ we recover the naive discretization of the action. In the following, for all our calculations, we have set $r = 1$. Our notation and the symmetries of the Wilson action, among others that will be introduced in the next sections, are summarized in App. A.1 and App. A.2 respectively.

The action given in Eq. (2.21) is local and the Wilson term vanishes in the continuum limit, recovering the desired continuum action. However this extra term, apart from removing the *doublers*, it also cancels other good features that the naive action had. It introduces $\mathcal{O}(a)$ terms destroying the $\mathcal{O}(a^2)$ continuum limit scaling that we had and it breaks explicitly chiral symmetry even for $m = 0$. This explicit breaking of chiral symmetry has strong consequences. Among others it induces an additive renormalization of the quark mass, as we explained in the previous chapter.

These two new aspects which the Wilson action introduces are crucial in lattice QCD. We reserve special sections for both of them: the recovery of the $\mathcal{O}(a^2)$ continuum limit scaling and the implementation of chiral symmetry on the lattice.

2.4. $\mathcal{O}(a^2)$ continuum limit scaling

When we introduced the Wilson term in the fermion action we solved the problem of the *doublers* but we also removed some nice features of our action, such as the $\mathcal{O}(a^2)$ scaling to the continuum limit, also known as $\mathcal{O}(a)$ improvement.

To decrease the cut-off effects in order to approach faster the continuum limit is a highly important issue in lattice QCD, since it is directly related to the accuracy of the final computation of physical observables in the continuum limit. Therefore a vigorous effort has been spent into solving this problem by developing $\mathcal{O}(a)$ improved actions which approach the continuum limit in $\mathcal{O}(a^2)$.

In the following we will discuss three different methods to improve our action in order to guarantee the $\mathcal{O}(a^2)$ scaling. Thus we will introduce three different $\mathcal{O}(a)$ improved actions which present different advantages and disadvantages. We will comment on their features, characteristics and requirements to guarantee $\mathcal{O}(a^2)$ scaling to finally motivate our choice.

First of all we describe the Symanzik effective theory which allows us to study the $\mathcal{O}(a)$ terms through the Symanzik expansion. This effective theory is a fundamental tool in lattice QCD since it offers the information about the approach to the continuum limit of the different observables.

We then introduce the so-called clover action which consist on the Wilson action with an additional term which is computed to explicitly cancel the $\mathcal{O}(a)$ terms that appear in the Symanzik expansion.

Immediately after we introduce the twisted mass action which has an automatic $\mathcal{O}(a^2)$ scaling due to symmetry properties of the action. This action is based on the Wilson action and contains an extra twisted mass term. In contrast to the clover action, where several parameters have to be tuned, the twisted mass action only requires the tuning of a single parameter to guarantee the $\mathcal{O}(a^2)$ scaling towards the continuum limit.

Finally, in the next section, we introduce the overlap fermions which respect chiral symmetry and is $\mathcal{O}(a)$ improved. Even though this discretization has all the desirable properties, its application entails a high computational cost which makes, nowadays, unaffordable its extensive used, except for very small lattices.

2.4.1. Symanzik Effective Theory

The Symanzik effective theory is one approach to decrease the discretization effects and it is introduced in order to, in particular, cancel the $\mathcal{O}(a)$ effects. The effective theory takes into consideration the improvement of the action but also the improvement of the observables which are used to calculate the Euclidean correlation functions; which is fundamental for a full improvement.

It will become relevant in the following chapters that the Symanzik expansion, as defined in this section, only holds for on-shell quantities. If our observable is affected by short distance singularities, extra terms will appear in the Symanzik expansion which have to be study independently.

However, in this section we want to present an overview of the Symanzik program and therefore we focus on on-shell quantities for now.

The main goal is to find the form of the $\mathcal{O}(a)$ terms that have to be added to the action and the composite fields to only have $\mathcal{O}(a^2)$ or higher order terms in the expansion.

We introduce a local effective theory whose action is

$$S_{\text{eff}} = S_0 + aS_1 + a^2 S_2 + \dots, \qquad S_k = a^4 \sum_x \mathcal{L}_k(x), \tag{2.23}$$

which describes our lattice theory in good approximation if we are close to the continuum. In Eq. (2.23) S_0 represents the action in the continuum and S_k is defined in terms of a linear combination of local composite fields of higher dimension $4 + k$.

All those terms should have the same quantum numbers and therefore be invariant under the same symmetries as the original action S_0.

Instead of introducing the general expression [30], for clarity we give a specific example and discuss the Symansik expansion of a 2-point correlation function $\langle \mathcal{O}(x)\mathcal{O}(y)\rangle$.

First of all we also need to introduce the effective expansion of the operator $\mathcal{O}(x)$ which, in practice, will generally be a composite field.

$$\mathcal{O}_{\text{eff}}(x) = \mathcal{O}_0(x) + a\mathcal{O}_1(x) + a^2\mathcal{O}_2(x) + \dots \tag{2.24}$$

where $\mathcal{O}_k$ are again linear combinations of local fields with the correct dimension and symmetry properties.

Thus we insert Eq. (2.23) and Eq. (2.24) in the Euclidean path integral that was introduced in Sec. 2.1

$$\begin{aligned}
\langle \mathcal{O}(x)\mathcal{O}(y)\rangle &= \frac{1}{\mathcal{Z}} \int DUD\psi D\bar{\psi} e^{-S[U,\psi,\bar{\psi}]} \mathcal{O}[U,\psi,\bar{\psi};x]\mathcal{O}[U,\psi,\bar{\psi};y] \qquad (2.25)\\
&= \frac{1}{\mathcal{Z}} \int D[\psi] e^{-[S_0 + aS_1 + \mathcal{O}(a^2)]} [\mathcal{O}_0(x) + a\mathcal{O}_1(x) + \mathcal{O}(a^2)][\mathcal{O}_0(y) + a\mathcal{O}_1(y) + \mathcal{O}(a^2)]\\
&= \frac{1}{\mathcal{Z}} \int D[\psi] e^{-S_0} e^{-[aS_1 + \mathcal{O}(a^2)]} [\mathcal{O}_0(x) + a\mathcal{O}_1(x) + \mathcal{O}(a^2)][\mathcal{O}_0(y) + a\mathcal{O}_1(y) + \mathcal{O}(a^2)]\\
&= \frac{1}{\mathcal{Z}} \int D[\psi] e^{-S_0} [1 - aS_1 - \mathcal{O}(a^2)][\mathcal{O}_0(x) + a\mathcal{O}_1(x) + \mathcal{O}(a^2)][\mathcal{O}_0(y) + a\mathcal{O}_1(y) + \mathcal{O}(a^2)].
\end{aligned}$$

Since we are only interested in the $\mathcal{O}(a)$ terms, which are the terms we want to cancel, we can reduce the expression to

$$\begin{aligned}
\langle \mathcal{O}(x)\mathcal{O}(y)\rangle = \frac{1}{\mathcal{Z}} \int D\psi e^{-S_0} \mathcal{O}_0(x)\mathcal{O}_0(y) - \frac{a}{\mathcal{Z}} \int D[\psi] e^{-S_0} S_1 \mathcal{O}_0(x)\mathcal{O}_0(y) \qquad (2.26)\\
+ \frac{a}{\mathcal{Z}} \int D\psi e^{-S_0} \mathcal{O}_1(x)\mathcal{O}_0(y) + \frac{a}{\mathcal{Z}} \int D\psi e^{-S_0} \mathcal{O}_0(x)\mathcal{O}_1(y) + \mathcal{O}(a^2).
\end{aligned}$$

To simplify the notation we write everything in terms of expectation values

$$\begin{aligned}
\langle \mathcal{O}(x)\mathcal{O}(y)\rangle = \langle \mathcal{O}(x)\mathcal{O}(y)\rangle_0 - a \int d^4z \, \langle \mathcal{L}_1(z)\mathcal{O}_0(x)\mathcal{O}_0(y)\rangle_0 \qquad (2.27)\\
+ a \langle \mathcal{O}_1(x)\mathcal{O}_0(y)\rangle_0 + a \langle \mathcal{O}_0(x)\mathcal{O}_1(y)\rangle_0 + \mathcal{O}(a^2),
\end{aligned}$$

where the subscript $\langle\rangle_0$ means continuum expectation value.

In order to cancel the second term we need to add a new term to the action as we explain below. To cancel the last two terms we need to improve our operator adding an improvement coefficient to the definition of the operator. In particular we need to compute $\mathcal{O}_1$ which will be a linear combination of all the possible operators of dimension $k+1$, where k is the dimension of $\mathcal{O}$, and that have the same symmetries as $\mathcal{O}$. The tuning of all those improvement coefficients drives the calculations more demanding and therefore other approaches have been developed and are used in practice, which, however, induce other complications.

Clover Fermions

As we have seen, to reduce discretization effects of our observables we need to improve our action. In the following lines we briefly present the necessary extra term which has to be added to the Wilson action to recover the $\mathcal{O}(a)$ improvement.

Our starting point is Eq. (2.27), where the first $\mathcal{O}(a)$ term contains the action

$$-a \int d^4z \, \langle \mathcal{L}_1(z)\mathcal{O}_0(x)\mathcal{O}_0(y)\rangle_0 \, . \tag{2.28}$$

In Eq. (2.28) $\mathcal{L}_1$ is a linear combination of all possible operators of dimension 5 which respect the same symmetries as the continuum action. In this case we find 5 different operators, however we can relate few of them through the field equation $(\gamma_\mu D_\mu + m)\psi = 0$. In the end only one extra coefficient in the action is needed to recover the $\mathcal{O}(a)$ improvement, the so-called clover term [31]. The improved action takes then the following form

$$S_{\text{imp}} = S_W + c_{sw} a^5 \sum_{n\in\Lambda} \sum_{\mu<\nu} \overline{\psi}(x) \frac{i}{2} \sigma_{\mu\nu} \mathcal{F}_{\mu\nu}(x) \psi(x) \tag{2.29}$$

where c_{sw} is the so-called Sheikholeslami-Wohlert parameter that, again, has to be tuned to exactly cancel the term in the Symanzik expansion, and

$$\begin{aligned} \mathcal{F}_{\mu\nu} = \frac{1}{8a^2} & U_{\mu\nu}(x) - U_{\nu\mu}(x) + U_{\nu(-\mu)}(x) - U_{\mu(-\nu)}(x) \\ & + U_{(-\mu)(-\nu)}(x) - U_{(-\nu)(-\mu)}(x) + U_{(-\nu)\mu}(x) - U_{(-\mu)\nu}(x). \end{aligned} \tag{2.30}$$

This improvement program has been successfully applied in many calculations such as Ref. [32].

2.4.2. Twisted Mass Wilson Fermions

There is an alternative method to obtain the desired $\mathcal{O}(a)$ improvement through the Symanzik effective program. The argument, in this case, is based on the symmetries of the action. Thus, one can avoid the tuning of the large number of parameter which is required, for instance, in the case of clover fermions described above.

In this section we discuss the twisted mass formulation of lattice QCD[2] which was first

[2] See Refs.[33, 34] for recent reviews.

introduced in Refs. [35, 36, 37]. This formulation was originally developed in order to avoid the instability in the simulations given by non-physical zero modes [35]. However, as mentioned above, other features like the automatic $\mathcal{O}(a)$ improvement [38] make this discretization a desirable choice for the simulations of lattice QCD.

The continuum twisted mass action is based on standard Yang-Mills action with an additional term, the twisted mass tem. The twisted mass action is given by the following expression

$$S_F[\chi, \overline{\chi}, U] = \int d^4x \overline{\chi}(x)(\gamma_\mu D_\mu + m_q + i\mu_q \gamma_5 \tau^3)\chi(x), \tag{2.31}$$

where m_q represents the bare Wilson quark mass and μ_q the twisted mass respectively. It is important to notice that τ^3 acts in flavor space and therefore the quarks are combined in spinor *doublets* χ, $\overline{\chi}$.

After the introduction of the twisted mass action in the continuum we will discuss several properties which make of this action a valuable choice, and the reason it was chosen to carry out all the calculations that will be presented in this work.

In the present section we first motivate the automatic $\mathcal{O}(a)$ improvement. We then discuss the tuning to maximal twist, a requirement needed to ensure $\mathcal{O}(a^2)$ scaling. At the end we present some technical details of its implementation which we find relevant to include.

Automatic $\mathcal{O}(a)$ improvement

To give the motivation of automatic $\mathcal{O}(a)$ improvement [38] with twisted mass fermions we use the following simplified notation of the Symanzik expansion

$$\langle \mathcal{O}_{\text{latt}} \rangle = \langle \mathcal{O}_0 \rangle_0 - a \langle S_1 \mathcal{O}_0 \rangle_0 + a \langle \mathcal{O}_1 \rangle_0 + \mathcal{O}(a^2), \tag{2.32}$$

where the effective action is $S = S_0 + aS_1 + \mathcal{O}(a^2)$ and the effective combined operator is defined as $\mathcal{O}_{\text{latt}} = \mathcal{O}_0 + a\mathcal{O}_1 + \mathcal{O}(a^2)$, as it was introduced in the previous section.

We will make use of the $\mathcal{R}_5^{1,2}$ symmetry, which is defined as

$$\mathcal{R}_5^{1,2} : \begin{cases} \chi(x) \to i\gamma_5 \tau^{1,2} \chi(x) \\ \overline{\chi}(x) \to \overline{\chi}(x) i\gamma_5 \tau^{1,2} \end{cases} . \tag{2.33}$$

In particular the Wilson term is not invariant under $\mathcal{R}_5^{1,2}$ and therefore to ensure the invariance of the twisted mass action under these transformations, it is needed to set the Wilson quark mass to zero. This is known as tuning to maximal twist, for reasons that will become clear later, and it is an essential requirement which has to be satisfied in order to guarantee the automatic $\mathcal{O}(a)$ improvement.

In addition the twisted mass lattice action is invariant under the combined symmetry $\mathcal{R}_5^{1,2} \times \mathcal{D} \times [\mu_q \to -\mu_q]$, where the symmetry $\mathcal{D}$ basically counts the dimension of the operators, i.e. if an operator has an even/odd dimension, it will be even/odd under the

following transformation

$$\mathcal{D}: \begin{cases} U(x,\mu) \to U^\dagger(-x - a\hat{\mu}, \mu) \\ \chi(x) \to e^{3i\pi/2}\chi(-x) \\ \overline{\chi}(x) \to \overline{\chi}(-x)e^{3i\pi/2} \end{cases} . \tag{2.34}$$

If our continuum action S_0, as it is our case, and the observable $\mathcal{O}_0$ under study are invariant under $\mathcal{R}_5^{1,2}$ transformations, it can be proven that the terms in the Symanzik expansion which are of $\mathcal{O}(a)$ will vanish, ensuring $\mathcal{O}(a)$ improvement.

The reason is that, as we show below, all the operators $\mathcal{O}_1$ which have a dimension higher than $\mathcal{O}_0$, and therefore correspond to $\mathcal{O}(a)$ terms in the Symanzik expansion, have the opposite $\mathcal{R}_5^{1,2}$ parity. In other words

$$\mathcal{O}_0 \xrightarrow{\mathcal{R}_5^{1,2}} \pm\mathcal{O}_0 \quad \longrightarrow \quad \mathcal{O}_1 \xrightarrow{\mathcal{R}_5^{1,2}} \mp\mathcal{O}_1. \tag{2.35}$$

The action given in Eq. (2.31) is invariant under $\mathcal{R}_5^{1,2}$ symmetry if the Wilson quark mass m_q is tuned to zero. We call this condition maximal twist and it is a requirement that has to be satisfied to guarantee automatic $\mathcal{O}(a)$ improvement.

After the introduction of all the necessary symmetries we can now analyze every term that appears in Eq. (2.32) to prove Eq. (2.35) and its direct consequence: automatic $\mathcal{O}(a)$ improvement.

Assuming that $\mathcal{O}_{\text{latt}}$ is even under $\mathcal{R}_5^{1,2}$ and has an even dimension, its expectation value $\langle\mathcal{O}_{\text{latt}}\rangle$ will be even under $\mathcal{R}_5^{1,2} \times \mathcal{D} \times [\mu_q \to -\mu_q]$. This implies that all the terms in the Symanzik expansion (r.h.s of Eq. (2.32)) will also be even under this transformation.

We now analyze term by term the right hand side of Eq. (2.32). The continuum value of $\mathcal{O}_0$ is also even under $\mathcal{R}_5^{1,2}$ and has an even dimension, therefore it will be even under the combine trasformation as well. In contrast, the operator $\mathcal{O}_1$ has an odd dimension and therefore it has to be odd under $\mathcal{R}_5^{1,2}$ to preserve the $\mathcal{R}_5^{1,2} \times \mathcal{D} \times [\mu_q \to -\mu_q]$ symmetry. Since the continuum action is even under $\mathcal{R}_5^{1,2}$ the expectation value of this term will vanish. The same reasoning can be applied to all the terms of the expansion with an odd power of a.

We can then conclude that for all operators which are even under $\mathcal{R}_5^{1,2}$, only the leading term and the terms with an even power of a will contribute to the Symanzik expansion, whereas the terms with odd power will be equal to zero, guaranteeing the $\mathcal{O}(a^2)$ scaling to the continuum limit

$$\langle\mathcal{O}_{\text{latt}}^{\text{even}}\rangle = \langle\mathcal{O}_0\rangle_0 + \mathcal{O}(a^2). \tag{2.36}$$

Moreover it can be proven, following the same strategy, that the expectation value of observables which are odd under $\mathcal{R}_5^{1,2}$ vanish up to $\mathcal{O}(a)$ effects. Thus only the terms with contributions of a to an odd power survive in the Symanzik expansion

$$\left\langle\mathcal{O}_{\text{latt}}^{\text{odd}}\right\rangle = -a\,\langle S_1\mathcal{O}_0\rangle + a\,\langle\mathcal{O}_1\rangle_0 + \mathcal{O}(a^2) \tag{2.37}$$

Furthermore we know that in the chiral limit Wilson fermions and twisted mass Wilson

fermions are equivalent. Another relevant result that can be obtained by following the same strategy is that massless Wilson fermions are also automatically improved [38, 33].

Maximal twist

The continuum action given in Eq. (2.31) is related to the Euclidean fermion action Eq. (1.5) by just applying the non-anomalous axial transformation to the fermion fields

$$\psi(x) = e^{i\frac{\omega}{2}\gamma_5\tau^3}\chi(x), \qquad \overline{\psi}(x) = \overline{\chi}(x)e^{i\frac{\omega}{2}\gamma_5\tau^3}, \tag{2.38}$$

where ω is the so-called twisted angle.

At the classical level both actions are equivalent and therefore share the same symmetries. The twisted mass action is just an alternative formulation of QCD since if we substitute

$$m_q \to m_q' = m_q\cos\omega + \mu\sin\omega, \tag{2.39}$$

$$\mu \to \mu' = -m_q\sin\omega + \mu\cos\omega \tag{2.40}$$

the action is left unchanged. Furthermore we can see that tuning $\omega = \frac{\pi}{2}$ would correspond to set $m_q = 0$. This particular set up is what we call maximal twist and leads to the automatic $\mathcal{O}(a)$ improvement.

We differentiate between the twisted and the physical basis depending on which spinor fields we are working with, the doublet χ or ψ respectively.

In the lattice twisted mass formulation the Wilson term breaks chiral symmetry explicitly at finite lattice spacing, even at $m_0 = 0$. For this reason, as we explained in the first chapter of this work, the mass becomes additively renormalizable

$$m_q = m_0 - m_{cr}. \tag{2.41}$$

This makes that tuning $m_0 = 0$ does not correspond to send the renormalized quark mass to zero.

In practice, to tune to maximal twist the partially conserved axial current (PCAC) relation is used [39],

$$m_{\text{pcac}} = \frac{\left\langle \partial_\mu A^a_\mu(\vec{x},t)P^a(0)\right\rangle}{\langle P^a(\vec{x},t)P^a(0)\rangle}, \tag{2.42}$$

a result which is obtained through the non-anomalous axial singlet Ward-Takahashi identity[3].

The chosen parameter to tune to maximal twist is m_{pcac} due to its symmetry properties, since it is an odd quantity under $\mathcal{R}_5^{1,2}$ transformations. This implies that if m_{pcac} vanishes all $\mathcal{R}_5^{1,2}$ even operators are free of O(a) effects [38].

Consequently tuning $m_{\text{pcac}} = 0$ corresponds to tune m_0 to its critical mass m_c and consequently our physical quark mass would be entirely defined by the twisted mass μ up to $\mathcal{O}(a)$ effects.

[3]Calculation of analogous W-T identities are presented in App. C.2

This method enables to gain $\mathcal{O}(a)$ improvement by tuning only one parameter, κ to κ_c (κ critical), which corresponds tune m_0 to m_c and therefore maximal twist. This procedure, however, is not unique, since we can define κ_c in different equivalent ways.

In twisted mass κ_c depends directly on the value of μ_q. Thus different values of μ would correspond to different values of κ_c. In principle the ideal definition of κ_c corresponds to the value at the chiral limit, since it would match κ_c^W which gives exact massless Wilson fermions, however this approach entail too much computational cost and it is therefore not affordable.

For this reason another equivalent definitions are used. One option is to compute κ_c for the smallest μ_q and then simulate at that κ_c for all the masses. Nevertheless if the simulations include the strange and the charm quarks, the dependency of κ_c with the mass increases and it becomes necessary to tune κ for each value of μ_q. This also allows to simulate ensembles at a smaller mass in the future.

Technical Details

The discretized Twisted Mass Wilson action that is used for the light degenerate flavor doublet (u,d) is given by the following expression

$$S_l^{tm}[\chi,\overline{\chi},U] = a^4 \sum_x \overline{\chi}(x)_l (D_W + m_0 + i\mu_l\gamma_5\tau^3)\chi(x)_l, \tag{2.43}$$

where the Wilson Dirac operator D_W is used to avoid the *doubling* problem. The subindex l indicates light.

In order to describe a situation which is closer to the real world we have to add the strange and the charm quarks to our theory and therefore we need to insert a non-degenerate doublet of flavors to our action. Thus to simulate the heavy sector the following action is used

$$S_h^{tm}[\chi,\overline{\chi},U] = a^4 \sum_x \overline{\chi}(x)_h (D_W + m_0 + i\mu_h\gamma_5\tau^1 + \tau^3\mu_\delta)\chi(x)_h, \tag{2.44}$$

where μ_h and μ_δ are related to the strange and charm quark masses by the relations

$$m_s = \mu_h - \mu_\delta, \qquad m_c = \mu_h + \mu_\delta. \tag{2.45}$$

For our calculations we have used gauge configurations generated by the European Twisted Mass Collaboration with $N_f = 2$ dynamical quarks [40, 41, 42], which correspond to two degenerate light quarks up and down, and $N_f = 2 + 1 + 1$ [43, 44, 45] where the strange and the charm dynamical quarks were included. All the details of the dynamical simulations that we use in this work are summarized in App. D.1.

2.5. Chiral Symmetry on the lattice

We have already devoted a full chapter to discuss the characteristics of chiral symmetry and its consequences and therefore the importance of its implementation on the lattice to study the related phenomena. However to implement chiral symmetry on the lattice has been unexpectedly challenging.

The Nielsen-Ninomiya no-go theorem [46] prevent us for having a regularization whose operator simultaneously satisfies

1. $D(p)$ is analytic and periodic in p_μ.
2. $D(p) \to p_\mu \gamma_\mu$, $a|p_\mu| << 1$.
3. $D(p)$ is invertible everywhere except in $\vec{p} = 0$.
4. $\{\gamma_5, D\} = 0$.

This implies that an operator cannot be local (a.), lead to the correct continuum limit (b.,c.) and preserve chiral symmetry (d.) at the same time.

To overcome this problem a slight modification of chiral symmetry on the lattice is required, which is introduced by the Ginsparg Wilson relation

$$D\gamma_5 + D\gamma_5 = aD\gamma_5 D. \tag{2.46}$$

This represents a mild but crucial variation with respect to the naive chiral symmetry that we expected. Notice that in the continuum limit the original expression, which summarize the essential of chiral symmetry in the continuum, and is given by

$$D\gamma_5 + D\gamma_5 = 0, \tag{2.47}$$

is recovered.

The Ginsparg-Wilson relation is then the lattice counterpart of Eq. (2.47). This relation was known for a very long time, since its introduction in 1982 [47]. However this result was forgotten for many years, until in 1998 an exact and usable solution was proposed [48, 49], the so-called overlap operator which we describe below.

As we mentioned above, Eq. (2.46) recovers the expression Eq. (2.47) after taking the continuum limit. This means that we recover the standard chiral symmetry in the continuum.

Moreover it is possible to describe a chiral rotation which leaves the lattice action invariant, i.e. it does exist an exact but modified chiral symmetry on the lattice [50] and it is given by the following transformation

$$\psi \to \psi' = e^{i\theta_5\gamma_5(1-\frac{a}{2}D)}\psi, \qquad \psi \to \overline{\psi}' = \overline{\psi}e^{i\theta_5\gamma_5(1-\frac{a}{2}D)}. \tag{2.48}$$

Where D is a solution of the Ginsparg-Wilson relation. Again we recover the standard continuum chiral transformation Eq. (1.25) in the limit $a \to 0$.

Moreover we can define the following modified projectors

$$P_{\pm} = \frac{1 \pm \gamma_5(1 - aD)}{2} \tag{2.49}$$

which allow us to write the fermionic lattice action in terms of left-handed and right-handed fermions. Eq. (2.49) represents the lattice counter-part of the chiral projectors introduced in Eq. (1.10), whose expression is again recovered in the continuum limit.

Index Theorem in lattice gauge theory

Chiral symmetry on the lattice leads to the question, whether the chiral anomaly is reproduced in lattice QCD. In principle, as we saw in the first chapter, the anomaly appears due to the infinite number of variables in the path integral. For this reason the Jacobian related to the chiral transformations of the fermion measure is ill-defined. Now in the lattice we regularize our theory in such a way that we work with a finite number of variables. The question is how to implement chiral symmetry in the lattice and still recover the anomaly in the continuum.

This is a remarkable feature of the Ginsparg-Wilson relation, since it states exactly how chiral symmetry is broken in the lattice and therefore how it reproduces the anomaly at finite lattice spacing and recover the original form in the continuum limit. The reason, as in the continuum, is that the action remains invariant under the chiral transformations given in Eq. (2.48) but the measure in the path integral is not, and therefore we again obtain the anomaly given in Eq. (1.26) in the Jacobian after applying the chiral transformations. This makes lattice gauge theories, in its Ginsparg-Wilson fermion formulation, a clear option for a natural formulation of chiral symmetry in contrast with other regularizations that break chiral symmetry explicitly in the Lagrangian and eliminate the chiral Jacobian factor.

It was first shown in Ref. [51] that the chiral Jacobian of a lattice formalism that respects chiral symmetry, i.e. using Ginsparg-Wilson fermions, after applying the chiral transformations given in Eq. (2.48) to the fermion measure $D[\psi]D[\overline{\psi}]$, carries the correct chiral anomaly.

Afterwards another derivation was proposed in Ref. [50]. In addition a continuum limit of the Jacobian was also computed in Ref. [52] where the continuous form of the chiral anomaly is recovered.

In the same way that in the last chapter we introduced the index theorem [15] in relation with the anomaly in the continuum, we can do it in the lattice. In that case, in principle all sides of the index theorem have problems

$$Q_{\text{top}} = \frac{1}{32\pi^2} \int d^4x \epsilon_{\mu\nu\rho\sigma} \text{tr}(F_{\mu\nu} F_{\rho\sigma}) = n_+ - n_-, \tag{2.50}$$

where $n_+ - n_-$ is the index as we explained in the previous chapter. However when an operator that fullfils Eq. (2.46) and therefore preserves chiral symmetry is used a natural

definition of the topological charge appears which is well defined for a given choice of D

$$Q_{\text{top}} = \frac{1}{2}\text{Tr}\left\{\gamma_5 D\right\} = n_- - n_+, \tag{2.51}$$

where $n_\pm$ corresponds to the number of zero modes of D $\gamma_5 u_\lambda = \pm u_\lambda$, i.e. which correspond to the zero modes u_λ in both chiralities.

2.5.1. Overlap Fermions

An exact solution of Ginsparg-Wilson relation was proposed by Neuberger in Ref. [48, 49]. This solution, the so-called overlap operator takes the following form

$$D_{ov} = \frac{1}{a}\left\{1 - A(A^\dagger A)^{-1/2}\right\}, \qquad A = 1 + s - aD_W \tag{2.52}$$

where D_W can be the Wilson operator given in Eq. (2.22), or any other local operator which is free of doublers, and s is a parameter defined between -1 and 1 which can be used to improve locality as it can be seen in App. B.

Without entering in details of the implementation of the overlap operator we want to remark the high computational cost required for its simulation on the lattice. It is for this reason that, even though it offers all those advantages, it is not extensively used, since, due to the current status, it only allows the computation at small volumes.

For this reason mixed action setups have been proposed. In particular in Ref. [53, 54] a mixed action setup is proposed where twisted mass fermions are simulated in the sea and overlap fermions in the valence.

2.6. Numerical Evaluation of the path integral

As we have already explained at the beginning of this chapter, in order to compute correlators we need to evaluate the path integral applying methods normally used in Statistical Mechanics. In this section we summarize few features of the application of those methods which we consider relevant for the understanding of this work. However the numerical evaluation using Monte Carlo methods is a very extended topic and we recommend specialized texts for a more detailed description, e.g, Refs. [21, 20].

2.6.1. Pure gauge simulations

We start our discussion with the simulation of pure $SU(3)$ gauge theory. As we explained in previous sections, the fermions in the lattice are represented by Grassman variables and therefore can be integrated out in form of a fermionic determinant.

The quenched approximation consists in ignoring the fermion contribution by setting the fermionic determinant, introduced in Eq. (2.15), to a constant. This corresponds to removing the vacuum polarization effects of the quark loops.

In this approximation the path integral is only over the gauge fields and takes the following form

$$\langle \mathcal{O} \rangle = \frac{1}{Z} \int D[U] e^{-S_G[U]} \mathcal{O}, \qquad Z = \int D[U] e^{-S_G[U]}. \tag{2.53}$$

To solve this integral we can not apply analytical methods due to its difficulty and, except for very small lattices, its high dimensionality. Therefore we need an approximative method. In particular we use Monte Carlo simulations to generate gauge field configurations U_n that sample the Boltzman factor. This method is called *importance sampling*.

Once we have generated the gauge field configurations we evaluate the observable $\mathcal{O}$ in every configuration and then average to obtain the expectation value

$$\langle \mathcal{O} \rangle = \frac{1}{N} \sum_{U_n} \mathcal{O}(U_n) + \mathcal{O}\left(1/\sqrt{N}\right). \tag{2.54}$$

There are different methods to generate the configurations, in particular in lattice QCD the *Markov chain* process is used. The Metropolis algorithm [55] was the first algorithm implemented for a quantum field theory on a lattice [56]. Since then, however, a very big progress has been made on this topic.

2.6.2. Dynamical simulations

The quenched approximation was used for many years as an approximation to full QCD when the algorithms and machines were not at the stage of facing the calculation of the fermionic determinant. The physics of both approaches are similar since Quenched QCD reproduce confinement, asymptotic freedom and spontaneous breaking of the chiral symmetry.

Nowadays, however, all the machinery is available to simulate full QCD including the vacuum polarization effects of the quark loops, the so-called dynamical simulations. This progress is in part due to the Hybrid Monte Carlo algorithm [57] and the substantial improvement developed[4].

In principle we could consider the fermion determinant within our observable but this produces big fluctuations in the data that are not under control unless excessively large statistics are available.

For this reason the fermion determinant is included in the Monte Carlo simulation as a weight factor of the probability distribution of the *importance sampling*. However, there can be a problem to use the fermion determinant as a probability factor since in that case we must be sure that the determinant is real and non negative. This can be shown for an even number of degenerate flavors since in that case the determinant goes with an even power ensuring the positivity. Using the γ_5 hermiticity property it can be proven that the determinant is real.

[4]For a review see Ref. [58]

For our calculations we have used gauge configurations generated by the European Twisted Mass Collaboration with $N_f = 2$ dynamical quarks [40][41][42], which correspond to two degenerate light quarks up and down, and $N_f = 2 + 1 + 1$ [43][44][45] where the strange and the charm dynamical quarks were included. All the details of the dynamical simulations that we use in this work are summarized in App. D.1.

CHAPTER 3

Spectral projectors

Contents

The present chapter is devoted to describe the spectral projectors method introduced by Lüscher and Giusti [59] to compute spectral observables, i.e. physical quantities which are closely related to the low-lying eigenvalue spectrum of the Dirac-operator. In the following section we discuss the method itself and point out why it is advantageous for the calculation of spectral quantities, focusing in particular on the mode numer from which we can derive the chiral condensate. As another quantity, we will consider the topological susceptibility. We will provide the details of the implementation and the tests we performed for the spectral projector method.

The spectrum of the Dirac operator contains very important information which is crucial to understand different phenomena in QCD, such as the spontaneous chiral symmetry breaking . A direct method to calculate spectral quantities is the explicit computation of many low-lying eigenvalues of the Dirac-operator. This requires, however, a substantial amount of computational time which renders it difficult to access spectral observables and therefore the important information that they can provide.

The method using spectral projectors [59] was designed to compute such spectral observables in a cost-effective way. Moreover, and maybe even more important, it allows us to define different spectral quantities in a theoretically clean way, such as the chiral condensate and the topological susceptibility. The spectral projector method opens the door to large volume and small lattice spacing calculations as a result of the low computational cost of its application. In addition, the method provides a conceptually clean tool to renormalize spectral observables and thus a well defined continuum limit can be carried out in an affordable way.

This chapter is organized as follows. We devote the first section to the introduction of the mode number ν, the most natural target of the method. We then continue to discuss quantities that can be derived from the mode number, such as the chiral condensate. After this introduction we present the basic principles of the method, the technical details and the implementation. Finally we show the different tests that we performed to ensure the correctness of our implementation and discuss the choice of the optimal values for different parameters as need by the spectral projector method.

3.1. Spectral density and mode number

The mechanism responsible for the spontaneous chiral symmetry breaking in QCD is still not well understood. There are, however, arguments which establish that it is directly related to the low lying spectrum of the Dirac operator [60]. Thus spectral observables, which are related to the low-lying eigenvalue spectrum, can play a paramount role to understand spontaneous chiral symmetry breaking and to provide quantitative information on e.g. the value of the chiral condensate.

If we consider the Dirac operator D on a lattice, most of the operators that are used in practice, including Wilson and twisted mass Wilson, do not obey the continuum anti-hermiticity property, since the Wilson term breaks this symmetry explicitly. The lattice

Dirac operators retain, however, the γ_5 hermiticity which is defined as

$$\gamma_5 D \gamma_5 = D^\dagger. \tag{3.1}$$

As a consequence of this property the eigenvalues of such operators are either real or complex pair conjugates. The eigenvalues of the Wilson Dirac operator then lie in the complex plane as is sketched in the following graph.

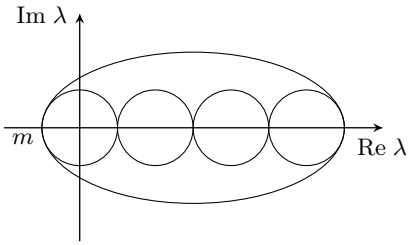

Notice that the eigenvalues of the twisted mass Wilson Dirac operator differ from this picture just by a shift on the imaginary axis which is given by the twisted mass.

In practice, it is more convenient to study the spectral properties of the hermitian Dirac operator, either $\gamma_5 D$ or $D^\dagger D$, whose eigenvalues are real. It is for this reason that in the following we refer to the hermitian Dirac operator only. Since we will be using configurations that are produced with the Wilson twisted mass action, our discussion is, in particular, focused on the twisted mass Wilson theory at maximal twist where an automatic $O(a)$-improvement can be obtained.

The spectral density $\rho(\lambda, \mu)$ of the hermitian twisted mass Dirac operator $D_{tm}^\dagger D_{tm}$ is defined as

$$\rho(\Lambda) = \frac{1}{V} \sum_{k=1}^{\infty} \langle \delta(\lambda - \lambda_k) \rangle \,. \tag{3.2}$$

As it is shown in Fig. 3.1, in the twisted mass case, the spectral density has a clear infrared cut-off at μ^2 provided by the twisted mass term. From the point of view of numerical simulations, this is a relevant feature of the twisted mass theory since it prevents instabilities in the simulations related to the appearance of very small eigenvalues. In the continuum theory, or in a theory which respects chiral symmetry, a similar picture is observed, since there the quark mass provides an infrared bound on the spectrum.

One can derive analytical results for the distributions of the smallest eigenvalues of the Dirac operator for fixed sectors of topological charge using random matrix theory [61]. The distribution of the accumulated spectral density at the low end of the spectrum, as plotted in Fig. 3.1, can be also described by random matrix theory for Wilson [62, 63] and for twisted mass [64] fermions. Although in this work we will not make use of these analytical results, it is worth mentioning that the eigenvalue distributions and a comparison to random matrix theory can provide in principle a valuable tool to extract information on fundamental parameters of QCD such as the chiral condensate.

In the following we are interested in a quantity which is closely related to the eigenvalues of the Dirac operator, the mode number ν. The mode number is the integrated

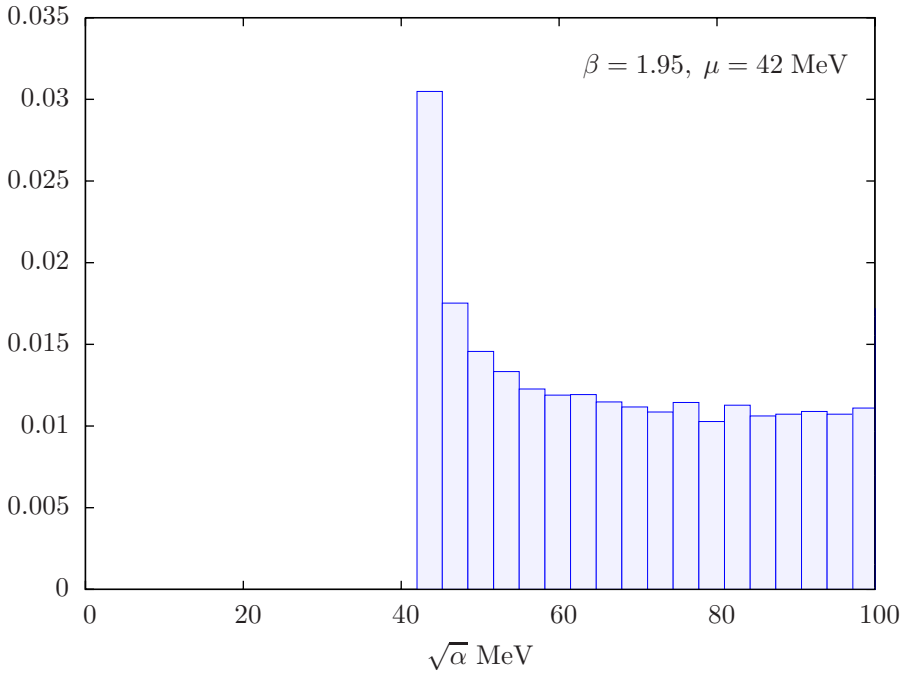

Figure 3.1.: Density of eigenvalues of $\gamma_5 D_{tm}$ for $N_f = 2{+}1{+}1$, $\beta = 1.95$ and $a\mu = 0.0085$.

spectral density and we define it as the average number of eigenvalues of the hermitian Dirac operator $D^\dagger D$ below a certain value of a threshold parameter which, in the following, we will call M. The mode number is directly related to the spectral density through the following expression

$$\nu(M, m) = V \int_{-\Lambda}^{\Lambda} d\lambda \rho(\lambda, m) = 2V \int_{0}^{\Lambda} d\lambda \rho(\lambda, m), \tag{3.3}$$

where Λ is related to the threshold parameter and the quark mass in the following way $\Lambda = \sqrt{M^2 - m^2}$. The mode number carries the same information as the spectral density. Consequently studying the properties of ν we can extract information of $\rho(\lambda, m)$. As we will see below the mode number can be computed very efficiently through a lattice calculation employing the method of spectral projectors.

The threshold parameter M will be an input parameter of our analysis. How rapidly the mode number increases when we increase M or vice versa, depends on several factors, such as the volume, the lattice spacing and the magnitude of M itself. The value of the chiral condensate depends directly on this relation between the mode number and M. Therefore a study of these dependencies is needed and we devote the next subsection to present such an investigation.

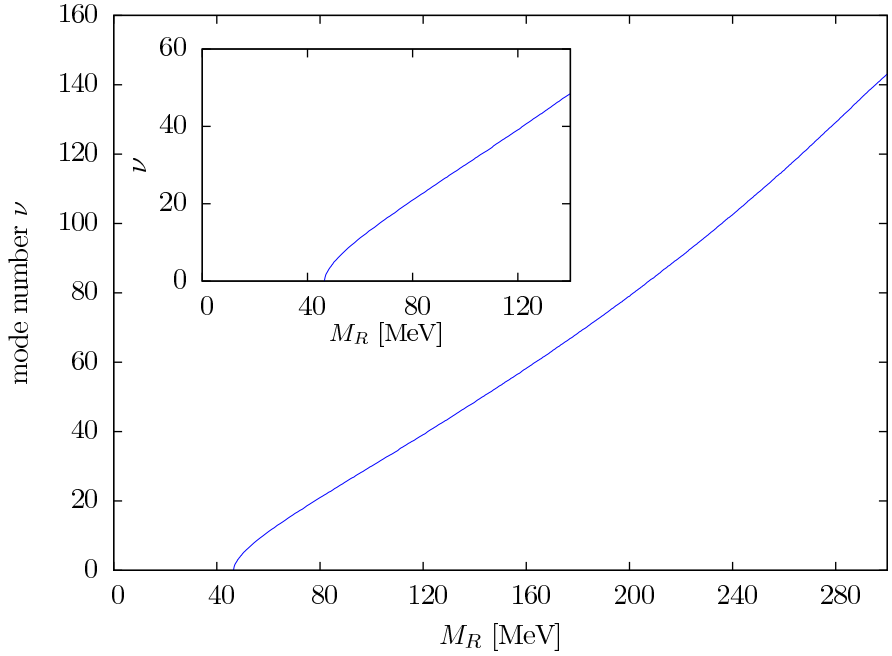

Figure 3.2.: Mode number ν with respect to the threshold parameter M_R for $\beta = 1.95$, $L = 32$ and $\mu = 42$ MeV. The inner plot is a zoom close to the origin, where the linear region is clearly observed. This plot corresponds to a direct computation of the first 150 eigenvalues of $D_{tm}^{\dagger} D_{tm}$.

3.1.1. Qualitative behavior of the mode number

Chiral perturbation theory (χPT) is an effective theory that describes the low energy dynamics of QCD [65, 66, 67]. It is based on the symmetries and fundamental principles of QCD. In particular, chiral symmetry plays a central role in this effective theory. χPT is a systematic expansion at low energies and is parametrized by so-called low-energy constants among which one can find the chiral condensate and the pion decay constant. χPT is a very useful tool to describe the low energy behavior of QCD and is often used to determine the pion mass dependence of physical quantities obtained from lattice calculations.

χPT also describes the behavior of the spectral density predicting that it behaves constant as a function of M for a given range of M [68, 69, 70]. This constant behavior of the spectral density corresponds to a linear behavior of the mode number, the integrated spectral density. In Fig. 3.2 the behavior of ν for a large range of M is shown. There one can clearly see the region where the linear behavior is found. On the other hand, at fairly large and very low values of M the linear regime disappears. In this work, we have to perform our calculations in the range of linear behavior. Consequently one of our main goals is to localize this region which in general appears between 50 MeV and 120 MeV, although this depends on the quark mass, the volume and the lattice spacing

of the ensembles analyzed.

If we carefully focus on the very low end of the spectrum, i.e. the lowest eigenvalues, we can observe some interesting features. One can clearly see that the spectrum rapidly goes to zero when the quark mass is approached. This is, in fact, an obvious feature of the twisted mass theory, since the twisted mass parameter provides an infrared cut-off. In the Wilson theory, however, this is not the case. It can also be seen that the slope of the curve close to μ is higher than for slightly larger values of M. This corresponds to a higher density of eigenvalues close to the threshold μ. In Fig. 3.1, where the spectral density for twisted mass fermions is plotted, we can clearly see both phenomena reproduced in the spectral density.

3.1.2. Mode number, spectral sums, and density chains

This section is devoted to the study of some important properties of the mode number such as the renormalizability. In order to demonstrate some of these properties we will establish the relation of the mode number with other observables whose properties are well known, such as the spectral sums or the density chains. As a next step, we first show the relation between ν and the spectral sums.

The spectral sums are defined through the following expression [59]

$$\sigma_k(\mu, m) = \left\langle \mathrm{Tr}\{(D_m^\dagger D_m + \mu^2)^{-k}\} \right\rangle = \sum_\lambda \frac{1}{(\lambda^2 + m_v^2)^k}, \tag{3.4}$$

where in the second equality the spectral decomposition has been applied.

The relation between σ_k and ν is given by

$$\sigma_k(\mu, m_q) = \int_0^\infty dM\ \nu(M, m_q) \frac{2kM}{(M^2 + \mu^2)^{k+1}}. \tag{3.5}$$

Even if this does not seem to be straightforward, it is not difficult to connect the right hand side of Eq. (3.5) to the original expression given in Eq. (3.4). We show the connection step by step in App. E.3.

Density chains

It can be very helpful to write the spectral sums, and consequently the mode number, in terms of correlation functions of local field operators, since the renormalization properties of these observables are very well known. This will help us to discuss the renormalization of the spectral sums and the mode number below.

In this framework we work in a partially quenched theory since we need to add $2k$ valence flavors to the theory, as shown below. This then leads to the introduction of the corresponding pseudo-fermions fields that are required to cancel the determinant.

Let us discuss the action for the particular case of $N_f = 2$ degenerate dynamical

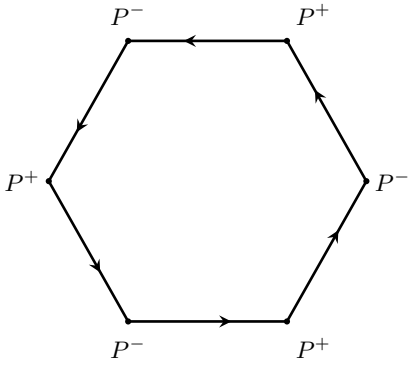

Figure 3.3.: Density chain of charged pseudoscalar densities corresponding to $\sigma_3(\mu, m)$

quarks, which reads as follows

$$S = S_g[U] + \sum_{i=1}^{2} S_{\text{sea}}[\psi_i, \overline{\psi}_i, U] + \sum_{f=1}^{2k} \left[S_{\text{val}}[\psi_f, \overline{\psi}_f, U] + S_{\text{gh}}[\phi_f, U] \right], \tag{3.6}$$

where S_g is the gluon action, S_{sea} is the fermion action of the quarks in the sea sector, S_{val} represents the action of the $2k$ flavors that we have introduced in the valence sector. S_{gh} is the action of the corresponding pseudo-fermion fields, the so-called ghosts, which are added to cancel the determinant of the valence quarks. Notice that the fermions whose action is given S_{val} do not have a corresponding dynamical quark. In this equation $\psi, \overline{\psi}$ denote doublets of mass degenerate flavors. In fact, in the following we assume that all the flavors are degenerate in mass to simplify our calculation.

The spectral sum σ_k can be written in terms of a density chain in the following way

$$\sigma_k(\mu, m) = -a^{4(2k)-4} \sum_{x_1,\ldots,x_{n-1}} \left\langle P_{12}(x_1) P_{23}(x_2) \ldots P_{(2k)1}(0) \right\rangle, \tag{3.7}$$

where the pseudo-scalar and scalar densities are given by $P_{ab}(x) = \psi_a(x)\gamma_5\psi_b(x)$ and $S_{ab}(x) = \psi_a(x)\psi_b(x)$ respectively, and $\psi_a, \overline{\psi}_a$ are singlet flavor component.

Since Eq. (3.6) is a general expression of a partially quenched QCD action, we can there include in the fermionic part either the Wilson action given in Eq. (2.21) or the twisted mass Wilson action given in Eq. (2.31). We are interested in twisted mass QCD, therefore we need to rewrite Eq. (3.7), which corresponds to a density chain in the Wilson theory, for twisted mass QCD.

In particular, for the case of $\sigma_3(\mu, m)$ one possible representation is given by

$$\sigma_3(\mu, m) = -a^{24} \sum_{x_1,\ldots,x_5} \left\langle P^+_{12}(x_1) P^-_{23}(x_2) P^+_{34}(x_3) P^-_{45}(x_4) P^+_{56}(x_5) P^-_{61}(0) \right\rangle \tag{3.8}$$

where $P^{\pm}_{ab} = \overline{\psi}_a \gamma_5 \tau^{\pm} \psi_b$ are charged pseudoscalar densities and $\tau^{\pm}$ are defined in flavor

space[1]. $\overline{\psi}_a = (\overline{u_a}, \overline{d_a})$ are isospin doublets of twisted mass valence fermions whose action is given by Eq. (2.31) as we explained above. The index $a = 1, \ldots, 2k$ indicates the flavor; in this particular example we add 6 flavors to the theory, which is the minimun number of flavors that still guarantees the renormalizability, as will be explained below.

Eq. (3.8) represents a chain (in flavor space) of interconnected pseudoscalar densities, as represented in Fig. 3.3.

Through the Wick theorem it can be straightforwardly proven that Eq. (3.4) and Eq. (3.8) are equivalent. Let us write $\sigma_3(\mu, m)$ with its flavor content and the Wick's contractions explicitly.

$$\sigma_3(\mu, m) = -a^{24} \sum_{x_1,\ldots,x_5} \tag{3.9}$$
$$\left\langle \overbrace{\overline{u_1}(x_1)\gamma_5 d_2(x_1)\overline{d_2}(x_2)\gamma_5 u_3(x_2)\overline{u_3}(x_3)\gamma_5 d_4(x_3)\overline{d_4}(x_4)\gamma_5 u_5(x_4)\overline{u_5}(x_5)\gamma_5 d_6(x_5)\overline{d_6}(0)\gamma_5 u_1(0)}^{} \right\rangle$$

If we now write everything in terms of propagators,

$$\begin{aligned}
\sigma_3(\mu, m) &= \left\langle \mathrm{Tr}\left\{ S_1^u(x_1, 0)\gamma_5 S_2^d(x_1, x_2)\gamma_5 S_3^u(x_2, x_3)\gamma_5 S_4^d(x_3, x_4)\gamma_5 S_5^u(x_4, x_5) S_6^d(x_5, 0) \right\} \right\rangle \\
&= \left\langle \mathrm{Tr}\left\{ S_1^u(x_1, 0)(S_2^u(x_2, x_1))^\dagger S_3^u(x_2, x_3)(S_4^u(x_4, x_3))^\dagger S_5^u(x_4, x_5)(S_6^u(0, x_5))^\dagger \right\} \right\rangle \\
&= \left\langle \mathrm{Tr}\{(Dm^\dagger D_m + \mu^2)^{-3}\} \right\rangle,
\end{aligned} \tag{3.10}$$

we recover the original expression given in Eq. (3.4) for a specific value of $k = 3$.

In order to obtain the last expression of Eq. (3.10), in the second step we have applied the γ_5 hermiticity property for twisted mass[2]

$$\gamma_5 S_2^d(x_1, x_2)\gamma_5 = S_2^u(x_2, x_1)^\dagger, \tag{3.11}$$

and in the last step we introduced the definition of the propagator as the inverse of the Dirac operator already introduced in the last chapter together with

$$D_{tm}^\dagger D_{tm} = (D_m^\dagger \mathbb{1}_\mathrm{f} - i\mu\gamma_5\tau_3)(D_m \mathbb{1}_\mathrm{f} + i\mu\gamma_5\tau_3) = (D_m^\dagger D_m + \mu^2)\mathbb{1}_\mathrm{f}. \tag{3.12}$$

Note that this trivial relation tells us that the eigenvalues of the hermitian twisted mass Dirac are just the eigenvalues of the hermitian Wilson Dirac operator shifted by μ^2.

3.1.3. Renormalization

One of the main goals of simulations in lattice QCD is to compare the obtained results with experiments and phenomenology. In order to compare results one needs to first guarantee that the observables which are being computed on the lattice have a well defined continuum limit, meaning that they are renormalizable. One essential task is

[1] More details are described in App. A.1
[2] More details can be found in App. A.2

then to compute the renormalization factors for the bare quantities extracted from the lattice[3]. The renormalization constants of different local field operators can be computed using perturbative and non-perturbative approaches on the lattice. One example of a non-perturbative method is the RI-MOM scheme [73], which is extensively used. Since one is mostly interested in comparing the lattice calculations with the phenomenological results, in general the renormalization factors are translated to the $\overline{\text{MS}}$ scheme at 2 GeV, one of the most common schemes and scales used.

In Ref. [59], through its relation to the spectral sums, it was proved that the mode number is a renormalization group invariant. It was also shown that the spectral sums defined as density chains are renormalizable and have a well defined continuum limit for adequate values of k in σ_k [74].

In this section we reproduce the proof of the renormalization invariance of the mode number and motivate the renormalizability of the density chains for $k \geq 3$.

Renormalization of the mode number

We have seen that the spectral sums can be written as density chains which only depend on pseudo-scalar densities. These local fields renormalize as

$$P_R^a(x) = Z_P P^a(x), \tag{3.13}$$

therefore to renormalize the spectral sums it should be sufficient to renormalize each density of the chain independently in the following way

$$\sigma_R(\mu_R, m_R) = Z_P^{2k} \sigma(\mu, m). \tag{3.14}$$

It can also be proven that the product of m_{pcac} times the pseudoscalar density is finite when removing the cut-off and therefore renormalization group invariant [4]. This implies that the partially conserved axial current (PCAC) quark mass renormalizes as

$$m_R = \frac{1}{Z_P} m = Z_m m. \tag{3.15}$$

In the case of twisted mass, the partially conserved vector current (PCVC) relation is exact and this implies that the product of μ and the pseudoscalar density is renormalization group invariant[4] and therefore

$$\mu_R = \frac{1}{Z_P} \mu = Z_\mu \mu. \tag{3.16}$$

Based on that statement it can be proven that the mode number is a renormalization group invariant if M renormalizes as a mass term

$$M_R = Z_\mu M. \tag{3.17}$$

[3] For a review on the topic we refer to, e.g., Refs. [71, 72]

[4] We refer to any specific text for this proof, e.g. [72]

Thus if we renormalize all the elements of Eq. (3.5) we are describing the renormalized spectral sum

$$\begin{aligned}\sigma_R(\mu_R, m_R) &= \int_0^\infty dM_R \nu_R(M_R, m_R) \frac{2kM_R}{(M_R^2+\mu_R^2)^{k+1}} = \\ &= \int_0^\infty Z_\mu dM\ \nu_R(M_R, m_R) \frac{2kZ_\mu M}{((Z_\mu M)^2+(Z_\mu\mu)^2)^{k+1}} = \\ &= \frac{1}{Z_\mu^{2k}} \int_0^\infty dM\ \nu_R(M_R, m_R) \frac{2kM}{(M^2+\mu^2)^{k+1}} \\ &= \frac{1}{Z_\mu^{2k}} \int_0^\infty dM\ \nu(M, m) \frac{2kM}{(M^2+\mu^2)^{k+1}} = Z_P^{2k}\sigma(\mu, m).\end{aligned} \tag{3.18}$$

As expected this leads to Eq. (3.14), proving that the mode number is a renormalization group invariant, as shown in Ref. [59].

Renormalization of density chains

If we study the expression given in Eq. (3.8) one can see that the sum over all space includes short-distance singularities, which arise when the coordinates x_i are scaled to the same point. Short-distance singularities can have strong consequences for the renormalizability and the improvement of observables since they give rise to (power) divergences that must be considered.

In this section we discuss the renormalizability of the density chains given in Eq. (3.8). In order to simplify the argument, and to have a clear understanding of how divergences occur, we start with the simplest example which corresponds to two densities and through a heuristic argument explain the origin of the singularities. Only then we extend the discussion to more complex density chains although without going into detail.

For completeness, we first introduce the basic ingredients of how we assign the dimension to a local operator, since we illustrate below the calculation through a dimensional analysis. The basic argument is that the free action has dimension 0 and therefore the Lagrangian density has dimension 4 since we assign a dimension 1 to any derivative of space-time and mass parameter. In addition a free field of spin 0 has dimension 1 and a fermion field of spin 1/2 has dimension 3/2.

To study the short distance behavior of a product of composite operators which are placed at the same point we need to apply the operator product expansion (OPE), a method that will be introduced below.

A product of operators $\mathcal{O}_1(x)\mathcal{O}_2(0)$ is related to a single local operator when the product is affected by short distance divergences close to 0. This correspondence can be established because the local divergence, which the product potentially contains, can be described by a local operator located at zero. The only requirement for the local operator is to have the same global symmetries as the product of $\mathcal{O}_1\mathcal{O}_2$.

Following this idea Wilson proposed an expansion of the product of two operators given by a linear combination of local operators of equal or lower dimension but having

the same quantum numbers as the product.

$$\mathcal{O}_1(x)\mathcal{O}_2(0) \sim \sum_i C_i(x)\mathcal{O}_i(0) \tag{3.19}$$

where the so-called Wilson coefficients $C_i(x)$ are c-numbers and carry all the dependence on x. This is independent of additional field operators appearing in Green functions.

After this more general discussion we now apply the OPE to the observables we are interested in. In particular, we start with the product of two pseudo-scalar densities with non-trivial flavor structure, which are given by

$$P_{ab}(x) = \psi_a(x)\tau^+\gamma_5\psi_b(x) \tag{3.20}$$

where ψ_a is a fermion doublet. The local operator of lowest dimension that mixes with the product is the scalar density

$$P_{ab}(x)P_{bc}(0) \sim C(x)S_{ac}(0) + \dots. \tag{3.21}$$

In Eq. (3.21), the Wilson coefficient behaves as $C(x) \sim \frac{1}{|x|^3}$, since the operator $S_{ac}(0)$ is dimension 3 and the product $P_{ab}(x)P_{bc}(0)$ is dimension 6.

For the sake of a better understanding we now apply an argument based on dimensional reasons, called power counting, to explain the origin of the divergence in the spectral sums. If we integrate Eq. (3.21)

$$\int_0^a d^4x P_{ab}(x)P_{bc}(0) \sim \int_0^a d^4x \frac{1}{x^3} S_{ac}(0) + \dots = S_{ac}(0)\int_0^a d^4x \frac{1}{x^3} + \dots \sim a\ S_{ac}(0) + \mathcal{O}(a^2), \tag{3.22}$$

the divergence that emerges in this case is integrable.

However if we consider a closed chain in flavor space then the product of density chains does mix with the identity in the following way

$$P_{ab}(x)P_{ba}(0) \sim C_1(x)\mathbb{1} + C_2(x)S_{ab}(0) + \dots \tag{3.23}$$

where $C_1(x)$ diverges like $\frac{1}{|x|^6}$. We consider only the operator with the lowest dimension because it corresponds to the leading divergence.

$$\int_0^a d^4x P_{ab}(x)P_{ba}(0) \sim \int_0^a d^4x \frac{1}{x^6}\mathbb{1} + \dots = \mathbb{1}\int_0^a d^4x \frac{1}{x^6} + \dots \sim \frac{1}{a}\mathbb{1} + O(a). \tag{3.24}$$

This product of densities with trivial flavor structure, which corresponds to the spectral sum $\sigma_1(\mu, m)$, is not integrable, moreover it is power divergent.

Furthermore if we have a product of four pseudo-scalar densities

$$\int d^4x_1 d^4x_2 d^4x_3\ P_{ab}(x_1)P_{bc}(x_2)P_{cd}(x_3)P_{da}(0) \tag{3.25}$$

which corresponds to the spectral sum σ_k for $k = 2$, we observe a similar problem. If we

again scale all the pseudo-scalar densities to zero, the operator with the lowest dimension which mixes with the product is the identity operator in flavor space and therefore, in this particular case, we have a 12 dimensional integral and a divergence of dimension 12, giving a logarithmically divergent quantity.

As mentioned in Ref. [74], however, the degree of the divergence goes like $4 - 2k$, and therefore when we have $k \geq 3$ the short distance singularities do not lead to a divergence any longer, since they are all integrable, including the case where all coordinates are scaled to zero and therefore a mixture with the identity operator occurs. The reason is that, for the case $k = 3$, the dimension of the integral is 20 whereas the divergence is only 18 and therefore is integrable. Thus for $k \geq 3$ we are guarantied that the spectral sums have a finite and well defined continuum limit.

3.2. Spectral Projectors

As a first and natural example for the application of the spectral projectors method, we now discuss the mode number ν. In principle one could directly compute ν by calculating the eigenvalues of the hermitian Dirac operator $D_{tm}^{\dagger} D_{tm}$ and then simply count them. The problem of this method, however, is that the computational cost of such a calculation grows with the square or even higher power of the volume V. This prevents the application to large volumes, as it is required at small lattice spacing and small quark masses. Nevertheless, a new method –the spectral projectors method– was recently introduced [59] which reduces the computational effort since it grows only with the volume V, making the calculation feasible. In this section we explain the basis of the method and its implementation.

Let us introduce $\mathbb{P}_M$ as an orthogonal projector to the subspace of fermion fields extended over the eigenmodes of the hermitian Dirac operator $D_{tm}^{\dagger} D_{tm}$ whose eigenvalues are below a certain threshold parameter M^2. Then another representation of the mode number can be found as the expectation value of the trace of such operator

$$\nu(M, \mu) = \langle \mathrm{Tr}\, \mathbb{P}_M \rangle \,. \tag{3.26}$$

In practice we evaluate $\mathrm{Tr}\, \mathbb{P}_M$ stochastically. To this end, randomized pseudo-fermion fields η are introduced satisfying the general properties

$$\left\langle \eta_i \eta_j^{\star} \right\rangle = \delta_{ij}, \qquad \langle \eta_i \rangle = 0, \tag{3.27}$$

where $\langle\rangle$ corresponds to the stochastic average over the ensemble of noise vectors whose degrees of freedom are given by spin, color and space-time. In particular we chose to use Z_4 noise which correspond to $\eta = (\pm 1 \pm i)/\sqrt{2}$, where each possibility is equally distributed, i.e. with a probability 1/4 each.

The stochastic evaluation of a propagator is a method generally used. In this method the matrix elements i, j of the matrix $M^{-}1$ can be computed as

$$\psi_j = M_{i,k}^{-1} \eta_k, \tag{3.28}$$

for each source (i.e. stochastic vector) in a given configuration.

This allows to compute the mode number by averaging over these random vectors in the following way

$$\mathrm{Tr}\ \mathbb{P}_M = \frac{1}{N}\sum_{i=1}^{N}(\eta_i, \mathbb{P}_M\eta_i). \tag{3.29}$$

Taking the average over gauge configurations we can then compute the expectation value of $\nu = \langle \mathrm{Tr}\ \mathbb{P}_M \rangle$.

Such a projector can be approximated by a rational function of the hermitian Dirac operator $D_{tm}^{\dagger}D_{tm}$. Following the suggestion made in Ref. [59] we approximate $\mathbb{P}_M$ to a step function given by

$$h(x) = \frac{1}{2}\left[1 - \frac{x}{\sqrt{x^2}}\right]. \tag{3.30}$$

In order to evaluate $\frac{x}{\sqrt{x^2}}$ we need again to make use of an approximation. To this end we insert a series of Chebyshev polynomials of degree n [75] which are evaluated using the Clenshaw recursion formula [76]. We also introduce an infrared cut-off parameter $\epsilon > 0$ which should be smaller than the lowest eigenvalue of $D_{tm}^{\dagger}D_{tm}$.

The maximal deviation of the approximation of the function $xP_n^{\epsilon}(x^2)$ to the sign function in the indicated range is then given by

$$\delta = \max_{\epsilon \le y \le 1} \left\| 1 - \sqrt{y}P_n^{\epsilon}(y) \right\|. \tag{3.31}$$

The approximation can be improved by increasing the degree of the polynomial n or decreasing ϵ. An increase in the degree of the polynomial means that a larger number of coefficients have to be computed and therefore the computational cost also increases, since it implies an increase in the number of times $D_{tm}^{\dagger}D_{tm}$ has to be applied. These two components have to be considered, the cost and the quality of the approximation, to find the optimal compromise.

Finally the spectral projector takes the form

$$\mathbb{P}_M \approx h(\mathbb{X})^4 \tag{3.32}$$

where the fourth power is added to improve the approximation and the operator $\mathbb{X}$ is given by

$$\mathbb{X} = 1 - \frac{2M_{\star}^2}{D_{tm}^{\dagger}D_{tm} + M_{\star}^2} \tag{3.33}$$

In this equation D_{tm} denotes the twisted mass Dirac operator and $M_{\star}$ an input parameter which is related to M. The relation between $M_{\star}$ and M is also a parameter which modifies the quality of the approximation. As suggested in Ref. [59] we choose $M/M_{\star} = 0.96334$ to ensure that the error in the approximation, given by

$$\Delta = \left\langle \mathrm{Tr}\left\{ \mathbb{P}_M - h(\mathbb{X})^4 \right\} \right\rangle, \tag{3.34}$$

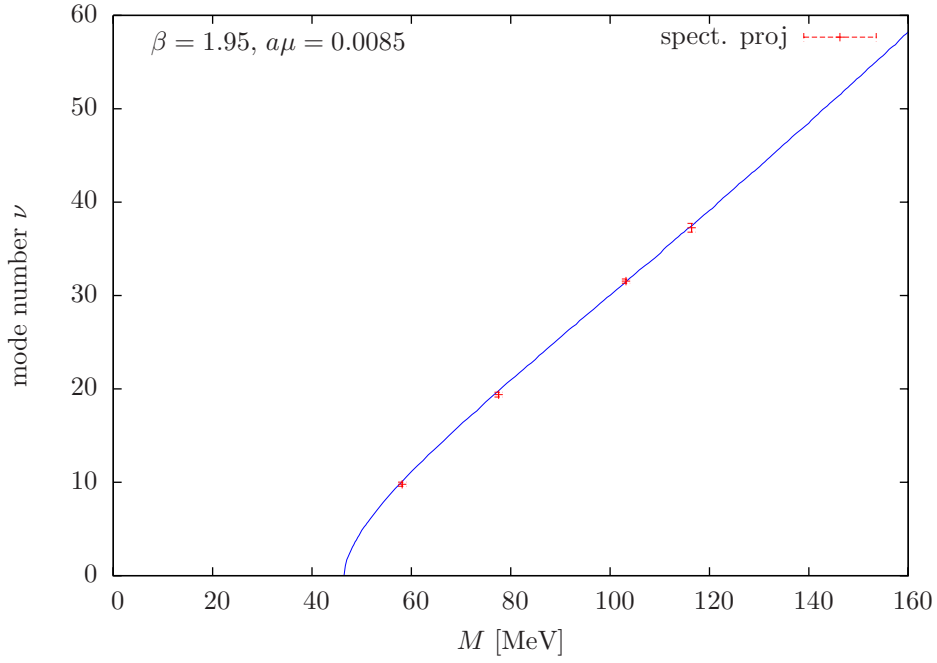

Figure 3.4.: Comparison of the mode number ν as a function of the threshold parameter M for $\beta = 1.95$ and $a\mu = 0.0085$ using spectral projectors (red points) and a direct computation of eigenvalues of $D_{tm}^{\dagger} D_{tm}$ (blue line). For the sake of clarity the blue line, which is originally a discrete line, it has been drawn continuous.

is negligible in comparison with the statistical error [5].

A moment of thought shows us that the method explained above, in fact, describes a simple procedure. If we consider an eigenvalue α^2 larger than $M_\star^2$, it will correspond to a positive value of the operator $\mathbb{X}$, whereas an eigenvalue below $M_\star^2$, which will count for the calculation of the mode number, will give us a negative value. Thereby a negative value of $\mathbb{X}$ will contribute to the trace, whereas a positive value of $\mathbb{X}$ has no contribution since the evaluation of the step function vanishes for such cases. For a better understanding we sketch this lines of reasonings below

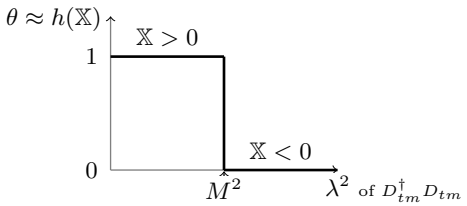

[5] We refer to the original source Ref. [59] for further details.

In practice, every time that we apply $\mathbb{X}$ to the randomly generated η field, we need to solve the following linear system

$$(D_{tm}^{\dagger} D_{tm} + M_{\star}^2)\psi = \eta. \tag{3.35}$$

The most computationally expensive part of the calculation is to find the solution of Eq. (3.35) and it requires a very efficient algorithm to be applied. In our case we used the conjugate gradient (CG) method[6].

As it was mentioned in the introduction, there is another way of extracting the mode number by simply computing the eigenvalues of $D_{tm}^{\dagger} D_{tm}$ and then manually counting how many modes lie below a certain threshold M^2. This method is, of course, very expensive and therefore can not be used extensively for large volumes since the cost of the calculation grows with the square or even higher power of the volume. However it offers a perfect opportunity to test our implementation, since we can directly compare the results obtained applying both methods: direct calculation and using spectral projectors. In Fig. 3.4 both results are plotted and one can see that the data show a perfect agreement.

The blue line corresponds to the results of the direct computation of the eigenmodes of $D_{tm}^{\dagger} D_{tm}$. There we chose several values of M and directly counted. Thus the line is in fact discrete, although we there are so many points that we plotted them as a continuous line to simplify the figure. The red points correspond to the results obtained using the spectral projectors method for 4 different values of M.

It is important to notice that the discrete points which build the blue line carry a statistical error since they are computed as expectation values. In order to make the figure better readable, the errors are not shown in the plot. In any case, both results are perfectly compatible providing an important test of the spectral projectors method.

3.3. Test of the implementation

We implemented the above explained method in the framework of the tmLQCD package [78]. We followed all the suggestions made in the article where the method was originally introduced [59]. To be concrete, the degree of the Chebyshev polynomial n was set to 32 and we chose ϵ, the parameter that gives the interval around the origin which should be excluded, to be $\epsilon = 0.01$. However we performed several tests where the value of n was varied in the range from 32 to 103 and we found that, even though the quality of the approximation was improved by increasing n, the results did not show any substancial change.

In Ref. [59] it was mentioned that, regarding the precision of the inversion, "a fairly loose stopping criterion can be chosen without compromising the correctness of the result". To test that statement and to be able to quantify the optimal precision of the chosen inverter, CG in our case, we performed a test where we computed the relevant observables which will be presented in this work for a range of relative precision of the CG inverter between $[10^{-2} - 10^{-10}]$. The corresponding observables to Fig. 3.5 and Fig. 3.6

[6]For details of the CG inverter we refer to any introductory book of numerical analysis, e.g Ref. [77]

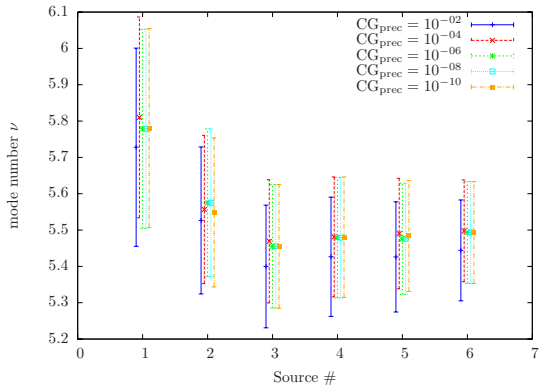

Figure 3.5.: Mode number for different number of stochastic sources and various values for the relative precision of the CG inverter

are defined as

$$\nu = \frac{1}{N}\sum_{k=1}^{N}(\mathbb{R}_M^2\eta_k,\ \mathbb{R}_M^2\eta_k). \tag{3.36}$$

$$\mathcal{B} = \frac{1}{N}\sum_{k=1}^{N}(\mathbb{R}_M\gamma_5\mathbb{R}_M\eta_k,\ \mathbb{R}_M\gamma_5\mathbb{R}_M\eta_k), \tag{3.37}$$

$$\mathcal{C} = \frac{1}{N}\sum_{k=1}^{N}(\mathbb{R}_M\eta_k,\ \gamma_5\mathbb{R}_M\eta_k). \tag{3.38}$$

For the moment we do not enter into the details of the given observables, since they will become relevant when the chiral condensate and the topological susceptibility are presented in the following chapters, where these observables will be studied in depth.

Our conclusion was surprising, since even a relative precision of 10^{-2} seems to give a correct result. Nevertheless we decided to be conservative and compute all our observables with a precision of 10^{-6}. In Fig. 3.6 we plot the result of three different observables for the mentioned range of precision of the inverter. The mode number is studied in Fig. 3.5.

Another parameter that needs to be tuned is the number of sources, which varies from one observable to other. In Fig. 3.5 and Fig. 3.6 we analyze the number of stochastic sources needed for 3 different observables. In Fig. 3.5 the mode number is shown, and we can conclude that one source is enough to accurately compute ν, although adding another source will decrease the error considerably. The use of a third source, in this particular case, does not seem worth, since the error remains almost constant in comparison with the result obtained using 2 sources. In the case of the observables plotted in Fig. 3.6, which will be introduced in the following chapters, we can immediately conclude that for the observable $\mathcal{C}$ one source is not enough. We will discuss more deeply the necessary

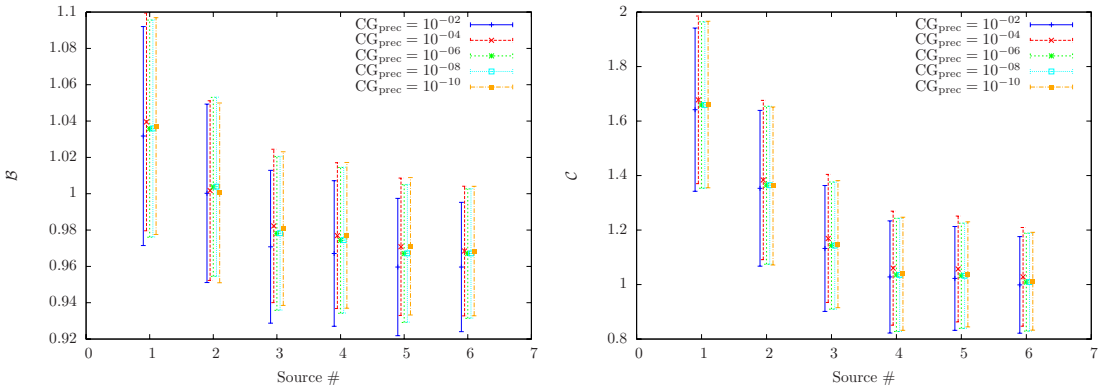

Figure 3.6.: Observables $\mathcal{B}$ and $\mathcal{C}$, used to compute χ_{rmtop} and Z_P/Z_C, for different number of stochastic sources and various values for the relative precision of the CG inverter

number of sources for those observables in their corresponding chapter.

CHAPTER 4

Computation of chiral condensate

Contents

Chiral symmetry and, in particular, its spontaneous breaking is a fundamental property of QCD with relevant phenomenological implications such as the low mass of the pions among others. The chiral condensate is an order parameter of spontaneous chiral symmetry breaking. For that reason it becomes an important quantity to compute and moreover its study can guide us to a better understanding of the mechanism behind the spontaneous breaking of chiral symmetry in QCD.

The present chapter is devoted to the computation of the chiral condensate using spectral projectors including a comprehensive discussion of systematic effects. Before presenting the details and results of the calculation, we prove that the short distance singularities of the spectral densities involved in the definition of the mode number do not spoil the $O(a)$ improvement, otherwise guaranteed of maximally twisted mass fermions. We then explain the application of the spectral projectors method to compute the chiral condensate and how we treat the statistical and systematic errors to give a reliable estimation of the final uncertainty. In Sec. 4.4 we study the finite volume effects to ensure that all our result are compatible with infinite volume. In Sec. 4.5 and Sec. 4.6 we reliably perform a chiral and continuum extrapolation of the data to obtain our final result of the chiral condensate for $N_f = 2$ and $N_f = 2 + 1 + 1$ flavors of maximally twisted mass dynamical fermions which are then compared with other results found in the literature finding a very good agreement.

4.1. Chiral condensate in chiral perturbation theory

The Banks-Casher relation [60] links the spontaneous chiral symmetry breaking with the low lying spectrum of the Dirac operator. Thus it directly relates the chiral condensate Σ with the spectral density ρ in the following way

$$\lim_{\lambda\to 0}\lim_{m\to 0}\lim_{V\to\infty}\rho(\lambda,m)=\frac{\Sigma}{\pi}. \tag{4.1}$$

It is important to notice that in Eq. (4.1) the limits are not interchangeable. We first need to go to the infinite volume limit to allow the spontaneous breaking to occur, then we need to remove the quark mass which is responsible for the explicit breaking of chiral symmetry, and finally we are interested in the low lying part of the spectrum, which contains the information about the chiral symmetry breaking mechanism we are interested in.

Simulations in lattice QCD entail a high computational cost, in particular, the value of the quark mass used is a factor that substantially increases the cost of the Monte Carlo simulation when the physical pion mass is approached. For this reason most simulations are carried out at larger pion masses and it is necessary to extrapolate to the physical pion mass to compute physical observables such as, e.g. decay constants. Nevertheless, simulations at the physical quark mass are currently being carried out, which implies a milestone for lattice QCD simulations. In this work, however, we will make use of gluon configurations that are simulated at larger than physical pion masses, hence the mentioned chiral extrapolation is needed.

In order to perform such an extrapolation, either to the physical mass or to the chiral limit, we rely on chiral perturbation theory, which predicts the behavior at low quark masses. This section is dedicated to present the relevant formulas of χPT for the chiral condensate that we apply in our study.

In infinite volume, a mass dependent effective chiral condensate can be defined at next to leading order [59], which at leading order coincides with the Banks-Casher relation and therefore with Σ in the chiral limit

$$\frac{\Sigma_{\text{eff}}}{\Sigma}|_{V=\infty} = 1 - \frac{m\Sigma}{16\pi^2 F^4}\left\{3\ln\frac{\Lambda\Sigma}{\bar{\mu}^2F^2} - 3\bar{l}_6 - 1 + \ln 2 + \ln\left(1+\frac{m^2}{\Lambda}\right) + \frac{m}{\Lambda}\arctan\frac{\Lambda}{m} + \frac{\Lambda}{m}\arctan\frac{m}{\Lambda}\right\} + \dots \tag{4.2}$$

In Eq. (4.2) the low energy constants F and l_6 are the pion decay constant in the chiral limit and a low energy effective renormalized coupling at scale $\bar{\mu}$ respectively [1].

This expression shows the deviation of the effective mass-dependent chiral condensate with respect to Σ in the chiral limit. There we can see a direct dependence on the spectrum of $D^\dagger D$ through $\Lambda = \sqrt{M^2 - m^2}$ and the quark mass m.

For low values of the quark mass m, the next-to-leading order corrections in Eq. (4.2) tend to be very small for any value of Λ or M. Moreover, in the chiral limit, those terms vanish.

Following the strategy in Ref. [59], we have computed the deviations of the ratio $\Sigma_{\text{eff}}/\Sigma$ for different values of M at the range of the quark masses relevant for the calculations presented in this work. Fig. 4.1 shows that the corrections are very small for low masses at various representative values of M. For all the calculations in this work a fixed value of M for each β was chosen around 90 MeV, where the corrections are almost negligible.

Recently a preliminary extended study has been presented [79] were it was observed that the NNLO effects seem to be larger than firstly expected. Following their strategy we repeated the test of the NNLO effects for our case, see App. E.2. However, we could not see any effects of the NNLO corrections. This situation needs to be clarified in the future but it goes beyond the scope of this thesis.

4.2. Short distance singularities and $\mathcal{O}(a^2)$ scaling

The study of different observables behavior when the continuum limit is approached is a fundamental issue in lattice QCD. Here, over the years, significant progress has been made. Nowadays all groups world-wide employ a lattice action for their computations which guarantees that the continuum limit is approached at a rate $\mathcal{O}(a^2)$. We speak of the usage of $O(a)$ *improved actions*. One additional difficulty in achieving an $O(a)$ *improvement* can appear in quantities which are affected by short distance singularities, as it is the case for the density chain used here to compute the chiral condensate.

[1] See Ref. [59] for more details.

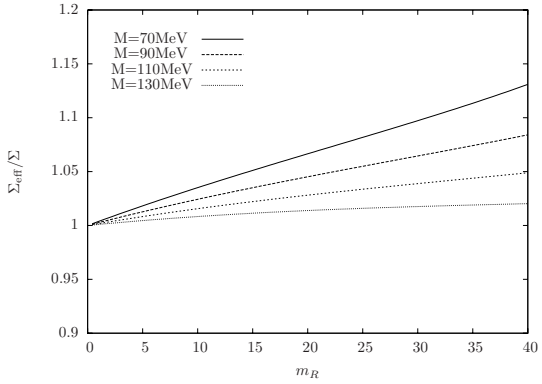

Figure 4.1.: Chiral behavior of the ratio $\Sigma_{\rm eff}/\Sigma$ described by Eq. (4.2) which corresponds to a NLO formula in χPT. In this plot the values chosen for the low energy constant which are $\Sigma^{1/3} = 250$ MeV, $\bar{l}_6 = 3$, $F = 90$ MeV and the scale $\bar{\mu} = 140$ MeV respectively.

The short distance singularities give rise to contact terms in the Symanzik expansion which, as commented above, can spoil the $O(a)$ improvement. The purpose of this section is to show that, in the case of the density chain given by Eq. (3.8), those terms are of $\mathcal{O}(am_q)$ and therefore vanish when twisted mass fermions at maximal twist are used.

First of all we need to prove that our observable is $\mathcal{R}_5^1$ parity even, a required property for automatic $O(a)$ improvement as it was previously explained. Thus we apply the transformation given in Eq. (2.33) to Eq. (3.8) and we recover the original expression

$$\sigma_3'(\mu, m) = -a^{24} \sum_{x_1,\ldots,x_5} \left\langle P_{12}^-(x_1) P_{23}^+(x_2) P_{34}^-(x_3) P_{45}^+(x_4) P_{56}^-(x_5) P_{61}^+(0) \right\rangle . \tag{4.3}$$

The $\mathcal{R}_5^1$ transformation merely interchanges the charges of the pseudo-scalar densities. Since we have a closed chain with an equal number of positively and negatively charged densities, we can conclude that both observables, given by Eq. (3.8) and Eq. (4.3) respectively, are equivalent and therefore Eq. (3.8) is invariant under $\mathcal{R}_5^1$ transformations. The reason is that a simple relabeling of the flavor indices in Eq. (4.3) leads to Eq. (3.8).

Additionally, we computed the off-shell tree-level propagator of twisted mass fermions to see that it does not have an explicit $O(a)$ term. If such a term appears at tree level it would remain in the interactive theory spoiling the $\mathcal{O}(a^2)$ scaling. In App. C.1 the details of the calculation are presented and it is in fact proven that $O(a)$ terms do not appear. We remark that the same calculation for Wilson fermions yields to an explicit $O(a)$ term at tree-level as shown in App. C.1.

In Chap. 2 the Symanzik effective theory was introduced. There we discussed the effective expansion of the action and the operators. In the discussion, we omitted the contact terms, since we had general on-shell observables in mind which are not affected by such short distance singularities. Here, we are interested in the Symanzik expansion of the density chain given in Eq. (3.8). For this we need to write the effective expansion

of the pseudo-scalar density in terms of the lattice spacing

$$P_{\rm eff}^{ab} = P_{ab} + a(m_q P_{ab} + \mu S_{ab}) + \mathcal{O}(a^2), \tag{4.4}$$

where P_{ab} corresponds to continuum limit pseudoscalar density. The second term contains all the operators of dimension 5 with the same quantum numbers as P_{ab}. The following terms which would include higher dimensional operators do not need to be considered, since they correspond to, at least, an $\mathcal{O}(a^2)$ contribution.

This implies the following Symanzik expansion

$$\begin{aligned}
&\int d^4x_1 d^4x_2 d^4x_3 d^4x_4 d^4x_5 \left\langle P_{12}^+(x_1) P_{23}^-(x_2) P_{34}^+(x_3) P_{45}^-(x_4) P_{56}^+(x_5) P_{61}^-(0)\right\rangle = \\
&= \int d^4x_1 d^4x_2 d^4x_3 d^4x_4 d^4x_5 \left\langle P_{12}^+(x_1) P_{23}^-(x_2) P_{34}^+(x_3) P_{45}^-(x_4) P_{56}^+(x_5) P_{61}^-(0)\right\rangle_0 \\
&+ a6c_1 m_q \int d^4x_1 d^4x_2 d^4x_3 d^4x_4 d^4x_5 \left\langle P_{12}^+(x_1) P_{23}^-(x_2) P_{34}^+(x_3) P_{45}^-(x_4) P_{56}^+(x_5) P_{61}^-(0)\right\rangle_0 \\
&+ a6c_1' \mu \int d^4x_1 d^4x_2 d^4x_3 d^4x_4 d^4x_5 \left\langle S_{12}^+(x_1) P_{23}^-(x_2) P_{34}^+(x_3) P_{45}^-(x_4) P_{56}^+(x_5) P_{61}^-(0)\right\rangle_0 \\
&+ \text{contact terms} + \mathcal{O}(a^2).
\end{aligned} \tag{4.5}$$

A first $O(a)$ term, which in principle is present in Eq. (4.5) and corresponds to the effective twisted mass action, does not contribute, for symmetry reasons, as it was already explained in detail in Chap. 2 and therefore it has been omitted. The second and third terms correspond to the $O(a)$ terms which appear in the effective pseudo-scalar density $P_{ab}^{\rm eff}$ given by Eq. (4.4). Both terms vanish for maximally twisted mass fermions; the former because m_q is tuned to zero and the latter because of symmetry reasons, i.e. the term is $\mathcal{R}_5^1$ odd and therefore it has to be zero, as it was explained in Chap. 2. In the Wilson case an analogous term to the former appears which leads to the introduction of an improvement coefficient in the renormalization factor in order to cancel the corresponding $O(a)$ contribution. In contrast, in the twisted mass case at maximal twist there is no need to tune any further parameter besides m_{pcac}. For the sake of clarity, in the following we omit all the $O(a)$ terms which vanish, therefore we are only left with the contact terms.

We are then interested in computing the contact terms which rise when two or more densities are placed in the same point. The operator product expansion (OPE) is a fundamental tool which allow us to study the singularities of a product of operators $\mathcal{O}_1(x)\mathcal{O}_2(0)$ when x approaches zero. We can apply OPE in this interactive case, which in principle is only applicable at tree level, due to the property of asymptotic freedom that QCD shows at short distance. Through OPE we can explicitly compute the form of the contact terms and study the divergences originated by them.

We need to study all the different combinations of densities placed at the same point. Thus, in principle, we need to consider two, three or even the whole chain placed at zero. However, a careful analysis of the singularities using power counting shows that the only case which give rise to $O(a)$ terms in the Symanzik expansion is a product of two operators. The reason is that the divergence originated by two pseudoscalar operators

goes like $|x|^{-3}$ which after a four dimensional integration give rise to an $O(a)$ term. In the case of three operators, the divergence goes like $|x|^{-6}$, but in this case the integral goes d^8x which corresponds to an $\mathcal{O}(a^2)$ term in the Symanzik expansion. A higher number of operators gives an even higher power of a. Even in the case where we place at zero all the densities and therefore a mixture with the identity in flavor space occurs, the divergence goes like $|x|^{-18}$ and the integral is over $d^{20}x$ leading to an $O(a^3)$ term according to power counting. In addition only consecutive operators share a common flavor structure and can, therefore, mix. In conclusion we are only interested in the case $P^+_{ab}(x)P^-_{bc}(0)$ when $x \to 0$.

To apply OPE we need to consider all the symmetries of the twisted mass action[2] to obtain all the operators which mix with the product $P^+_{ab}(x)P^-_{bc}(0)$. In principle we are interested only in the operators with the lowest dimension since they correspond to the dominant singularity and therefore can give rise to $O(a)$ contact terms. All the higher dimensional operators, which in principle also mix, correspond to $\mathcal{O}(a^2)$ or higher power and are therefore neglected.

The quark content of the product $P^+_{ab}(x)P^-_{bc}(0)$ constrains the mixing with operators of dimension 3 to only two operators:

$$S^{\uparrow}_{ac} = \overline{\psi}_a \frac{1}{2}(\mathbb{1} \pm \tau^3)\psi_c, \tag{4.6}$$

$$P^{\uparrow}_{ac} = \overline{\psi}_a \gamma_5 \frac{1}{2}(\mathbb{1} \pm \tau^3)\psi_c, \tag{4.7}$$

and the modified parity $\tilde{P}$ restricts the mixing even more eliminating $P^{\uparrow}_{ac}$ which is $\tilde{P}$ odd whereas the product is even under this transformation[3]. Therefore we can conclude that

$$P^+_{ab}(x)P^-_{bc}(0) \overset{x\to 0}{\sim} C(x)S^{\uparrow}_{ac}(0) + \dots. \tag{4.8}$$

The Wilson term $C(x)$ contains a singularity of the form $|x|^{-3}$, which leads to $O(a)$ terms in the Symansik expansion after integration. As we previously explained the identity operator does not mix with the product due the non-trivial flavor structure of the product of densities.

We are thus lead to include a term for each singularity in the Symansik expansion

$$\begin{aligned}
&\int d^4x_1 d^4x_2 d^4x_3 d^4x_4 d^4x_5 \left\langle P^+_{12}(x_1)P^-_{23}(x_2)P^+_{34}(x_3)P^-_{45}(x_4)P^+_{56}(x_5)P^-_{61}(0)\right\rangle = \\
&= \int d^4x_1 d^4x_2 d^4x_3 d^4x_4 d^4x_5 \left\langle P^+_{12}(x_1)P^-_{23}(x_2)P^+_{34}(x_3)P^-_{45}(x_4)P^+_{56}(x_5)P^-_{61}(0)\right\rangle_0 \\
&+ ac_2 \int d^4x_2 d^4x_3 d^4x_4 d^4x_5 \left\langle S^{\uparrow}_{13}(x_2)P^+_{34}(x_3)P^-_{45}(x_4)P^+_{56}(x_5)P^-_{61}(0)\right\rangle_0 + \\
&+ ac_2 \int d^4x_1 d^4x_3 d^4x_4 d^4x_5 \left\langle P^+_{12}(x_1)S^{\uparrow}_{24}(x_3)P^-_{45}(x_4)P^+_{56}(x_5)P^-_{61}(0)\right\rangle_0 +
\end{aligned} \tag{4.9}$$

[2]For a detailed introduction to twisted mass symmetries see App. A.2.

[3]If we were interested in 4-dimensional operators $\mu P^{\uparrow}_{ac}$ would mix since it is even under $\tilde{P}$.

$$
\begin{aligned}
&+ ac_2 \int d^4x_1 d^4x_2 d^4x_4 d^4x_5 \left\langle P^+_{12}(x_1) P^-_{23}(x_2) S^\uparrow_{35}(x_4) P^+_{56}(x_5) P^-_{61}(0) \right\rangle_0 + \\
&+ ac_2 \int d^4x_1 d^4x_2 d^4x_3 d^4x_5 \left\langle P^+_{12}(x_1) P^-_{23}(x_2) P^+_{34}(x_3) S^\uparrow_{46}(x_5) P^-_{61}(0) \right\rangle_0 + \\
&+ ac_2 \int d^4x_1 d^4x_2 d^4x_3 d^4x_4 \left\langle P^+_{12}(x_1) P^-_{23}(x_2) P^+_{34}(x_3) P^-_{45}(x_4) S^\uparrow_{51}(0) \right\rangle_0 + \\
&+ ac_2 \int d^4x_2 d^4x_3 d^4x_4 d^4x_5 \left\langle P^-_{23}(x_2) P^+_{34}(x_3) P^-_{45}(x_4) P^+_{56}(x_5) S^\uparrow_{62}(0) \right\rangle_0 + \mathcal{O}(a^2).
\end{aligned}
$$

It is possible to find a relation between the contact terms and the original density chain through non-singlet axial Ward-Takahashi identities. We performed such calculation, which is presented and explained in detail in App. C.2, and obtained the following identities

$$
\begin{aligned}
&\int d^4x_2 d^4x_3 d^4x_4 d^4x_5 \left\langle S^\uparrow_{13}(x_2) P^+_{34}(x_3) P^-_{45}(x_4) P^+_{56}(x_5) P^-_{61}(0) \right\rangle + \\
&+ \int d^4x_2 d^4x_3 d^4x_4 d^4x_5 \left\langle P^-_{23}(x_2) P^+_{34}(x_3) P^-_{45}(x_4) P^+_{56}(x_5) S^\uparrow_{62}(0) \right\rangle \\
&= 2m_q \int d^4x_2 d^4x_3 d^4x_4 d^4x_5 \int d^4x_1 \left\langle P^+_{12}(x_1) P^-_{23}(x_2) P^+_{34}(x_3) P^-_{45}(x_4) P^+_{56}(x_5) P^-_{61}(0) \right\rangle
\end{aligned}
\tag{4.10a}
$$

$$
\begin{aligned}
&\int d^4x_2 d^4x_3 d^4x_4 d^4x_5 \left\langle P^+_{12}(x_1) S^\uparrow_{24}(x_3) P^-_{45}(x_4) P^+_{56}(x_5) P^-_{61}(0) \right\rangle + \\
&+ \int d^4x_2 d^4x_3 d^4x_4 d^4x_5 \left\langle P^+_{12}(x_1) P^-_{23}(x_2) P^+_{34}(x_3) P^-_{45}(x_4) S^\uparrow_{51}(0) \right\rangle \\
&= 2m_q \int d^4x_2 d^4x_3 d^4x_4 d^4x_5 \int d^4x_1 \left\langle P^+_{12}(x_1) P^-_{23}(x_2) P^+_{34}(x_3) P^-_{45}(x_4) P^+_{56}(x_5) P^-_{61}(0) \right\rangle
\end{aligned}
\tag{4.10b}
$$

$$
\begin{aligned}
&\int d^4x_2 d^4x_3 d^4x_4 d^4x_5 \left\langle P^+_{12}(x_1) P^-_{23}(x_2) S^\uparrow_{35}(x_4) P^+_{56}(x_5) P^-_{61}(0) \right\rangle + \\
&+ \int d^4x_2 d^4x_3 d^4x_4 d^4x_5 \left\langle P^-_{23}(x_2) P^+_{34}(x_3) P^-_{45}(x_4) P^+_{56}(x_5) S^\uparrow_{46}(x_5) P^-_{61}(0) \right\rangle \\
&= 2m_q \int d^4x_2 d^4x_3 d^4x_4 d^4x_5 \int d^4x_1 \left\langle P^+_{12}(x_1) P^-_{23}(x_2) P^+_{34}(x_3) P^-_{45}(x_4) P^+_{56}(x_5) P^-_{61}(0) \right\rangle
\end{aligned}
\tag{4.10c}
$$

If we now substitute Eq. (4.10a-4.10c) in Eq. (4.9) we obtain the final result for 6 flavors.

$$
\begin{aligned}
&\int d^4x_1 d^4x_2 d^4x_3 d^4x_4 d^4x_5 \left\langle P_{12}(x_1) P_{23}(x_2) P_{34}(x_3) P_{45}(x_4) P_{56}(x_5) P_{61}(0) \right\rangle = \\
&= \int d^4x_1 d^4x_2 d^4x_3 d^4x_4 d^4x_5 \left\langle P_{12}(x_1) P_{23}(x_2) P_{34}(x_3) P_{45}(x_4) P_{56}(x_5) P_{61}(0) \right\rangle_0
\end{aligned}
\tag{4.11}
$$

$$+ a6c_2 m_q \int d^4x_1 d^4x_2 d^4x_3 d^4x_4 d^4x_5 \, \langle P_{12}(x_1) P_{23}(x_2) P_{34}(x_3) P_{45}(x_4) P_{56}(x_5) P_{61}(0) \rangle_0$$
$$+ \mathcal{O}(a^2)$$

Generalizing this expression for N_f number of flavors is straightforward, we chose to write a specific example just for simplicity.

Our final result given by Eq. (4.11) shows that the contact terms that arise in the Symanzik expansion are proportional to the Wilson quark mass. However, in the twisted mass formulation at maximal twist, the Wilson mass is tuned to zero. This directly implies that the contact terms vanish at maximal twist.

This concludes our proof where we have shown that the mode number, and consequently, the chiral condensate have an $\mathcal{O}(a^2)$ scaling towards the continuum for twisted mass fermions at maximal twist, as it is our case.

Note that an identical conclusion is found if, instead of Ward identities, symmetry arguments are applied [4]. The motivation to follow the procedure shown above was the analogy to the calculation done in the Wilson case to obtain the improvement coefficients introduced in Ref. [74].

4.3. Chiral condensate with spectral projectors

In this section we describe the strategy to compute the chiral condensate through the Banks-Casher relation using spectral projectors, a method that was already introduced in the previous chapter. We first introduce the procedure to compute the chiral condensate through the mode number, which is computed using the spectral projectors. We then explain the technical details of the implementation of the method through a particular example. We also discuss our error analysis which includes a comprehensive calculation of all systematic uncertainties.

4.3.1. Procedure

We computed the chiral condensate through the Banks-Casher relation given by Eq. (4.1). Instead of computing the spectral density ρ, we calculated the mode number ν and then extract the effective chiral condensate through the following equation

$$\Sigma_R = \frac{\pi}{2V} \sqrt{1 - \left(\frac{\mu_R}{M_R} \right)} \frac{\partial}{\partial M_R} \nu_R(M_R, \mu_R). \tag{4.12}$$

which was proposed in Ref. [59]. In Eq. (4.12) the pre-factor was chosen to match the chiral condensate to leading order of chiral perturbation theory. We comment further on this formula in the following.

[4] In following chapters we will use this alternative strategy, based on symmetry properties of twisted mass, to study the improvement of the topological susceptibility.

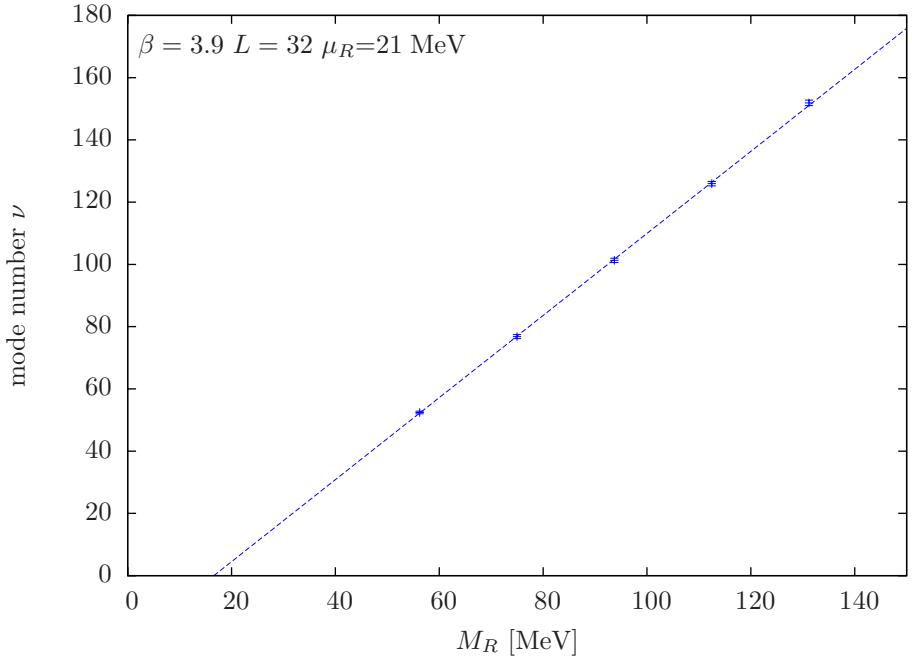

Figure 4.2.: Mode number ν as a function of the renormalized threshold parameter M_R for $N_f = 2$ at $\beta = 3.9$ and $a\mu = 0.004$. The line corresponds to a linear fit to all 5 points.

The value of Σ_R in Eq. (4.12) is constant in the region where the mode number shows a linear behavior in M_R. Performing then a simple linear fit to our data points, will allow us to compute the mass dependent effective chiral condensate from the slope of this fit.

In our experience the linear regime extends from about 50 MeV until at least 110 MeV, although this range depends on the parameters of the simulation. The quark mass is directly related to the lower bound given above and therefore a mass larger than 40 MeV can decrease the interval of linearity. Therefore we concluded that it is important to avoid the region below 1.5μ. The identification of the linear regime for the mode number as a function of M has been carefully studied and by changing the fitting range we were able to provide a systematic error stemming from a possible mis-identification of the linear region.

We illustrate the spectral projectors method with one example which corresponds to the $N_f = 2$ ensemble b40.32[5] where $\mathcal{O}(200)$ independent configurations were analyzed. As it is shown in Fig. 4.2, the mode number computed using spectral projectors for 5 values of M_R clearly falls onto a straight line in the chosen region [50,120] MeV. The plotted line corresponds to a linear fit which is performed over all points in order to extract the slope. In general we avoid to convert M_R to MeV, since it would introduce an error coming from the estimation of the lattice spacing in physical units, and therefore

[5]All the details of the gauge ensembles that have been used in this work can be found in App. D

all the fits are performed using aM_R. The term $\partial\nu/\partial M_R$ in Eq. (4.12) is given by the extracted slope m_R is the quark mass and M_R corresponds to the middle point of the fitting interval.

The linear behavior of our data in the presented example is actually observed in all the ensembles for the region of M that we specified above, except for some small deviations that are taken into account in the systematic error. Moreover if instead of M we choose the quantity Λ, the same linear behavior is observed. All the results and a further discussion about the linearity and its implications in the calculation of Σ_{eff} can be found in App. E.2.

A main issue in lattice calculations is that the Monte Carlo simulations are affected by autocorrelations. Autocorrelations can have a big influence in the determination of the error of the expectation value of a given observable, usually leading to an underestimation of the statistical uncertainty. In order to consider the autocorrelation to compute the statistical errors, in all our calculations we applied the method described in Ref.[80]. For each quantity we computed the integrated autocorrelation time τ_{int} which gives an estimation of the autocorrelation that affects a given observable. If $\tau_{int} > 0.5$ the effective statistics are lower and therefore the naive error, taken every measurement as being independent, is expected to be underestimated. All the results of each computed observable together with its error and the corresponding τ_{int} are given in App. E.1. An additional and completely independent analysis using the bootstrap method was made to cross-check all the results [81].

In order to demonstrate the accuracy that can be obtained with the spectral projectors method, we give the value of the chiral condensate for the example shown in Fig. 4.2. The chiral condensate is extracted from the slope of the linear fit, as explained above which leads to $a\Sigma^{1/3} = 0.13372(34)$ if only the statistical error is consider.

In order to reduce the statistical error for $a\Sigma^{1/3}$ we need to compute the mode number more accurately. To this end we can either increase statistics, which reduces the error as $\mathcal{O}(1/\sqrt{N})$, or increase the number of stochastic sources.

Increase the number of stochastic sources decreases the variance given by [59]

$$\left\langle (\mathcal{O}_N - \langle \mathcal{O}_N \rangle)^2 \right\rangle = \left\langle (\mathrm{Tr}\{\mathbb{P}_M\} - \langle \mathrm{Tr}\{\mathbb{P}_M\} \rangle)^2 \right\rangle + \frac{1}{N}\nu(M, m), \tag{4.13}$$

where

$$\mathcal{O}_N = \frac{1}{N}\sum_{k=1}^{N} (\eta_k, \mathbb{P}_M \eta_k). \tag{4.14}$$

In all the calculations presented in this work only one stochastic source was used since, as we explain in detail below, the computation is dominated by systematic effects, being the statistical error almost negligible. However, in our experience, if a decrease of the statistical uncertainty is desired, an additional source would be a good choice, whereas beyond two sources the cost of the calculation do not seem to compensate the low improvement in the precision.

Nevertheless, it is important to notice that, when we increase the volume, the mode number increases, whereas the statistical error remains of the same order, i.e. the mode

lowest M		largest M		χ^2/dof	$r_0\Sigma^{1/3}$
aM_R	M_R(MeV)	aM_R	M_R(MeV)		
0.0225	56	0.0375	93	0.004	0.7085(43)
0.0225	56	0.0450	112	0.018	0.7116(24)
0.0225	56	0.0525	131	0.588	0.7154(18)
0.0300	75	0.0450	112	0.006	0.7141(46)
0.0300	75	0.0525	131	0.567	0.7189(33)
0.0375	93	0.0525	131	0.549	0.7235(57)

Table 4.1.: Values of $r_0\Sigma^{1/3}$ for $\beta = 3.9$ and $a\mu = 0.004$ corresponding to different fit interval ranges. The value quoted as our final result corresponds to the fit which contains all the available points. The results obtained through different fits are used to compute the systematic error. The errors given are only statistical.

number is an extensive quantity. Therefore, the relative error decreases when the volume is increased. Moreover the error it is expect to decrease with a rate of $O(V^{-1/2})$ [59]. This remarkable property will be very useful for the different applications addressed in this work. A further discussion about the systematic effects that affect our calculation can be found in the next section.

4.3.2. Statistical and systematic errors

As showed above, the spectral projectors method yields to very accurate statistical results, such that a careful treatment of the systematic errors needs to be performed.

First of all, we need the renormalized value of M and hence the renormalization constant Z_μ [82, 83, 84], whose determination is dominated by systematic effects.

In addition, in order to be able to compare our results with others we need to express the chiral condensate $a\Sigma^{1/3}$ in either physical units MeV (typically in the $\overline{\text{MS}}$ scheme at 2 GeV) or as the dimensionless ratio $r_0\Sigma^{1/3}$. In both cases a new source of error is introduced in our result. The former is caused by the uncertainty in the estimation of the lattice spacing and the latter by the error in the calculation of r_0/a. However the spread of estimations of the lattice spacing in physical units[6] amounts to a relative error of around 7%, which leads to a systematic uncertainty in the chiral condensate much larger than the error introduced by r_0/a. Nevertheless we present both final results, dimensionless and dimension-full, although we chose to express all the intermediate values in terms of $r_0\Sigma^{1/3}$ due to the smaller systematic uncertainty of this choice. A further discussion about the current uncertainty of setting the scale in lattice calculations which affects also the parameter r_0 can be found at the end of the present chapter.

Finally we need to carefully examine the linearity of the mode number in the fitting region. In principle we expect that the slope of the linear fit and therefore $\partial\nu/\partial M_R$

[6]For instance for $\beta = 3.9$ we can find a=0.079 fm [40], a=0.085 fm[85], a=0.089 fm[86].

$N_f = 2$		
$L^3 \times T$	L [fm]	$r_0\Sigma^{1/3}$
$16^3 \times 32$	1.4	0.7121 (86)(53)(38)
$20^3 \times 40$	1.7	0.7214 (74)(54)(39)
$24^3 \times 48$	2.0	0.7246 (39)(54)(38)
$32^3 \times 64$	2.7	0.7154 (19)(53)(38)

Table 4.2.: Values of $r_0\Sigma^{1/3}$ for different volumes for $N_f = 2$. The errors quoted correspond to the statistical uncertainty, the error coming from r_0 and the error resulting from Z_P respectively.

remains constant as a function of M_R. However this is not strictly true, since reducing the number of points considered in the fit, which correspond to perform the fit in different intervals, leads to slightly different results. Nevertheless all the results are always compatible within errors. However, the differences found by choosing different fitting intervals will be taken into account as a systematic error.

In Tab. 4.1 we show the different results obtained through fits over various ranges for a given example, which again correspond to the ensemble b40.32. The spread of the results is considered to compute the systematic error which will be denoted as $()_{\text{fit}}$.

At the end, considering all the systematic errors that affect our calculation, we obtain the following result for the ensemble b40.32

$$r_0\Sigma^{1/3} = 0.7154(18)_{\text{stat}}(38)_{\text{fit}}(39)_{Z_P}(53)_{r_0/a}. \tag{4.15}$$

We can thus conclude that the uncertainty of our result is dominated by systematic effects. Moreover we can confirm that $\mathcal{O}(200)$ independent configurations is enough to have an almost negligible statistical error. Therefore we suggest to increase the number of values of M_R to decrease the systematic error originated by the choice of the linear fit range. Of course, the errors coming from r_0/a and Z_P are independent from this work and, in order to decrease the corresponding error of $r_0\Sigma^{1/3}$, even further improved estimates of the quantities need to be provided.

4.4. Finite volume effects for $N_f = 2$ and $N_f = 2 + 1 + 1$

By nature of the lattice simulations are restricted to a finite volume. It is for this reason that the study of finite volume effects (FVE) is a fundamental aspect in lattice QCD. In particular, we need to ensure that our results are not affected by FVE, since we are interested in the infinite volume theory.

Chiral perturbation theory (χPT) can be used to study systematic effects in lattice calculations such as, for example, finite volume effects. Theoretical arguments have been given [59] to show that the difference between the finite-volume Σ_{eff} and the infinite-

$N_f = 2+1+1$		
$L^3 \times T$	L [fm]	$r_0\Sigma^{1/3}$
$20^3 \times 40$	1.7	0.8541 (93)(62)(48)
$24^3 \times 48$	2.0	0.7979 (79)(58)(45)
$32^3 \times 64$	2.8	0.8000 (32)(58)(41)

Table 4.3.: Values of $r_0\Sigma^{1/3}$ for different volumes for $N_f = 2+1+1$. The errors quoted correspond to the statistical uncertainty, the error coming from r_0 and the error resulting from Z_P respectively.

volume Σ_{eff} decays exponentially in the following way

$$\Sigma_{\text{eff}} - \Sigma_{\text{eff}}|_{V=\infty} \propto e^{-\frac{1}{2}M_\Lambda L}, \tag{4.16}$$

where

$$M_\Lambda^2 = \frac{2\Lambda\Sigma}{F^2}, \qquad \Lambda = \sqrt{M^2 - \mu^2}. \tag{4.17}$$

In Eq. (4.16) the parameter F represents the pion decay constant in the chiral limit. Taken physical values for F it can be shown that the finite volume corrections are small since the mass dependent effective condensate is computed for large values of M with respect to the quark mass. In fact, the corrections should be of the order of 1% for $L \geq 2$ fm when typical values of M and m are used [59].

As it was explained in Ref. [59], M_Λ would correspond to the mass of a pseudo-scalar meson whose valence quarks would have a mass equivalent to Λ. We can then expect that the finite volume effects would be much smaller than for the pion mass, since we choose Λ to be much larger than the quark mass.

Furthermore an explicit calculation of the finite volume corrections of the integrated spectral density, i.e. the mode number, was performed in SU(2) chiral perturbation theory [70]. The corresponding analytic formula again predicts that the finite volume corrections are small $\mathcal{O}(\leq 1\%)$ for a range of M between 50 and 110 MeV and quark masses from 10 to 40 MeV if $L \geq 2$ fm. In addition the corrections that this formula predict are larger for larger values of M. The expression reads

$$\Delta N^V(m, \Lambda_2, m)_{\text{NLO}} = \int_m^{\Lambda_2} [\Delta\rho_Q^V(\lambda, m) + \Delta\rho_Q^V(-\lambda, m)]_{\text{NLO}} d\lambda = \tag{4.18}$$
$$\frac{2\Sigma^2}{4F^2} \frac{\sqrt{\Lambda_2^2 - m^2}}{(4\pi)^2 F^4} \sum_{\{n1,n2,n3,n4\}\neq 0} \left\{ \frac{2}{\sqrt{\Lambda_2^2 - m^2}} \text{Im} \left[F_{-2}\left(\frac{\Sigma q_n^2}{2F^2}, i\sqrt{\Lambda_2^2 - m^2} + m \right) \right] \right.$$
$$\left. - \frac{m}{\sqrt{\Lambda_2^2 - m^2}} \text{Im} \left[F_{-1}\left(\frac{\Sigma q_n^2}{2F^2}, i\sqrt{\Lambda_2^2 - m^2} \right) \right] + \text{Re} \left[F_{-1}\left(\frac{\Sigma q_n^2}{2F^2}, i\sqrt{\Lambda_2^2 - m^2} \right) \right] \right\}.$$

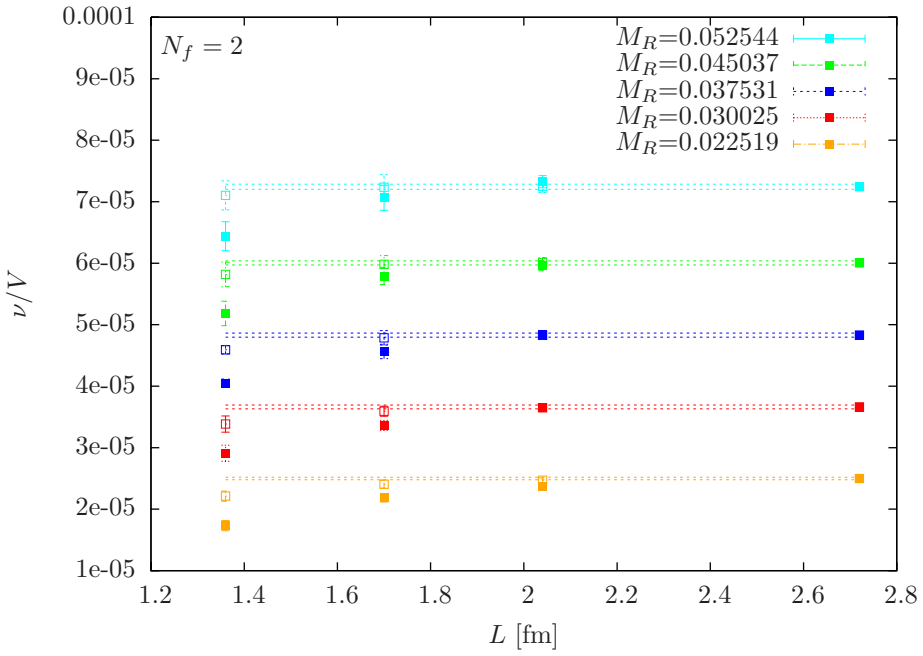

Figure 4.3.: Mode number computed for 4 different volumes and 4 different values of M_R are plotted as filled symbol. The open symbols correspond to the predicted finite volume corrections given by Eq. (4.18). The dotted lines are given by the values for the largest volume. The data shown in this plot corresponds to $N_f = 2$ dynamical fermions at $\beta = 3.9$ and $a\mu = 0.004$.

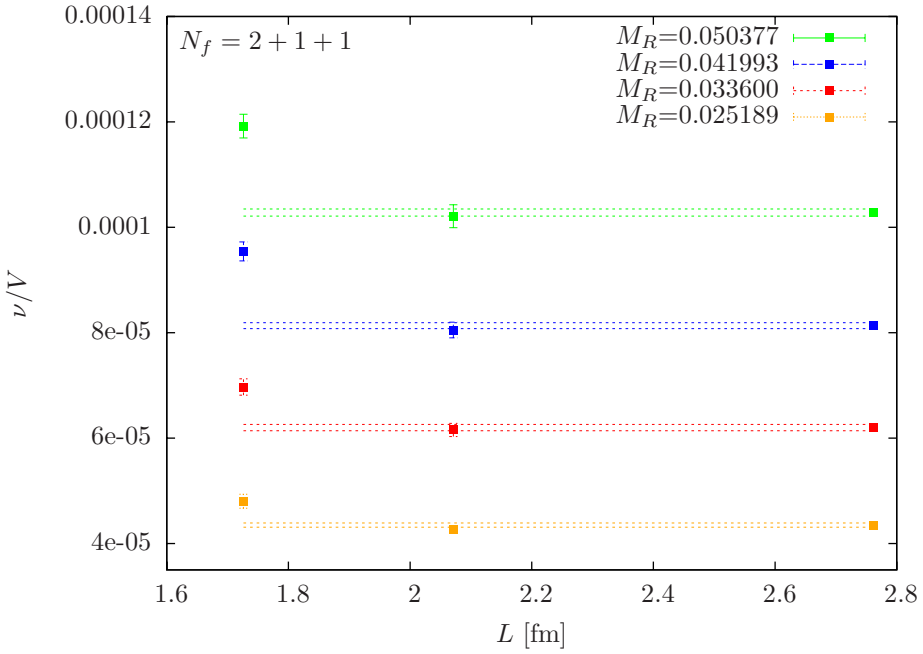

Figure 4.4.: Mode number computed for 4 different volumes and 4 different values of M_R. The dotted lines are given by the values for the largest volume. The data shown in this plot corresponds to $N_f = 2+1+1$ dynamical fermions at $\beta = 1.90$ and $a\mu = 0.004$.

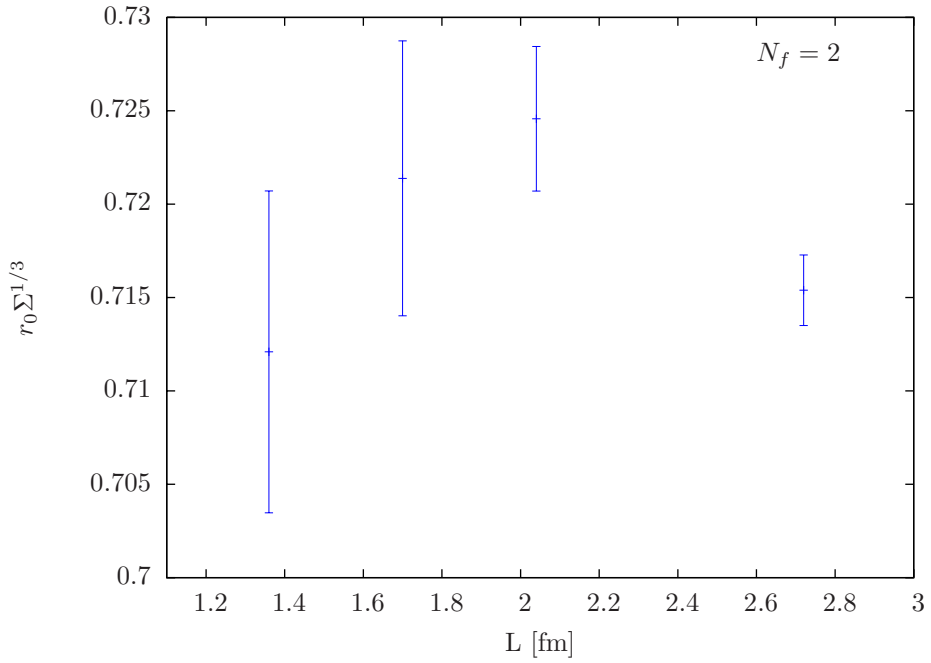

Figure 4.5.: Chiral condensate $r_0\Sigma^{1/3}$ for 4 different volumes for $N_f = 2+1+1$ dynamical fermions at $\beta = 1.90$, $a\mu = 0.004$. Only statistical errors are plotted.

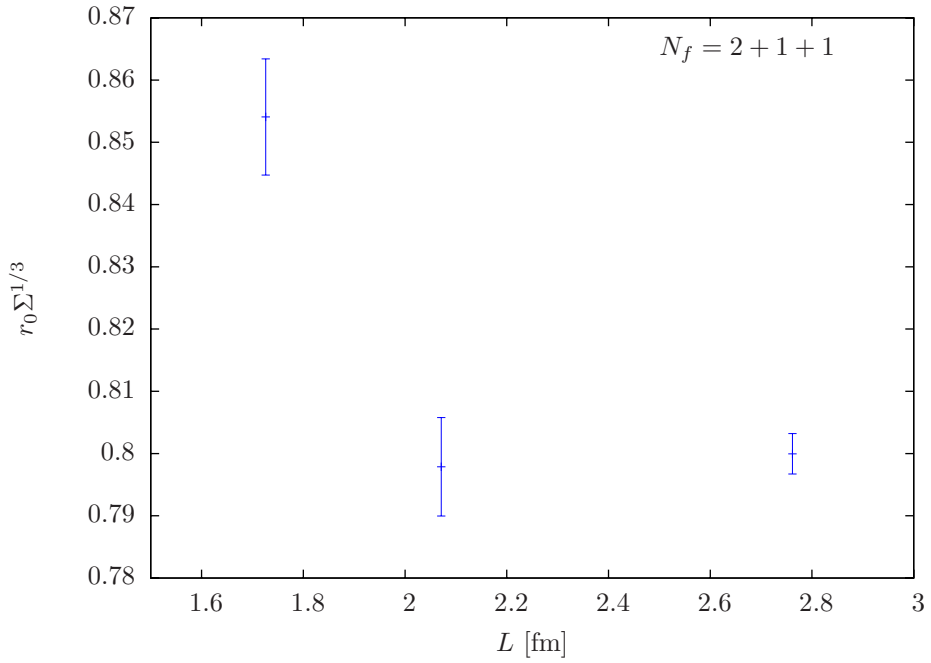

Figure 4.6.: Chiral condensate $r_0\Sigma^{1/3}$ for 4 different volumes for $N_f = 2+1+1$ dynamical fermions at $\beta = 1.90$, $a\mu = 0.004$. Only statistical errors are plotted.

In this section we present an extended study of FVE to show that the expectations described above apply to our setup. To this end we computed the mode number and the chiral condensate for different volumes. We report on the results for $N_f = 2$ and $N_f = 2 + 1 + 1$ at fixed lattice spacing and fixed quark mass for four and three different volumes respectively.

Fig. 4.3 shows the mode number computed for five values of M at four different volumes for the case of $N_f = 2$ dynamical twisted mass fermions at maximal twist. There it can be seen that the finite volume corrections are almost negligible, as expected, for $L \geq 2$ fm. It is also interesting to observe that the deviations seem to increase for lower values of M, as it was predicted by Eq. (4.16).

In the same figure (Fig. 4.3) we also plotted the analytical prediction for the finite volume corrections given by Eq. (4.18). We can confirm that for values $L \geq 2$ fm the predicted corrections describe the lattice data, confirming that the corrections are $\mathcal{O}(1\%)$ for large volumes. However, for smaller volumes, Eq. (4.18) seems to underestimate the corrections by a factor of $\mathcal{O}(2)$.

The corresponding values of the chiral condensate are plotted in Fig. 4.5. The fact that the finite volume corrections depend on the value of M has a direct consequence in the slope from which we extract Σ_{eff}. Thus we observe a statistically significant different between the largest volumes. However, if we consider the other systematic uncertainty discussed above, we can conclude that within these large systematic errors all the results are compatible. Thus, in the following, we will neglect the small systematic error coming from FVE.

The analogous study for $N_f = 2 + 1 + 1$ is shown in Fig. 4.4 and Fig. 4.6 for the mode number and the chiral condensate respectively. Fig. 4.6 shows the chiral condensate where, in this case, we observe large FVE for $L \leq 2$ fm. Somewhat surprisingly, in the case of the mode number the finite volume corrections tend to go in the opposite direction than in the case of $N_f = 2$. Also, the difference in the FVE between the largest and the lowest value of M seems to be enhanced. This behavior could not be foreseen although it can be due to the addition of the strange and the charm quarks in the dynamical simulations. For this reason it would be very interesting to have a similar expression to Eq. (4.18) but extended to twisted mass QCD in order to compare both cases and see if this change of behavior is described by chiral perturbation theory.

In order to interpret Fig. 4.5 and Fig. 4.6 it is important to consider that the mode number is an extensive quantity. This implies that for larger volumes the relative error decreases, as it was already explained in the last section. The direct consequences of this peculiarity is that, for a comparable number of statistics, the error of the chiral condensate is smaller for larger volumes.

As a conclusion of the study presented above we perform [7], all the calculations on volumes $L \geq 2$ fm to ensure that our results are either not affected by FVE or that those are negligible.

[7] The only exception is the ensemble for $\beta = 4.2$ and $a\mu = 0.0065$ whose volume correspond to $L \approx 1.7$ fm. However the value of $m_\pi L > 4$ for this ensemble, which ought to be sufficiently large to suppress FVE.

4.5. Chiral extrapolation for $N_f = 2$ and $N_f = 2 + 1 + 1$

In this section we present the results of the chiral condensate for $N_f = 2$ and $N_f = 2{+}1{+}1$ dynamical twisted mass fermions at maximal twist for several quark masses a different values of β. This allow us to perform an extrapolation to the chiral limit for each β. The results extrapolated to the chiral limit will be used in the following section to perform the continuum limit and to obtain thus our final results for the chiral condensate.

We follow the procedure introduced in Sec. 4.3.1, in order to extract the chiral condensate. We compute the mode number for five, in the case of $N_f = 2$, or four, in the case of $N_f = 2 + 1 + 1$, values of M from around 50 MeV to 120 MeV. We extract the slope of the mode number through a linear fit, which we then insert in Eq. (4.12) in order to obtain the mass dependent effective condensate Σ_{eff}. We computed Σ_{eff} for several masses at three different lattice spacings in both cases. This allow us to perform the continuum limit of chirally extrapolated data as will be shown in the next section. For the moment we focus the discussion on the chiral behavior.

The chiral condensate is extrapolated to the chiral limit using the analytical description introduced in Sec. 4.1 where a NLO chiral perturbation theory formula was introduced, which describes the chiral behavior of Σ_{eff}. It was shown there that the NLO effects are negligible for low quark masses and therefore a linear extrapolation in the quark mass can be performed to extract Σ in the chiral limit.

In Fig. 4.7 and Fig. 4.8 all the results for $N_f = 2 + 1 + 1$ and $N_f = 2$ respectively are plotted. As we can see, the data, in both cases, show a linear behavior in the quark mass demonstrating that we are, in fact, not sensitive to higher order corrections of χPT.

The errors plotted in Fig. 4.7 and Fig. 4.8 are only statistical, since the relative errors which are introduced by Z_P and r_0 enter at the same level for all the values of the quark masses. However, in Tab. 4.5 and Tab. 4.4 we give all results including the corresponding systematic errors. We also incorporate in the tables the explicit results for the chiral extrapolation for each value of β. The systematic error, which is quoted for the chiral extrapolated values corresponds to the uncertainty in the fit range and was computed by performing a fit in three different fit intervals.

In order to present a reliable systematic error, given by the uncertainty in the linear regime, we perform three different calculations. We first avoid the lowest value of M in order to be sufficiently above the renormalized quark mass and therefore include possible deviations coming from this source. In a second estimation we ignore the largest value of M to consider deviations from the linear behavior at larger values of M. Our quoted value corresponds to the analysis where all the points are included. However, the differences in the chirally extrapolated results obtained through the three independent analysis are taken as the systematic error of the chiral extrapolation.

Ensemble	$a\mu$	$r_0\Sigma^{1/3}$
b30.32	0.003	0.7132 (30)(53)(38)
b40.32	0.004	0.7154 (19)(54)(38)
b64.24	0.0064	0.7243 (33)(54)(39)
b85.24	0.0085	0.7359 (25)(55)(39)
extrapolation	0	0.6981 (36)(52)(38)(162)
c30.32	0.003	0.7187 (50)(43)(30)
c60.32	0.006	0.7338 (40)(44)(30)
c80.32	0.008	0.7404 (26)(44)(31)
extrapolation	0	0.7062 (80)(42)(30)(174)
d20.48	0.002	0.7020 (42)(50)(60)
d65.32	0.0065	0.7429 (41)(53)(64)
extrapolation	0	0.6821 (68)(49)(60)(280)

Table 4.4.: Results of the chiral condensate $r_0\Sigma^{1/3}$ for all the $N_f = 2$ ensembles. The first error quoted corresponds to the statistical uncertainty, the second and third are resulting from r_0 and Z_P respectively. The result of the chiral extrapolation is also shown ($a\mu = 0$), where the last given error corresponds to the uncertainty resulting from the fit range. All the results correspond to $M_R \approx 90$ MeV.

Ensemble	$a\mu$	$r_0\Sigma^{1/3}$
A30.32	0.003	0.7916 (68)(58)(45)
A40.32	0.004	0.8000 (33)(58)(46)
A50.32	0.005	0.8118 (30)(59)(46)
A60.32	0.006	0.8130 (66)(59)(46)
A80.32	0.008	0.8246 (43)(60)(47)
extrapolation	0	0.7752 (71)(56)(44)(183)
B25.32	0.0025	0.7525 (54)(54)(25)
B35.32	0.0035	0.7550 (46)(54)(25)
B55.32	0.0055	0.7620 (34)(55)(25)
B75.32	0.0075	0.7734 (30)(56)(26)
extrapolation	0	0.7391(64)(53)(25)(128)
D15.48	0.0015	0.7281 (49)(56)(14)
D20.48	0.002	0.7410 (30)(57)(14)
D30.48	0.003	0.7400 (31)(57)(14)
extrapolation	0	0.7281 (82)(56)(14)(84)

Table 4.5.: Results of the chiral condensate $r_0\Sigma^{1/3}$ for all the $N_f = 2+1+1$ ensembles. The first error quoted corresponds to the statistical uncertainty, the second and third are resulting from r_0 and Z_P respectively. The result of the chiral extrapolation is also shown ($a\mu = 0$), where the last given error corresponds to the uncertainty resulting from the fit range. All the results correspond to $M_R \approx 80$ MeV.

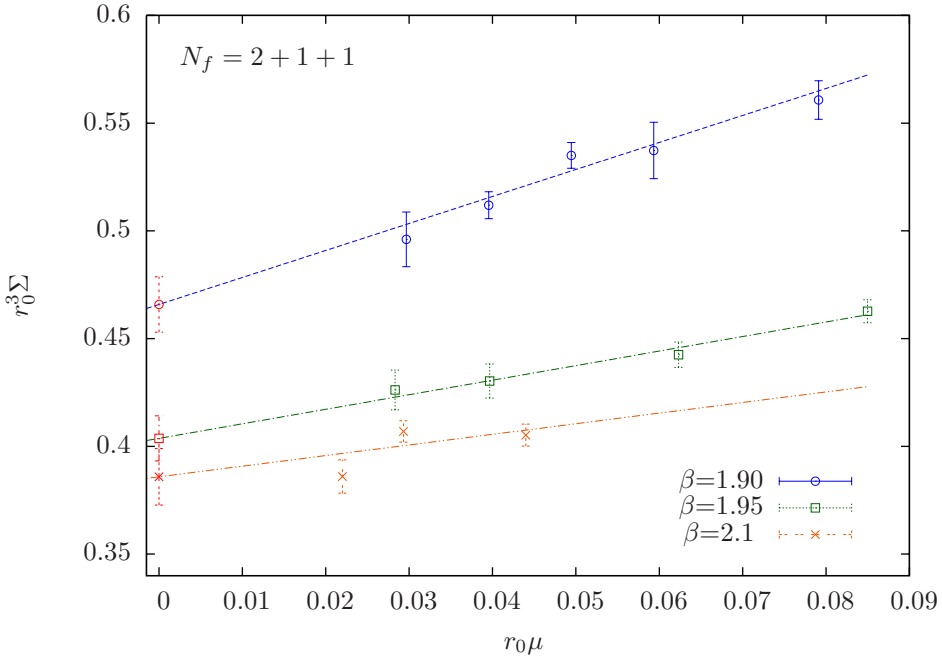

Figure 4.7.: Chiral extrapolation of the chiral condensate $r_0^3\Sigma$ for $N_f = 2+1+1$ dynamical fermions at $\beta = 2.1,\ 1.95$ and 1.90 respectively. The lines correspond to a chiral extrapolation linear in the quark mass. The red points are the extrapolated values at $\mu = 0$.

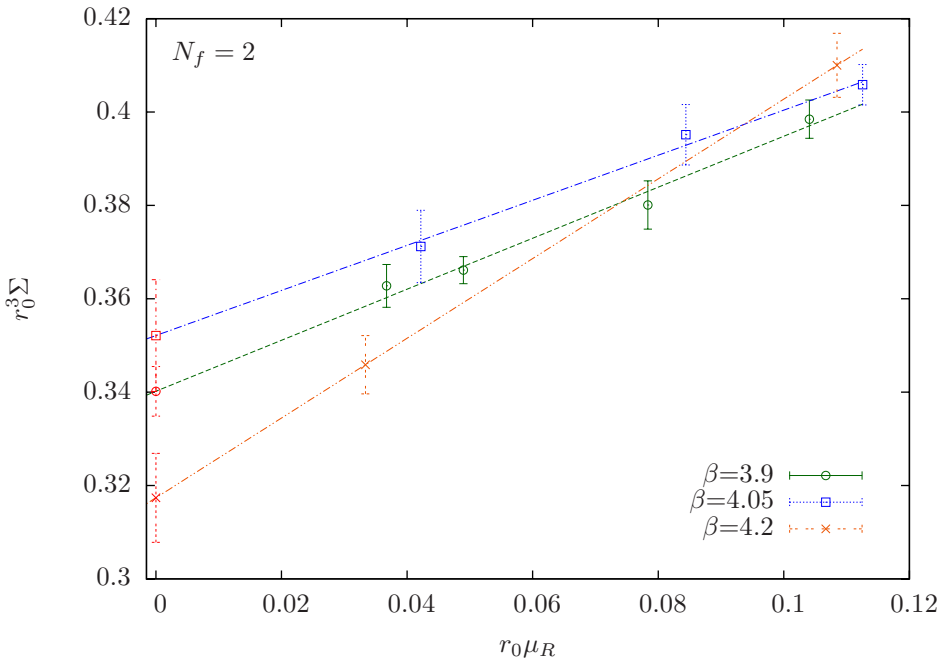

Figure 4.8.: Chiral extrapolation of the chiral condensate $r_0^3\Sigma$ for $N_f = 2$ dynamical fermions at $\beta = 3.9,\ 4.05$ and 4.2 respectively. The lines correspond to a chiral extrapolation linear in the quark mass. The red points are the extrapolated values at $\mu = 0$

4.6. Continumm limit for $N_f = 2$ and $N_f = 2 + 1 + 1$

One of the main goals of this thesis is to compute the continuum limit of the chiral condensate Σ for the values that have been previously extrapolated to the chiral limit, as discussed in the previous section. In this section we provide the continuum limit results for $N_f = 2$ and $N_f = 2 + 1 + 1$ and compare them with other calculations found in the literature.

The chiral condensate defined through the method of spectral projectors is an $O(a)$ improved quantity since it is $\mathcal{R}_5^1$ even, which guarantees the $\mathcal{O}(a^2)$ scaling to the continuum limit for twisted mass fermions at maximal twist. Moreover we showed in Sec. 4.2 that the short distance singularities do not spoil this remarkable feature, since the contact terms, which we explicitly computed, and which arise in the Symanzik expansion, are proportional to m_q and therefore vanish at maximal twist. We are thus led to perform a continuum limit linear extrapolation in a^2.

In Sec. 4.5 the chiral extrapolation of the chiral condensate was performed for 3 different values of the lattice spacing in the 2-flavor case and for $N_f = 2 + 1 + 1$. We now use that data to compute the continuum limit in both cases. In Fig. 4.10 the continuum extrapolation is shown for $N_f = 2$. For the case of $N_f = 2 + 1 + 1$ the results of the continuum limit are plotted in Fig. 4.9. Performing the linear extrapolation in $(a/r_0)^2$ we obtain as our final result for $N_f = 2$

$$r_0\Sigma^{1/3} = 0.685(16)(32) \tag{4.19}$$

which is perfectly compatible with the result for the case $N_f = 2 + 1 + 1$ given by

$$r_0\Sigma^{1/3} = 0.683(19)(18). \tag{4.20}$$

The first error quoted in Eq. (4.19) and Eq. (4.20) combines in quadrature the statistical error, the error coming from the estimation of Z_P and from r_0. The second error quoted corresponds to the uncertainty in the fit range in M to extract the linear slope of the mode number. In order to quantify the latter we performed three different continuum limit extrapolation, as we did for the chirally extrapolated result. Again, the first extrapolation contains all the data and gives the final result quoted above. The other two fits ignore the lowest and the largest value of M respectively to account for possible deviations of the linearity. The difference between all the fit results give us the estimation of the systematic error of varying the fit interval in M. To illustrate this procedure we show all the results in Tab. 4.6. We can see that the $N_f = 2 + 1 + 1$ data is less sensitive to the variations in the fit interval than the $N_f = 2$ data. This is partly due to the fact that for $N_f = 2 + 1 + 1$ more masses are available at each β than for $N_f = 2$. In addition, the slopes for the case of $N_f = 2 + 1 + 1$ flavors are smaller. Both effects reduce the response of a change in the interval fit. Another possible factor is that the central values of M_R in the fit are lower and therefore we have less deviations from the linearity which appears at large values of M, hence the discrepancy between the results is reduced, decreasing the corresponding systematic effect.

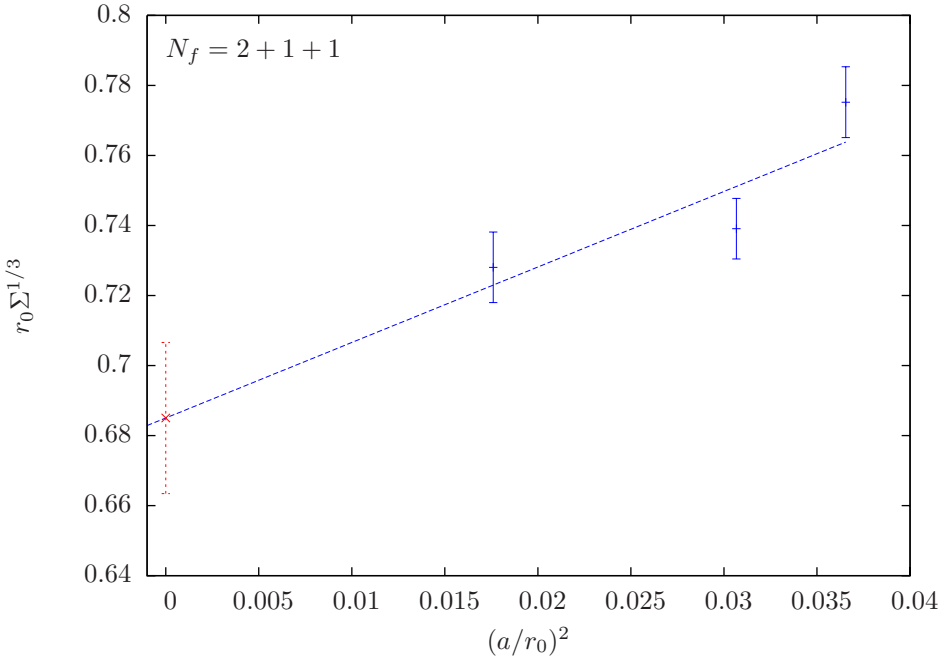

Figure 4.9.: Continuum limit extrapolation of the chiral condensate $r_0\Sigma^{1/3}$ linear in a^2 for $N_f = 2 + 1 + 1$ dynamical fermions. The red point corresponds to the extrapolated value in the continuum limit.

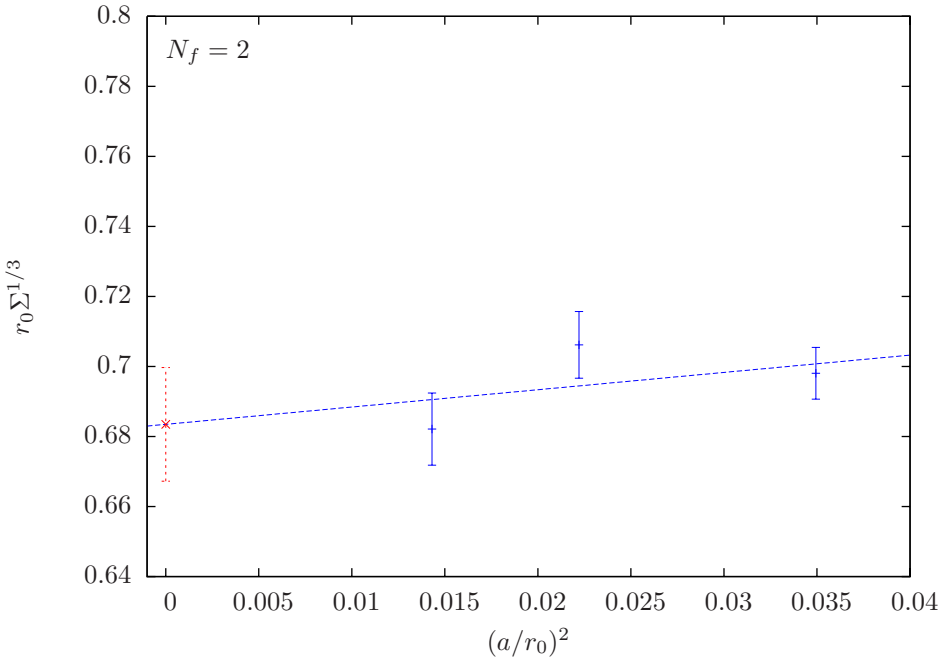

Figure 4.10.: Continuum limit extrapolation of the chiral condensate $r_0\Sigma^{1/3}$ linear in a^2 for $N_f = 2$ dynamical fermions. The red point corresponds to the extrapolated value in the continuum limit.

M_R [MeV]	$r_0\Sigma^{1/3}$	N_f
~ 80	0.6726	2
$\sim$ *90*	*0.6835*	2
~ 100	0.7155	2
~ 70	0.6757	2+1+1
$\sim$ *80*	*0.6850*	2+1+1
~ 90	0.6812	2+1+1

Table 4.6.: Results of the continuum limit of $r_0\Sigma^{1/3}$ for different fit intervals. The analysis which led to the highlighted values considers all the data, whereas the values for lower or larger values of M_R correspond to the data where the largest or the lowest values of M respectively have been ignored.

4.6.1. Comparison with other results

In this thesis we have computed the chiral condensate through the Banks-Casher relation using the method of spectral projectors. However, there are other techniques to computate Σ. One method is to use chiral perturbation theory where Σ appears as a low energy constant in the quark mass dependence of light pseudoscalar mesons. It can also be computed through the topological susceptibility or calculating directly the quark propagator. For a summary of recent results we refer to Ref. [87].

In this section we compare our results with such other calculations that can be found in the literature. However, we make a selection by considering only large volume calculations with continuum limit results. We gather all the different results in Tab. 4.7 and in Fig. 4.11 for a more visual comparison. We see a very good agreement among all the values for the dimensionless quantity $r_0\Sigma$.

All the values that have been given in this chapter correspond to the dimensionless product $r_0\Sigma^{1/3}$. The reason is the uncertainty which currently exist in the determination of the lattice spacing a which is used to convert lattice results to MeV in order to compare with phenomenology or experiments.

To illustrate the uncertainty stemming from the scale setting, we refer to example of the lattice spacing as being computed within the ETM collaboration for 2 flavors. For example for the ensemble $\beta = 3.9$ there are 3 different estimations which use 3 different techniques. Using the nucleon mass a=0.089 fm [86], through chiral fits a=0.079 fm [40] and more recently a=0.085 fm [85], which would correspond to $\Sigma^{1/3}$ [MeV] = 288.8(1.4), 303.2(1.5), and 327.9(1.6) respectively for the chiral extrapolation at $\beta = 3.9$, where only statistical errors are quoted.

In order to take into account this uncertainty we need to include the spread of the results in the error. This will give an additional error to our result which is almost an order of magnitude higher than the errors quoted above. Since the computation of the scale is not part of our work but it is computed using different observables, we cannot control ourselves the error coming from setting the scale. We decided therefore to give all the results avoiding this discussion by constructing a dimensionless product.

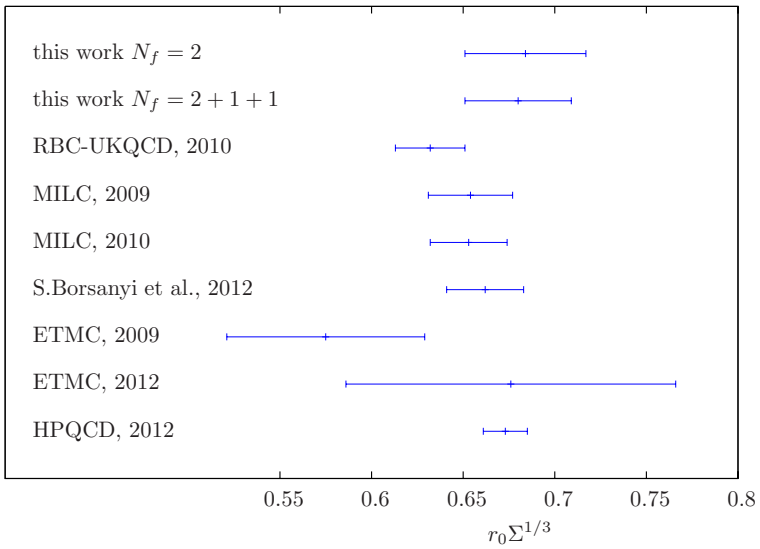

Figure 4.11.: Comparison of the dimensionless product $r_0\Sigma^{1/3}$ found in the literature. All the data plotted correspond to the values which can be found in Tab. 4.7. The errors have been summed in quadrature.

method	N_f	fermion	$r_0\Sigma^{1/3}$	$\Sigma^{1/3}$ [MeV]	r_0 [fm]
spect. proj.	2	tm	0.684 (16)(32)	281 (7)(13)	0.48 [86]
spect. proj.	2+1+1	tm	0.683(19)(18)	280 (8)(7)	0.48 [86]
chiral fits	2+1	dw	0.632 (15)(12)	256 (6) [88]	0.487(9) [88]
chiral fits	2+1	st	0.654 (15)(12)	278 (6) [89]	from r_1 [1]
chiral fits	2+1	st	0.653 (18)(11)	281.5(7.9) [90]	from r_1 [2]
chiral fits	2+1	st	0.662 (5)(20)	272.3(1.2) [91]	0.48(1)(1)[92]
chiral fits	2	tm	0.575 (14)(52)	269.9(6.5) [40]	0.420(38) [3]
quark prop.	2	tm	0.676 (89)(14)	299(26)(29) [93]	0.446(9) [93]
quark prop.	2+1+1	st	0.673 (5)(11)	283(2) [94]	from r_1 [4]

Table 4.7.: Comparison of our result of the chiral condensate with continuum limit results found in the literature. To fit the table we have used the following abbreviations: tm stays for twisted mass, dw for domain wall and st for staggered. The original results are given in MeV, in order to compute $r_0\Sigma$ we have combined the values of r_0, also given in the table, with the values in MeV. The first error correspond to the error given for Σ and the second corresponds to the uncertainty of r_0. When several errors are given we sum them in quadrature.

[1] $r_1 = 0.318(7)$ fm [89] and $r_0/r_1 = 1.46(1)(2)$ [95].
[2] $r_1 = 0.3133(23)$ fm [90] and $r_0/r_1 = 1.46(1)(2)$ [95].
[3] It was originally used $r_0 = 0.420(14)$ fm, however, recent estimations give a higher value of $r_0 \approx 0.45$ fm. We take the spread of values into account in the quoted error.
[4] $r_1 = 0.3209(26)$ fm [96] and $r_0/r_1 = 1.46(1)(2)$ [95]

The issue of setting the scale is actually a more general problem affecting all groups working on lattice QCD world-wide. This can be seen, for instance, in the comparison of the chiral condensate showed in Tab. 4.7. If we consider $r_0\Sigma^{1/3}$ we observe a good agreement within different groups. On the other hand if we compare the results of the chiral condensate in MeV we observe a big spread and different groups give values that are no longer compatible. This inconsistency comes mainly from the scale setting issue mentioned above and before this problem is not solved, it is preferable to compare the dimensionless quantities such as the product $r_0\Sigma^{1/3}$.

CHAPTER 5

Computation of the ratio of renormalization constants Z_P/Z_S

Contents

The lack of chiral symmetry on the lattice at non-vanishing lattice spacing has important consequences for the renormalization of composite operators such as the pseudoscalar and the scalar densities. If a formulation is used where chiral symmetry (even only in its lattice modified form) is respected, such as the overlap formulation, then both densities renormalize in the same way with $Z_P = Z_S$, since they belong to the same chiral multiplet. On the other hand if the lattice formulation breaks chiral symmetry, such as the Wilson or the twisted mass formulation, then this equality is not fulfilled any longer and $Z_P/Z_S \neq 1$. Nevertheless, in the continuum limit, where chiral symmetry is restored, the renormalization constants Z_P and Z_S again coincide. Additionally it can be proven using Ward identities [1] that this ratio of renormalization constants is scale and scheme independent and has a well defined continuum limit.

One of the main targets of this work is to compute the topological susceptibility χ_{top} using spectral projectors, as will be explained in the following chapter. Since the formulation that we apply, tmQCD, breaks chiral symmetry, this observable needs to be renormalized by the ratio Z_P/Z_S as it will be explained in detail in the next chapter. For this reason the calculation of Z_P/Z_S is a necessary intermediate step in order to achieve our goal. Additionally we are interested in the calculation of the topological susceptibility in the quenched approximation, χ_∞, for which we explicitly generated quenched ensembles. For this setup, the renormalization constants are not known and hence need to be computed explicitly.

There are several strategies that one can follow to compute Z_P/Z_S, applying different renormalization schemes such as the commonly used RI-MOM scheme. However, spectral projectors offers a new approach to compute this ratio of renormalization constants in an efficient way as proposed in Ref. [59].

In this chapter we report on the results of the computation of Z_P/Z_S using spectral projectors. In Sec. 5.1 we introduce the method and comment on the subtleties of its application. In Sec. 5.4 a test for $N_f = 2$ in small volume is performed, where the outcome is compared with RI-MOM and X-space results of the same ratio to demonstrate that both methods agree. In Sec. 5.5 we compute Z_P/Z_S for the quenched ensembles that were explicitly generated for the computation of χ_∞.

5.1. Z_P/Z_S using spectral projectors

In previous chapters we studied the renormalization properties of the spectral sums through the density chains, whose properties are well known. In the following, we will describe, how the ratio of renormalization constants Z_P/Z_S can be computed by using spectral projectors.

Let us start by recalling the form of the spectral sums σ_k that were introduced in Chap. 2

$$\sigma_k(\mu, m) = \left\langle \mathrm{Tr}\{(D_m^\dagger D_m + \mu^2)^{-k}\} \right\rangle, \tag{5.1}$$

[1] We refer to any general text, e.g.[72]

which, as shown in App. E.3, can be represented by

$$\sigma_k(\mu, m) = -a^{4(2k)-4} \sum_{x_1,\ldots,x_{n-1}} \left\langle P^+_{12}(x_1) P^-_{23}(x_2) \ldots P^-_{(2k)1}(0) \right\rangle . \tag{5.2}$$

In the same way we can define the spectral sums $\sigma_{r,s}$

$$\sigma_{r,s}(\mu, m) = \left\langle \mathrm{Tr}\{\gamma_5 (D_m^\dagger D_m + \mu^2)^{-r} \gamma_5 (D_m^\dagger D_m + \mu^2)^{-s}\} \right\rangle , \tag{5.3}$$

which for a given example, e.g. $r = 2,\ s = 1$ can be represented by

$$\sigma_{r,s}(\mu, m) = -a^{24-4} \sum_{x_1,\ldots,x_6} \left\langle S^+_{12}(x_1) P^+_{23}(x_2) P^-_{34}(x_3) P^+_{45}(x_4) S^+_{56}(x_5) P^-_{61}(x_6) \right\rangle . \tag{5.4}$$

In general the renormalization properties of the spectral sums are well known, since they consist on a chain of pseudoscalar and/or scalar operators, which renormalize with familiar factors, Z_P and Z_S respectively. Thus the renormalized spectral sums take the following form

$$\sigma_{k,R}(\mu_R, m_R) = Z_P^{2k} \sigma_k(\mu, m), \tag{5.5}$$

$$\sigma_{r,s,R}(\mu_R, m_R) = Z_P^2 Z_S^{(2(r+s)-2)} \sigma_k(\mu, m). \tag{5.6}$$

In the continuum limit chiral symmetry is restored and therefore the Dirac operator anticommutes with γ_5. This implies that Eq. (5.1) and Eq. (5.3) coincide since $\gamma_5 (D^\dagger D)^{-1} \gamma_5 = (D^\dagger D)^{-1}$.

In particular, if we choose the case where $k = r + s$, then the renormalized spectral sums $\sigma_{r+s,R}$ and $\sigma_{r,s,R}$ give the same result in the continuum limit [59]. We can use this property to extract the ratio of renormalization constants Z_P/Z_S in the following way. We start with the relation

$$\sigma_{r,s,R} = \sigma_{r+s,R} \rightarrow \tag{5.7}$$

$$Z_P^{2(r+s)-2} Z_S^2 \sigma_{r,s} = Z_P^{2(r+s)} \sigma_{r+s,R}, \tag{5.8}$$

which directly implies

$$\frac{Z_P^2}{Z_S^2} = \frac{\sigma_{r,s,R}}{\sigma_{r+s}}. \tag{5.9}$$

Eq. (5.9) can be generalized for any rational function of $D^\dagger D$ which decays rapidly enough. The definition includes the spectral projectors which were already introduced in Chap. 3. Thus, as proposed in Ref. [59], we can substitute the spectral sums in Eq. (5.9) by

$$\frac{Z_P^2}{Z_S^2} = \frac{\langle \mathrm{Tr}\{\gamma_5 \mathbb{P}_M \gamma_5 \mathbb{P}_M\} \rangle}{\langle \mathrm{Tr}\{\mathbb{P}_M\} \rangle}. \tag{5.10}$$

In practice we compute the following spectral observables

$$\mathcal{A} = \frac{1}{N}\sum_{k=1}^{N}(\mathbb{R}_M^2\eta_k, \mathbb{R}_M^2\eta_k), \tag{5.11}$$

$$\mathcal{B} = \frac{1}{N}\sum_{k=1}^{N}(\mathbb{R}_M\gamma_5\mathbb{R}_M\eta_k, \mathbb{R}_M\gamma_5\mathbb{R}_M\eta_k), \tag{5.12}$$

where $\mathbb{R}_M$ is the rational approximation of $\mathbb{P}_M$ and N is the number of stochastic sources η_k that has been introduced for each configuration. The connection between Eq. (5.10) and the stochastic observables $\mathcal{A}$ and $\mathcal{B}$ can be easily be made in the following way.

We start with the observable $\mathcal{A}$:

$$\mathcal{A} = \frac{1}{N}\sum_{k=1}^{N}(\mathbb{R}_M^2\eta_k, \mathbb{R}_M^2\eta_k) = \frac{1}{N}\sum_{k=1}^{N}(\mathbb{R}_M^*)^{ab}(\mathbb{R}_M^*)^{bc}(\eta_k^*)^c\mathbb{R}_M^{ad}\mathbb{R}_M^{de}\eta_k^e. \tag{5.13}$$

Applying that $\mathbb{R}_M$ is hermitian and therefore $(\mathbb{R}_M^*)^{ab} = \mathbb{R}_M^{ba}$ and permuting the first two elements

$$\mathcal{A} = \frac{1}{N}\sum_{k=1}^{N}\mathbb{R}_M^{cb}\mathbb{R}_M^{ba}\mathbb{R}_M^{ad}\mathbb{R}_M^{de}(\eta_k^*)^c\eta_k^e. \tag{5.14}$$

Now we contract the stochastic sources obtaining the following expression

$$\mathcal{A} = \frac{1}{N}\sum_{k=1}^{N}\mathbb{R}_M^{ba}\mathbb{R}_M^{cb}\mathbb{R}_M^{ad}\mathbb{R}_M^{de}\delta_{ce}\delta_{kk} = \frac{1}{N}\sum_{k=1}^{N}\mathbb{R}_M^{cb}\mathbb{R}_M^{ba}\mathbb{R}_M^{ad}\mathbb{R}_M^{dc}\delta_{kk}, \tag{5.15}$$

and since $\sum_{k=1}^{N}\delta_{kk} = N$ we can write

$$\mathcal{A} = \mathbb{R}_M^{ba}\mathbb{R}_M^{cb}\mathbb{R}_M^{ad}\mathbb{R}_M^{de} = \mathrm{Tr}\{\mathbb{R}_M^4\}. \tag{5.16}$$

We can then conclude $\langle A\rangle = \langle \mathrm{Tr}\{\mathbb{R}_M^4\}\rangle$ which is equivalent to $\langle \mathrm{Tr}\{\mathbb{P}_M\}\rangle$. To compute the trace of the fourth power of the projector, instead of just $\mathbb{R}_M$, simply increases the precision of the calculation. Notice that $\langle\mathcal{A}\rangle$ corresponds to the mode number computed in the last chapter to extract the chiral condensate.

Equally for $\mathcal{B}$ we have

$$\mathcal{B} = \frac{1}{N}\sum_{k=1}^{N}(\mathbb{R}_M\gamma_5\mathbb{R}_M\eta_k, \mathbb{R}_M\gamma_5\mathbb{R}_M\eta_k) = \frac{1}{N}\sum_{k=1}^{N}(\mathbb{R}_M^*)^{ab}(\gamma_5^*)^{bc}(\mathbb{R}_M^*)^{cd}(\eta_k^*)^d\mathbb{R}_M^{ae}\gamma_5^{ef}\mathbb{R}_M^{fg}\eta_k^g, \tag{5.17}$$

and following the same steps as above we obtain

$$\mathcal{B} = \frac{1}{N}\sum_{k=1}^{N}\mathbb{R}_M^{ba}\gamma_5^{bc}\mathbb{R}_M^{dc}\mathbb{R}_M^{ae}\gamma_5^{ef}\mathbb{R}_M^{fg}(\eta_k^*)^d\eta_k^g \tag{5.18}$$

$$= \frac{1}{N}\sum_{k=1}^{N} \gamma_5^{cb}\mathbb{R}_M^{ba}\mathbb{R}_M^{ae}\gamma_5^{ef}\mathbb{R}_M^{fg}\mathbb{R}_M^{dc}\delta_{fg}\delta_{kk} \tag{5.19}$$

$$= \gamma_5^{cb}\mathbb{R}_M^{ba}\mathbb{R}_M^{ae}\gamma_5^{ef}\mathbb{R}_M^{fd}\mathbb{R}_M^{dc} = \mathrm{Tr}\{\gamma_5\mathbb{R}_M^2\gamma_5\mathbb{R}_M^2\}. \tag{5.20}$$

Therefore $\langle B\rangle = \left\langle \mathrm{Tr}\{\gamma_5\mathbb{R}_M^2\gamma_5\mathbb{R}_M^2\}\right\rangle$ which is equivalent to $\langle \mathrm{Tr}\{\gamma_5\mathbb{P}_M\gamma_5\mathbb{P}_M\}\rangle$.
Our final expression for the ratio of renormalization constants Z_P/Z_S is then given by

$$\frac{Z_P^2}{Z_S^2} = \frac{\left\langle \mathrm{Tr}\{\gamma_5\mathbb{R}_M^2\gamma_5\mathbb{R}_M^2\}\right\rangle}{\left\langle \mathrm{Tr}\{\mathbb{R}_M^4\}\right\rangle} = \frac{\langle A\rangle}{\langle B\rangle}. \tag{5.21}$$

5.2. Details of the implementation

In principle the implementation of the spectral projectors to compute Z_P/Z_S is completely analogous to the calculation of the mode number. However there are a few subtleties that have to be taken into consideration before starting the computation.

First of all, since we are evaluating stochastically the observables, we need to find the appropriate number of random sources that we need to insert. Fig. 5.1 shows the values of $\mathcal{A}$ and $\mathcal{B}$ for different number of stochastic sources. The errors plotted correspond to statistical errors computed taking into account autocorrelations following the method described in Ref. [80]. A discussion about the autocorrelations that are observed for these observables can be found in App. F, together with all the numerical results that will be discussed in this chapter.

The data suggest that the number of stochastic sources does not influence the central value of the result, since all the values are compatible among each other. However the error does decrease when the number of sources is increased, as expected. In particular adding two sources seems to be worthwhile since the error decreases. Additional sources do not seem to compensate the cost of the calculation because the error only decreases

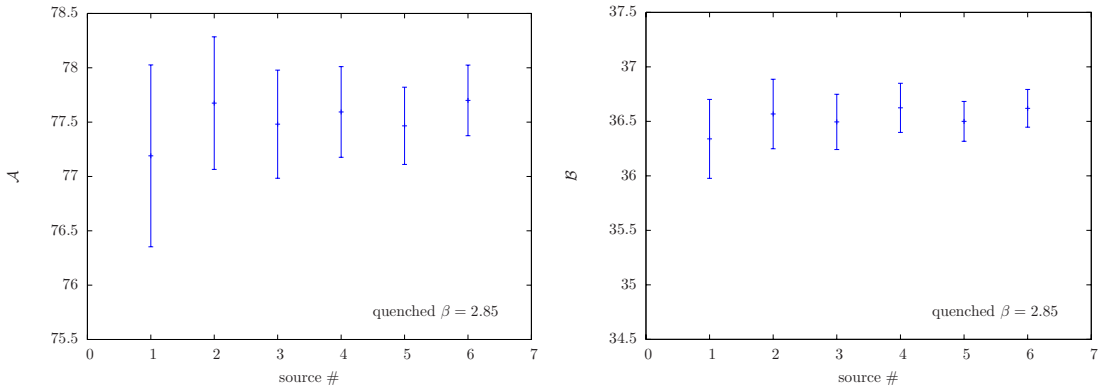

Figure 5.1.: Stochastic observables $\mathcal{A}$ and $\mathcal{B}$, used to compute Z_P/Z_S, for different number of stochastic sources.

slightly. Nevertheless we only used one stochastic source for this calculation since the systematic error, as will be explained below, is the largest uncertainty present in the calculation.

The next parameter to be tuned before starting the calculation is the threshold parameter M. In principle Z_P/Z_S should be scale independent, and therefore we should obtain the same results for different values of M. However we are affected by the non-perturbative effects that come from the low energy regime and by lattice artifacts which complicate the picture. Previously, to compute the mode number, we set M to be in a range between 50 and 110 MeV, i.e. close to the infrared cut-off, since we were interested in the low energy part of the spectrum. In this case we need to avoid that region since we observe very large non-perturbative effects as will be discussed below in more detail. The window where we expect to observe a plateau to extract Z_P/Z_S is given by $\Lambda_{QCD} > M > a^{-1}$, where Λ_{QCD} is the typical QCD scale around few hundreds MeV and a^{-1} is the inverse of the lattice spacing which acts as a ultraviolet cut-off.

As an example of the observe deviations one can take for instance Fig. 5.2, although it will appear in all the calculations presented in this chapter.

The deviation from the plateau behavior is mostly due to lattice artifacts. Thus we expect that for the finest lattice spacings we would observe a plateau in the mentioned region.

5.3. Finite volume effects for $N_f = 2$

In the previous chapter we dedicated a full section to discuss about the finite volume effects (FVE) that affect the calculation of the mode number. There we concluded that FVE are exponentially suppressed and directly depend on the value of M. Even in that case where the chosen window contained values below 150 MeV, the FVE were of the order of 1% for lattices where $L \geq 2$ fm.

In the present case the values of M_R where we perform the calculations are much larger, of around $\mathcal{O}(1 - 2GeV)$, and therefore we expect the finite volume effects to be even more suppressed.

In Fig. 5.2 a comparison of Z_P/Z_S for different volumes is shown. This plot confirms that the finite volumes effects depend on the values of M_R as expected. One can see that for values of $M_R > 1.5$ GeV all the points fall on top of each other, even for the smallest volume which corresponds to $L = 0.7$ fm. For $L > 1.3$ fm, even values below 500 MeV seem to perfectly agree showing that FVE are completely negligible for Z_P/Z_S.

The data in Fig. 5.2 shows that the value of Z_P/Z_S computed using the RI-MOM scheme [83] is reached for values around $M_R = 1.5$ GeV. However we still do not observe a clear plateau at this coarse lattice spacing. This is due to discretization effects, therefore we expect that a plateau behavior will be recovered when we approach the continuum limit. This issue will be addressed in more detail in the next section, where Z_P/Z_S will be computed for four different lattice spacings. There it will be shown that when we decrease the lattice spacing a a better plateau behavior is observed.

In conclusion we observe that values of Z_P/Z_S obtained for $M_R < 1$ GeV are af-

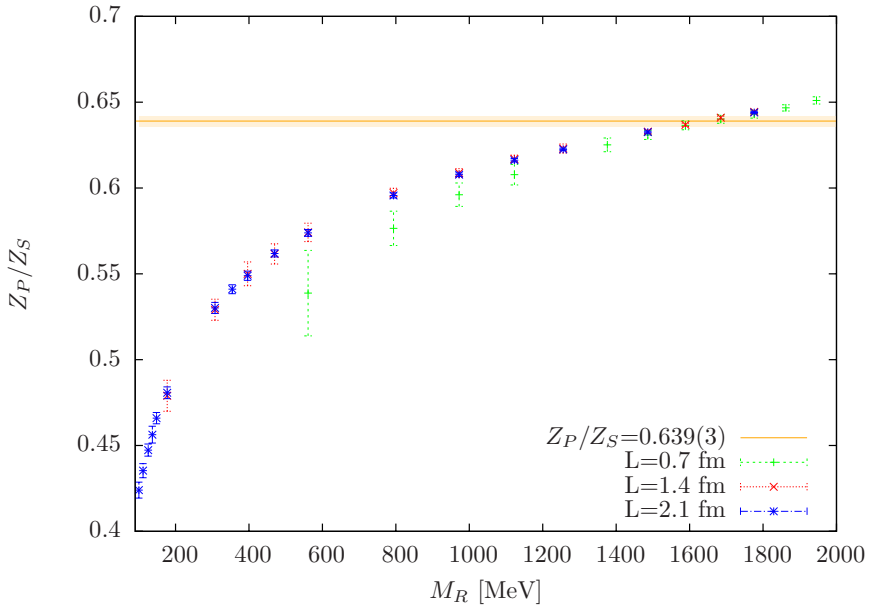

Figure 5.2.: Comparison of the ration Z_P/Z_S as a function of M_R for 3 different volumes. All the points correspond to $N_f = 2$ at $\beta = 3.9$ and $a\mu = 0.004$. The straight lines give the value of Z_P/Z_S for $\beta = 3.9$ computed in the RI-MOM scheme [83] and its corresponding error.

fected by large non perturbative effects. In addition a strong deviation from a constant plateau behavior is encountered. Consequently the error of the calculation of Z_P/Z_S from the spectral projectors method will be dominated by systematic effects, such as the discretization effects.

5.4. Results and comparison for $N_f = 2$

In this section we report on the results for the ratio of renormalization constants Z_P/Z_S for $N_f = 2$ twisted mass fermions at maximal twist. We computed Z_P/Z_S for four different lattice spacings at fixed volume and quark mass. We compare our results with the ones obtained through two different methods, the RI-MOM scheme [83] and the X-space scheme [97] in order to confirm that spectral projectors offers an affordable new procedure to compute Z_P/Z_S. However, the large systematic effects that are involved in the calculation, especially for coarse lattice spacings, prevent us from presenting this method as a realistic alternative to other established methods like RI-MOM.

Fig. 5.3 shows the results for $N_f = 2$ at four different lattice spacings for a fixed volume around $L \approx 1.4$ fm. It has been shown, in the previous section, that the finite volume effects at the range of M_R where $\mathcal{A}$ and $\mathcal{B}$ were evaluated are negligible even for this small volume. Therefore conclusions obtained here can be applied to infinite volume.

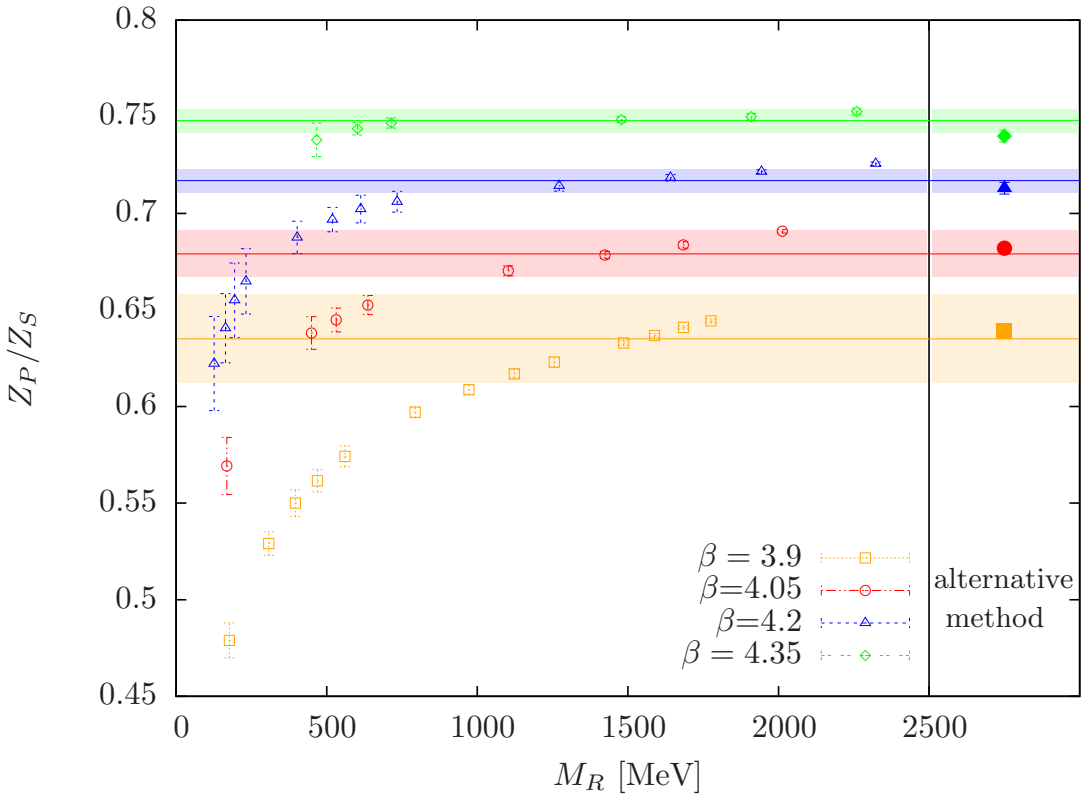

Figure 5.3.: Results of Z_P/Z_S as a function of M_R using spectral projectors. The straight lines correspond to the value at $M_R = 1500$ MeV and the shaded band to the spread of the results in the range $M_R = [1000 - 2000]$ MeV. The values to the right of the vertical line correspond to the RI-MOM computation for $\beta = 3.9,\ 4.05,\ 4.2$ [83] and X-space calculation for $\beta = 4.35$ [97].

As expected, the data show that approaching the continuum limit the dependence of Z_P/Z_S with respect to M_R becomes flatter and more plateau like given that always M_R is large enough.

In order to extract our final result for Z_P/Z_S we choose a central value of M_R around $M_R \approx 1.5$ GeV. This is far enough from the low energy regime where we observe a strong curvature in Z_P/Z_S and also sufficiently away from the ultraviolet regime where also large cut-off effects are expected. In order to take the discretization effects that are observed into account, we choose a range $M_R \in [1\text{ GeV}, 2\text{ GeV}]$ and account for the spread of the values of Z_P/Z_S as the systematic error. Following this strategy we obtain the results illustrated in Tab. 5.1.

In the same table, Tab. 5.1, the corresponding values of Z_P/Z_S obtained using RI-MOM or X-space calculations are shown. An overall agreement among all methods can be observed, showing that spectral projectors is an affordable and correct method to compute the ratio of renormalization constants Z_P/Z_S, although it is affected by rather

β	Z_P/Z_S spectral proj.	Z_P/Z_S RI-MOM/X-space
3.9	0.635(1)(23)	0.639(3)
4.05	0.679(2)(12)	0.682(2)
4.2	0.717(2)(5)	0.713(3)
4.35	0.749(2)(2)	0.740(3)

Table 5.1.: Comparison between results of Z_P/Z_S using spectral projectors and results obtained from RI-MOM [83] and X-space [97] calculations. The errors quoted with the results from spectral projectors correspond to, first, statistical and , second, systematic (coming from the dependence on M_R).

large systematic uncertainties for coarse values of the lattice spacing. Note also that the RI-MOM scheme values have been extrapolated to the chiral limit, whereas the X-space and the spectral projectors results have not. However the finite quark mass effects were found to be small in both schemes, RI-MOM and X-space [82, 83, 97]. Although the above discussion showed that the spectral projectors method is less precise as the RI-MOM or X-space methods, it will be very useful when we discuss below the quenched calculations, since for that setup no results from the RI-MOM or X-space schemes are available.

Finally, it is important to mention that the computational cost of the spectral projectors method decreases with increasing values of M_R. This is due to the fact that Eq. (3.35) is, for larger values of M_R, better conditioned. As a consequence, the solution of Eq. (3.35) needs less computational effort and therefore the calculation becomes very efficient.

5.5. Results of Z_P/Z_S for quenched ensembles

One of the main goals of this thesis is to compute the topological susceptibility in the pure gluon theory χ_∞ in order to attempt a first test of the Witten-Veneziano formula, which relates the mass of the η' meson with χ_∞. To this end we generated four ensembles at four different lattice spacings and at fixed physical volume and quark mass, so that we can perform a continuum limit extrapolation. In App. D.2 one can find the details of the generation of the quenched ensembles and the tuning of the parameters involved.

As it was discussed at the beginning of the present chapter, in order to compute $\chi_{\rm top}$ with spectral projectors using twisted mass fermions, one needs to renormalize with Z_P/Z_S. In this section we perform the calculation of this ratio of renormalization constants for the quenched ensembles that we generated with the purpose of computing χ_∞.

Fig. 5.4 shows the results of Z_P/Z_S for the quenched ensembles at $\beta = 2.37,\ 2.48,\ 2.67$ and 2.85. On can clearly see how for the lowest value of the lattice spacing which corresponds to $\beta = 2.85$ and at large enough M, the ratio Z_P/Z_S is independent of the scale M, as expected since Z_P/Z_S is a scale and scheme independent quantity. This

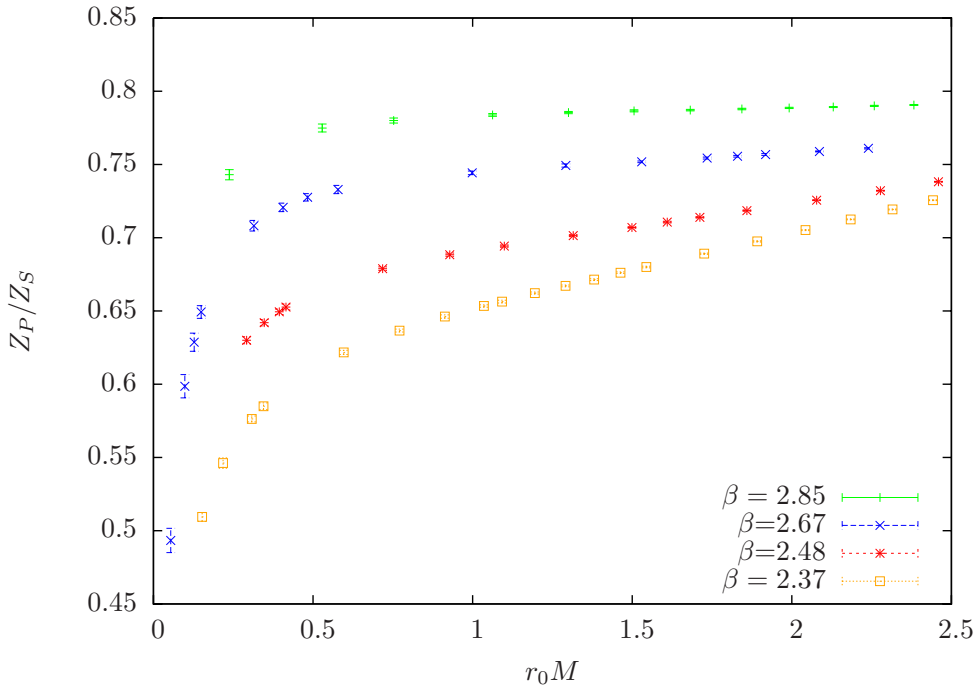

Figure 5.4.: Results of Z_P/Z_S as a function of r_0M for four different β values of quenched ensembles.

clearly indicate that indeed the cut-off effects are responsible for the strong curvature at small values of M_R and thus the deviation from the scale independent behavior. The figures suggests that this deviation is suppressed for lattice spacings below $a < 0.07$ fm.

In Tab. 5.2 the results obtained for Z_P/Z_S are displayed, together with the parameters of the quenched ensembles. The central error quoted corresponds to the value of Z_P/Z_S computed at $r_0M \approx 2$. The first error is the statistical error given by the spectral projectors method where autocorrelations were taken into account. The second error corresponds to the systematic error introduced in our calculation through the residual dependence of Z_P/Z_S on M. In order to give a reliable estimation we consider the spread

β	$L^3 \times T$	r_0/a	a [fm]	Z_P/Z_S
2.37	$20^3 \times 40$	3.60	0.139	0.680(1)(27)
2.48	$24^3 \times 48$	4.23	0.118	0.707(1)(19)
2.67	$32^3 \times 64$	5.71	0.088	0.752(1)(7)
2.85	$40^3 \times 80$	7.28	0.069	0.787(1)(3)

Table 5.2.: Results of Z_P/Z_S using spectral projectors for the quenched ensembles. The errors quoted correspond to, first, statistical and , second, systematic (coming from the dependency on M_R).

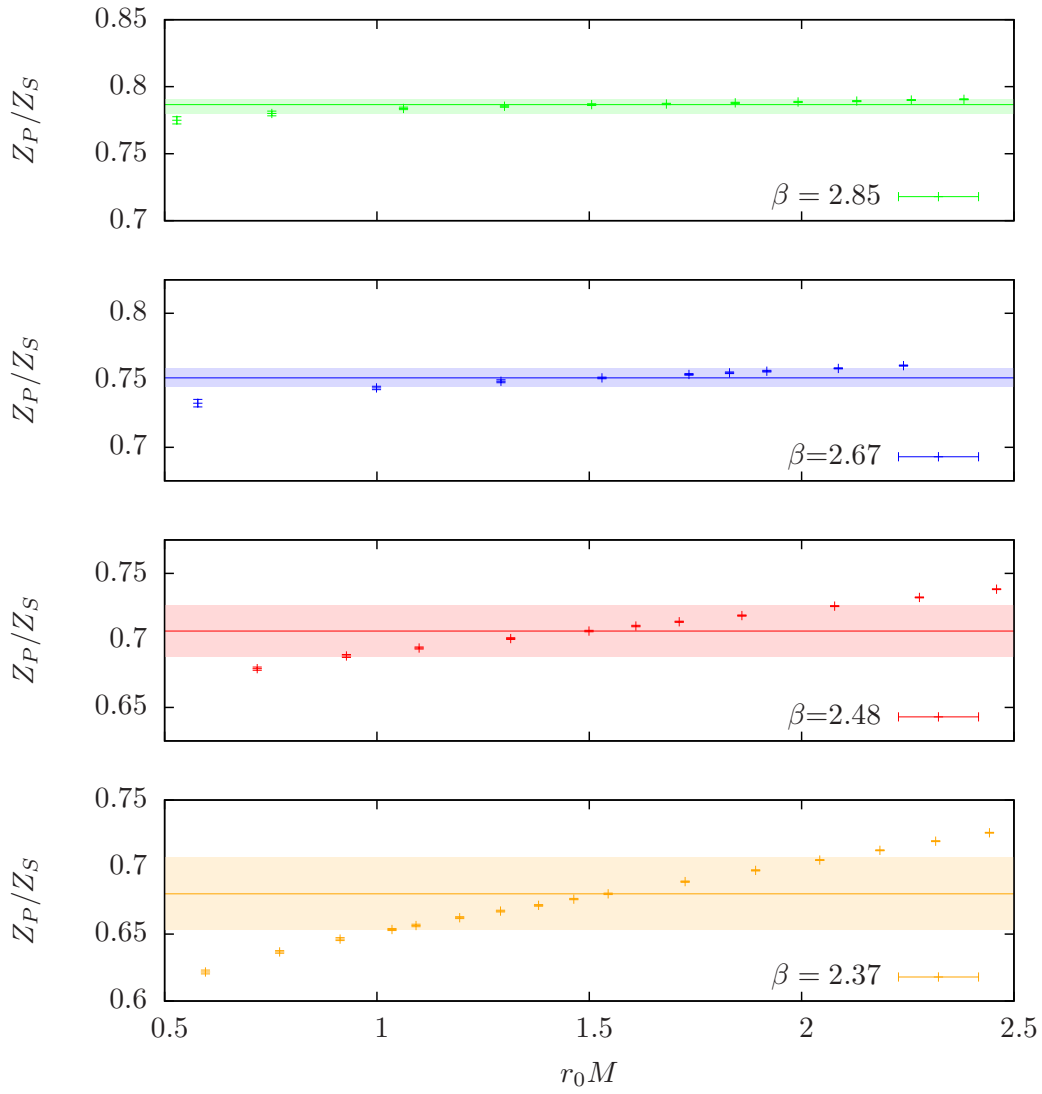

Figure 5.5.: Results of Z_P/Z_S as a function of $r_0 M$ for quenched ensembles. The straight lines correspond the final result and the shaded areas to the systematic error..

of the results given in the range $r_0 M = [1.5, 2.5]$. In Fig. 5.5 we present the results individually for each β with the corresponding systematic error given by the shaded area computed following the strategy explained above.

CHAPTER 6

Computation of the Topological Susceptibility in the dynamical case

Contents

The present chapter is devoted to the computation of the topological susceptibility χ_{top} in the case when the quarks appear as dynamical degrees of freedom. In this particular scenario, chiral perturbation theory predicts a suppression of the topological character when the chiral limit is approached. Moreover it relates the slope of the linear quark mass dependence of the topological susceptibility with the chiral condensate in the chiral limit. Consequently the study of the quark mass dependence of χ_{top} is of high importance, but, as we will see, it also represents a challenge for lattice QCD calculations.

The use of (sufficiently many) density chains leads to a well defined expression of χ_{top} which is free of divergences and hence a correct continuum limit can be carried through. This definition can also be applied to non-chiral fermions. This fact, together with the usage of the spectral projectors method provides a conceptually clean computation of χ_{top} with a reasonable computational cost.

This chapter is organized as follows, we first present the theoretical representation of the topological susceptibility and immediately after the equivalent expression using spectral projectors. We then report on the subtleties appearing in the implementation of the spectral projectors. A more important point will be the crucial role that autocorrelations play in the study of this quantity. Before presenting our results we perform a study of the finite volume effects and finally present the chiral behavior of the topological susceptibility for $N_f = 2$ and $N_f = 2 + 1 + 1$ where one and three different values of the lattice spacing were used respectively. In both cases we compute the chiral condensate from the quark mass behavior of χ_{top} and compare the value of the condensate with our determination presented in previous chapter. We anticipate already here that both determinations are compatible, as expected.

6.1. Definition of Topological susceptibility

The topological fluctuations of the gauge fields are responsible for relevant low energy properties of QCD such as the breaking of the $U_A(1)$ symmetry and the unexpected large mass of the η' meson. The quantity most directly related to the fluctuations of the gauge fields is the topological susceptibility, which in the continuum is defined as follows

$$\chi_{\text{top}} = \int d^4x \ \langle q(x)q(0)\rangle \,. \tag{6.1}$$

The topological charge density $q(x)$ in QCD is given by

$$q(x) = \frac{1}{32\pi^2}\epsilon_{\mu\nu\lambda\sigma}\text{tr}F_{\mu\nu}F_{\lambda\sigma}, \tag{6.2}$$

where $\epsilon_{\mu\nu\lambda\sigma}$ is the totally antisymmetric Levy-Civita tensor and $F_{\mu\nu}$ is the field strength tensor.

Direct computations of Eq. (6.1) have been carried out in pure lattice gauge theories since the eighties. Some important early steps were done in Refs. [98, 99, 100, 101, 102, 103].

Serious problems remained until now: the proper renormalization of the field theoretic

gluonic definition, the critical dependence of the homotopy based topological charge definitions on lattice artifacts as well as the uncontrollable application of smearing or cooling techniques. Moreover, this definition is affected by non-integrable short distance singularities which make the expression ill-defined unless an explicit subtraction prescription is applied.

There is a natural definition of the topological susceptibility on the lattice given by the index theorem, which was already introduced in Sec. 2.5, and which relates the zero modes of the Dirac operator, with positive and negative chirality, with the topological charge. The establishment of the index theorem on the lattice appears naturally if a formulation which respects a lattice chiral symmetry is applied. Unfortunately for such formulations the cost of the simulations increase enormously and this approach is, therefore, in practice, only applicable to very small lattices.

For this reason several lattice definitions have been proposed over the years [1], including the direct discretization of the continuum formula as explained above. Unfortunately, all the computationally affordable suggested definitions have led to problems and it remained unclear whether they lead to the correct continuum limit. Recently, however, a substantial progress has been made which provided the necessary tools to perform the theoretically clean calculation that will be presented in this chapter.

Initially it was shown that the topological susceptibility, constructed from density chains of 3 or more quark degenerate flavors, is at most logarithmically divergent, i.e. any power divergent subtraction was no longer needed [105]. This proof was based on anomalous flavor singlet Ward identities using Ginsparg-Wilson fermions, and it extended a previous study [18, 19] to full QCD with dynamical quarks.

Based on this work, as another step forward, a lattice representation of the topological susceptibility which is free of short distance singularities and remains well defined in the continuum limit was proposed in Ref. [106]. Using Ginsparg-Wilson fermions, the following identity can be established:

$$\mathrm{Tr}\{\gamma_5 f(D)\} = \{f(0)\}Q, \tag{6.3}$$

where $f(\lambda)$ is any bounded function on the spectral circle which characterizes the spectrum of the Dirac operator which satisfies the Ginsparg-Wilson relation. In Eq. (6.3) Q represents the topological charge.

Using Eq. (6.3), different definitions of the topological charge can be obtained. In particular the left-hand side of Eq. (6.3) can be given by

$$\mathrm{Tr}\gamma_5 f(D) = \mathrm{Tr}\{\gamma_5 D_{m_1}^{-1} \dots D_{m_n}^{-1}\}, \tag{6.4}$$

which resembles the form of the spectral sums which were introduced in Chap. 3. However in this case Eq. (6.4) depends on the massive Dirac operator D_m itself instead of its hermitian counterpart $D_m^\dagger D_m$. After few simple steps of algebra, one can see that

[1] For a comparison of different definitions of the topological charge we refer to Ref. [104].

Eq. (6.4) is directly related to [2]

$$a^{4n} \sum_{x_1,\ldots,x_n} \langle P_{n1}(x_1) S_{12}(x_2) S_{13}(x_3) \ldots S_{n-1\,n}(x_n) \rangle \,. \tag{6.5}$$

The topological susceptibility based on the definition of the topological charge given by the choice $f(D) = D_{m_1}^{-1} \ldots D_{m_n}^{-1}$, would take then the following form

$$\begin{aligned} \chi_{\text{top}} =& m_1 \ldots m_s \times a^{4s-4} \sum_{x_1 \ldots x_{s-1}} \langle P_{r1}(x_1) S_{12}(x_2) \ldots S_{r-1r}(x_r) \\ & \times P_{sr+1}(x_{r+1}) S_{r+1r+2}(x_{r+2}) \ldots S_{s-1s}(0) \rangle \,. \end{aligned} \tag{6.6}$$

In Eq. (6.6) $r,\ s$ are in the range $1 \leq r < s \leq N_f$ and N_f indicates the number of flavors. It can be shown that, with N_f being at least equal or larger than five, the definition of Eq. (6.6) is divergence free. Notice that the masses arise from the $f(0)$ terms which appear on the right hand side of Eq. (6.3).

Thus we are led to an unambiguous definition [106] of the topological susceptibility in the continuum which, for five flavors, takes the following form:

$$\chi_{\text{top}} = m_1 \ldots m_5 \int d^4x_1 \ldots d^4x_4 \, \langle P_{31}(x_1) S_{12}(x_2) S_{23}(x_3) P_{54}(x_4) S_{45}(0) \rangle \,. \tag{6.7}$$

This represents a breakthrough in the study of the topological susceptibility, since for the first time a finite representation could be provided when the cut-off is removed.

This representation can be extended to Wilson-like fermions which are computationally much less demanding than, for instance, the overlap, which respects chiral symmetry. As it will be explained below, in practice, the topological susceptibility will be evaluated through the spectral projectors [107], and therefore the direct computation of the zero modes is avoided. In this way, computations on large lattices become feasible, allowing to study systematic effects of the lattice calculation.

Integrability of the topological susceptibility

The number of flavors plays a crucial role in the renormalizability of observables based on density chains. We already discussed this observation for the mode number in Sec. 3.1.3 when we studied its renormalizability. In the case of the topological susceptibility given by Eq. (6.7) an analogous study can be performed which leads to the conclusion that, in order to guarantee the renormalizability of χ_{top}, at least 5 flavors need to be inserted.

The integrability of density chains directly depends on the short distance singularities that appear when two or more operators are placed at the same space-time point.

The study of the integrability of χ_{top} is analogous to the case of the mode number with one important difference; χ_{top} is constructed using two closed density chains instead of

[2] More details about this and other relations given in the current and further sections can be found in App. G.1

a single one. This is an important fact since each of the density chains represents the topological charge, whose square defines the topological susceptibility.

If the operator product expansion is applied, one can again see that the highest power divergence corresponds to the case where all operators are scaled to zero distance. The reason is that, in this specific case, a mixing with the identity in flavor space occurs. If we have 5 flavors the divergence goes like $|x|^{-15}$, since the final product of pseudoscalar densities, each of which corresponds to a different density chain, are singlet flavor independent, and therefore mix with the identity. Since we have an integration over 16 variables, power counting ensures the integrability for this case. However, if we have only four flavors, the corresponding divergence goes as $|x|^{-12}$ and so does the integral power which is also 12, therefore our observable is, in that case, logarithmically divergent. Less than four flavors then leads to power divergences.

Analogous representation of the topological susceptibility

Due to the relation, already introduced, between the spectral projectors, the spectral sums and the density chain correlation functions, we are interested in a representation of the topological susceptibility in terms of the hermitian Dirac operator $D_m^\dagger D_m$. The left-hand side of Eq. (6.3) will be then given by

$$\mathrm{Tr}\{\gamma_5 f(D_m^\dagger D_m)\} = \mathrm{Tr}\{\gamma_5 (D_m^\dagger D_m)^{-1} \dots (D_m^\dagger D_m)^{-1}\}. \tag{6.8}$$

This expression can be directly linked to the spectral sums introduced in Chap. 3. In fact, a few steps of algebra shows that Eq. (6.8) is related to

$$a^{4n} \sum_{x_1,\dots,x_n} \langle S_{n1}(x_1) P_{12}(x_2) P_{13}(x_3) \dots P_{n-1\,n}(x_n) \rangle \,. \tag{6.9}$$

Notice the differences between Eq. (6.5) and Eq. (6.9), which account for the fact that the former is a function of D_m and the latter of $D_m^\dagger D_m$.

Eq. (6.8) implies, by definition, the use of an even number of operators in the construction of the topological charges (Eq. (6.9)). As we mentioned above, Eq. (3.8) is a rational function of D_m and therefore an odd number of operators is valid.

In addition, the application of the twisted mass discretization entails the insertion of doublets in the definition of the topological susceptibility. For an even number of densities in both closed density chains, i.e. topological charges, this leads to a straightforward and completely analogous expression

$$\sigma_{2;1}(\mu) = a^{20} \sum_{x_1 \dots x_5} \left\langle S_{41}^+(x_1) P_{12}^-(x_2) P_{23}^+(x_3) P_{34}^-(x_4) S_{56}^+(x_5) P_{65}^-(0) \right\rangle , \tag{6.10}$$

which is a representation of the topological susceptibility related to the following spectral sum

$$\sigma_{k;l}(\mu) = \left\langle \mathrm{Tr}\{\gamma_5 (D^\dagger D + \mu^2)^{-k}\} \mathrm{Tr}\{\gamma_5 (D^\dagger D + \mu^2)^{-l}\} \right\rangle \tag{6.11}$$

and therefore allow us to evaluate it using spectral projectors.

We can then conclude that, in order to fulfill all the requirements mentioned above, we need to apply the following representation of the topological susceptibility

$$\chi_{\text{top}} = \mu_1 \dots \mu_6 \int d^4x_1 \dots d^4x_5 \left\langle S^+_{2k\ 1}(x_1) P^-_{12}(x_2) P^+_{23}(x_3) \dots P^+_{2k-1\ 2k}(x_{2k}) \right. \\ \left. S^+_{2k+2l\ 2k+1}(x_{2k+1}) P^-_{2k+1\ 2k+2}(x_{2k+2}) \dots P^+_{2k+2l-1\ 2k+2l}(0) \right\rangle \tag{6.12}$$

where $2k, 2l$ correspond to the number of operators of each closed chain, i.e. each topological charge, respectively. The sign of the charge has to be alternated in order to guarantee that the chains are individually closed in flavor space as it was explained in Chap.4.

The integrability conditions apply in exactly the same way in this new representation, therefore, and since we always have an even number of densities, we need to insert at least six flavors to the theory to guarantee that Eq. (6.12) is free of divergences and well defined in the continuum.

Moreover it can be shown that the topological susceptibility defined in this way scales with $\mathcal{O}(a^2)$ towards the continuum limit. The reason is that the contact terms, that arise in the Symanzik expansion due to the short distance singularities, vanish in the continuum if we use the twisted mass formulation at maximal twist, as it is our case. All the details of this calculation can be found in App. G.1.

In contrast with the mode number, however, which was found to be renormalization group invariant, we have to carefully study the corresponding renormalization factors. Notice that this definition can be overtaken to different kinds of lattice regularization, e.g. Wilson or twisted mass fermions which do not obey a lattice chiral symmetry. This has direct implications in the renormalization of χ_{top}, since, for instance, the ratio of renormalization constants Z_P/Z_S is not equal to unity any longer.

The renormalization of all the components which appear in Eq. (6.12) is well known. It is then straightforward to compute the renormalization factor of χ_{top} given by Eq.(6.12) for an arbitrary number of operators.

$$\chi_{\text{top,R}} = \frac{Z_S^2 Z_P^{2k-2}}{Z_P^{2k}} \chi_{\text{top}} = \frac{Z_S^2}{Z_P^2} \chi_{\text{top}}. \tag{6.13}$$

We can then conclude that the $\frac{Z_S^2}{Z_P^2}$ renormalizes this representation of the topological susceptibility for a generic number $2k$ of operators which constitute both chains.

6.2. Topological susceptibility with spectral projectors

In the previous section a representation of the topological susceptibility that is free of short distance singularities has been introduced. A practical and a completely analogous way to compute the topological susceptibility is given by spectral projectors which leads

to the following definition of the topological susceptibility χ_{top} [107]

$$\chi_{\text{top}} = \frac{Z_S^2}{Z_P^2}\frac{1}{V}\left\langle \text{Tr}\{\gamma_5 \mathbb{R}_M^2\}\text{Tr}\{\gamma_5 \mathbb{R}_M^2\}\right\rangle \tag{6.14}$$

where $\mathbb{R}_M$ is the rational approximation of the orthogonal projector $\mathbb{P}_M$, introduced in detail in Sec. 3.2, and $(Z_S/Z_P)^2$ is the renormalization factor whose origin was explained in the previous section.

As explained in Ref. [107], the choice of $\mathbb{R}_M$ can be any arbitrary rational function of $D_{tm}^\dagger D_{tm}$ which is equal to one below the threshold parameter M^2 and decays rapidly enough above M^2, where M correspond to the spectral threshold parameter previously introduced.

Notice that Eq. (6.14) is analogous to the index theorem, since it implies the computation of the zero modes of the hermitian Dirac operator. We already discussed in detail that the projector $\mathbb{P}_M$, or equivalently $\mathbb{R}_M$, is a very efficient way to count eigenmodes. In this case, due to the γ_5 factor which appears in the trace, we are effectively counting the eigenmodes of γ_5 and $D^\dagger D$, which correspond to the zero modes. The reason is that the only terms that will contribute to the trace are those where $\gamma_5\psi \neq 0$, which correspond to the zero modes where $\gamma_5 = \pm 1$.

In practice we compute the following stochastic observables introduced in Ref. [107].

$$\mathcal{B} = \frac{1}{N}\sum_{k=1}^{N}(\mathbb{R}_M\gamma_5\mathbb{R}_M\eta_k,\ \mathbb{R}_M\gamma_5\mathbb{R}_M\eta_k), \tag{6.15}$$

$$\mathcal{C} = \frac{1}{N}\sum_{k=1}^{N}(\mathbb{R}_M\eta_k,\ \gamma_5\mathbb{R}_M\eta_k).. \tag{6.16}$$

Notice that the observable $\mathcal{B}$ was already introduced in the previous chapter since it is one of the components which appeared in the spectral projectors definition of the ratio of renormalization constants Z_P/Z_S.

The observables $\mathcal{C}$ and $\mathcal{B}$ are directly related to the expectation value which appears on the right-hand side of Eq. (6.14) in the following way

$$\left\langle \text{Tr}\{\gamma_5 \mathbb{R}_M^2\}\text{Tr}\{\gamma_5 \mathbb{R}_M^2\}\right\rangle = \left\langle \mathcal{C}^2\right\rangle - \frac{\langle\mathcal{B}\rangle}{N}, \tag{6.17}$$

where N is the number of stochastic sources.

In the following we will call *unbiased* $\left\langle \mathcal{C}^2\right\rangle$ to the right hand side of Eq. (6.17) and will denote it by $\left\langle \mathcal{C}'^2\right\rangle$. All the expectation values in Eq. (6.17) correspond to the average over stochastic sources and the average over gauge fields configurations combined in the order of first averaging over stochastic sources per configuration and then over the gauge field configurations.

In order to decrease the computational effort required to compute χ_{top} we used the same set of stochastic sources $\eta_1 \ldots \eta_N$ to compute both $\mathcal{C}$ observables involved in $\left\langle \mathcal{C}^2\right\rangle$. This introduces a bias that is corrected by the second term of Eq. (6.17). If two separate

sets of N random sources are used to compute $\langle \mathcal{C}_1 \mathcal{C}_2 \rangle$ instead, where

$$\mathcal{C}_1 = \frac{1}{N} \sum_{k=1}^{N} (\mathbb{R}_M \eta_k,\ \gamma_5 \mathbb{R}_M \eta_k), \quad \mathcal{C}_2 = \frac{1}{N} \sum_{N+1}^{2N} (\mathbb{R}_M \eta_k,\ \gamma_5 \mathbb{R}_M \eta_k), \tag{6.18}$$

then Eq. (6.14) would be reduced to

$$\chi_{\text{top}} = \frac{Z_S^2}{Z_P^2} \frac{\langle \mathcal{C}_1 \mathcal{C}_2 \rangle}{V}. \tag{6.19}$$

The full proof of the statement made above can be found in App. G.3. In addition, notice that the correction given by $\langle \mathcal{B} \rangle / N$ vanishes for an infinite number of stochastic sources.

If chiral symmetry is preserved one can apply the definition of the topological susceptibility given by the index theorem which reads as follows

$$\chi_{\text{top}} = \frac{\langle Q^2 \rangle}{V}, \tag{6.20}$$

where the topological charge Q is given by the index ν and $Z_P / Z_S = 1$. Eq. (6.19) is analogous to Eq. (6.20) and therefore the observable $\mathcal{C}$ is very closely related to the topological charge. Hence, we expect $\mathcal{C}$ to have the very similar properties as Q such as the autocorrelation time. A difference exists in the fact that Q is by definition an integer whereas $\mathcal{C}$ does not have to be an integer unless chiral symmetry is preserved.

6.2.1. Tuning of parameters

In order to compute the topological susceptibility with spectral projectors, a few parameters need to be set. Analogously to Chap.4 the parameters n, ϵ, which are involved in the construction of the Chebyshev polynomial, define the accuracy of the approximation given by $\mathbb{R}_M$ and are taken to be $n = 32$ and $\epsilon = 0.01$ as suggested in Ref. [59].

The value of the threshold parameter M is chosen to be in the region where the spectral density is constant as a function of M. Thus it has to be sufficiently larger than the quark mass but still not too large to avoid deviations from the constant behavior. In practice we set the renormalized threshold parameter to $M_R \approx 100$ MeV in the $\overline{\text{MS}}$ scheme at 2 GeV.

Fig. 6.1 shows the results of the topological susceptibility obtained using different values of M_R. The data shows that the results of χ_{top} are compatible for different values of M_R in the indicated range, although the error increases for large values of M_R. This justifies our choice of $M_R \approx 100$ MeV.

However, the dependency of our result with the parameters mentioned above is expected to be very mild. Moreover, as it will become relevant in the next chapter, the continuum limit extrapolation of χ_{top} should coincide for any chosen value of M.

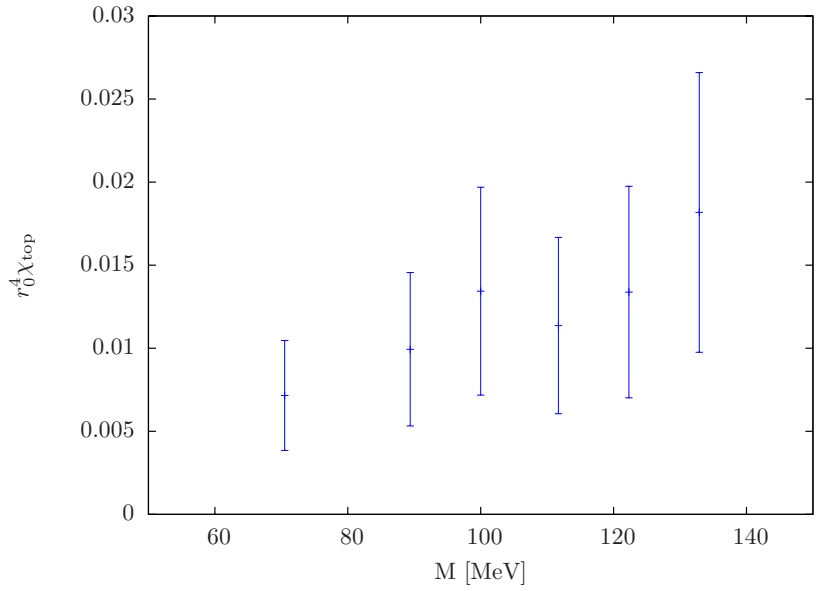

Figure 6.1.: Dependence of χ_{top} on the threshold parameter M_R in the $\overline{\text{MS}}$ scheme at 2 GeV, for $\beta = 3.9$, $L = 32$, $a\mu = 0.004$. In this example 12 stochastic sources were used.

6.3. Computation of χ_{top}

As explained in previous sections, the stochastically computed observable $\mathcal{C}$ is closely related to the topological charge. In the large volume regime the distribution of the topological charge is expected to be a Gaussian [108] centered at zero, and we expect the same behavior for the distribution of $\mathcal{C}$ with correspondingly $\langle \mathcal{C} \rangle = 0$.

This offers an alternative to compute χ_{top} which should be completely equivalent to the direct calculation given by the application of Eq. (6.17). This amounts to extract the value of *unbiased* $\langle \mathcal{C}^2 \rangle$ through a fit of our data for histograms of C to a Gaussian distribution of the form

$$p(\mathcal{C}) = \frac{N}{\sigma\sqrt{2\pi}} e^{\frac{-(\mathcal{C}-\bar{\mathcal{C}})^2}{2\sigma^2}}, \tag{6.21}$$

which corresponds to the width of the distribution given by σ^2. In Eq. (6.21) N represents a normalization factor and $\bar{\mathcal{C}}$ is the mean of the distribution which should also coincide with the median in a Gaussian distribution.

Moreover the histograms of $\mathcal{C}$ allow to control the simulations themselves. By demanding that the histogram is symmetric around $\mathcal{C} = 0$ and that $\bar{\mathcal{C}} = 0$, we can test whether the histograms fulfill these conditions and whether correspondingly we have sufficient statistics to reliably determine the histograms and consequently χ_{top}.

6.3.1. Autocorrelations of the topological charge

Lattice simulations are affected by autocorrelations due to the use of the Markov chain in the Monte Carlo (MC) simulations [109]. Autocorrelations depend on several factors like the discretization, the algorithm and, especially, the observable under study.

The topological charge is particularly affected by severe autocorrelations when the continuum limit is approached [110, 111]. This is due to the fact that the transitions between topological sectors are suppressed, which implies a freezing of the topological charge in Monte Carlo time. Consequently, in order to study the topological charge and reliably determine its uncertainty, a particularly long Monte Carlo simulation may be needed.

In this section, through the study of the stochastic observable $\mathcal{C}$, we give a warning that the statistics provided by dynamical MC simulations, which are typically available nowadays, may not be sufficient to sample all the topological sectors adequately. Therefore a reliable estimation of the topological susceptibility may not be possible and some unknown systematic errors may affect the results from Monte Carlo simulations.

Being aware of this warning, we will nevertheless give a discussion of our determination of the topological susceptibility for our setup of twisted mass fermions. Using the example of a high statistics run, we will show what kind of statistics may be necessary to reliably determine the topological susceptibility. Barring the difficulty of having too small statistics in a number of cases, we will confront our results for the topological susceptibility with predictions of chiral perturbation theory to extract a value for the chiral condensate. As anticipated above, we will find a consistent value with the one extracted from the mode number, which indicates that our results for the topological susceptibility are still reasonable, although the error is most probably underestimated for most of the ensembles.

Fig. 6.3 shows the histograms of the stochastically computed observable $\mathcal{C}$ for three different ensembles: B55.32 (Fig. 6.3.a.), B75.32 (Fig. 6.3.b.) and D15.48 (Fig. 6.3.c.)[3]. We present three different ensembles to discuss, on the one hand, how the size of the statistics used influences the shape of the histograms. On the other hand, we compare different lattice spacings to achieve a more quantitative understanding of the autocorrelation time as a function of the lattice spacing.

Let us first compare the results obtained using simulations performed in a similar physical situation for which the volume and the lattice spacing was kept fixed. The difference between these simulations is that the statistics of the simulation differs by a factor of 5. Fig. 6.3.a. and Fig. 6.3.b. correspond to around 20000 and 4000 MC trajectories, respectively, whereas in both cases $a \approx 0.086$ fm and $L = 2.5$ fm.

Comparing both figures one can clearly see that the histogram which corresponds to the longer run (Fig. 6.3.a.) is perfectly described by a Gaussian distribution centered at zero. In contrast, for the short run (Fig. 6.3.b.), the histogram does not show a clear Gaussian distribution. This leads to the conclusion that in the case of the short run not all the topological sectors have been covered sufficiently and therefore we expect that an

[3]All the details of the simulations can be found in App. D.1

ensemble	N_{traj}	N_{meas}	direct			fit	
			$\langle \mathcal{C} \rangle$	τ_{int}	$\langle \mathcal{C}'^2 \rangle$	$\bar{\mathcal{C}}$	σ^2
B55.32	20000	538	-0.06(16)	0.6(1)	10.9(7)	0.02(8)	10.7(5)
B75.32	4000	201	0.04(35)	1.1(3)	11.0(1.0)	-0.19(30)	12.5(2.1)
D15.48	4000	163	0.9(1.0)	3.0(1.3)	27.1(3.3)	1.13(53)	29.9(5.8)

Table 6.1.: Comparison of the results obtained through a Gaussian fit and a direct calculation of $\langle \mathcal{C} \rangle$ and *unbiased* $\langle \mathcal{C}^2 \rangle$. The integrated autocorrelation time τ_{int} of the observable $\mathcal{C}$ is also included. N denotes the number of analyzed configurations and the number of Monte Carlo trajectories between configurations.

increase in the MC time would give the appropriate Gaussian shape of the distribution as we have seen in the case of the high statistics run.

In Tab. 6.1 we give the integrated autocorrelation time τ_{int} of the observable $\mathcal{C}$ together with the total number of simulated trajectories and the number of configurations analyzed. Tab. 6.1 also shows the average values of $\mathcal{C}$, the unbiased values of $\mathcal{C}^2$, given by $\mathcal{C}'^2$, and the results obtained through a Gaussian fit for the mean and the width σ of the distribution.

In addition Fig. 6.2.a. and Fig. 6.2.b. represent the MC history of the observable $\mathcal{C}$. In Fig. 6.2.b. one can graphically observe the autocorrelations that affect the calculation of this observable. The data show the tendency to remain in the same topological sector for few consecutive configurations, a phenomena which is directly related to autocorrelation and topological barriers. On the other hand Fig. 6.2.a. shows random fluctuations around zero, which correspond to the expected behavior.

The above discussion suggests that the number of independent configurations ($\approx$100) as we have for the case of B75.32 (Fig. 6.3.b.) is not enough to compute the topological susceptibility reliably such that we have all the systematics under control. It should be emphasized that this statement is independent from the method used to compute the topological susceptibility. Rather, the problem has its origin in the characteristics of the gauge fields themselves and, of course, in the algorithm used to perform the Monte Carlo simulations.

In contrast, a MC simulation which consists of $\approx$ 20000 trajectories, of which $\approx$ 500 are independent, for a lattice spacing $a = 0.086$ fm is certainly enough to reliably compute the topological susceptibility with an error below 10% using spectral projectors. Unfortunately most of the current lattice simulations of ETMC do not have such high statistics due to the large computational cost of of dynamical lattice ensemble generation.

Furthermore Fig. 6.3.c. and Fig. 6.2.c. show an example of how autocorrelations can cause serious problems in the determination of the topological susceptibility. As discussed above, firstly the histogram is far from showing a Gaussian distribution, with obvious insufficient statistics in certain bins. Secondly, comparing Fig. 6.2.b. and Fig. 6.2.c, much enhanced autocorrelations are observed in Fig. 6.2.c.. In fact, the value of τ_{int} is three times larger for D15.48 than for B75.32 as it is shown in Tab. 6.1. Given that the statistics of both runs are completely comparable, see Tab. 6.1, this implies that for

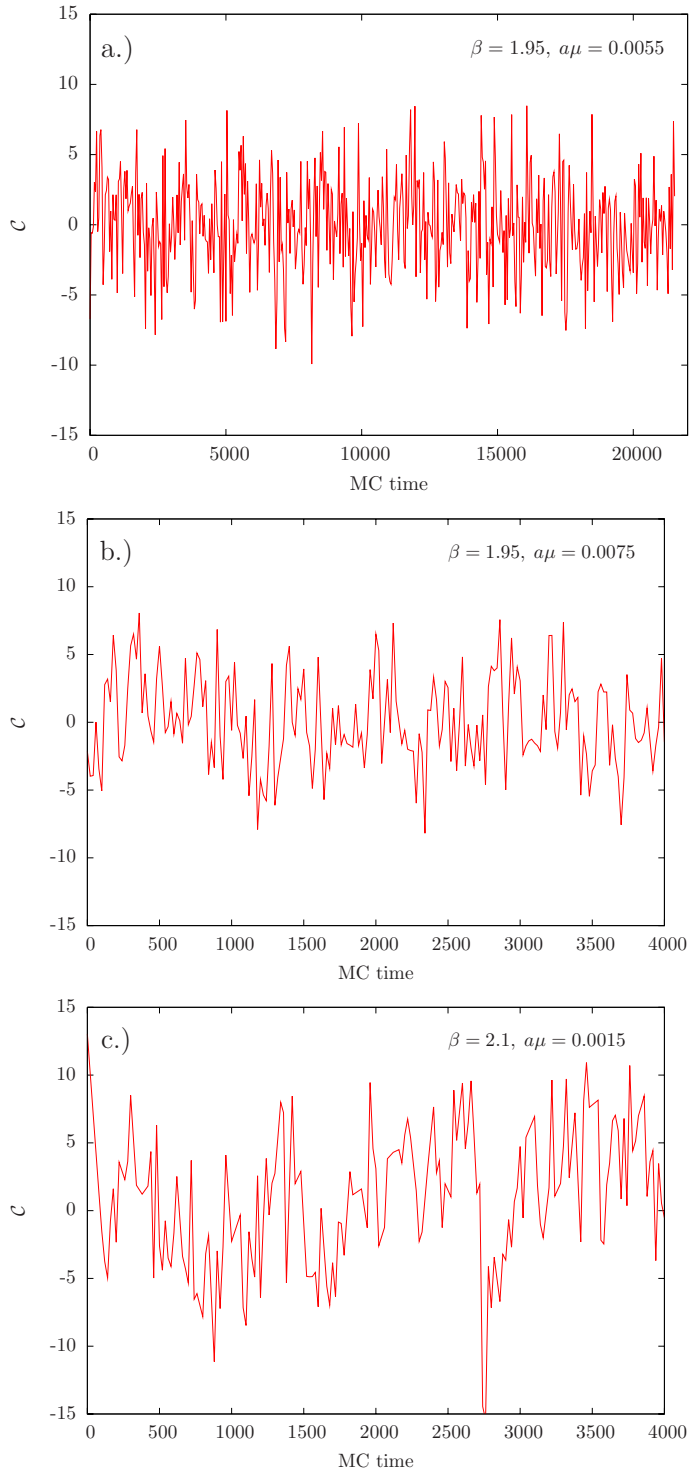

Figure 6.2.: MC history of the observable $\mathcal{C}$ for $\beta = 1.95$,$a\mu = 0.0055$ (a.), $a\mu = 0.0075$ (b.) and $\beta = 2.1$ at $a\mu = 0.0015$ (c.).

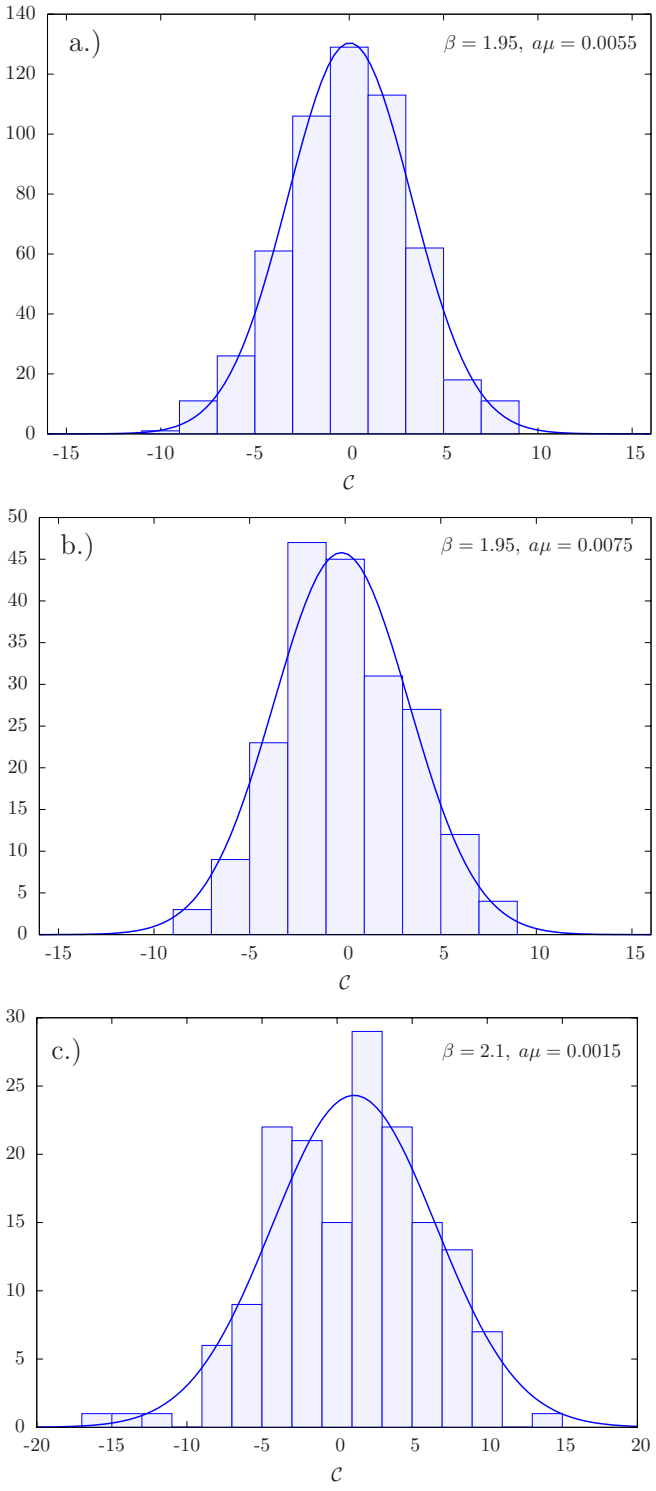

Figure 6.3.: Histograms of the observable $\mathcal{C}$ for $\beta = 1.95$,$a\mu = 0.0055$ (a.), $a\mu = 0.0075$ (b.) and $\beta = 2.1$ at $a\mu = 0.0015$ (c.).

Ensemble	L [fm]	N_s	N_{traj}	N_{meas}	$\langle \mathcal{C}'^2 \rangle$	$r_0^4 \chi_{\text{top}}$
b40.16	1.4	12	5430	272	0.6(1)	0.097(16)(1)(3)
b40.20	1.7	6	5280	264	1.5(2)	0.0092(11)(1)(3)
b40.24	2.0	6	9760	454	3.2(4)	0.0096(11)(1)(3)
b40.32	2.7	12	4000	217	8.6(1.3)	0.0082(13)(1)(3)
A40.20	1.7	6	3200	200	2.7(5)	0.0130(22)(5)(4)
A40.24	2.1	6	4000	198	3.7(6)	0.0086(13)(3)(3)
A40.32	1.7	6	1600	190	10.2(1.4)	0.0074(10)(3)(2)

Table 6.2.: Results of χ_{top} and the unbiased $\mathcal{C}^2$ for the finite volume effects study for $N_f = 2$ and $N_f = 2 + 1 + 1$ respectively. N_s represents the number of stochastic sources whereas N_{meas} is the number of evaluated configurations and N_{traj} gives the corresponding number of thermalized MC trajectories. L corresponds to the lattice size. The errors quoted of χ_{top} are statistical, coming from Z_P/Z_S and from r_0/a respectively.

the case of D15.32 we effectively have less than 40 independent configurations, which does not allow us to perform any reliable calculation of the topological susceptibility. Consequently we do not consider the results obtained evaluating this ensemble in our final conclusions.

6.4. Finite volume effects for $N_f = 2$ and $N_f = 2 + 1 + 1$

On the lattice, as previously mentioned, due to the fact that the calculations are restricted to a finite volume, the study of finite volume effects (FVE) becomes a fundamental aspect of the study systematic effects.

The finite volume effects of the topological susceptibility are expected to decrease exponentially with the lattice size L [112]. Therefore for lattices with $L > 1$ fm, as it is our case, the FVE are expected to be below the statistical uncertainty.

In the present section we report on the results of finite volume effects (FVE) study

Ensemble	L [fm]	$\langle \mathcal{A} \rangle$	τ_{int}	$\langle \mathcal{B} \rangle$	τ_{int}	$\langle \mathcal{C} \rangle$	τ_{int}
b40.16	1.4	5.3(1)	1.9(6)	0.92(4)	2.0(6)	-0.19(9)	1.6(5)
b40.20	1.7	14.6(4)	3.5(1.3)	2.6(1)	3.1(1)	-0.10(12)	0.9(2)
b40.24	2.0	32.1(2)	1.0(2)	5.72(5)	1.1(2)	-0.13(17)	1.5(4)
b40.32	2.7	100.5(5)	1.7(6)	17.8(1)	1.4(4)	-0.38(38)	1.5(5)
A40.20	1.7	29.9(6)	2.6(1.0)	5.4(1)	1.9(6)	-0.1(2)	1.1(3)
A40.24	2.1	53.8(1.3)	6.7(3.1)	9.8(2)	3.7(1.6)	-0.03(21)	0.8(2)
A40.32	2.8	170.5(1.2)	1.8(6)	30.7(2)	1.3(4)	0.2(3)	0.7(2)

Table 6.3.: Results of $\langle \mathcal{A} \rangle$, $\langle \mathcal{B} \rangle$ and $\langle \mathcal{C} \rangle$ their corresponding values of τ_{int} for the finite volume effects study for $N_f = 2$ and $N_f = 2 + 1 + 1$ respectively.

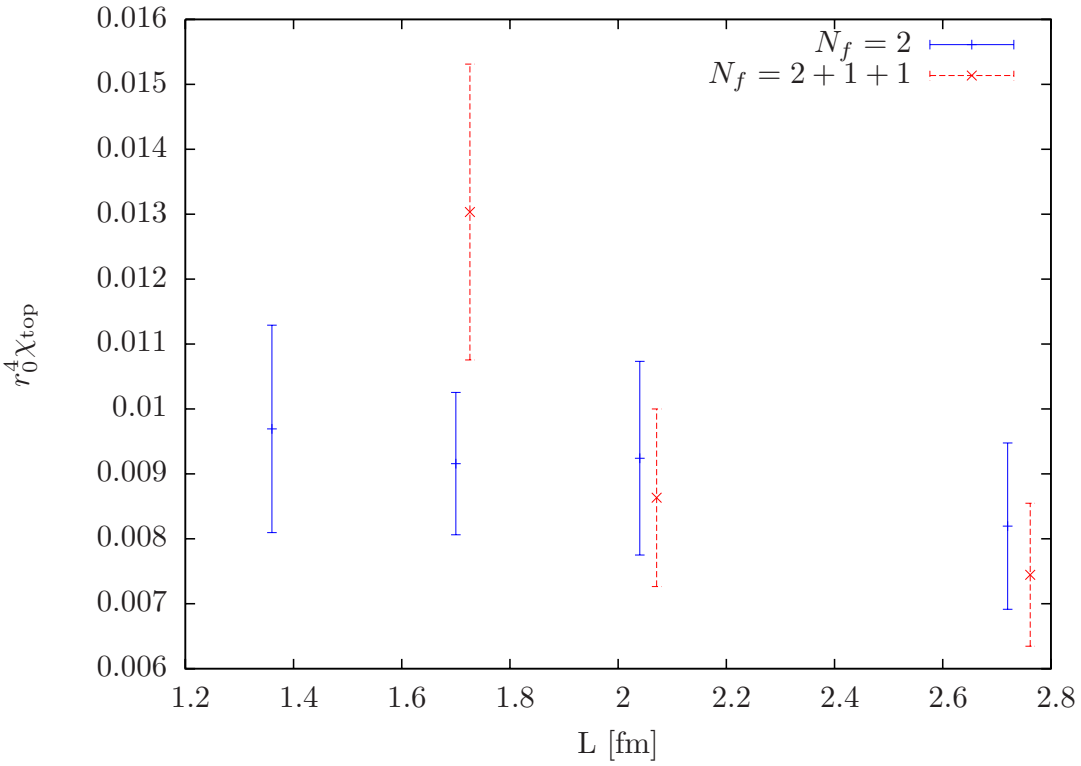

Figure 6.4.: Finite volume effects of the topological susceptibility for $N_f = 2$ and $N_f = 2+1+1$.

of the topological susceptibility for $N_f = 2$ and $N_f = 2+1+1$. We compute $\chi_{\rm top}$ for different volumes at a fixed lattice spacing. All the results are plotted in Fig. 6.4 and the corresponding numerical values are displayed in Tab. 6.2. Also in Tab. 6.3 the values of $\langle \mathcal{A} \rangle$, $\langle \mathcal{B} \rangle$, $\langle \mathcal{C} \rangle$, necessary to compute $\chi_{\rm top}$, and their corresponding $\tau_{\rm int}$ are given.

The data does not show any indication of finite volume effects, as we expected. Thus we conclude that $\chi_{\rm top}$ is independent of the volume for $L > 1.3$ fm. Another confirmation comes from the fact that Eq. (6.21) describes well the data at least when we have a sufficiently large statistics to compute $\chi_{\rm top}$ reliably.

As a remark let us mention that, even though the result is compatible within 1.5σ, the smaller volume considered for $N_f = 2+1+1$ seems to be slightly large. However, this result does not affect our calculations since all the analyzed ensembles of $N_f = 2+1+1$ correspond to $L \geq 2$ fm.

6.5. Chiral behavior of $\chi_{\rm top}$

The main goal of this chapter is to study the chiral behavior of the topological susceptibility in the dynamical case, which is presented here for one lattice spacing in the $N_f = 2$

case and for three different values of a in the $N_f = 2+1+1$ case.

6.5.1. χ_{top} in chiral perturbation theory

The chiral behavior of the topological susceptibility was first derived by Leutwyler and Smilga at LO of χPT [61] and takes the form

$$\chi_{\text{top}} = \frac{\Sigma}{m_u^{-1} + m_d^{-1}} \quad \text{for } N_f = 2, \qquad \chi_{\text{top}} = \frac{\Sigma}{m_u^{-1} + m_d^{-1} + m_s^{-1}} \quad \text{for } N_f = 3. \tag{6.22}$$

This formula implies that the topological susceptibility is suppressed for vanishing quark mass due to internal quark loops. Furthermore, it provides an alternative way to extract the chiral condensate in the chiral limit.

More recently, a NLO formula has been provided in Ref. [113], which includes other low energy constants such as F_π, L_6, L_7 and L_8. This formula for $N_f = 2$ reads as follows

$$\begin{aligned}\chi_{\text{top}} =& \Sigma \left(\frac{1}{m_u} + \frac{1}{m_d}\right)^{-1} \left[1 - \frac{3}{2F_\pi^2}\frac{M_\pi^2}{16\pi^2} \ln \frac{M_\pi^2}{\mu_{sub}^2}\right. \\ &\left. + K_6(m_u + m_d) + 2(2K_7 + K_8)\frac{m_u m_d}{m_u + m_d}\right].\end{aligned} \tag{6.23}$$

In Ref. [113] it was also proposed to add non-degenerate strange and charm quarks at tree-level to Eq. (6.23). However, in this work we will concentrate only on the small quark mass dependence of the topological susceptibility.

6.5.2. Results for $N_f = 2$

In this section we present the results of the topological susceptibility for three different quark masses at fixed lattice spacing $a \approx 0.086$ for $N_f = 2$ degenerate twisted mass fermions at maximal twist.

Fig. 6.5 shows the chiral behavior of χ_{top} and the fit to LO of χPT. In Tab. 6.4 the results of the stochastic observables $\mathcal{A}$, $\mathcal{B}$ and $\mathcal{C}$ and their corresponding integrated autocorrelation time τ_{int} are displayed. Tab. 6.5 shows the details of the calculation and also includes the results of χ_{top} and the unbiased $\mathcal{C}^2$. The data shows the suppression of the topological susceptibility that is predicted in χPT. If we apply Eq. (6.22) for $N_f = 2$ and fit the data we obtain the following result for the chiral condensate

$$r_0 \Sigma^{1/3} = 0.650(22) \tag{6.24}$$

which would correspond to $\Sigma^{1/3} = 267(9)$ MeV if we use $r_0 = 0.48$ [86]. This result is perfectly compatible with the values of the chiral condensate showed in Tab. 4.7 and to our previous determination presented in Chap.4. Note that this result is obtained at a fixed lattice spacing, whereas our results presented in Chap.4 were extrapolated to the

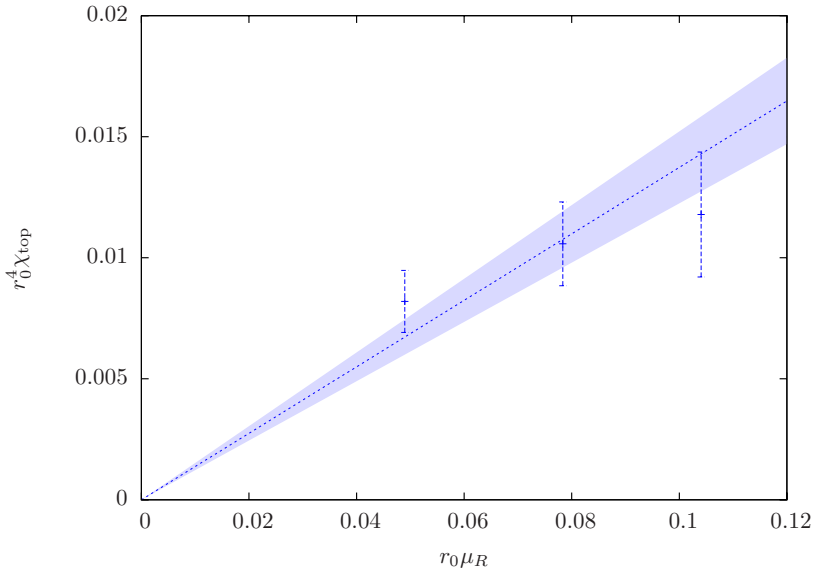

Figure 6.5.: Chiral behavior of the topological susceptibility for $N_f = 2$. The straight line corresponds to a LO fit of χPT.

Ensemble	$\langle\mathcal{A}\rangle$	τ_{int}	$\langle\mathcal{B}\rangle$	τ_{int}	$\langle\mathcal{C}\rangle$	τ_{int}
b40.32	100.5(5)	1.7(6)	17.8(1)	1.4(4)	-0.38(38)	1.5(5)
b64.24	30.9(3)	1.0(3)	5.39(7)	1.2(4)	-0.02(27)	1.8(6)
b85.24	29.3(24)	0.6(1)	5.03(6)	0.8(2)	0.46(29)	1.4(5)

Table 6.4.: Results of $\langle\mathcal{A}\rangle$, $\langle\mathcal{B}\rangle$ and $\langle\mathcal{C}\rangle$ their corresponding values of τ_{int} for different quark masses for $N_f = 2$.

Ensemble	μ_R	N_s	N_{traj}	N_{meas}	$\langle\mathcal{C}'^2\rangle$	$r_0^4\chi_{\text{top}}$
b40.32	21	12	4000	217	8.6(1.3)	0.0082(13)(1)(2)
b64.24	34	6	4740	219	3.5(6)	0.0106(17)(1)(2)
b85.24	45	6	3640	160	3.9(9)	0.0118(25)(1)(2)

Table 6.5.: Results of χ_{top} and the unbiased $\mathcal{C}^2$ for different quark masses for $N_f = 2$. N_s represents the number of stochastic sources whereas N_{meas} is the number of evaluated configurations and N_{traj} gives the corresponding number of thermalized MC trajectories. The errors quoted correspond to the statistical error, the error of Z_P/Z_S and the error coming from r_0/a respectively.

continuum limit. Moreover, it is important to notice that the values of the largest quark masses used in the fit are large in the range of applicability of χPT recently suggested [114]. Therefore it maybe questionable, whether the data at these large quark masses can indeed be used in the fit.

We introduced in the last section a NLO χPT formula of the topological susceptibility and its quark mass dependence (Eq.6.23). Our data, however, is not sensitive to the NLO corrections due to the large uncertainty obtained for the topological susceptibility ($\approx 20\%$). We estimate that in order to give a conclusive result for the NLO effects the precision of the data should be below 10% which would correspond to an extension of the current MC history available for the dynamical simulations of at least 4 times.

6.5.3. Results for $N_f = 2 + 1 + 1$

In this section we present the main results of this chapter which consists of a study of the chiral behavior of the topological susceptibility for $N_f = 2+1+1$ dynamical twisted mass fermions at maximal twist. We perform the calculation of χ_{top} for several quark masses at three different lattice spacings which allow us to, firstly study the lattice artifacts present in the results, and secondly compute the chiral condensate in the continuum limit.

Tab. 6.6 shows the results of the stochastically computed observables $\mathcal{A}$, $\mathcal{B}$ and $\mathcal{C}$ and their corresponding values of the integrated autocorrelation time τ_{int}. The results of the topological susceptibility for each ensemble are displayed in Tab. 6.7 together with the most relevant information of the calculation such as the number of stochastic sources, or the number of analyzed configurations.

In order to study the suppression of the topological susceptibility when the chiral limit is approached we first present the results for each individual β in Fig. 6.6. There we can see how for $\beta = 1.90$ and even more clearly for $\beta = 2.1$ the topological susceptibility tends to vanish when the quark mass decreases. In the case of $\beta = 1.95$ this behavior is not so clear. At this point we need to emphasize the conclusion obtained in the previous section where the histograms were analyzed. There we concluded that, due to the short MC histories of the dynamical ensembles available, in most cases the topological sectors are not well sampled and therefore the uncertainty of the calculation can not be precisely determined.

In particular, the values of $\langle \mathcal{C} \rangle$ which corresponds for the ensembles for the lowest masses of $\beta = 1.95$ the histograms are clearly non-Gaussian which is also signalled by a non-zero value of $\langle \mathcal{C} \rangle$. Therefore, for these cases, we expect that the errors are being underestimated.

An interesting result we found is that, for a similar length of the MC history at different lattice spacings, we do not observe a large difference in the autocorrelation times of $\mathcal{C}$. It is therefore most likely that the lattice spacings analyzed in this work are still not close enough to the continuum limit to encounter the topological barriers that were described in Ref. [111] for Wilson fermions.

Let us now discuss the results of the chiral condensate extracted from the slope of the topological susceptibility given by a LO formula of χPT which describes the chiral

Ensemble	$\langle \mathcal{A} \rangle$	τ_{int}	$\langle \mathcal{B} \rangle$	τ_{int}	$\langle \mathcal{C} \rangle$	τ_{int}
A30.32	167.9(2.3)	4.8(2.1)	30.3(4)	3.8(1.5)	-0.18(26)	0.5(1)
A40.32	170.5(1.2)	1.8(6)	30.7(2)	1.3(4)	0.25(34)	0.7(2)
A50.32	175.6(1.1)	1.9(7)	31.7(3)	2.2(8)	0.36(31)	0.6(1)
A60.24	54.5(6)	1.6(5)	9.9(1)	1.4(5)	-0.26(25)	0.9(3)
A80.24	53.7(4)	1.6(5)	9.7(10)	1.5(5)	0.76(24)	1.0(3)
B25.32	91.9(1.3)	1.7(6)	18.9(2)	1.3(4)	-0.57(32)	1.2(3)
B35.32	95.6(9)	2.3(9)	19.5(1)	1.2(4)	-0.55(23)	0.6(2)
B55.32	95.6(3)	1.1(2)	19.47(7)	0.9(2)	-0.06(16)	0.6(1)
B75.32	92.6(5)	1.4(5)	18.7(1)	1.3(4)	0.04(35)	1.1(3)
B85.24	31.5(2)	0.8(2)	6.52(5)	0.6(1)	-0.09(14)	0.7(1)
D20.48	157.1(1.3)	1.5(6)	49.7(4)	1.3(6)	-0.42(48)	0.7(2)
D30.48	158.2(0.9)	1.0(4)	50.2(2)	0.6(2)	-0.44(64)	0.9(3)
D45.32	29.1(5)	2.3(1.0)	9.4(2)	1.5(6)	-0.33(45)	2.1(0.9)

Table 6.6.: Results of $\langle \mathcal{A} \rangle$, $\langle \mathcal{B} \rangle$ and $\langle \mathcal{C} \rangle$ their corresponding values of τ_{int} for $N_f = 2+1+1$ at different values of the quark mass and different lattice spacings.

Ensemble	N_s	N_{traj}	N_{conf}	$\langle \mathcal{C}'^2 \rangle$	$r_0^4 \chi_{\text{top}}$
A30.32	6	4480	223	9.8(1.4)	0.0072(10)(3)(2)
A40.32	6	4000	190	10.2(1.4)	0.0074(10)(3)(2)
A50.32	6	4000	201	11.0(1.7)	0.0081(12)(3)(2)
A60.24	6	1608	163	4.0(6)	0.0092(14)(3)(3)
A80.24	6	1600	201	4.9(7)	0.0114(17)(4)(3)
B25.32	8	4000	199	6.7(1.0)	0.0070(11)(1)(2)
B35.32	8	4000	198	6.4(8)	0.0067(9)(1)(2)
B55.32	6	21560	538	7.7(7)	0.0080(7)(2)(2)
B75.32	8	4000	201	8.7(1.0)	0.0090(10)(2)(3)
B85.24	12	4780	236	3.2(4)	0.0106(14)(2)(3)
D20.48	6	2000	97	7.4(2.0)	0.0041(11)(1)(1)
D30.48	6	2000	101	13.2(4.3)	0.0073(24)(1)(2)
D45.32	6	2320	96	4.4(7)	0.0125(20)(1)(3)

Table 6.7.: Results of χ_{top} and the unbiased $\mathcal{C}^2$ for $N_f = 2+1+1$ at different values of the quark mass $a\mu$. N_s represents the number of stochastic sources whereas N_{meas} is the number of evaluated configurations and N_{traj} gives the corresponding number of thermalized MC trajectories. The errors quoted correspond to the statistical error, the error of Z_P/Z_S and the error coming from r_0/a respectively.

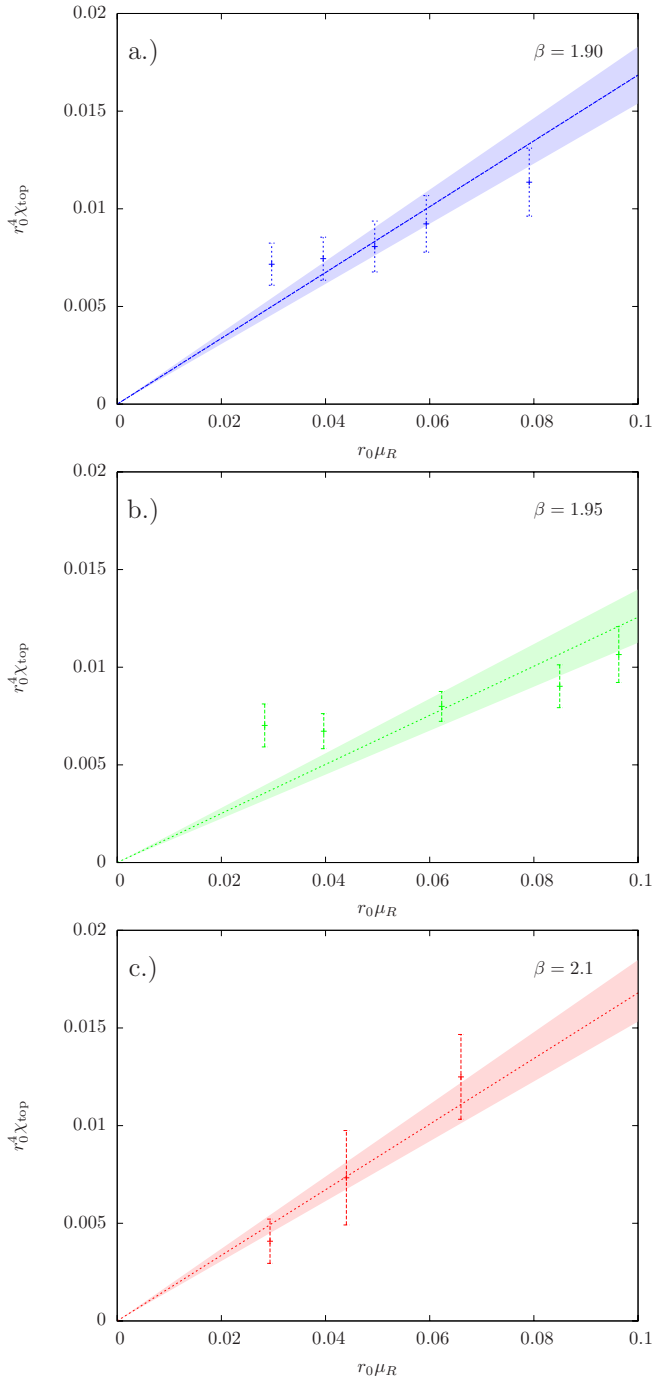

Figure 6.6.: Plots of the chiral behavior of the topological susceptibility for $N_f = 2{+}1{+}1$ at three different values of the lattice spacing: $a = 0.086$fm (a.), $a = 0.078$fm (b.) and $a = 0.061$fm (c.) respectively. The straight line corresponds to a LO fit of χPT.

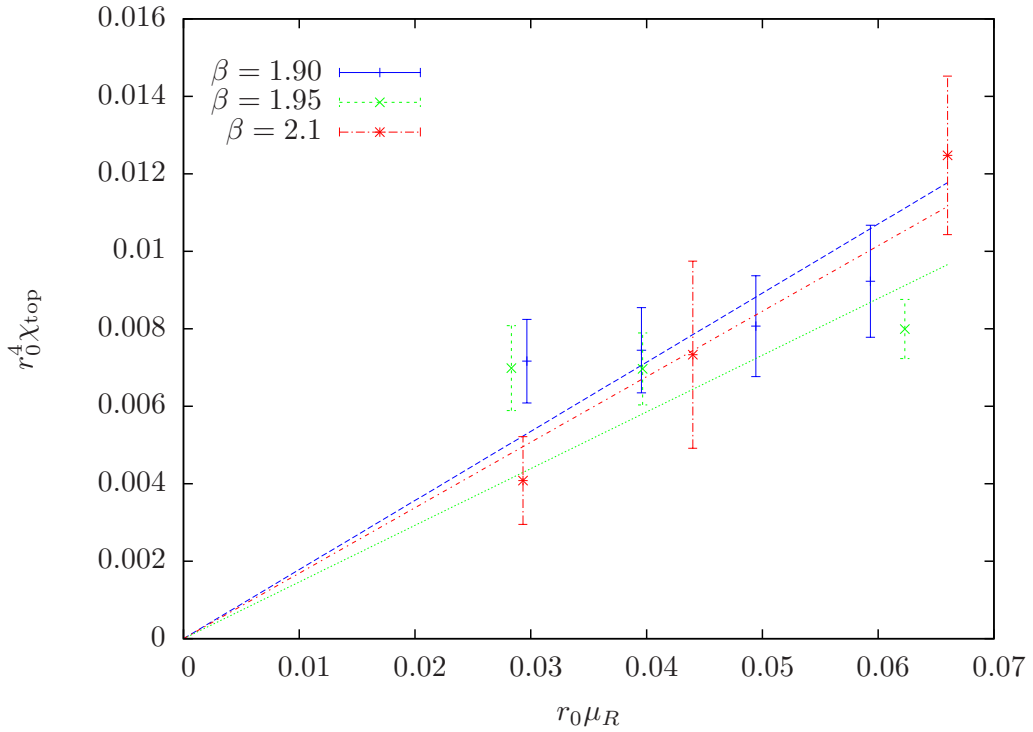

Figure 6.7.: Chiral behavior of the topological susceptibility for $N_f = 2+1+1$ at three different β values. The straight lines corresponds to a LO fit of χPT.

dependence of $\chi_{\rm top}$ (Eq.6.22 for $N_f = 2$). In principle χPT is only applicable at low quark masses [114], for this reason we computed Σ considering only $r_0\mu < 0.7$.

Although we do see a tendency of concavity in some cases, which could be due to the NLO effects, we only apply the LO formula of χPT to extract Σ. The reason is that, due to the large uncertainties in $\chi_{\rm top}$, we are not sensitive to the NLO effects. In order to give a quantitative estimate of the NLO corrections we would need to decrease the error below 10%, which would imply to extend the MC simulation by a factor of at least 4. The current length of the simulations leads to an error between 15%-25%, as it can be seen in Tab. 6.6, which does not allow to disentangle the NLO corrections.

In Tab. 6.8 all the results of the chiral condensate for the three different lattice spacing are presented; Tab. 6.8 also includes the continuum limit extrapolated result. Fig. 6.8 shows the corresponding continuum extrapolation graphically where only the low masses are included in the fit and plotted in the figure. The continuum limit extrapolated result of the chiral condensate obtained through the chiral behavior of $\chi_{\rm top}$ is

$$r_0\Sigma_\chi^{1/3} = 0.651(61). \tag{6.25}$$

In order to show the robustness of our results for the chiral condensate, we performed the same analysis considering all the quark masses that were available and obtained

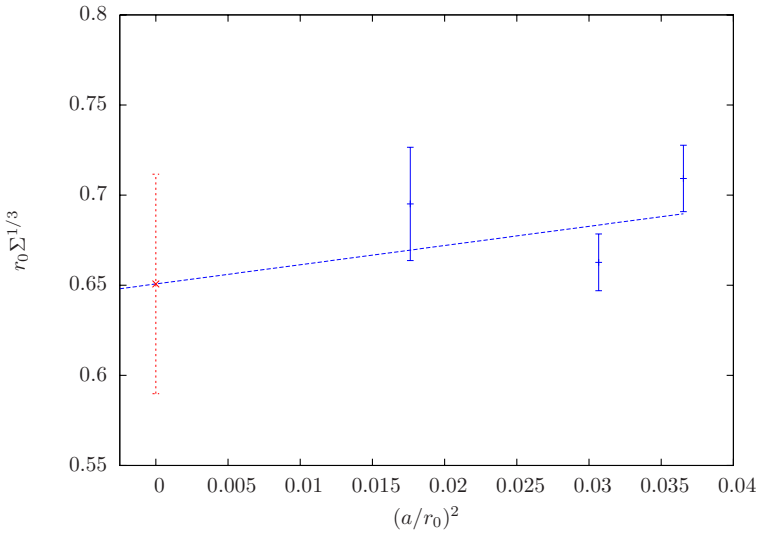

Figure 6.8.: Continuum limit of the chiral condensate $r_0\Sigma_\chi^{1/3}$ extracted from χ_{top}. The red point corresponds to the continuum limit extrapolation and the straight line to a linear fit.

$r_0\Sigma_\chi^{1/3} = 0.619(58)$.

Both results are perfectly compatible with the continuum limit results displayed in Tab. 4.7. The precision of the results for the chiral condensate is directly related to the uncertainty of χ_{top} and therefore to the length of the simulations. In order to decrease the error to obtain a more precise determination of χ_{top} a substantial extension of the dynamical simulations would be required.

This final result shows that the predictions made by χPT which provides the dependence of the topological susceptibility with respect to the quark mass gives a result of the chiral condensate which is compatible with other determinations obtained through different methods. This confirms that spectral projectors is a completely valid method to compute the topological susceptibility, based on a theoretical sound definition with a well-defined continuum limit and whose computational cost is affordable given the

a fm	$(a/r_0)^2$	$r_0\Sigma_\chi^{1/3}$	$\Sigma_\chi^{1/3}$ [MeV]
0.086	0.036	0.709(18)	291.4(7)
0.078	0.031	0.663(16)	272.9(7)
0.061	0.018	0.695(31)	286.1(13)
0	0	0.651(61)	268(25)

Table 6.8.: Results of the chiral condensate extracted from χ_{top} at three different values of the lattice spacing including the continuum limit extrapolation.

current computing power available for large volumes.

Our main conclusion is therefore that if simulations can be performed with sufficiently large statistics, corresponding to $\mathcal{O}(500)$ independent configurations, the spectral projectors method is very well suited to extract topological properties of gauge field configurations. Since it can be directly applied to Wilson-like fermions, it could therefore overcome a long-standing problem in lattice QCD, namely to understand the quark mass behavior of the topological susceptibility.

CHAPTER 7

Computation of the Topological Susceptibility in the pure Yang-Mills theory

Contents

We dedicate this final chapter to attempt a first test of the Witten-Veneziano formula which relates the topological susceptibility in the pure Yang-Mills theory (χ_∞) to the masses of kaon, η, and especially to the η' mass.

To do so we computed the topological susceptibility in the continuum limit using spectral projectors for pure gauge configurations which were generated to match the physical situation of the dynamical simulations which were used to compute the masses of the above listed mesons [115].

This chapter is organized as follows, we first present our strategy to generate the pure gauge configurations and motivate our choice of the simulation parameters used. We then present a study of the Monte Carlo (MC) history of the topological charge and their corresponding histograms for a number of lattice spacings. This is followed by showing the results of χ_∞ at fixed lattice spacing and a discussion on the continuum limit extrapolation. Finally we discuss the Witten-Veneziano formula which is evaluated using our results for the quenched topological susceptibility and the results for the meson masses taken from another work which also uses twisted mass fermions at maximal twist in a matched physical situation.

7.1. Continuum limit of the topological susceptibility

7.1.1. Introduction

In the introductory chapter of this work we already presented the Witten-Veneziano formula [16, 17] which relates the topological susceptibility in the pure gauge theory to the unexpected large mass of the η' meson. For completeness, however, we present here again the expression, which for $SU(3)$ reads as follows

$$\frac{f_\pi^2}{2N_f}(m_\eta^2 + m_{\eta'}^2 - 2m_K^2) = \chi_\infty, \tag{7.1}$$

where f_π is the pion decay constant.

Our goal is to compute the right-hand side of Eq. (7.1) in order to show that we obtain a compatible result with the left-hand side of Eq. (7.1) which we compute through the meson masses provided in Ref. [115].

In order to compute the continuum limit of χ_∞ in the pure Yang Mills theory we generated four ensembles at four different lattice spacings. Since our main goal is to test the Witten-Veneziano formula, we matched the physical situation given by the ensemble B55.32 which was used to compute the meson masses [115].

Following this strategy we first generated a $32^3 \times 64$ pure gauge ensemble with $\beta = 2.67$ which corresponds to a value of $r_0/a = 5.71$ to match the physical volume of B55.32 which has the same value of r_0/a. We kept the quark mass of the ensemble B55.32 at $a\mu = 0.0055$ as well.

To extend the number of ensembles to different values of the lattice spacing we kept the physical volume constant by demanding that $L \cdot a$ is constant. Thus when we increase the lattice size L we decrease a adequately to keep $L = 2.8$ fm when we use $r_0 = 0.5$ fm.

β	Volume	r_0/a	a [fm]	L [fm]	$a\mu$	$r_0\mu$	κ_c^χ
2.37	$20^3 \times 40$	3.59(2)(3)	0.1393	2.79	0.0087	0.0312	0.158738
2.48	$24^3 \times 48$	4.28(1)(5)	0.1182	2.83	0.0073	0.0309	0.154928
2.67	$32^3 \times 64$	5.69(2)(3)	0.0879	2.81	0.0055	0.0314	0.150269
2.85	$40^3 \times 80$	7.29(7)(1)	0.0686	2.74	0.0043	0.0313	0.147180

Table 7.1.: All relevant parameters of the pure gauge ensembles for $\beta = 2.37$, 2.48, 2.67 and 2.85. The errors of r_0/a correspond to statistical and systematic uncertainties, respectively.

In order to compute the quark mass we chose the product $r_0\mu \approx 0.03$ to remain constant.

Tab. 7.1 shows all the relevant parameters of the generated ensembles including the lattice spacing, the quark masses and the volume among others. The details of generation of the quenched ensembles as well as the strategy to compute r_0/a and κ_c^χ and additional information can be found in App. D.2.

7.1.2. Matching M for the calculation

In principle the value of the spectral threshold M_R should not influence the result, since we expect that the values of the topological susceptibility computed using different values of M_R should coincide in the continuum limit.

However, we chose $M_\star$ for the ensemble $\beta = 2.67$ to match the value that we use for B55.32 which in that case corresponded to $M_R = 90$ MeV.

Notice that it is very important to keep the value of M_R constant for the different ensembles in order to perform the continuum limit. Due to the fact that the renormalization constant Z_P for the different quenched ensembles are not available, this task needed a particular strategy. To this end, we used one property of the mode number which guarantees that for equal physical volumes the mode number should remain constant for a fixed M_R:

$$\frac{a_1}{a_2} = \left(\frac{\nu_1 n_2}{\nu_2 n_1}\right), \tag{7.2}$$

where n_i denotes the number of points in the corresponding lattice, a_i the lattice spacing and ν_i the mode number [59]. This property allows us then to compute the values of $M_\star$ for the different quenched ensembles which lead to equal values of M_R.

β	a [fm]	$M_\star^2$	ν
2.37	0.139	0.000102	79.4(2)
2.48	0.118	0.000068	78.7(2)
2.67	0.088	0.000036	78.5(3)
2.85	0.069	0.000025	78.1(4)

Table 7.2.: Values of $M_\star$ and their corresponding ν for four quenched ensembles at different lattice spacing and fixed physical volume.

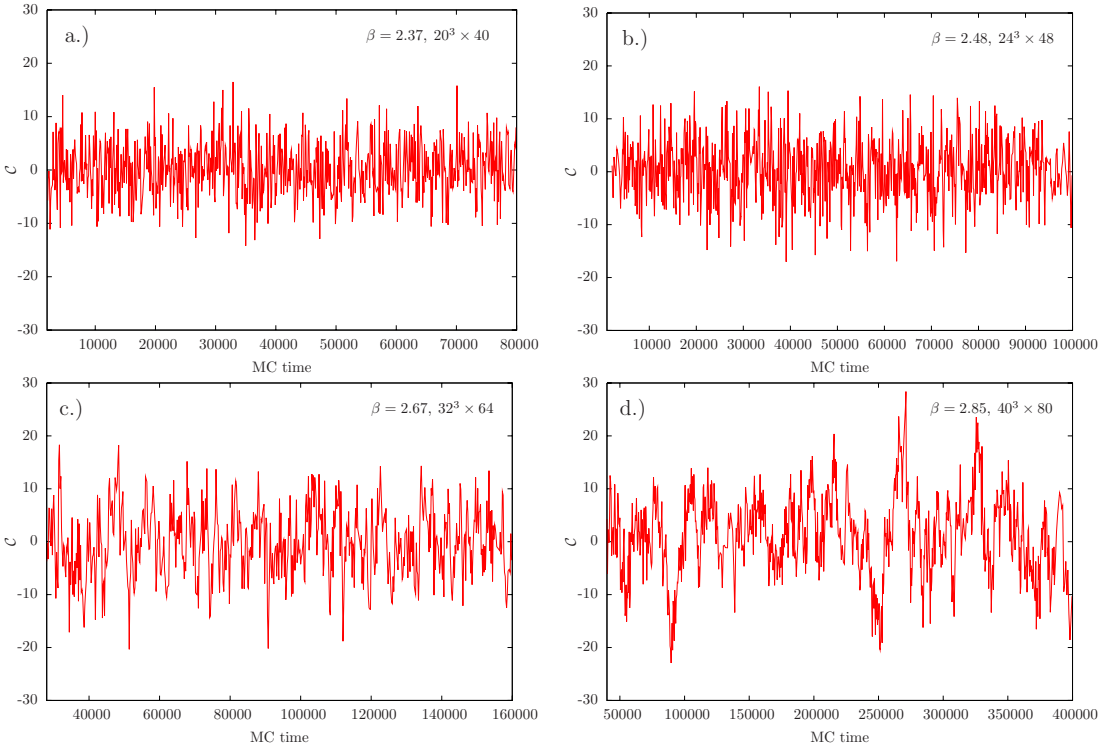

Figure 7.1.: Monte Carlo histories of the observable $\mathcal{C}$ for four quenched ensembles at $\beta = 2.37$ (a.), $\beta = 2.48$ (b.), $\beta = 2.67$ (c.) and $\beta = 2.85$ (d.).

We finally used those value of $M_\star$ which correspond to the mode number obtained for $\beta = 2.67$. In Tab. 7.2 the values of $M_\star^2$ for the four different ensembles are displayed and one can confirm that all the results of the mode number are compatible within each other, as expected. This implies that the value of M_R is constant for all the ensembles, as intended.

7.1.3. Study of autocorrelations of the topological charge

As we have discussed in the previous sections, the topological charge is a quantity severely affected by autocorrelations towards the continuum limit due to the topological barriers that appear when the continuum limit is approached.

The quenched approximation gives us an excellent opportunity to study the autocorrelations of the observable $\mathcal{C}$, since, due to the low computational cost of its simulations, it allows us to extend the MC history until all the topological sectors have been sufficiently covered. Notice, however, that it has been observed that the autocorrelations are enhanced when the simulations are purely gluonic [110].

Fig. 7.1 shows the Monte Carlo history of the observable $\mathcal{C}$ for four quenched ensembles at different lattice spacings. There it can be clearly seen that when the lattice spacing

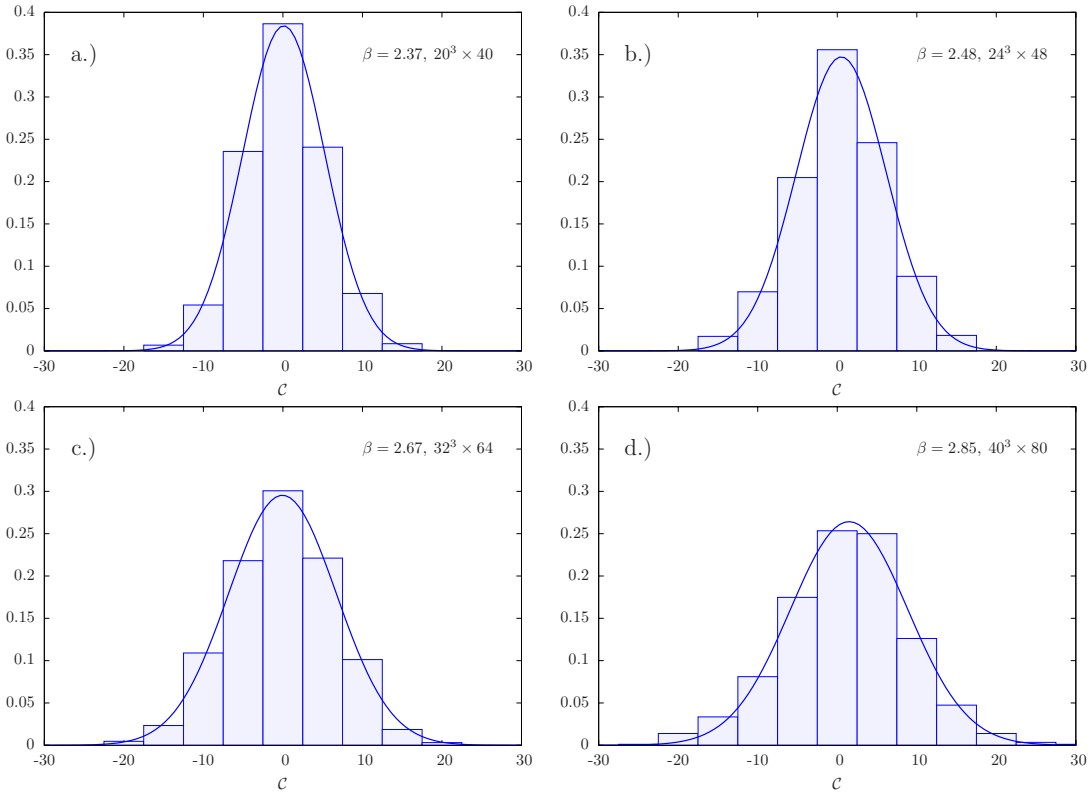

Figure 7.2.: Histograms of the observable $\mathcal{C}$ for four quenched ensembles at $\beta = 2.37$ (a.), $\beta = 2.48$ (b.), $\beta = 2.67$ (c.) and $\beta = 2.85$ (d.).

is decreased, and therefore the continuum limit is approached, the autocorrelation increases. In Fig. 7.1.d, which corresponds to the finest lattice spacing ($\beta = 2.85$), large autocorrelations are clearly visible indicating that a large number of MC trajectories is needed for such a fine lattice spacing a.

Moreover, since Fig. 7.1 shows the length of the MC histories, one can compare the order of magnitud of the length of the dynamical simulations introduced in the previous chapter and conclude that in the quenched approximation the length of the MC simulation has to be at least 10 times larger than in the dynamical case in order to obtain an $\mathcal{O}(100)$ independent measurements for comparable values of the lattice spacing. This supports the conclusion of previous studies which showed that the autocorrelation in the dynamical case is largely suppressed by the fermionic determinant [110]. However, as it was mentioned above, in the case of dynamical simulations the high computational cost prevents to extend the statistics to a desirable length.

In Fig. 7.2 one can find the histograms of the stochastic observable $\mathcal{C}$, which is closely related to the topological charge, for all the quenched ensembles at 4 different values of the lattice spacing a. In all cases we are able to construct a histogram compatible with a Gaussian distribution. However, even though the ensemble at $\beta = 2.85$ has four

β	$\langle \mathcal{A} \rangle$	τ_{int}	$\langle \mathcal{B} \rangle$	τ_{int}	$\langle \mathcal{C} \rangle$	τ_{int}
2.37	79.4(2)	0.5(1)	17.51(5)	0.5(1)	0.19(19)	0.5(1)
2.48	78.7(2)	0.5(1)	22.00(8)	0.5(1)	0.29(32)	0.4(1)
2.67	78.5(3)	0.5(1)	29.4(2)	0.5(1)	-0.61(64)	0.7(2)
2.85	78.1(4)	0.5(1)	36.5(2)	0.4(1)	0.93(0.93)	0.8(3)

Table 7.3.: Results of $\langle \mathcal{A} \rangle$, $\langle \mathcal{B} \rangle$ and $\langle \mathcal{C} \rangle$ their corresponding values of τ_{int} for quenched ensembles at four different lattice spacings.

times more MC trajectories than, for instance, $\beta = 2.48$, the corresponding histogram (Fig. 7.2.d) suggests that it is possibly lacking statistics since it is not completely symmetric. Due to the especially large autocorrelation that affects this ensemble as we already observed in the corresponding MC history (Fig. 7.1.d), it can be that $\mathcal{O}(400000)$ trajectories is still not enough to sample reliably all topological sectors. This implies that for $\beta = 2.85$ we could be underestimating the error.

7.1.4. Continuum limit of χ_∞

We have computed the topological susceptibility in the pure gluon theory using spectral projectors for four different lattice spacings. In Tab. 7.3 the results for the observables $\mathcal{A}$, $\mathcal{B}$ and $\mathcal{C}$ with their corresponding integrated autocorrelation time τ_{int} are shown. As it can be seen in Tab. 7.3, the topological susceptibility has been evaluated only in independent configurations where $\tau_{\text{int}} < 1$ for $\mathcal{C}$.

All additional information is displayed in Tab. 7.4, which includes the results of χ_∞ for each ensemble together with the number of independent measurements and the length of each simulation. In this table the increase of the autocorrelation time when the continuum limit is approached can clearly be observed.

In App. G.2 we show that the topological susceptibility approaches the continuum limit with a rate of $O(a^2)$. This demonstration makes use of the same symmetry arguments that are used to prove automatic $O(a)$ improvement for twisted mass fermions at maximal twist. In particular, all the contact terms of $O(a)$, which arise in the Symanzik expansion due to short distance singularities, do not contribute because, by construction, they are R_5^1 odd and therefore vanish in the continuum.

Consequently we have performed a linear extrapolation in $(a/r_0)^2$ to extract the continuum limit. Fig. 7.3 shows the continuum limit extrapolation of the data for the topological susceptibility which leads to a value of χ_∞ of

$$r_0^4 \chi_\infty = 0.049(6), \tag{7.3}$$

which corresponds to

$$\chi_\infty = (185.3(5.6)\ \text{MeV})^4 \tag{7.4}$$

for $r_0 = 0.5$. In the next section we comment on this result and compare it with other lattice determinations and using the experimentally known meson masses and finding a very good agreement.

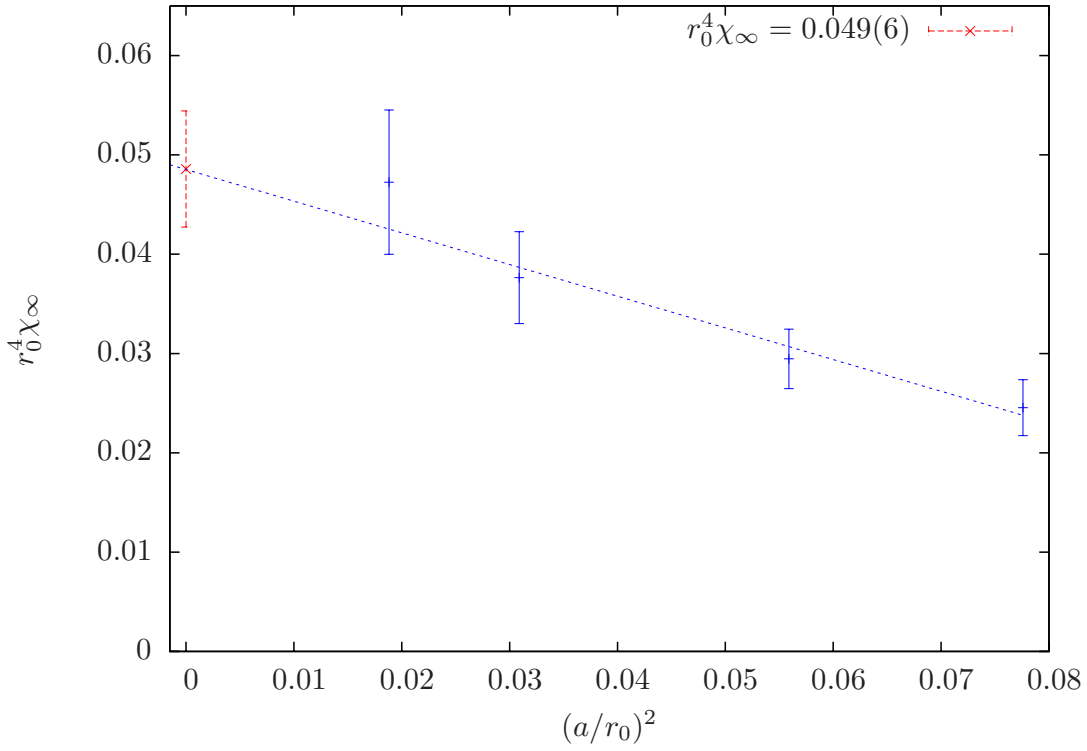

Figure 7.3.: Continuum limit extrapolation of χ_∞ as a function of $(a/r_0)^2$ for quenched ensembles.

β	N_s	N_{traj}	N_{meas}	$\langle \mathcal{C}'^2 \rangle$	$r_0^4\chi_{\text{top}}$
2.37	6	78000	769	25.9(1.3)	0.025(14)(22)(8)
2.48	6	98000	412	32.8(2.4)	0.0295(24)(16)(8)
2.67	6	132000	157	47.5(5.1)	0.0376(45)(7)(8)
2.85	6	380000	119	60.9(7.9)	0.0485(70)(4)(18)

Table 7.4.: Results of χ_{top} for the continuum limit in the pure gauge theory. N_s represents the number of stochastic sources whereas N_{meas} is the number of evaluated configurations and N_{traj} gives the corresponding number of thermalized MC trajectories. The errors quoted of χ_{top} are statistical, coming from Z_P/Z_S and from r_0/a respectively.

7.2. Witten-Veneziano formula

One of the main goals of this chapter was to attempt a first test of the continuum limit scaling behavior of the topological susceptibility in the Yang-Mills theory and to find a continuum limit value of the topological susceptibility in order to test the Veneziano-Witten relation.

The results of the meson masses presented in Ref. [115], which are needed for such a test, were computed using twisted mass ensembles at maximal twist whose physical situation we aimed to match in quenched simulations. Thus if we compute the left-hand side of Eq. (7.1) using the value of the masses given in Ref. [115] for the ensemble B55.32, we can directly test the Witten-Veneziano relation.

Tab. 7.5 shows the needed meson masses in lattice units and the result of the left-hand side of Witten-Veneziano formula obtained with these masses. It also includes our continuum limit extrapolation of the topological susceptibility given in Eq. (7.3). If we compare both results we find a very good agreement.

am_η	$am_{\eta'}$	am_K	af_π	$r_0^4\chi_\infty$
0.249(14)	0.60(10)	0.22799(34)	0.0365	
$r_0^4 \frac{f_\pi^2}{2N_f}\left(m_\eta^2 + m_{\eta'}^2 - 2m_K^2\right) = 0.044(4)$				0.049(6)

Table 7.5.: Lattice results of the meson masses and the corresponding left-hand side of the Witten-Veneciano formula. χ_∞ is the topological susceptibility in the pure gauge theory computed using spectral projectors.

Moreover if we directly compute the left-hand side of Eq. (7.1) using the experimental results [116] for the meson masses and the pion decay constant and compare it with our result given in Eq. (7.4) we again find a very good agreement as it can be seen in Tab. 7.6

am_η	$am_{\eta'}$	am_K	af_π	χ_∞
547.85(2)	957.78(6)	497.61(2)	92.4	
$\frac{f_\pi^2}{2N_f}\left(m_\eta^2 + m_{\eta'}^2 - 2m_K^2\right) = (180\text{ MeV})^4$				$(185(6)\text{ MeV})^4$

Table 7.6.: Experimental results of the meson masses and the corresponding left-hand side of the Witten-Veneciano formula. χ_∞ is the topological susceptibility in the pure gauge theory computed using spectral projectors. All the values are in MeV in the $\overline{\text{MS}}$ scheme at 2 GeV

On the lattice there are several results available of χ_∞ which can be directly compared with our finding. Using the index theorem and a formulation which respects chiral symmetry, in Ref.[112] a value of $\chi_\infty = 191(5)$MeV is found using $r_0 F_K$ to set the scale. If we use $r_0 = 0.5$, as we do to convert our result to MeV, then $\chi_\infty = 194.5(2.4)$. Using spectral projectors, a value of $\chi_\infty = 196.5(5.1)$ is found in Ref.[107]. Both results are compatible with our determination.

We can then conclude that our result supports the mechanism, expressed in the Witten-Veneziano relation, that the unexpectedly large mass of the η' meson is directly related to the chiral anomaly and therefore to the topological properties of the underlying gluon field configurations.

Conclusions

This dissertation has addressed conceptual questions related to spontaneous chiral symmetry breaking and topology in quantum chromodynamics, our theory of the strong interaction.

The basic tool for our investigation has been lattice QCD. In particular, we made use of the recently introduced spectral projector method [59] which offers a new approach to the study of observables related to chiral symmetry breaking and topology. The bridge to these questions is that the spectral projector method allows us to compute the low lying spectrum of the Dirac operator, which is directly linked via the Banks-Casher relation to the chiral condensate and through the zeromodes to the topological susceptibility. A major advantage of the spectral projector method is that it allows us to compute the spectrum in an affordable and efficient way. As a main result of our computations, we have performed a calculation of the chiral condensate, the order parameter of chiral symmetry breaking. In addition, we have studied the chiral behavior of the topological susceptibility, through which we obtained an alternative determination of the chiral condensate. Finally, we successfully performed a first test of the Witten-Veneziano relation through the calculation of the topological susceptibility in the pure gluon theory.

As said above, the Banks-Casher relation links the low lying spectrum of the Dirac operator with the chiral condensate. Thus, through the study of the spectral density, or equivalently of the mode number, i.e. the number of eigenvalues below a certain threshold parameter M, we were able to compute the chiral condensate. It is crucial for this study that the regime of the threshold parameter M is identified where the mode number shows a linear behavior in M, corresponding to the region where the spectral density is constant. One of the main subjects of this thesis has been to clearly identify this linear regime in order to obtain a reliable determination of the chiral condensate.

Finite volume effects (FVE) are a very important source of systematic errors in lattice QCD. We have therefore carried out an investigation of the dependence of the chiral condensate on the volume in order to guarantee that our final results are compatible with the infinite volume results.

To this end, we studied the FVE for $N_f = 2$ mass degenerate and $N_f = 2 + 1 + 1$ flavors twisted mass fermions at maximal twist. We computed Σ at four and three different volumes respectively. As a result, we found that that the calculations must be performed on lattices with an extent $L \geq 2$ fm in order to guarantee that FVE are negligible. Since we employ finite volumes that are significantly larger than 2 fm, we can

conclude that our final result for the chiral condensate are not affected by FVE.

In order to obtain a reliable result for the chiral condensate the additional systematic errors resulting from discretization effects and from the chiral extrapolation have to be investigated. To this end we have presented the results of the computation of the chiral condensate for several quark masses and at three different lattice spacings. This allowed us to perform a chiral extrapolation guided by the description of the quark mass dependence of the chiral condensate given by chiral perturbation theory. Once we had obtained the result for the chiral condensate in the chiral, i.e. massless limit we were able to perform a continuum limit of chirally extrapolated data. This study was independently done for $N_f = 2$ and $N_f = 2 + 1 + 1$ twisted mass fermions at maximal twist and both results were discussed and presented in this thesis.

The analysis of the systematic uncertainties of our lattice QCD calculation has been indispensable to achieve a reliable value for the chiral condensate since they were rather significant. We concluded that the largest systematic error stems from the uncertainty in the location of the linear regime of the mode number with respect to the threshold parameter M. Thus we suggested that in order to improve the accuracy of the chiral condensate, it would be more effective to compute the mode number at additional values of M than to increase statistics.

We finally obtained the following continuum limit result for $N_f = 2$

$$r_0\Sigma^{1/3} = 0.685(16)(32)$$
$$\Sigma^{1/3} = 281(7)(13)\ [\text{MeV}]$$

and for the $N_f = 2 + 1 + 1$ case

$$r_0\Sigma^{1/3} = 0.683(19)(18)$$
$$\Sigma^{1/3} = 280(8)(7)\ [\text{MeV}]$$

where in both cases the first error corresponds to a combination in quadrature of the statistical error, Z_P and, if applied, r_0 and the second error represents the uncertainty in the fit range of M. The values quoted in MeV correspond to the $\overline{\text{MS}}$ scheme at 2 GeV.

We compared our final results, which included the statistical and all systematic errors, with other continuum limit lattice calculations of the chiral condensate, obtaining a very good agreement.

As an important theoretical part of this thesis, we have proven that the continuum limit of the chiral condensate defined in terms of density chain correlators, scales like $\mathcal{O}(a^2)$, i.e. the automatic $\mathcal{O}(a)$ improvement, which characterizes maximally twisted mass fermions, is not spoiled by the short distance singularities that affect this observable. We have explicitly computed the contact terms that arise in the Symanzik expansion and written them in terms of the original density chain through non-singlet Ward-Takahashi identities which were computed specifically for this proof. This theoretical study of the short-distance singularities and its connection to the Symanzik expansion of certain observables, which determines the scaling towards the continuum limit, fills a gap in the

literature, where this issue had not been discussed so far.

As a second main goal of this thesis we have studied the chiral behavior of the topological susceptibility χ_{top} for $N_f = 2$ and $N_f = 2 + 1 + 1$ flavors of quark. Using density chains a theoretically clean definition of the topological susceptibility can be given which is free of short-distance singularities and which leads to the correct continuum limit. This definition can also be applied to Wilson-type fermions. Employing the spectral projector method to evaluate the topological susceptibility from this definition, reduces considerably the computational cost of the calculation and allows for the possibility of its application to large volumes.

We have computed the topological susceptibility for several values of the quark mass at three different lattice spacings for $N_f = 2 + 1 + 1$ flavors of twisted mass fermions at maximal twist. Chiral perturbation theory predicts the suppression of the topological susceptibility χ_{top} when the chiral limit is approached. Moreover it relates the quark mass dependence of the topological susceptibility to the chiral condensate in the chiral limit. Consequently, through the study of the chiral behavior of χ_{top}, we were able to extract an alternative determination of the chiral condensate which turned out to be fully compatible with our previous result using the mode number, although it has larger uncertainty, as expected.

The calculation of the topological susceptibility presents additional difficulties which prevent us from reliably estimating the systematic uncertainty. The reason is that we observed a large autocorrelation of the topological charge in the Monte Carlo simulations. Thus the transition between topological sectors is suppressed when the continuum limit is approached, generating the so-called topological barriers.

The stochastic observable $\mathcal{C}$, which enters the calculation of the topological susceptibility and which is closely related to the topological charge, can be used as a very good monitor to study autocorrelations and examine whether the lattice simulation has a sufficiently long Monte Carlo history such that quantities, which are related to the topological charge, can be reliably computed.

It is our observation from the study of the autocorrelation time of the stochastic observable $\mathcal{C}$ that the nowadays typical Monte Carlo histories which involve about 5000 trajectories in MC time, do not cover the topological sectors appropriately. This implies that the results obtained using the currently accessible ensembles do not allow to reliably estimate the systematic effects which correspond to the incomplete sampling of the topological sectors.

However, using an ensemble with a substantially larger, about four times, number of Monte Carlo trajectories, we found that all topological sectors were sampled and the distribution of the topological charge is reliable, indicated by the fact that the distribution is symmetric and has a zero mean. Thus, we estimate that the length of the MC simulation should be around four times larger than the currently employed ones.

Nevertheless, the fact that the chiral condensate obtained through a χPT fit is compatible with our previous estimate implies that the results obtained are reasonable, although, most probably, the errors have been underestimated. The data was not sensitive to higher order terms in χPT and therefore only leading order χPT was applied. In addition we performed a finite volume effect study of the topological susceptibility and found that

FVE are negligible even for small lattices with an extent $L = 1.3$ fm, at least for the statistics we presently have for this quantity.

As a third result, we successfully computed the continuum limit of the topological susceptibility in the pure gauge theory in order to test the Witten-Veneziano formula. We generated four gauge ensembles in the quenched approximation at different lattice spacings in order to perform a continuum limit extrapolation. We aimed to match the physical situation of the dynamical ensembles which were used to compute the meson masses, such as the action, the same physical volume and the quark mass.

Due to the low computational cost of the pure gauge field generation, in this case we were able to overcome the problem of autocorrelations which we had to face in the dynamical case presented above and we extended the simulations to achieve a sufficient statistics to reliably estimate the uncertainties of the topological susceptibility.

The renormalization of the topological susceptibility using the representation given by spectral projectors when a formulation which does not respect chiral symmetry is applied, as is the case for the twisted mass formulation, implies the use of the ratio of renormalization constants Z_P/Z_S. This ratio of renormalization constants can be obtained again by certain observables calculated by the spectral projector method. We tested this approach in this thesis and applied this method to compute Z_P/Z_S in the quenched case.

This allowed us to find a very good agreement between our result for the quenched topological susceptibility and its relation to the kaon, η and η' meson masses (computed on the lattice using twisted mass fermions), as predicted by Witten and Veneziano. We also included a comparison of the quenched topological susceptibility with the experimentally determined meson masses and again found fully compatible results. Thus, our results strongly support the mechanism which relates the unexpectedly large mass of the η' meson to the topological fluctuations of the gauge field configurations.

In summary, we have successfully applied the spectral projector method to compute several observables which are directly related to the spontaneous breaking of chiral symmetry and topology of QCD. We first presented a precise and reliable continuum determination of the chiral condensate for $N_f = 2$ and $N_f = 2 + 1 + 1$ flavors of twisted mass fermions at maximal twist. We have shown that our results are in good agreement with other lattice determinations. In addition we have computed the topological susceptibility in the dynamical case and extracted a compatible value of the chiral condensate through the study of its chiral behavior. We finally perform a continuum limit extrapolation of the topological susceptibility in the pure gluonic theory which allowed us to test the Witten-Veneziano formula. Our result confirms the validity of this relation.

Thus, we believe that the definition of the chiral condensate and the topological susceptibility through density chains and its practical computation through the mode number using the method of spectral projectors offers a conceptually clean and practically affordable way to compute these important quantities from lattice QCD calculations.

Acknowledgments

First of all I would like to thank my scientific supervisor, Dr. Karl Jansen, for offering me the great opportunity to do my PhD under his supervision. I am very thankful for all his support and for his infinite patience during these years. I am truly grateful for all the insightful discussions which enormously contributed to my development as a scientist, and deeply appreciate his involvement and constant supervision which guided the completion of this work. I am also thankful for the nice work atmosphere that he always builds around him.

I am deeply thankful also to my academic supervisor, Prof. Michael Müller-Preußker, for giving me the possibility of doing my PhD at the Humbold-Universität zu Berlin. I am especially grateful for his kind support and encouragement during one of the most challenging moments of this period, which was for me teaching in a foreign language. I am also truly grateful for all the useful discussions and comments which improved this work and his guidance and support through all the bureaucratic processes which led to the realization of this PhD thesis.

I am especially indebted to Dr. Krzysztof Cichy for all the long and insightful discussions which encouraged me every day and helped me develop scientifically. I am extremely thankful for his patient and constant support and for closely following the supervision of this thesis. I also would like to thank him for the crosschecks of all the results which are presented in this thesis.

I would like to thank to all the scientists I have had the pleasure to collaborate with. I would like to make a special mention of Dr. Gregorio Herdoíza and Dr. Andrea Shindler for all the enlightening discussions with them from which I have learned so much. I have enormously profited from their knowledge and experience.

I would like to acknowledge many other scientists for all the discussions which helped the development of this project. In particular, I would like to thank Dr. Vincent Drach, Prof. Carsten Urbach, Dr. Alberto Ramos, Prof. Giancarlo Rossi, Prof. Marc Wagner, and Prof. Rainer Sommer among others.

I am deeply thankful to all my officemates, with whom I shared so many discussions, laughs and good moments, especially to Attila Nagy and Pan Kessel. In particular I would like to thank Attila Nagy who strongly supported me during our teaching experience.

Without doubt, I would like to thank to all my friends and colleagues in DESY-Zeuthen and the Humboldt-Universität zu Berlin. I am truly grateful for all the discussions, and the nice moments that we have shared during all these years. They all have contributed to make this period of my life a sweet moment that I will always remember. Especially I

would like to thank, at a more personal level, to Alberto Ramos, Vincent Drach, Gavin Cullen, Patrick Fritzsch, Attila Nagy, Pan Kessel, Marina Marinkovich, Jennifer González López, Dirk Hesse, Simone Alioli and Gregorio Herdoíza for making these years a bit more special in their company. In particular I would like to thank Alberto Ramos for making me feel a little bit more at home and the countless times he help me and answer my many times trivial questions, especially during the preparation for the defense of this thesis.

In Berlin I had the pleasure to get to know my dear friends Matxalen Rey Abasolo, Maia García Vergniory and Itziar Goikoetxea, with whom I have shared all these years, and who always were there, encouraging me when I most needed it. I am truly thankful to them for all their support. Eskerrik asko denagatik.

I am certainly thankful to my friend, and former summer student at DESY-Zeuthen, Rosa Clavero, who encouraged me to contact Dr. Karl Jansen to write my Masters thesis within his research group and which ultimately resulted in this dissertation.

For always being there, I am very grateful to all my friends from Madrid, and especially my oldest and best friends, Teresa Talaván Paniagua, Iris Garbayo de la Piedad, Layla Calero Navarro and María Elena Sánchez Garciafilia who are always by my side, despite the distance, giving me the support that I need.

Very especially, I would like to thank Michael Donnellan, my biggest support, for all these years, for always making me laugh when I most needed it and always encouraging me with kindness and tenderness. Thanks for all the moments which gave me the energy to finish, and for always being there.

I am truly indebted to my parents Luis García Rojas and Lourdes Ramos Fernández-Torrecilla, and to Manuela Ruiz Castro. I am profoundly grateful for their constant support and encouragement, which gave me the strength to make the decisions which led me to this moment. I am enormously thankful to them for always being there, by my side, giving me the support that I needed with love and tenderness during my whole life.

I would like to make a special mention to my family for all the advice, the support and the affection that I always find when I am with them. Very especially I would like to thank my brother, Carlos García Ramos, for all the support over the years and his infinite kindness. Muchísimas gracias.

I would like to thank the SFB-TR9 for the financial support and together with the Humboldt-Universität zu Berlin for making this Ph.D. thesis possible. I am also grateful to the NIC group in DESY-Zeuthen for providing a working space for me.

All the numerical part of this work has been carried out on the PC-Farm in DESY-Zeuthen with the support of the NIC-group, and in the supercomputers JUGENE and SUPERMUC, located in Jülich Supercomputing Centre in Germany and Leibniz-Rechenzentrum near Munich respectively. I would like to thank them for the opportunity to use their resources and for the assistance provided by their technical support.

I am thankful to the Graduiertekolleg “Masse Spektrum Symmetrie" (GK 1504) for providing additional financial support for travelling and for the organization and support of the block courses from which I highly profited.

Finally, I would like to thank Silvia Richter for all her help with the bureaucracy regarding this thesis.

APPENDIX A

Notation and Symmetries

A.1. Notation

Pauli matrices

The Pauli matrices σ_k are given by

$$\sigma_1 = \begin{pmatrix} 0 & 1 \\ 1 & 0 \end{pmatrix}, \quad \sigma_2 = \begin{pmatrix} 0 & -i \\ i & 0 \end{pmatrix}, \quad \sigma_3 = \begin{pmatrix} 1 & 0 \\ 0 & -1 \end{pmatrix}, \tag{A.1}$$

which satisfy the following relations

$$\{\sigma_i, \sigma_j\} = 2\delta_{ij}, \qquad [\sigma_i, \sigma_j] = i2\epsilon_{ijk}\sigma_k. \tag{A.2}$$

When we refer to the flavor group we denote the Pauli matrices as τ^a where $a = 1, 2, 3$ and we often refer to the identity $\mathbb{1}$ as τ^0. Let us also introduce other variants such as

$$\tau^{\pm} = \frac{1}{2}(\tau^1 \pm i\tau^2), \quad \tau^{\uparrow} = \frac{1}{2}(\tau^0 + \tau^3), \quad \tau^{\downarrow} = \frac{1}{2}(\tau^0 - \tau^3), \tag{A.3}$$

which correspond to

$$\tau^{+} = \begin{pmatrix} 0 & 1 \\ 0 & 0 \end{pmatrix}, \quad \tau^{-} = \begin{pmatrix} 0 & 0 \\ 1 & 0 \end{pmatrix}, \quad \tau^{\uparrow} = \begin{pmatrix} 1 & 0 \\ 0 & 0 \end{pmatrix}, \quad \tau^{\downarrow} = \begin{pmatrix} 0 & 0 \\ 0 & 1 \end{pmatrix}. \tag{A.4}$$

When we add additional flavors to the theory we use another representation τ^{ab} using two indices ab which correspond to the flavors involved. τ^{ab} represents then a $N_f \times N_f$ matrix whose elements are $\tau^{ab}_{ij} = 1$ for $ij = ab$ and 0 otherwise. This corresponds to τ^{+} of a subalgebra $SU(2)$ which involves only two flavors a and b.

The matrices τ^{ab} satisfy the following commutation relations

$$[\tau^{ab}, \tau^{cd}] = \{\tau^{ab}, \tau^{cd}\} = \delta_{bc}\tau^{ad}. \tag{A.5}$$

Let us give an example in $SU(3)$ to clarify the notation. In this particular case we can construct τ^{12}, τ^{23} and τ^{13} which would correspond to

$$\tau^{12} = \begin{pmatrix} 0 & 1 & 0 \\ 0 & 0 & 0 \\ 0 & 0 & 0 \end{pmatrix}, \quad \tau^{23} - = \begin{pmatrix} 0 & 0 & 0 \\ 0 & 0 & 1 \\ 0 & 0 & 0 \end{pmatrix}, \quad \tau^{13} = \begin{pmatrix} 0 & 0 & 1 \\ 0 & 0 & 0 \\ 0 & 0 & 0 \end{pmatrix}, \tag{A.6}$$

which can also be written as a representation of the subgroup SU(2)

$$\tau^{12} = \begin{pmatrix} 0 & 1 \\ 0 & 0 \end{pmatrix}_{12}, \quad \tau^{23} - = \begin{pmatrix} 0 & 1 \\ 0 & 0 \end{pmatrix}_{23}, \quad \tau^{13} = \begin{pmatrix} 0 & 1 \\ 0 & 0 \end{pmatrix}_{13} \tag{A.7}$$

In the case of twisted mass we introduce an extended representation to include the doublers and we denote as λ^{ab}. In this case λ^{ab} is a $2N_f \times 2N_f$ matrix acting in flavor space.

Dirac matrices

We use the chiral representation of the Dirac matrices which is given by

$$\gamma_\mu = \begin{pmatrix} 0 & e_\mu \\ e_\mu^\dagger & 0 \end{pmatrix}, \tag{A.8}$$

where e_μ are the 2×2 matrices $e_0 = -\mathbb{1}$ and $e_k = -i\sigma_k$.

The Dirac matrices satisfy

$$\gamma_\mu = \gamma_\mu^\dagger = \gamma_\mu^{-1}, \qquad \{\gamma_\mu, \gamma_\nu\} = 2\delta_{\mu\nu}. \tag{A.9}$$

Furthermore we can define

$$\gamma_5 = \gamma_0\gamma_1\gamma_2\gamma_3 \quad \text{or more explicitly} \quad \gamma_5 = \begin{pmatrix} 1 & 0 \\ 0 & -1 \end{pmatrix}, \tag{A.10}$$

which fulfills the following properties:

$$\gamma_5 = \gamma_5^\dagger, \quad \gamma_5^2 = 1, \quad \{\gamma_\mu, \gamma_5\} = 0. \tag{A.11}$$

We can also define the hermitian matrices $\sigma_{\mu\nu} = \frac{i}{2}[\gamma_\mu, \gamma_\nu]$ explicitly given by

$$\sigma_{0k} = \begin{pmatrix} \sigma_k & 0 \\ 0 & -\sigma_k \end{pmatrix}, \qquad \sigma_{ij} = -\epsilon_{ijk} \begin{pmatrix} \sigma_k & 0 \\ 0 & \sigma_k \end{pmatrix}. \tag{A.12}$$

Covariant lattice derivatives

The gauge covariant lattice derivative in an infinite lattice acting on a spinor field $\psi(x)$ is defined as follows

$$\overrightarrow{\nabla}_\mu \psi(x) = \frac{1}{a}[U(x,\mu)\psi(x+a\hat{\mu}) - \psi(x)], \tag{A.13}$$

$$\overrightarrow{\nabla}^\star_\mu \psi(x) = \frac{1}{a}[\psi(x) - U^\dagger(x-a\hat{\mu},\mu)\psi(x-a\hat{\mu})]. \tag{A.14}$$

If it acts on the left side then it is defined as

$$\overline{\psi}\overleftarrow{\nabla}_\mu = \frac{1}{a}[\overline{\psi}(x+a\hat{\mu})U^\dagger(x,\mu) - \overline{\psi}(x)], \tag{A.15}$$

$$\overline{\psi}\overleftarrow{\nabla}_\mu = \frac{1}{a}[\overline{\psi}(x) - \overline{\psi}(x-a\hat{\mu})U(x-a\hat{\mu},\mu)]. \tag{A.16}$$

The symmetric derivatives that appears in the definition of the Dirac operator take the following form

$$\frac{1}{2}(\overrightarrow{\nabla}_\mu + \overrightarrow{\nabla}^\star_\mu)\psi(x) = \frac{1}{2a}[U_\mu(x)\psi(x+\hat{\mu}) - U^\dagger_\mu(x-\hat{\mu})\psi(x-\hat{\mu})], \tag{A.17}$$

$$\overline{\psi}(x)\frac{1}{2}(\overleftarrow{\nabla}_\mu + \overleftarrow{\nabla}^\star_\mu) = \frac{1}{2a}[\psi(x+\hat{\mu})U^\dagger_\mu(x) - \psi(x-\hat{\mu})U_\mu(x-\hat{\mu})]. \tag{A.18}$$

In the same way we can define the covariant lattice D'Alambert operator

$$\overrightarrow{\nabla}^\star_\mu\overrightarrow{\nabla}_\mu\psi(x) = \frac{1}{a^2}[U_\mu(x)\psi(x+\hat{\mu}) + U^\dagger_\mu(x-\hat{\mu})\psi(x-\hat{\mu}) - 2\psi(x)], \tag{A.19}$$

$$\overleftarrow{\nabla}^\star_\mu\overleftarrow{\nabla}_\mu\psi(x) = \frac{1}{a^2}[\overline{\psi}(x+\hat{\mu})U_\mu(x) + \overline{\psi}(x-\hat{\mu})U^\dagger_\mu(x-\hat{\mu}) - 2\psi(x)]. \tag{A.20}$$

A.2. Symmetries

A.2.1. Discrete Symmetries

Charge Conjugation

Before introducing the charge conjugation symmetry, which transforms particles into antiparticles, we need to introduce the charge conjugation matrix C

$$C\gamma_\mu C^{-1} = -\gamma^\star_\mu, \tag{A.21}$$

which acts on the Dirac indices. If we use the explicit chiral representation of the gamma matrices, as previously defined, then we can define C in the following way.

$$C = i\gamma_0\gamma_2. \tag{A.22}$$

The charge conjugation matrix obeys $C = C^{-1} = C^\dagger = -C^T$.

Once the properties of C have been established, the charge conjugation transformation can be introduced, which is given by

$$\mathcal{C}: \begin{cases} U_\mu(n) & \to & U_\mu(n)^\star = (U_\mu^\dagger)^T, \\ \psi(n) & \to & C^{-1}\overline{\psi}(n)^T, \\ \overline{\psi}(n) & \to & -\psi(n)^T C, \end{cases} \tag{A.23}$$

where T means transposition and acts on color and Dirac indices.

Parity and time-reversal transformation

The charge conjugation, as the gauge symmetry or the discrete rotations and translations, are symmetries of both, the Wilson and the twisted mass action. However the parity transformations that leave the action invariant differ for both actions.

Wilson fermions

The ordinary Parity $\mathcal{P}$ and time reversal $\mathcal{T}$ transformations which leave the Wilson action invariant are, respectively,

$$\mathcal{P}: \begin{cases} U_\mu(x_0, \mathbf{x}) & \to & U_\mu(x_0, -\mathbf{x}) \\ U_\mu(x_0, \mathbf{x}; k) & \to & U_\mu^{-1}(x_0, -\mathbf{x} - \mathbf{a}\hat{\mathbf{k}}; k), \qquad k = 1,2,3 \\ \psi(x_0, \mathbf{x}) & \to & \gamma_0 \psi(x_0, -\mathbf{x}), \\ \overline{\psi}(x_0, \mathbf{x}) & \to & \overline{\psi}(x_0, -\mathbf{x})\gamma_0. \end{cases} \tag{A.24}$$

$$\mathcal{T}: \begin{cases} U_\mu(x_0, \mathbf{x}) & \to & U_\mu(-x_0, \mathbf{x}), \\ U_\mu(x_0, \mathbf{x}; k) & \to & U_\mu(-x_0, \mathbf{x}; k), \qquad k = 1,2,3 \\ \psi(x_0, \mathbf{x}) & \to & i\gamma_0\gamma_5 \psi(-x_0, \mathbf{x}), \\ \overline{\psi}(x_0, \mathbf{x}) & \to & \overline{\psi}(-x_0, \mathbf{x}) i\gamma_0\gamma_5. \end{cases} \tag{A.25}$$

Twisted mass fermions

In the case of the twisted mass Wilson action the ordinary parity is not a symmetry of the action. In order to find a symmetry, the parity transformation has to be combined with a rotation in flavor in the following way

$$\mathcal{P}_f^{1,2}: \begin{cases} U_\mu(x_0, \mathbf{x}; 0) & \to & U_\mu(x_0, -\mathbf{x}; 0), \\ U_\mu(x_0, \mathbf{x}; k) & \to & U_\mu^{-1}(x_0, -\mathbf{x} - \mathbf{a}\hat{\mathbf{k}}; k), \qquad k = 1,2,3 \\ \chi(x_0, \mathbf{x}) & \to & i\gamma_0 \tau^{1,2} \chi(x_0, -\mathbf{x}), \\ \overline{\chi}(x_0, \mathbf{x}) & \to & -\overline{\chi}(x_0, -\mathbf{x}) i\gamma_0 \tau^{1,2}, \end{cases} \tag{A.26}$$

or it we need in addition a change in the sign of the twisted mass term

$$\tilde{\mathcal{P}} = \mathcal{P} \times [\mu \to -\mu]. \tag{A.27}$$

Equivalently the time reversal transformations are given by

$$\mathcal{T}_f^{1,2} : \begin{cases} U_\mu(x_0,\mathbf{x}) & \to & U_\mu^{-1}(-x_0-a,\mathbf{x}), \\ U_\mu(x_0,\mathbf{x};k) & \to & U_\mu(-x_0,\mathbf{x};k), \\ \chi(x_0,\mathbf{x}) & \to & i\gamma_0\gamma_5\tau^{1,2}\chi(x_0,-\mathbf{x}), \\ \overline{\chi}(x_0,\mathbf{x}) & \to & -\overline{\chi}(x_0,-\mathbf{x})i\gamma_0\gamma_5\tau^{1,2}, \end{cases} \qquad k=1,2,3 \tag{A.28}$$

or

$$\tilde{\mathcal{T}} = \mathcal{T} \times [\mu \to -\mu]. \tag{A.29}$$

Due to its relation with the automatic $\mathcal{O}(a)$ improvement of the twisted mass fermions at maximal twist, other relevant symmetries are the discrete chiral symmetry $\mathcal{R}_5^{1,2}$ which is defined as follows

$$\mathcal{R}_5^{1,2} : \begin{cases} \chi(x_0,\mathbf{x}) & \to & i\tau^{1,2}\gamma_5\chi(x_0,\mathbf{x}), \\ \overline{\chi}(x_0,\mathbf{x}) & \to & i\overline{\chi}(x_0,\mathbf{x})\gamma_5\tau^{1,2}, \end{cases} \tag{A.30}$$

and the symmetry $\mathcal{D}$, which basically counts the dimension of an operator

$$\mathcal{D} : \begin{cases} U(x;\mu) & \to & U^\dagger(-x-a\hat{\mu};\mu), \\ \chi(x) & \to & e^{3i\pi/2}\chi(-x) \\ \overline{\chi}(x) & \to & \overline{chi}(-x)e^{3i\pi/2}. \end{cases} \tag{A.31}$$

The combine symmetry $\mathcal{R}_5^{1,2} \times \mathcal{D} \times [\mu \to -\mu]$ is a symmetry of the action.

The proof of $\mathcal{O}(a)$ improvement can also be derived using a twisted parity symmetry $\mathcal{P}_{\frac{\pi}{2}}$ defined as

$$\mathcal{P}_{\frac{\pi}{2}} : \begin{cases} U_\mu(x_0,\mathbf{x};0) & \to & U_\mu(x_0,-\mathbf{x};0), \\ U_\mu(x_0,\mathbf{x};k) & \to & U_\mu^{-1}(x_0,-\mathbf{x}-\mathbf{a}\hat{\mathbf{k}};k), \\ \chi(x_0,\mathbf{x}) & \to & \gamma_0(i\gamma_5\tau^3)\chi(x_0,-\mathbf{x}), \\ \overline{\chi}(x_0,\mathbf{x}) & \to & -\overline{\chi}(x_0,-\mathbf{x})(i\gamma_5\tau^3)\gamma_0. \end{cases} \qquad k=1,2,3 \; . \tag{A.32}$$

A.2.2. Hermiticity

Almost all the lattice Dirac operators are γ_5 hermitian, i.e. the relation

$$\gamma_5 D \gamma_5 = D^\dagger \tag{A.33}$$

is fulfilled by most of them. This property has important consequences, specially in the Monte Carlo simulations, since the eigenvalues of any γ_5-hermitian operator are either real or come in conjugate pairs, which corresponds to a real determinant. An exception is, among others, the introduction of a non-zero chemical potential which gives a complex determinant making imposible the application of the usual techniques of the MC method. This is known as the sign problem, and a big effort is being put at the moment into solving it.

Wilson type fermions

In particular the kernel of the Wilson Dirac operator in the free theory fullfils the following γ_5-hermiticity relation

$$\gamma_5 K_W^\dagger(z,y)\gamma_5 = K_W(y,z), \tag{A.34}$$

The relation between the Wilson kernel and its corresponding propagator $S_W(x,y)$ is given by

$$K_W(x,y)S_W(y,z) = \delta_{xz}, \tag{A.35}$$

Combining Eq. (A.35) and Eq. (A.34) the γ_5-hermiticity relation of the propagator can be derive

$$\gamma_5 S_W^\dagger(z,y)\gamma_5 = S_W(y,z). \tag{A.36}$$

Twisted mass Wilson type fermions

In the case of the twisted mass Wilson operator, which is directly related to the Wilson operator with the addition of a twisted mass term in the following way

$$K_{tm}(x,y) = K_W(x,y) + i\mu\gamma_5\tau^3\delta_{xy}, \tag{A.37}$$

the γ_5 hermiticity relation slightly differs from the case of Wilson fermions. In this particular case it is necessary to make explicit the flavor content of the doublets $\chi, \overline{\chi}$

$$\chi = \begin{pmatrix} u \\ d \end{pmatrix}, \qquad \overline{\chi} = (\overline{u}, \overline{d}). \tag{A.38}$$

Thus we need to explicit write the kernel which corresponds to each flavor

$$\gamma_5 K_{tm}^{\dagger u}(x,y)\gamma_5 = K_{tm}^d(y,x), \tag{A.39}$$

$$\gamma_5 K_{tm}^{\dagger d}(x,y)\gamma_5 = K_{tm}^u(y,x), \tag{A.40}$$

since a change of flavor of the kernel is involved in the relation.

Again we apply the relation between the kernel and the propagator to construct the γ_5 hermiticity relation for the propagators,

$$K_{tm}^u(z,y)S_{tm}^u(y,z) = \delta_{xz}, \quad K_{tm}^d(z,y)S_{tm}^d(y,z) = \delta_{xz} \tag{A.41}$$

which is finally given by

$$\gamma_5 S_{tm}^{\dagger u}(z,y)\gamma_5 = S_{tm}^d(y,z), \tag{A.42}$$

$$\gamma_5 S_{tm}^{\dagger d}(z,y)\gamma_5 = S_{tm}^u(y,z), \tag{A.43}$$

where, as in the case of the kernel, a change of flavor appears.

APPENDIX B

Locality of the overlap operator

Throughout the process that led us to write this work, we studied the locality of the overlap operator in detail and we would like to briefly summarize our results here.

The overlap operator is not strictly local since it does not fullfil

$$D\psi(n) = \sum_m D(n,m)\psi(m) \tag{B.1}$$
$$D(n,m) = 0, \qquad \|n-m\| = \epsilon,$$

where n, m are lattice points. But it can be proven [117] that it is local if a more general definition of locality is given

$$\|D(n,m)\| \leq C\, \mathrm{e}^{\hat{\rho}\|n-m\|}, \tag{B.2}$$

where the operator is local if the norm decays exponentially with the distance. However a numerical study where it is shown that the strict locality is recovered in the continuum limit was missing in the literature.

We start with the definition of the *taxi-driver* distance, important because we work with periodic boundary conditions,

$$\|x\|_{1,N} \equiv \sum_\mu \min\{|x_\mu|, |N - x_\mu|\}, \quad 0 \leq x_\mu < N \tag{B.3}$$

and the norm of the operator

$$\|D(n,m)\| \equiv \max_{1\leq\mu\leq 4} \sum_{\nu=1}^{4} |D(n,m)_{\mu,\nu}| \tag{B.4}$$

Since for the same *taxi-driver* distance we have different values for $\|D\|$ due to the different

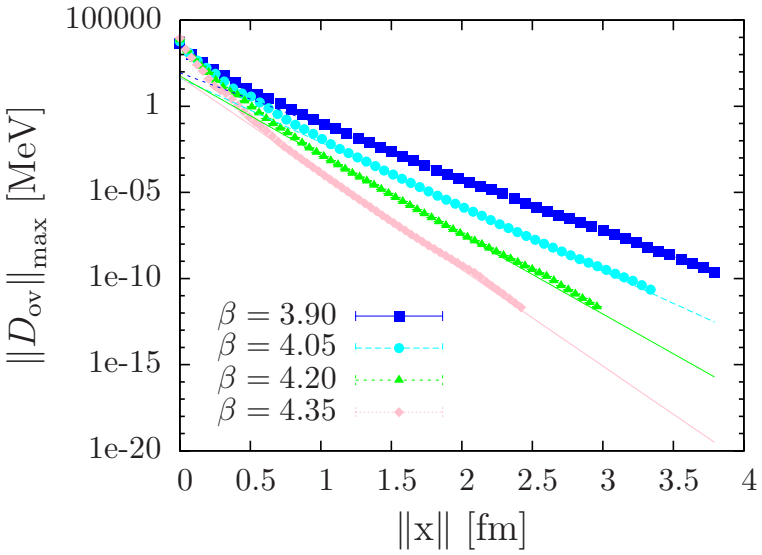

Figure B.1.: Exponential decay of the maximum norm of the overlap Dirac operator at four different lattice spacings for N_f=2 and fixed volume and quark mass

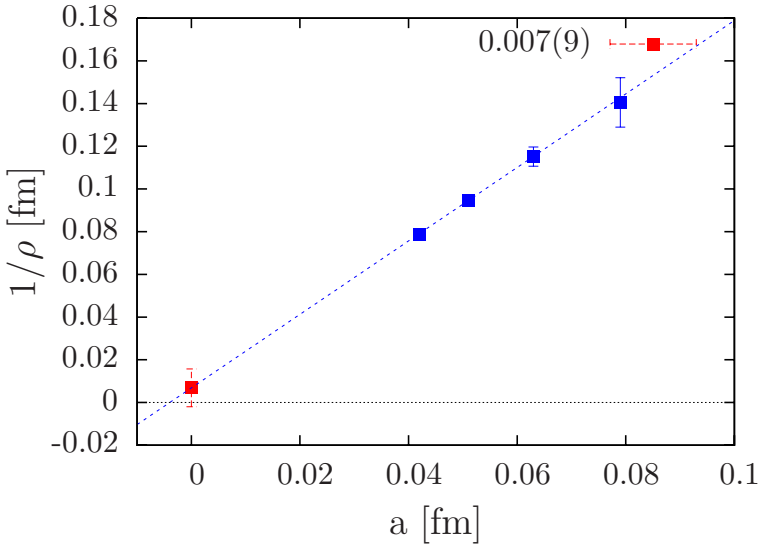

Figure B.2.: Continuum limit scaling of the inverse decay rate ($1/\rho$) for N_f=2 at fixed volume and quark mass.

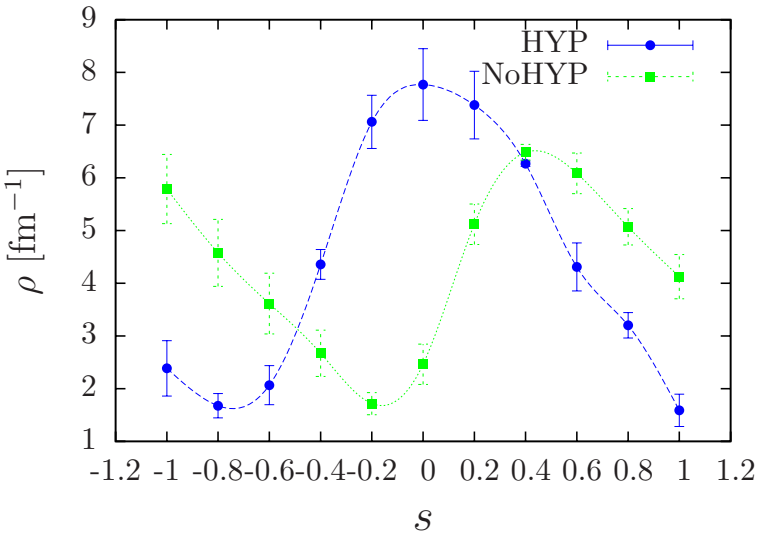

Figure B.3.: Dependence of the decay rate ρ on the value of the s parameter for HYP and non HYP smeared configurations. This ensemble corresponds to N_f=2 at $\beta = 3.9$ and $L = 16$.

paths that connect two points on the lattice we need to define also the maximum norm

$$\|D\|_{max}(d) \equiv max_{\|n-m\|_{1,N}=d} \|D(n-m,0)\| \tag{B.5}$$

which corresponds to the slowest possible decay of $\|D(n,m)\|$ in the study of locality.

We perform a continuum limit study of the decay constant defined as

$$\hat{\rho}_{\text{eff}} = \ln\left(\frac{\|D(n_i)\|}{\|D(n_{i+1})\|}\right) \tag{B.6}$$

which is an observable that gives us a good estimation about the exponential behavior of the norm, since the larger ρ is, the closer we are to the strict locality defined in Eq. (B.1) and which we should recover in the continuum.

In Figure B.2 we plot the norm and the inverse of the decay constant $1/\rho$ for four different values of the lattice spacing. As we can see we recovered the locality in the continuum limit. For details of the calculation we refer to [54].

Another interesting study is the optimal value of the parameter s that appears in the definition of the overlap operator given in Eq. (2.52). The data plotted Figure B.3 suggest that the optimal value depends on the particular setup used to construct the overlap operator. We see for HYP-smeared configurations the optimal value is $s = 0$ but for non-HYP configurations the value of s that gives the best locality is $s = 0.4$. Therefore we conclude that in order to simulate the overlap operator on the lattice it is recomendable to set $s = 0, 4$ for non-HYP and HYP configurations respectively. Furthermore, in general we recommend to perform such a locality test to find the optimal value of s.

APPENDIX C

Notes on $O(a)$ improvement

C.1. Correlator $\left\langle P^{12}(x)P^{21}(0)\right\rangle$ at tree-level

C.1.1. Wilson formulation

We start with the inverse of the tree-level propagator in momentum space:

$$\begin{aligned} S_{tl}^{-1}(p,m) &= \frac{i}{a}\sum_{\mu}\gamma_\mu \sin(ap_\mu) + m + \frac{1}{a}\sin^2(\frac{ap_\mu}{2}) \\ &= i\not{p} + m + ap^2 + \mathcal{O}(a^2) \\ &= (i\not{p} + m - \frac{1}{2}am^2)(1+am)(1-\frac{1}{2}a(i\not{p}+m)) + \mathcal{O}(a^2), \end{aligned} \tag{C.1}$$

where the last step is introduced for convenience in the following calculation.

But we are interested in the propagator itself

$$\begin{aligned} S_{tl}(p,m) &= \frac{1}{(i\not{p} + m - \frac{1}{2}am^2)(1+am)(1-\frac{1}{2}a(i\not{p}+m))} + \mathcal{O}(a^2) \\ &= \frac{(1-am)(1+\frac{1}{2}a(i\not{p}+m))}{(i\not{p} + m - \frac{1}{2}am^2)(1-a^2m^2)(1-\frac{1}{4}a^2(i\not{p}+m)^2)} + \mathcal{O}(a^2) \\ &= (1-am)\frac{1}{i\not{p} + m - \frac{a}{2}m^2} + \frac{a}{2}\frac{i\not{p} + m + \frac{a}{2}m^2 - \frac{a}{2}m^2}{i\not{p} + m - \frac{a}{2}m^2} + \mathcal{O}(a^2) \\ &= (1-am)S_I(p,m_\star) + \frac{a}{2} + \mathcal{O}(a^2), \end{aligned} \tag{C.2}$$

where S_I is the improved operator and $m_\star = m - \frac{a}{2}m^2$ is the improved mass.

If we write it in coordinate space we see that the contact term only appears at short distance.

$$S_{tl}(x,y,m) = (1-am)S_I(x,y,m_\star) + \frac{a}{2}\delta(x-y) + \mathcal{O}(a^2). \tag{C.3}$$

We want to construct the correlator $\left\langle P^{12}(x)P^{21}(0)\right\rangle$

$$\left\langle P^{12}(x)P^{21}(0)\right\rangle = \bar{\psi}(x)\gamma_5\tau^+\psi(x)\bar{\psi}(0)\gamma_5\tau^-\psi = \bar{u}(x-0)\gamma_5 d(x-0)\bar{d}(0-x)\gamma_5 u(0-x). \tag{C.4}$$

After Wick contractions we obtain

$$S_u(x)\gamma_5 S_d(-x)\gamma_5 = S_u(x)S_d^\dagger(x) = S(x)S^\dagger(x), \tag{C.5}$$

where we have applied the γ_5 hermiticity $\gamma_5 S_d(x)\gamma_5 = S_d^\dagger(-x)$ and since we have degenerate u and d flavors, both propagators S_u and S_d are equivalent.

Starting with the expression

$$S_{tl}(p,m) = (1-am)\frac{1}{i\not{p} + m - \frac{a}{2}m^2} + \frac{a}{2} + \mathcal{O}(a^2) = (1-am)S_I(p,m^\star) + \frac{a}{2} + \mathcal{O}(a^2). \tag{C.6}$$

We compute the correlator we are interested in

$$\begin{aligned} & \langle P(x)P(0)\rangle = S(p,m)S^\dagger(p,m) \\ = \;& \left[(1-am)S_I(p,m^\star) + \frac{a}{2} + \mathcal{O}(a^2)\right] \times \left[(1-am)S_I^\dagger(p,m^\star) + \frac{a}{2} + \mathcal{O}(a^2)\right] \\ = \;& S_I(p,m^\star)S_I^\dagger(p,m^\star) + 2amS_I(p,m^\star)S_I^\dagger(p,m^\star) \\ + \;& \frac{a}{2}\left[S_I(p,m^\star) + S_I^\dagger(p,m^\star)\right] + \mathcal{O}(a^2). \end{aligned} \tag{C.7}$$

The next step is to compute $[S_I + S_I^\dagger]$. Our starting point is the following expression

$$\begin{aligned} S^I(p,m^\star) &= \frac{1}{i\not{p} + m^\star} = \frac{1}{i\gamma^\mu p_\mu + m^\star \mathbb{1}} \\ &= \frac{i\gamma^\mu p_\mu - m^\star\mathbb{1}}{(i\gamma^\mu p_\mu + m^\star\mathbb{1})(i\gamma^\mu p_\mu - m^\star\mathbb{1})} = \frac{i\gamma^\mu p_\mu - m^\star\mathbb{1}}{-p^2 + m^2} \\ &= \frac{i\gamma^\mu p_\mu}{-p^2+m^2} + \frac{-m^\star\mathbb{1}}{-p^2+m^2} = S_\mu\gamma_\mu + S_0\gamma^0. \end{aligned} \tag{C.8}$$

$$S_\mu = \frac{i\gamma^\mu p_\mu}{-p^2+m^2} = -S_\mu^\dagger, \qquad S_0 = \frac{-m^\star\mathbb{1}}{-p^2+m^2} = S_0^\dagger. \tag{C.9}$$

Therefore

$$[S_I + S_I^\dagger] = [(S_\mu + S_0) + (-S_\mu + S_0)] = 2S_0 = \frac{-2m}{-p^2+m^2}. \tag{C.10}$$

In the end we obtain the following expression for the full correlator in coordinates space

$$\langle P(x)P(0)\rangle = (1-am)S_I(x,y,m^\star)S_I^\dagger(x,y,m^\star) + \frac{a}{2}\delta(x-y)\frac{-2m}{-p^2+m^2} + \mathcal{O}(a^2). \tag{C.11}$$

C.1.2. Twisted Mass formulation

We start again with the inverse of the tree-level propagator in momentum space where we now have instead of $m \to -i\mu\gamma_5$ since we are at maximal twist.

$$\begin{aligned} S_{tm}^{-1}(p,m) &= \frac{i}{a}\sum_\mu \gamma_\mu \sin(ap_\mu) + \frac{1}{a}\sin^2(\frac{ap_\mu}{2}) - i\mu\gamma_5 \\ &= i\not{p} - i\mu\gamma_5 + ap^2 + \mathcal{O}(a^2) \\ &= (i\not{p} - i\mu\gamma_5 + \frac{1}{2}a\mu^2)(1 - ia\mu\gamma_5)(1 - \frac{1}{2}a(i\not{p} - i\mu\gamma_5)) + \mathcal{O}(a^2), \end{aligned} \tag{C.12}$$

where again we introduce the last step for convenience.

But we are interested in the propagator itself

$$\begin{aligned} S_{tl}(p,m) &= \frac{1}{(i\not{p} - i\mu\gamma_5 + \frac{1}{2}a\mu^2)(1 - ia\mu\gamma_5)(1 - \frac{1}{2}a(i\not{p} - i\mu\gamma_5))} + \mathcal{O}(a^2) \\ &= \frac{(1 - ia\mu\gamma_5)(1 + \frac{1}{2}a(i\not{p} - i\mu\gamma_5)}{(i\not{p} - i\mu\gamma_5 + \frac{1}{2}a\mu^2)(1 - a^2\mu^2)(1 - \frac{1}{4}a^2(i\not{p} - i\mu\gamma_5)^2)} + \mathcal{O}(a^2) \\ &= (1 - ia\mu\gamma_5)\frac{1}{i\not{p} - i\mu\gamma_5 + \frac{a}{2}\mu^2} + \frac{a}{2}\frac{i\not{p} - i\mu\gamma_5 + \frac{a}{2}\mu^2 - \frac{a}{2}mu^2}{i\not{p} - i\mu\gamma_5 - \frac{a}{2}\mu^2} + \mathcal{O}(a^2) \\ &= (1 - ia\mu\gamma_5)S_I(p,\mu_\star) + \frac{a}{2} + \mathcal{O}(a^2), \end{aligned} \tag{C.13}$$

where S_I is the improved operator. If we write it in the coordinates space we see that the contact term only appears at short distance.

$$S_{tm}(x,y,m) = (1 - ia\mu\gamma_5)S_I(x,y,\mu^\star) + \frac{a}{2}\delta(x-y) + \mathcal{O}(a^2). \tag{C.14}$$

We want to construct the correlator $\left\langle P^{12}(x)P^{21}(0)\right\rangle$

$$\left\langle P^{12}(x)P^{21}(0)\right\rangle = \bar\psi(x)\gamma_5\tau^+\psi(x)\bar\psi(0)\gamma_5\tau^-\psi = \bar u(x-0)\gamma_5 d(x-0)\bar d(0-x)\gamma_5 u(0-x). \tag{C.15}$$

After Wick contractions we obtain

$$S_u(x)\gamma_5 S_d(-x)\gamma_5 = S_u(x)S_u^\dagger(x) = S(x)S^\dagger(x), \tag{C.16}$$

where we have applied the γ_5 hermiticity $\gamma_5 S_d(x)\gamma_5 = S_u^\dagger(-x)$.

Starting again with the expression

$$S_{tl}(p,\mu) = (1 - ia\mu\gamma_5)\frac{1}{i\not{p} - i\mu\gamma_5 + \frac{a}{2}\mu^2} + \frac{a}{2} + \mathcal{O}(a^2) = (1 - ia\mu\gamma_5)S_I(p,\mu) + \frac{a}{2} + \mathcal{O}(a^2). \tag{C.17}$$

We compute the correlator we are interested in

$$\begin{aligned}
&\langle P(x)P(0)\rangle = S(p,\mu)S^{\dagger}(p,\mu) = \\
&= \Big[(1 - ia\mu\gamma_5)S_I(p,\mu) + \frac{a}{2} + \mathcal{O}(a^2)\Big] \times \Big[(1 + ia\mu\gamma_5)S_I^{\dagger}(p,\mu) + \frac{a}{2} + \mathcal{O}(a^2)\Big] \\
&= S_I(p,\mu)S_I^{\dagger}(p,\mu) + ia\mu\gamma_5 S_I(p,\mu)S_I^{\dagger}(p,\mu) - ia\mu\gamma_5 S_I(p,\mu)S_I^{\dagger}(p,\mu) \\
&\quad + \frac{a}{2}\Big[S_I(p,\mu) + S_I^{\dagger}(p,\mu)\Big] + \mathcal{O}(a^2).
\end{aligned} \tag{C.18}$$

We finally obtain the following expression

$$\langle P(x)P(0)\rangle = S(p,\mu)S^{\dagger}(p,\mu) = S_I(p,\mu)S_I^{\dagger}(p,\mu) + \frac{a}{2}\Big[S_I(p,\mu) + S_I^{\dagger}(p,\mu)\Big] + \mathcal{O}(a^2). \tag{C.19}$$

The next step is to compute $[S_I + S_I^{\dagger}]$ to see if this contact term also remains as it happened in the Wilson case.

$$\begin{aligned}
S^I(p,\mu) &= \frac{1}{i\not{p} + i\mu\gamma_5} = \frac{1}{i\gamma^{\mu}\not{p} + i\mu\gamma_5} \\
&= \frac{i\gamma^{\mu}\not{p} + i\mu\gamma_5}{(i\gamma^{\mu}\not{p} - i\mu\gamma_5)(i\gamma^{\mu}\not{p} + i\mu\gamma_5)} = \frac{i\gamma^{\mu}\not{p} - i\mu\gamma_5}{-p^2 - \mu^2} \\
&= \frac{i\gamma^{\mu}\not{p}}{-p^2 - \mu^2} + \frac{-i\mu\gamma_5}{-p^2 - \mu^2} = S_{\mu}\gamma_{\mu} + S_5\gamma^5,
\end{aligned} \tag{C.20}$$

$$S_{\mu} = \frac{i\gamma^{\mu}\not{p}}{-p^2 - \mu^2} = -S_{\mu}^{\dagger}, \qquad S_5 = \frac{-i\mu\gamma_5}{-p^2 - \mu^2} = -S_5^{\dagger}. \tag{C.21}$$

Therefore

$$[S_I + S_I^{\dagger}] = [(S_{\mu} + S_5) + (-S_{\mu} - S_5)] = 0. \tag{C.22}$$

In the end we obtain the following expression for the full correlator in coordinates space

$$\langle P(x)P(0)\rangle = S_I(x,y,\mu)S_I^{\dagger}(x,y,\mu) + \mathcal{O}(a^2) \tag{C.23}$$

We can then conclude that, in the case of maximal twist, our operator is automatically $O(a)$ improved as expected. The contact that appeared in the Wilson formalism, automatically disappears in the twisted mass formulation at maximal twist.

C.2. QCD Ward-Takahashi Identities

In this section we report on Ward identities for Wilson and twisted mass fermions. Our main goal is the computation of the non-singlet Ward identities for twisted mass that are needed for the explicit calculation of the contact terms that arise in the Symanzik expansion of the mode number among others. However, for pedagogical reasons we show the whole calculation including the origin of the basic statements which allow to derivation of the Ward identities. For a deeper understanding on the topic we recommend the lecture notes [118], based on [72], which we found very helpful and guided us for the first part of the calculation.

As we have already seen, the expectation value of an operator $\mathcal{O}$ in QCD in terms of a path integral is given by

$$\langle \mathcal{O} \rangle = \frac{1}{Z} \int D[\psi, \bar{\psi}, A_\mu] \mathcal{O}[\psi, \bar{\psi}, A_\mu] e^{-S[\psi, \bar{\psi}, A_\mu]}. \tag{C.24}$$

The QCD action takes the following form

$$S = \int d^4x \; \mathcal{L}[\psi, \overline{\psi}, A_\mu] = \int d^4x \; [\bar{\psi}(x)(\gamma^\mu D_\mu + M)\psi(x) + \frac{1}{4g^2} F^{(i)}_{\mu\nu}(x) F^{\mu\nu(i)}(x)] \tag{C.25}$$

where $D_\mu(x) = \partial_\mu + iA_\mu(x)$ and $F^{(i)}_{\mu\nu} = \partial_\mu A^{(i)}_\nu(x) - \partial_\nu A^{(i)}_\mu(x) - c_{ijk} A^{(j)}_\mu(x) A^{(k)}_\nu(x)$. In this particular case we work with two degenerate light fermions and therefore $\psi, \overline{\psi}$ represent doublets of fermions and M is a 2×2 matrix. In order to give a result as general as possible, we do not specify the form of the matrix M since it will differ depending on the chosen formulation, being

$$M_W = m\mathbb{1} = \begin{bmatrix} m & 0 \\ 0 & m \end{bmatrix}, \qquad M_{tm} = m\mathbb{1} + i\mu\gamma_5\tau^3 = \begin{bmatrix} m + i\mu\gamma_5 & 0 \\ 0 & m - i\mu\gamma_5 \end{bmatrix},$$

for the Wilson and the twisted mass case respectively.

If we apply a general local infinitesimal transformation $\alpha(x)$ to the fermion fields

$$\psi(x) \to \psi(x)' = \psi(x) + \delta\psi(x) = \psi(x) + \alpha(x)\psi(x), \tag{C.26}$$
$$\bar{\psi}(x) \to \bar{\psi}(x)' = \bar{\psi}(x) + \delta\bar{\psi}(x) = \bar{\psi}(x) - \bar{\psi}(x)\alpha(x), \tag{C.27}$$

the expectation value of our observable $\mathcal{O}(\psi', \overline{\psi}')$ should remain invariant, since ψ' is just a redefinition of the field. Therefore we can write

$$\left\langle Q[\psi', \overline{\psi}'] \right\rangle - \left\langle Q[\psi, \overline{\psi}] \right\rangle = 0, \tag{C.28}$$
$$\left\langle Q[\psi, \overline{\psi}] \right\rangle + \delta \left\langle Q \right\rangle - \left\langle Q[\psi, \overline{\psi}] \right\rangle = 0. \tag{C.29}$$
$$\tag{C.30}$$

This directly implies that

$$\delta \left\langle \mathcal{O} \right\rangle = \int d^4x \frac{\delta \left\langle \mathcal{O} \right\rangle}{\delta\alpha(x)} \delta\alpha(x) = 0. \tag{C.31}$$

If we develop Eq. (C.31) we obtain the basic statement on which the Ward-Takahashi identities are based on

$$\int d^4x \frac{\delta \left\langle \mathcal{O}[\psi, \overline{\psi}, A_\mu] \right\rangle}{\delta\alpha(x)} \delta\alpha(x) = \int d^4x \frac{\delta}{\delta\alpha(x)} \left[\frac{1}{\mathcal{Z}} \int D\psi D\overline{\psi} D A_\mu \delta e^{-S} \right] \delta\alpha(x) \tag{C.32}$$
$$= \int d^4x \int D\psi D\overline{\psi} D A_\mu \frac{\delta \mathcal{O}[\psi, \overline{\psi}, A_\mu]}{\delta\alpha(x)} \delta\alpha(x) e^{-S}$$

$$+\int d^4x \int D\psi D\overline{\psi} DA_\mu \mathcal{O}[\psi,\overline{\psi},A_\mu]\frac{-\delta S}{\delta\alpha(x)}\delta\alpha(x)e^{-S}=0.$$

This last equation can be rewritten in the following way

$$\left\langle \frac{\delta\mathcal{O}}{\delta\alpha(x)} \right\rangle = \left\langle \mathcal{O}\frac{\delta S}{\delta\alpha(x)} \right\rangle, \tag{C.33}$$

which constitutes the basic ingredient of the Ward-Takahashi identities.

We can now specify a kind of infinitesimal local transformation we are interested in. In the present work the applied transformations are the non-singlet axial transformations, given by

$$\psi(y)\to\psi(y)'=\psi(y)+\delta\psi(y)=\psi(y)+i\alpha^a(y)\frac{\tau^a}{2}\gamma_5\psi(y) \tag{C.34}$$

$$\bar{\psi}(y)\to\bar{\psi}(y)'=\bar{\psi}(y)+\delta\bar{\psi}(y)=\bar{\psi}(y)+i\bar{\psi}(y)\alpha^a(y)\frac{\tau^a}{2}\gamma_5, \tag{C.35}$$

and the non-singlet vector transformations

$$\psi(y)\to\psi(y)'=\psi(y)+\delta\psi(y)=\psi(y)+i\alpha^a(y)\frac{\tau^a}{2}\psi(y) \tag{C.36}$$

$$\bar{\psi}(y)\to\bar{\psi}(y)'=\bar{\psi}(y)+\delta\bar{\psi}(y)=\bar{\psi}(y)-i\bar{\psi}(y)\alpha^a(y)\frac{\tau^a}{2}, \tag{C.37}$$

where τ^a represent the Pauli matrices acting in flavor space.

In this first part of the calculation we are interested in computing the right-hand side of Eq. (C.33). To simplify the derivation we apply the axial transformation given by Eq. (C.34) to the QCD Lagrangian and only comment on the vector case which is completely analogous. Notice that only the term $(\gamma_\mu\partial_\mu+M)$ of Eq. (C.25) will be affected by the transformation.

$$\begin{aligned}
\delta S &= \int d^4x \frac{\delta S}{\delta\alpha^a(x)}\alpha^a(x) \qquad\qquad (C.38)\\
&= \int d^4x \int d^4y \frac{\delta}{\delta\alpha^a(x)}\left\{(i\bar{\psi}(y)\alpha^b(y)\frac{\tau^b}{2}\gamma_5)(\gamma_\mu\partial_\mu+M)(i\alpha^b(y))\frac{\tau^b}{2}\gamma_5\psi(y)\right\}\\
&= \int d^4x \int d^4y \frac{\delta}{\delta\alpha^a(x)}\Big\{i\bar{\psi}(y)\alpha^b(y)\frac{\tau^b}{2}\gamma_5\gamma_\mu\partial_\mu\psi(y)+i\bar{\psi}(y)\gamma_\mu\partial_\mu(\alpha^b(y)\frac{\tau^b}{2}\gamma_5\psi(y))\\
&\quad + i\bar{\psi}(y)\alpha^b(y)\frac{\tau^b}{2}\gamma_5 M\psi(y)+i\psi(y)M\alpha^b(y)\frac{\tau^b}{2}\gamma_5\psi(y)\Big\}\alpha^a(x)+\mathcal{O}(\alpha^2)
\end{aligned}$$

$$\begin{aligned}
\delta S = \int d^4x \int d^4y \frac{\delta}{\delta\alpha^a(x)}\Big\{&i\bar{\psi}(y)\alpha^b(y)(\frac{\tau^b}{2}\gamma_5\gamma_\mu+\gamma_\mu\frac{\tau^b}{2}\gamma_5)\partial_\mu\psi(y) \qquad (C.39)\\
&+i\bar{\psi}(y)\gamma_\mu\frac{\tau^b}{2}\gamma_5\psi(y)\partial_\mu(\alpha^b(y))+i\alpha^b(y)\bar{\psi}(y)(\frac{\tau^b}{2}\gamma_5 M+M\frac{\tau^b}{2}\gamma_5)\psi(y)\Big\}\alpha^a(x).
\end{aligned}$$

The first term of Eq. (C.39) vanishes due to the following property

$$\frac{\tau^a}{2}\gamma_5\gamma_\mu + \gamma_\mu\frac{\tau^a}{2}\gamma_5 = 0, \quad [\gamma_5, \gamma_\mu] = 0.$$

In the case of the vector transformation we find $\frac{\tau^a}{2}\gamma_\mu - \gamma_\mu\frac{\tau^a}{2} = 0$.

We need to solve the integral that appears in the second term of Eq. (C.39) using integration by parts:

$$\int \underbrace{i\bar{\psi}(y)\gamma_\mu\frac{\tau^b}{2}\gamma_5\psi(y)}_{u}\underbrace{\partial_\mu(\alpha^b(y))}_{dv} = -\int \alpha^b(y)\partial_\mu(\bar{\psi}(y)\gamma_\mu\frac{\tau^b}{2}\gamma_5\psi(y)).$$

We are thus left with the following expression

$$\begin{aligned}\delta S = &\int d^4x \int d^4y \frac{\delta}{\delta\alpha^a(x)}\alpha^b(y)\left\{-i\partial_\mu(\bar{\psi}(y)\gamma_\mu\frac{\tau^b}{2}\gamma_5\psi(y)) \right. \\ &\left. +i\bar{\psi}(y)\left\{M, \frac{\tau^b}{2}\right\}\gamma_5\psi(y)\right\}\alpha^a(x) \\ = -i&\int d^4x \int d^4y\, \delta^4(x-y)\left\{\partial_\mu(\bar{\psi}(y)\gamma_\mu\frac{\tau^b}{2}\gamma_5\psi(y)) - \bar{\psi}(y)\left\{M, \frac{\tau^b}{2}\right\}\gamma_5\psi(y)\right\}\alpha^a(x).\end{aligned} \tag{C.40}$$

If we now apply $\int \delta(x-y)f(x)dx = f(y)$ we obtain

$$\delta S = -i\int d^4x \left\{\partial_\mu(\bar{\psi}(x)\gamma_\mu\frac{\tau^b}{2}\gamma_5\psi(x)) - \bar{\psi}(x)\left\{M, \frac{\tau^b}{2}\right\}\gamma_5\psi(x)\right\}\alpha^a(x). \tag{C.41}$$

In particular, we are interested in $\frac{\delta S}{\delta\alpha(z)}$

$$\frac{\delta S}{\delta\alpha(z)} = -i\int dx^4 \frac{\delta(f(x)\alpha(x))}{\delta\alpha(z)}\delta^4(x-z) = f(z). \tag{C.42}$$

This leads to the final result for the axial case

$$\frac{\delta S}{\delta\alpha^a(x)} = \partial_\mu(\bar{\psi}(x)\gamma_\mu\frac{\tau^b}{2}\gamma_5\psi(x)) - \bar{\psi}(x)\left\{M, \frac{\tau^b}{2}\right\}\gamma_5\psi(x). \tag{C.43}$$

Equivalently for the vector case we obtain

$$\frac{\delta S}{\delta\alpha^a(x)} = \partial_\mu(\bar{\psi}(x)\gamma_\mu\frac{\tau^b}{2}\psi(x)) - \bar{\psi}(x)\left[M, \frac{\tau^b}{2}\right]\psi(x). \tag{C.44}$$

All the equations introduced above correspond to the basic ingredients for the calculation of the Ward-identities we are interested in and can be found in specialized text and lectures [118, 72]. In the next sections we compute some particular non-singlet Ward-Takahashi identities for the Wilson and for twisted mass action that are relevant for the

prove of automatic $O(a)$ improvement derived in Sec.4.2.

C.2.1. Wilson formulation

An important theoretical part of this work was to prove that the chiral condensate is an $O(a)$ improved quantity in the twisted mass formulation at maximal twist. To this end we first reproduce the results given in [74] which are based on improved Wilson fermions. For this reason we show in this section the results necessary to reproduced such calculation which consists on flavored Ward-Takahashi identities for the Wilson action. In the next section we present the results relevant for our work in the twisted mass formulation.

In the following we consider the $SU(N_f)$ flavor group of a partially quenched theory with N_f valence quarks. In the present section we focus on the Wilson formulation. In particular we are interested in the flavored axial transformation given by,

$$\psi(x_1) \to \psi(x_1)' = \psi(x_1) + i\alpha_A^{ab}(x_1)\frac{\tau^{ab}}{2}\gamma_5\psi(x_1) \tag{C.45}$$

$$\bar{\psi}(x_1) \to \bar{\psi}(x_1)' = \bar{\psi}(x_1) + i\bar{\psi}(x_1)\alpha_A^{ab}(x_1)\frac{\tau^{ab}}{2}\gamma_5 \tag{C.46}$$

where τ^{ab} corresponds to a extended $(N_f \times N_f)$ Pauli matrix acting in flavor space, where the indices a, b represent its only non-vanishing elements. In this representation ψ, $\overline{\psi}$ are N_f-component spinors.

Then Eq. (C.43) takes the following form

$$\frac{\delta S}{\delta\alpha_A^{ab}(x_1)} = -i[\partial_\mu(\bar{\psi}(x_1)\gamma_\mu\gamma_5\tau^{ab}\psi(x_1)) - 2m\bar{\psi}(x_1)\gamma_5\tau^{ab}\psi(x_1)], \tag{C.47}$$

$$\text{where} \qquad A_\mu^{ab} = \bar{\psi}(x_1)\gamma_\mu\gamma_5\tau^{ab}\psi(x_1)), \tag{C.48}$$

$$P^{ab}(x_1) = \bar{\psi}(x_1)\gamma_5\tau^{ab}\psi(x_1), \tag{C.49}$$

are the flavored axial current and the flavored pseudoscalar density respectively.

Inserting Eq. (C.47) in Eq. (C.33) and simplifying the notation we obtain

$$\left\langle \delta_A^{ab,x_1}\mathcal{O}\right\rangle = -i\left\langle [\partial_\mu A_\mu^{ab}(x_1)]\mathcal{O}\right\rangle + i2m\left\langle P^{ab}(x_1)\mathcal{O}\right\rangle. \tag{C.50}$$

We particularly interested in the integrated Ward identity

$$\int d^4y \left\langle \delta_A^{ab,x_1}\mathcal{O}\right\rangle = i2m\int d^4y \left\langle P^{ab}(x_1)\mathcal{O}\right\rangle. \tag{C.51}$$

Notice that after integration the term which contains the total derivative of the axial current vanishes.

Our main goal is to solve Eq. (C.51) in the case where $\mathcal{O}$ corresponds to a density chain constituted by five pseudo-scalar densities. However, for the sake of a good understand-

ing, we start analyzing the left-hand side of Eq. (C.51) considering only one pseudo-scalar density. We apply the transformations given in Eq. (C.45) to our observable which is defined as

$$\mathcal{O} = P^{cd}(x_2) = \bar{\psi}(x_2)\gamma_5\tau^{cd}\psi(x_2), \tag{C.52}$$

and obtain the following result

$$\begin{aligned} P^{cd}(x_2)' &= P^{cd}(x_2) + \alpha^{ab}(x_1)\delta P^{cd}(x_2) = \\ &= [\bar{\psi}(x_2) + i\alpha^{ab}(x_1)\gamma_5\tau^{ab}\bar{\psi}(x_2)]\gamma_5\tau^{cd}[\psi(x_2) + i\alpha^{ab}(x_1)\gamma_5\tau^{ab}\psi] \\ &= \bar{\psi}(x_2)\gamma_5\tau^{cd}\psi(x_2) + i\alpha^{ab}(x_1)[\bar{\psi}(x_2)\gamma_5\gamma_5\{\tau^{ab},\tau^{cd}\}\psi(x_2)] + \mathcal{O}(\alpha^2(x_1)) \\ &= \bar{\psi}(x_2)\gamma_5\tau^{cd}\psi(x_2) + i\alpha^{ab}(x_1)[\bar{\psi}(x_2)\{\tau^{ab},\tau^{cd}\}\psi(x_2)] + \mathcal{O}(\alpha^2(x_1)). \end{aligned} \tag{C.53}$$

Therefore

$$\begin{aligned} \delta_A^{ab,x_1}P^{cd}(x_2) = \frac{\delta P^{cd}(x_2)}{\delta\alpha^{ab}(x_1)} &= i\bar{\psi}(x_2)\{\tau^{ab},\tau^{cd}\}\psi(x_2)\delta(x_2-x_1) \\ &= i\bar{\psi}(x_2)\tau^{ad}\psi(x_2)\delta(x_2-x_1) = iS^{ad}(x_2)\delta(x_2-x_1). \end{aligned} \tag{C.54}$$

In the last expression we have applied the commutation relations of the τ^{ab} matrices introduced in App.A.1 $\{\tau^{ab},\tau^{cd}\} = \tau^{ad}\delta_{bc} + \tau^{cb}\delta^{ab}$ considering that the indices b and c are equal which is relevant in our case.

We now insert the result given in Eq. (C.54) in the left-hand side of Eq. (C.51) and after integrating the δ function we obtain the following Ward identity.

$$i\left\langle S^{ad}(x_2)\right\rangle = 2im\int d^4x_1\left\langle P^{ab}(x_1)P^{cd}(x_2)\right\rangle. \tag{C.55}$$

However we actually need to insert in Eq. (C.51) a density chain wich consists on five pseudoscalar densities. We will start by inserting $\mathcal{O} = P^{23}(x_2)P^{34}(x_3)$ in Eq. (C.51) and solving the left-hand side to understand the mechanism and then will generalize for an operator with five densities.

$$\begin{aligned} \delta_A^{ab,x_1}P^{23}(x_2)P^{34}(0) &= \frac{\delta P^{23}(x_2)}{\delta\alpha^{12}(x_1)}P^{34}(0) + P^{23}(x_2)\frac{\delta P^{34}(0)}{\delta\alpha^{12}(x_1)} = \\ = \quad \bar{\psi}(x_2)\{\tau^{12},\tau^{23}\}\psi(x_2)\bar{\psi}(0)\gamma_5\tau^{34}\psi(0) &+ \bar{\psi}(x_2)\gamma_5\tau^{23}\psi(x_2)\bar{\psi}(0)\{\tau^{12},\tau^{34}\}\psi(0). \end{aligned} \tag{C.56}$$

Since $\{\tau^{12},\tau^{34}\} = 0$ the derivative of P_{34} with respect to α_{12} vanishes, leading this term to be irrelevant.

$$\begin{aligned} \delta_A^{ab,x_1}P^{23}(x_2)P^{34}(0) &= \bar{\psi}(x_2)\{\tau^{12},\tau^{23}\}\psi(x_2)\bar{\psi}(0)\gamma_5\tau^{34}\psi(0) \\ &= \bar{\psi}(x_2)\tau^{13}\psi(x_2)\bar{\psi}(0)\gamma_5\tau^{34}\psi(0) = S^{13}(x_2)P^{34}(0). \end{aligned} \tag{C.57}$$

Finally for $\mathcal{O} = P^{23}(x_2)P^{34}(x_3)P^{45}(x_4)P^{56}(x_5)P^{61}(0)$ an additional contribution appears due to the fact that we have a closed chain in flavor space.

$$\begin{aligned} & \delta_A^{ab,x_1} P^{23}(x_2)P^{34}(x_3)P^{45}(x_4)P^{56}(x_5)P^{61}(0) = \\ = & \frac{\delta P^{23}(x_2)}{\delta\alpha^{12}(x_1)} P^{34}(x_3)P^{45}(x_4)P^{56}(x_5)P^{61}(0) + P^{12}(x_2)P^{34}(x_3)P^{45}(x_4)P^{56}(x_5)\frac{\delta P^{61}(0)}{\delta\alpha^{12}(x_1)} \\ = & S^{13}(x_2)P^{34}(x_3)P^{45}(x_4)P^{56}(x_5)P^{61}(0) + P^{23}(x_2)P^{34}(x_3)P^{45}(x_4)P^{56}(x_5)S^{62}(0). \end{aligned} \tag{C.58}$$

Notice that in Eq. (C.58) only $\{\tau^{12}, \tau^{23}\} = \tau^{13}$ and $\{\tau^{61}, \tau^{12}\} = \tau^{62}$ are different than zero. We are thus led to the following expression

$$\begin{aligned} & S^{13}(x_2)P^{34}(x_3)P^{45}(x_4)P^{56}(x_5)P^{61}(0) + P^{23}(x_2)P^{34}(x_3)P^{45}(x_4)P^{56}(x_5)S^{62}(0) \\ = & 2m \int d^4x_1 \left\langle P^{12}(x_1)P^{23}(x_2)P^{34}(x_3)P^{45}(x_4)P^{56}(x_5)P^{61}(0)\right\rangle . \end{aligned} \tag{C.59}$$

In order to obtain our final result, the non-singlet Ward identity which involves the expression given in Eq. (4.3), we need to integrate Eq. (C.59)

$$\begin{aligned} & \int d^4x_2 d^4x_3 d^4x_4 d^4x_5 S^{13}(x_2)P^{34}(x_3)P^{45}(x_4)P^{56}(x_5)P^{61}(0) + \\ + & \int d^4x_2 d^4x_3 d^4x_4 d^4x_5 P^{23}(x_2)P^{34}(x_3)P^{45}(x_4)P^{56}(x_5)S^{62}(0) \\ = & 2m \int d^4x_2 d^4x_3 d^4x_4 d^4x_5 \int d^4x_1 \left\langle P^{12}(x_1)P^{23}(x_2)P^{34}(x_3)P^{45}(x_4)P^{56}(x_5)P^{61}(0)\right\rangle \end{aligned} \tag{C.60}$$

Including different flavors in the axial transformation Eq. (C.45) would give us the corresponding Ward identities which would allow us to substitute each term arising in the Symanzik expansion of the Wilson case due to the short distance singularities.

C.2.2. Twisted mass formulation

This section is devoted to present the analogous calculation, showed for pure Wilson in the last section, for the twisted mass case. The results obtained below were used in Sec.4.2 to show that the chiral condensate is $O(a)$ improved. In the following we consider the twisted mass action introduced in Eq. (2.31). In this particular case we are interested in both, the axial and the vector flavored Ward-Takahashi identities.

Axial Ward identity

We start introducing the notation for twisted mass since we now consider the group $SU(2N_f)$ of a partially quenched theory with N_f replicas of degenerate fermions. According to our notation for $N_f = 3$ we define the charge pseudoscalar density as follows

$$P^+_{12} = \overline{\psi}\gamma_5\lambda^{14}\psi = \overline{\psi}_1\gamma_5\tau^+\psi_2 = \overline{u}^1\gamma_5 d^2, \tag{C.61}$$

where $\psi = (u_1, d_1, u_2, d_2, u_3, d_3)$ is a $2N_f$ component spinor and λ^{ab} is a $2N_f \times 2N_f$ extended Pauli matrix acting on flavor space whose elements are equal to zero except for the element ab which corresponds to one. Another representation is possible and given by a $SU(2)$ subalgebra of $SU(N)$ where the spinors are doublets of degenerate fermions $\psi_1 = (u_1, d_1)$, $\psi_2 = (u_2, d_2)^T$. In this case λ^{ab} corresponds to the 2×2 Pauli matrix τ^+ acting in flavor space.

Considering the introduced notation for the axial transformations which are given by

$$\psi(x_1) \rightarrow \psi\prime = \psi(x_1) + i\alpha(x_1)\gamma_5\lambda^{14}\psi(x_1) \tag{C.62}$$
$$\overline{\psi}(x_1) \rightarrow \overline{\psi}\prime = \overline{\psi}(x_1) + i\overline{\psi}(x_1)\alpha(x_1)\gamma_5\lambda^{14}. \tag{C.63}$$

The variation of the action under this transformation gives

$$\frac{\delta S}{\delta\alpha_A(x_1)} = -i[\partial_\mu(\overline{\psi}(x_1)\gamma_\mu\gamma_5\lambda^{14}\psi(x_1)) - 2m\overline{\psi}(x_1)\gamma_5\lambda^{14}\psi(x_1)], \tag{C.64}$$

$$\text{where} \qquad A_\mu = \overline{\psi}(x_1)\gamma_\mu\gamma_5\lambda^{14}\psi(x_1)), \tag{C.65}$$
$$P^+_{12}(x_1) = \overline{\psi}(x_1)\gamma_5\lambda^{14}\psi(x_1), \tag{C.66}$$

corresponds to the flavored axial current and the flavored pseudoscalar density respectively. In the axial case only $m\mathbb{1}$ contributes since the term $i\mu\gamma_5\tau^3$ cancels.

If we insert Eq. (C.64) in Eq. (C.33) we obtain after simplifying the notation the following expression

$$\left\langle \delta_A^{x_1}\mathcal{O}\right\rangle = -i\left\langle[\partial_\mu A_\mu(x_1)]\mathcal{O}\right\rangle + i2m\left\langle P^+_{12}(x_1)\mathcal{O}\right\rangle. \tag{C.67}$$

In particular we are interested in the integrated Ward identity

$$\int d^4y \left\langle \delta_A^{x_1}\mathcal{O}\right\rangle = i2m\int d^4y \left\langle P^+_{12}(x_1)\mathcal{O}\right\rangle. \tag{C.68}$$

Notice that, after integration, the term in Eq. (C.67), which contains the total derivative of the current, vanishes.

Again, for the sake of a good understanding we start analyzing the left-hand side of Eq. (C.68) considering our observable $\mathcal{O}$ to be a single charged pseudoscalar density which is analogous to Eq. (C.61)

$$\mathcal{O} = P^-_{23}(x) = \psi_2\gamma_5\tau^-\psi_3 = \overline{d}^-\gamma_5 s^+ = \psi\gamma_5\lambda^{45}\psi. \tag{C.69}$$

We then apply the axial transformations introduced in Eq. (C.62) to our observable $P^-_{23}(x)$

$$\begin{aligned} P^{23}(x_2)' &= P^{23}(x_2) + \alpha(x_1)\delta P^{23}(x_2) = \\ &= [\overline{\psi}(x_2) + i\alpha^{ab}(x_1)\gamma_5\lambda^{14}\overline{\psi}(x_2)]\gamma_5\lambda^{45}[\psi(x_2) + i\alpha(x_1)\gamma_5\lambda^{14}\psi] = \end{aligned} \tag{C.70}$$

$$\begin{aligned} &= \overline{\psi}2(x_2)\gamma_5\lambda^{45}\psi(x_2) + i\alpha(x_1)[\overline{\psi}(x_2)\gamma_5\gamma_5\{\lambda^{14},\lambda^{45}\}\psi(x_2)] + \mathcal{O}(\alpha^2(x_1)) = \\ &= \overline{\psi}(x_2)\gamma_5\lambda^{45}\psi(x_2) + i\alpha(x_1)[\overline{\psi}(x_2)\lambda^{15}\psi(x_2)] + \mathcal{O}(\alpha^2(x_1)), \end{aligned}$$

where we have used the anticommutation relations of λ^{ab}, $\{\lambda^{14},\lambda^{45}\} = \lambda^{15}$, and $\gamma_5^2 = \mathbb{1}$.

The result that we obtain corresponds to a particular scalar density defined as

$$S^{\uparrow}_{13} = \overline{\psi}_1 \frac{1}{2}(\mathbb{1} + \tau^3)\psi_3. \tag{C.71}$$

Finally the left hand side of Eq. (C.68) reads

$$\delta_A^{x_1} P^{23}(x_2) = \frac{\delta P^{23}(x_2)}{\delta\alpha(x_1)} = i\overline{\psi}(x_2)\lambda^{15}\psi(x_2)\delta(x_2 - x_1) = iS^{\uparrow}_{13}(x_2)\delta(x_2 - x_1). \tag{C.72}$$

The result obtained in Eq. (C.72) leads to the following Ward identity

$$i\left\langle S^{\uparrow}_{13}(x_2)\right\rangle = i2m\int d^4x_1 \left\langle P^{+}_{12}(x_1)P^{-}_{23}(x_2)\right\rangle. \tag{C.73}$$

It is straightforward to generalize this result to n pseudoscalar densities. In particular for $\mathcal{O} = P^{+}_{34}(x_3)P^{-}_{45}(x_4)P^{+}_{56}(x_5)P^{-}_{61}(0)$ we obtain the following result

$$\begin{aligned} & S^{\uparrow}_{13}(x_2)P^{+}_{34}(x_3)P^{-}_{45}(x_4)P^{+}_{56}(x_5)P^{-}_{61}(0) + P^{-}_{23}(x_2)P^{+}_{34}(x_3)P^{-}_{45}(x_4)P^{+}_{56}(x_5)S^{\uparrow}_{62}(0) \\ = \;& 2m\int d^4x_1 \left\langle P^{+}_{12}(x_1)P^{-}_{23}(x_2)P^{+}_{34}(x_3)P^{-}_{45}(x_4)P^{+}_{56}(x_5)P^{-}_{61}(0)\right\rangle. \end{aligned} \tag{C.74}$$

As a final step we integrate over the corresponding variables to obtain the integrated non-singlet axial Ward identity we are interested in

$$\begin{aligned} & \int d^4x_2 d^4x_3 d^4x_4 d^4x_5 S^{\uparrow}_{13}(x_2)P^{+}_{34}(x_3)P^{-}_{45}(x_4)P^{+}_{56}(x_5)P^{-}_{61}(0) + \\ + \;& \int d^4x_2 d^4x_3 d^4x_4 d^4x_5 P^{-}_{23}(x_2)P^{+}_{34}(x_3)P^{-}_{45}(x_4)P^{+}_{56}(x_5)S^{\uparrow}_{62}(0) \\ = \;& 2m\int d^4x_2 d^4x_3 d^4x_4 d^4x_5 \int d^4x_1 \left\langle P^{+}_{12}(x_1)P^{-}_{23}(x_2)P^{+}_{34}(x_3)P^{-}_{45}(x_4)P^{+}_{56}(x_5)P^{-}_{61}(0)\right\rangle. \end{aligned} \tag{C.75}$$

If we exchange the flavors involved in the axial transformation introduced in Eq. (C.62) we can derive a series of analogous results which are needed to prove that the $O(a)$ terms in the Symanzik expansion given in Eq. (4.9) vanish.

Vector Ward identity

In this section we compute the non-singlet vector Ward identity for twisted mass. The notation remains as in the last section.

We first introduce the flavored vector transformations

$$\psi(x_1) \rightarrow \psi' = \psi(x_1) + i\alpha(x_1)\lambda^{14}\psi(x_1), \tag{C.76}$$
$$\overline{\psi}(x_1) \rightarrow \overline{\psi}' = \overline{\psi}(x_1) - i\overline{\psi}(x_1)\alpha(x_1)\lambda^{14}. \tag{C.77}$$

If we apply these transformations to the twisted mass action we obtain the following result

$$\frac{\delta S}{\delta \alpha_V(x_1)} = -i[\partial_\mu(\overline{\psi}(x_1)\gamma_\mu\lambda^{14}\psi(x_1)) - 2i\mu\overline{\psi}(x_1)\gamma_5\lambda^{14}\psi(x_1)], \tag{C.78}$$

$$\text{where} \quad V_\mu^{ab} = \overline{\psi}(x_1)\gamma_\mu\lambda^{14}\psi(x_1)) \tag{C.79}$$
$$P_{12}^{+}(x_1) = \overline{\psi}(x_1)\lambda^{14}\psi(x_1) \tag{C.80}$$

are the flavored vector current and the flavored pseudoscalar density respectively. In the vector case the term which corresponds to the Wilson mass $m\mathbb{1}$ does not contribute. An important remark is that in the twisted mass case, due to the γ_5 that appears in the commutator, in the PCVC relation a pseudoscalar density appears, in contrast with the Wilson case where we obtained a scalar density.

Following the steps introduced in the last section we now insert Eq. (C.78) in Eq. (C.33) and simplify the notation

$$\left\langle \delta_V^{x_1}\mathcal{O}\right\rangle = -i\left\langle [\partial_\mu V_\mu(x_1)]\mathcal{O}\right\rangle - 2\mu\left\langle P_{12}^{+}(x_1)\mathcal{O}\right\rangle. \tag{C.81}$$

Again we are interested in the integrated Ward identity, which corresponds to

$$\int d^4y \left\langle \delta_V^{x_1}\mathcal{O}\right\rangle = -2\mu\int d^4y \left\langle P_{12}^{+}(x_1)\mathcal{O}\right\rangle, \tag{C.82}$$

where the total derivative of the current vanishes after the integration.

The next step would be to apply the vector transformations to the operator $\mathcal{O}$, which we choose to be $P^{23}(x_2)$ for simplicity. However we are interested in a chain with six flavors which corresponds to $\mathcal{O} = P_{23}^{-}(x_2)P_{34}^{+}(x_3)P_{45}^{-}(x_4)P_{56}^{+}(x_5)P_{61}^{-}(0)$. We will explain in detail the simple case and then generalize for a 6 flavors chain.

$$\begin{aligned} P^{23}(x_2)' &= P^{23}(x_2) + \alpha(x_1)\delta P^{23}(x_2) = \\ &= [\overline{\psi}(x_2) - i\alpha(x_1)\lambda^{14}\overline{\psi}(x_2)]\gamma_5\lambda^{45}[\psi(x_2) + i\alpha(x_1)\lambda^{14}\psi] = \\ &= \overline{\psi}2(x_2)\gamma_5\lambda^{45}\psi(x_2) + i\alpha(x_1)[\overline{\psi}(x_2)\gamma_5[\lambda^{14},\lambda^{45}]\psi(x_2)] + \mathcal{O}(\alpha^2(x_1)) = \\ &= \overline{\psi}(x_2)\gamma_5\lambda^{45}\psi(x_2) + i\alpha(x_1)[\overline{\psi}(x_2)\gamma_5\lambda^{3}\psi(x_2)] + \mathcal{O}(\alpha^2(x_1)), \end{aligned} \tag{C.83}$$

where

$$P_{13}^{\uparrow} = \overline{\psi}_1\gamma_5\frac{1}{2}(\mathbb{1}+\tau^3)\psi_3. \tag{C.84}$$

We can then conclude that

$$\delta_A^{x_1} P^{23}(x_2) = \frac{\delta P^{23}(x_2)}{\delta\alpha(x_1)} = i\overline{\psi}(x_2)\gamma_5\lambda^{15}\psi(x_2)\delta(x_2-x_1) = iP_{13}^{\uparrow}(x_2)\delta(x_2-x_1). \quad \text{(C.85)}$$

Eq. (C.85) leads to the following Ward-identity

$$i\left\langle P_{13}^{\uparrow}(x_2)\right\rangle = -2\mu\int d^4x_1\left\langle P_{12}^{+}(x_1)P_{23}^{-}(x_2)\right\rangle. \quad \text{(C.86)}$$

The generalization to six or n flavors is straightforward and gives as a result

$$\begin{aligned} & P_{13}^{\uparrow}(x_2)P_{34}^{+}(x_3)P_{45}^{-}(x_4)P_{56}^{+}(x_5)P_{61}^{-}(0) + P_{23}^{-}(x_2)P_{34}^{+}(x_3)P_{45}^{-}(x_4)P_{56}^{+}(x_5)P_{62}^{\uparrow}(0) \\ = \; & -2i\mu\int d^4x_1\left\langle P_{12}^{+}(x_1)P_{23}^{-}(x_2)P_{34}^{+}(x_3)P_{45}^{-}(x_4)P_{56}^{+}(x_5)P_{61}^{-}(0)\right\rangle. \end{aligned} \quad \text{(C.87)}$$

We are originally interested in the integrated Ward-identity, since we need to use them in the Symanzik expansion of the spectral sum defined in Eq. (4.3). After integration we obtain our final result

$$\begin{aligned} & \int d^4x_2d^4x_3d^4x_4d^4x_5P_{13}^{\uparrow}(x_2)P_{34}^{+}(x_3)P_{45}^{-}(x_4)P_{56}^{+}(x_5)P_{61}^{-}(0) + \\ + \; & \int d^4x_2d^4x_3d^4x_4d^4x_5P_{23}^{-}(x_2)P_{34}^{+}(x_3)P_{45}^{-}(x_4)P_{56}^{+}(x_5)P_{62}^{\uparrow}(0) \\ = \; & -2i\mu\int d^4x_2d^4x_3d^4x_4d^4x_5\int d^4x_1\left\langle P_{12}^{+}(x_1)P_{23}^{-}(x_2)P_{34}^{+}(x_3)P_{45}^{-}(x_4)P_{56}^{+}(x_5)P_{61}^{-}(0)\right\rangle. \end{aligned} \quad \text{(C.88)}$$

A set of analogous Ward identities can be derived applying different flavors in the original vector transformation.

APPENDIX D

Details of the simulations

D.1. Dynamical simulations

The dynamical simulations used in this work were performed by the European Twisted Mass Collaboration. They correspond to two different sets, the first for $N_f = 2$ dynamical flavors of maximally twisted mass fermions [40, 41, 42], which correspond to two degenerate light quarks up and down, and the second where the strange and the charm quarks were added and correspond to $N_f = 2 + 1 + 1$ [43, 44, 45]. For the former the tree-level Symanzik improved gluon action [25, 26] was chosen, whereas for the latter, due to peculiarities introduced by the addition of the strange and the charm quark, the Iwasaki gluon action [27, 28] was used.

In Tab. D.1 and Tab. D.2 all the relevant information of all the ensembles for $N_f = 2$ and $N_f = 2 + 1 + 1$ respectively is provided, such as the lattice spacing [45, 85], r_0/a [43, 85, 115] and the renormalization constant Z_P in the $\overline{\text{MS}}$ scheme at 2 GeV [82, 84]. To help the reader we plot the most relevant parameters in Fig. D.1.

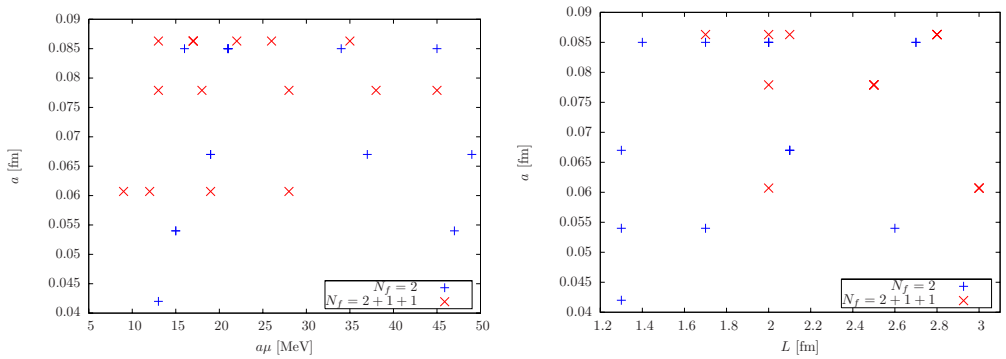

Figure D.1.: a vs. $a\mu$ (left) and a vs L (right) of all ETMC ensembles used in this work. The blue points correspond to $N_f = 2$ and the red to $N_f = 2 + 1 + 1$.

ensemble	β	L	T	$a\mu$	μ_R [MeV]	κ_c	r_0/a	a [fm]	Z_P	Z_P/Z_S	L [fm]
b30.32	3.90	32	64	0.003	16	0.160856	5.35(4)	0.085	0.437(7)	0.639(3)	2.7
b40.16	3.90	16	32	0.004	21	0.160856	5.35(4)	0.085	0.437(7)	0.639(3)	1.4
b40.20	3.90	20	40	0.004	21	0.160856	5.35(4)	0.085	0.437(7)	0.639(3)	1.7
b40.24	3.90	24	48	0.004	21	0.160856	5.35(4)	0.085	0.437(7)	0.639(3)	2.0
b40.32	3.90	32	64	0.004	21	0.160856	5.35(4)	0.085	0.437(7)	0.639(3)	2.7
b64.24	3.90	24	48	0.0064	34	0.160856	5.35(4)	0.085	0.437(7)	0.639(3)	2.0
b85.24	3.90	24	48	0.0085	45	0.160856	5.35(4)	0.085	0.437(7)	0.639(3)	2.0
c30.20	4.05	20	40	0.003	19	0.157010	6.71(4)	0.067	0.477(6)	0.682(2)	1.3
c30.32	4.05	32	64	0.003	19	0.157010	6.71(4)	0.067	0.477(6)	0.682(2)	2.1
c60.32	4.05	32	64	0.006	37	0.157010	6.71(4)	0.067	0.477(6)	0.682(2)	2.1
c80.32	4.05	32	64	0.008	49	0.157010	6.71(4)	0.067	0.477(6)	0.682(2)	2.1
d20.24	4.20	24	48	0.002	15	0.154073	8.36(6)	0.054	0.501(13)	0.713(3)	1.3
d20.48	4.20	48	96	0.002	15	0.154073	8.36(6)	0.054	0.501(13)	0.713(3)	2.6
d65.32	4.20	32	64	0.002	47	0.154073	8.36(6)	0.054	0.501(13)	0.713(3)	1.7
e17.32	4.35	32	64	0.00175	15	0.151740	9.81(13)	0.046	0.503(13)	0.740(3)	1.3

Table D.1.: Relevant parameters of the gauge configurations for $N_f = 2$. The value of Z_P corresponds to $\overline{\text{MS}}$ scheme at 2GeV. All references are given in the main text.

ensemble	β	L	$a\mu_l$	μ_R [MeV]	$a\mu_\sigma$	$a\mu_\delta$	κ_c	r_0/a	a [fm]	Z_P	Z_P/Z_S	L [fm]
A30.32	1.90	32	0.003	13	0.15	0.190	0.1632720	5.231(38)	0.0863(4)	0.529(9)	0.699(13)	2.8
A40.20	1.90	32	0.004	17	0.15	0.190	0.1632700	5.231(38)	0.0863(4)	0.529(9)	0.699(13)	1.7
A40.24	1.90	32	0.004	17	0.15	0.190	0.1632700	5.231(38)	0.0863(4)	0.529(9)	0.699(13)	2.1
A40.32	1.90	32	0.004	17	0.15	0.190	0.1632700	5.231(38)	0.0863(4)	0.529(9)	0.699(13)	2.8
A50.32	1.90	32	0.005	22	0.15	0.190	0.1632670	5.231(38)	0.0863(4)	0.529(9)	0.699(13)	2.8
A60.24	1.90	24	0.006	26	0.15	0.190	0.1632650	5.231(38)	0.0863(4)	0.529(9)	0.699(13)	2.1
A80.24	1.90	24	0.008	35	0.15	0.190	0.1632600	5.231(38)	0.0863(4)	0.529(9)	0.699(13)	2.1
B25.32	1.95	32	0.0025	13	0.135	0.170	0.1612400	5.710(41)	0.0779(4)	0.504(5)	0.697(7)	2.5
B35.32	1.95	32	0.0035	18	0.135	0.170	0.1612400	5.710(41)	0.0779(4)	0.504(5)	0.697(7)	2.5
B55.32	1.95	32	0.0055	28	0.135	0.170	0.1612360	5.710(41)	0.0779(4)	0.504(5)	0.697(7)	2.5
B75.32	1.95	32	0.0075	38	0.135	0.170	0.1612320	5.710(41)	0.0779(4)	0.504(5)	0.697(7)	2.5
B85.24	1.95	24	0.0085	45	0.135	0.170	0.1612312	5.710(41)	0.0779(4)	0.504(5)	0.697(7)	1.9
D45.32	2.10	32	0.0045	28	0.0837	0.1077	0.156315	7.538(58)	0.0607(2)	0.514(3)	0.740(5)	1.9
D30.48	2.10	48	0.0030	19	0.120	0.1385	0.156355	7.538(58)	0.0607(2)	0.514(3)	0.740(5)	2.9
D20.48	2.10	48	0.0020	12	0.120	0.1385	0.156357	7.538(58)	0.0607(2)	0.514(3)	0.740(5)	2.9
D15.48	2.10	48	0.0015	9	0.120	0.1385	0.156361	7.538(58)	0.0607(2)	0.514(3)	0.740(5)	2.9

Table D.2.: Relevant parameters of the gauge configurations for $N_f = 2 + 1 + 1$. The value of Z_P corresponds to $\overline{\text{MS}}$ scheme at 2GeV. All references are given in the main text. In all cases $T = 2L$.

D.2. Pure gauge simulations

In order to compute the topological susceptibility in the pure gluon theory we generated four quenched ensembles at different β values keeping the volume and the quark mass constant. In this Appendix we report on the details of the generation of the gauge configurations and the tuning of all parameters involved.

D.2.1. Details of the generation of the pure gauge ensembles

Since one of our goals was to attempt a first test of the Witten-Veneziano formula we were interested in computing the topological susceptibility matching the physical situation of the masses of the mesons η and η' which were computed using the ensemble B55.32. For this reason we used the Iwasaki gauge action introduced in Eq. (2.14), to generate the configurations, since this was the action chosen by the ETM Collaboration to generate the $N_f = 2 + 1 + 1$ ensembles. This action is implemented in the tmLQCD package [78], which we used to generate all the configurations using the HMC algorithm. We are aware that there are more efficient algorithms to generate quenched ensembles, however, due to the choice of the action which was only implemented in tmLQCD package where the HMC algorithm was, at the time, the only available algorithm.

We were also interested in matching the volume and the quark mass of the ensemble B55.32. To this end we tuned our first ensemble with a volume $32^3 \times 64$ at $\beta = 2.67$, which corresponds to a value of $r_0/a \approx 5.71$, matching r_0/a and the volume of B55.32. We kept the mass fixed at $a\mu = 0.0055$ as well.

Once we had the first set of configurations we decided to generate three more ensembles at different lattice spacings while keeping constant the physical volume and the quark mass. This allows us to perform the continuum limit extrapolation of quantities evaluated in these ensembles.

All the details of the ensembles and their corresponding parameters can be found in Tab. D.3. In the following sections we explain in detail the computation of r_0/a and the tuning to κ_c for the ensembles. In order to compute the quark mass value we maintained constant the product $r_0\mu$.

In Chap.2 we already introduced the quenched approximation and the methods which are typically in use. In the following lines we explain the technical details involved in the production of the pure gauge configurations used in this work.

During the generation of gauge configurations it is common to compute few variables online to control that the production is going as expected. These variables are typically the plaquette, ΔH, $e^{-\Delta H}$ and a logical variable which informs about the acceptance of the configuration among others [1]. In particular we use the plaquette to study the *thermalization* of the configurations. For instance, for $\beta = 2.37$ the thermalization of the plaquette is reached after less than 40 trajectories. However the thermalization depends on the observable evaluated and the parameters of the configurations and for this reason we, conservatively, consider thermalized configurations after 1000 trajectories. Fig. D.2

[1] We refer to any general reference about Monte Carlo algorithm for more details, e.g. [21, 20].

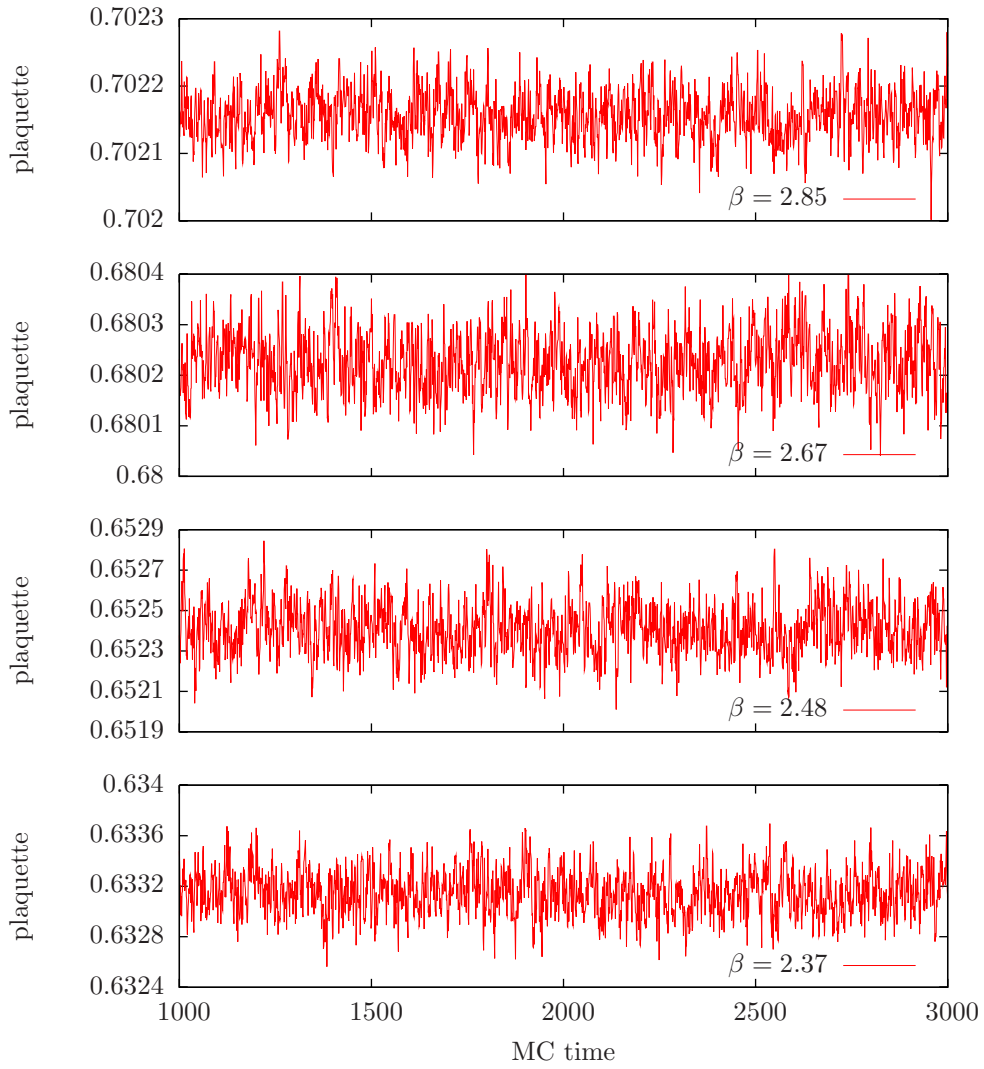

Figure D.2.: Monte Carlo history of the plaquette for the first 2000 thermalized trajectories for the quenched ensembles at $\beta = 2.37,\ 2.48,\ 2.67$ and 2.85.

β	Volume	r_0/a	a [fm]	$a\mu$	κ_c^χ
2.37	$20^3 \times 40$	3.59(2)(3)	0.1393	0.0087	0.158738
2.48	$24^3 \times 48$	4.28(1)(5)	0.1182	0.0073	0.154928
2.67	$32^3 \times 64$	5.69(2)(3)	0.0879	0.0055	0.150269
2.85	$40^3 \times 80$	7.29(7)(1)	0.0686	0.0043	0.147180

Table D.3.: All relevant parameters of the pure gauge ensembles for $\beta = 2.37,\ 2.48,\ 2.67$ and 2.85. The errors of r_0/a are statistical and systematic as explained in the text.

shows the plaquette of the first 3000 thermalized configurations for the different ensembles that we generated for this work.

Another important parameter, that is controlled by the number of integration steps, is the acceptance of the configurations. Due to the computational cost of the generation of gauge configurations, it is important to guarantee a high acceptance rate which is directly related to the quantity $e^{-\Delta H}$. In all our cases over 90% of all configurations were accepted. In Tab. D.4 we show the details of the run where we include the average plaquette and its corresponding integrated autocorrelation time, together with the approximated number of trajectories generated for each ensemble and the acceptance rate.

In the following sections we report on the calculation of r_0/a and the strategy followed to tune to κ_c in the chiral limit for the quenched case.

β	Plaquette	τ_{int} Plaq.	trajectories	Acceptance
2.37	0.633125(13)	2.77(9)	∼80000	0.985
2.48	0.652407(10)	2.67(8)	∼100000	0.979
2.67	0.680220(10)	2.49(7)	∼150000	0.971
2.85	0.702151(8)	2.37(6)	∼200000	0.936

Table D.4.: Relevant parameters for the generation of quenched ensembles for $\beta = 2.37,\ 2.48,\ 2.67$ and 2.85. τ_{int} corresponds to the plaquette.

D.2.2. Computation of r_0/a

In order to set the scale of the pure gauge configurations that we generated we used the so-called Sommer parameter r_0 [24] which is directly related to the static quark potential.

We briefly summarize the method to compute r_0/a, however for a more detailed explanation we refer to [119]. To perform all the calculations of this section we used a code provided by Marc Wagner. We first compute planar Wilson loops $W(r,t)$ of size $r \times t$, which were already introduced in Chap.2 and illustrated in Fig. 2.3, whose expectation value is directly related to the static potential $V(r)$ of a quark-antiquark pair separated

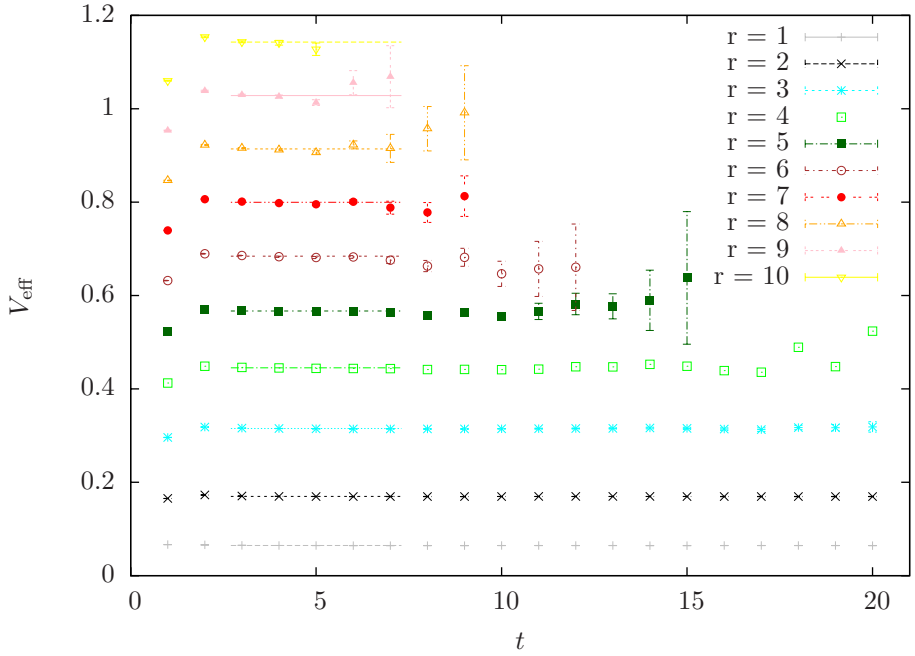

Figure D.3.: Effective potential V_{eff} given by Eq. (D.2) as a function of t for different values of r for $\beta = 2.37$. The lines correspond to the constant fit in the range of t where we observe a plateau for each r.

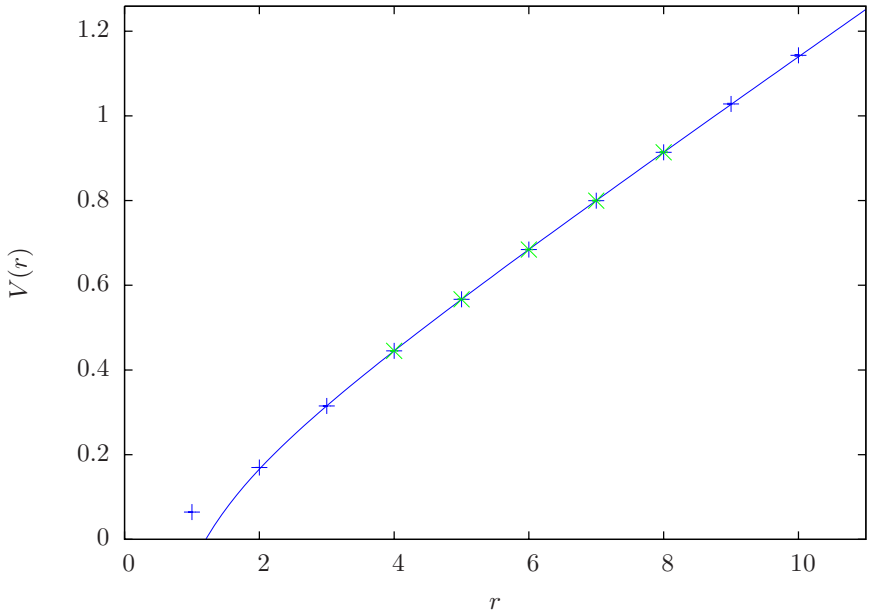

Figure D.4.: Static quark-antiquark potential $V(r)$ for $\beta = 2.37$. The line corresponds to a fit to Eq. (D.3) where only the highlighted points were taken into account.

β	t	r	V	α	σ	χ^2/dof	r_0/a
2.37	3-7	4-8	0.062(10)	0.230(23)	0.1099(10)	0.03	3.593(15)
2.48	5-8	5-9	0.136(14)	0.335(39)	0.0733(13)	0.01	4.281(14)
2.67	5-8	6-11	0.123(5)	0.208(17)	0.0445(4)	0.04	5.691(15)
2.85	8-14	5-8	0.160(10)	0.283(26)	0.0257(9)	0.00	7.290(68)

Table D.5.: Results of the potential $V(r)$, the parameters of the fit α and σ and the corresponding value of r_0/a for quenched ensembles. All the errors are only statistical.

for a distance r:

$$\langle W(r,t)\rangle = C_1\, \mathrm{e}^{-tV(r)}, \quad t >> 1 \tag{D.1}$$

To obtain $V(r)$ we first compute the Wilson loops $W(r,t)$ for different values of the temporal extend t keeping the spatial extend r fixed. In this way we can construct an effective potential which is defined as

$$V_{\mathrm{eff}}(r,t) = \frac{1}{a}\ln\left(\frac{\langle W(r,t)\rangle}{\langle W(r,t+a)\rangle}\right). \tag{D.2}$$

As can be seen in Fig. D.3, V_{eff} shows a plateau for large enough values of t where the excited states are suppressed and small enough to keep the statistical error under control. A constant fit to the plateau gives a value of the potential $V(r)$ which is now independent from t.

If we repeat this calculation for different values of the spatial extend r we can finally fit the potential $V(r)$ to the function

$$V(r) = V_0 + \frac{\alpha}{r} + \sigma r \tag{D.3}$$

and extract the value of the parameters α and σ. An example of $V(r)$ and the corresponding fit is shown in Fig. D.4.

We are interested in those parameters because the force $F(r)$, defined as

$$F(r) = \frac{d}{dr}V(r) = -\frac{\alpha}{r^2} + \sigma, \tag{D.4}$$

is directly related to the Sommer parameter r_0 through the following expression

$$F(r_0)r_0^2 = 1.65. \tag{D.5}$$

This allows us to compute the ratio r_0/a for each ensemble if we consider the equation in lattice units

$$\frac{r_0}{a} = \sqrt{\frac{1.65+\alpha}{\sigma a^2}}. \tag{D.6}$$

Moreover, since the physical value of r_0 is known for the quenched approximation to

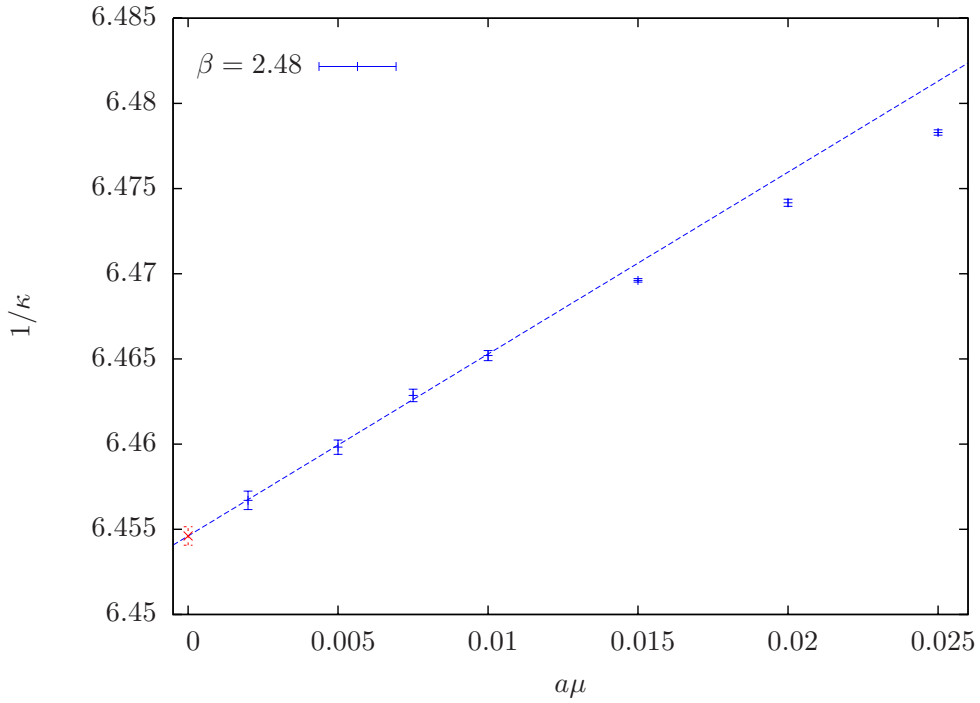

Figure D.5.: Chiral extrapolation of κ_c for the quenched ensemble at $\beta = 2.48$. The red point corresponds to the linear chiral extrapolation.

be $r_0 \approx 0.5$ fm we can set the scale of our lattices.

The values of r_0/a, and the relevant parameters of the fit performed to obtain that result can be found in Tab. D.5 for all the quenched ensembles generated for this work. In this case only statistical errors are quoted which in the case of r_0/a were computed using jackknife with blocking. However, Tab. D.3 shows the statistical and the systematic error which was computed from the spread obtained through different fits performed at different intervals of t and r for the case of V_{eff} and $V(r)$ respectively.

D.2.3. Computation of κ_c

In order to perform calculations on the configurations one needs to tune κ to κ_c for the valence quarks to guarantee $\mathcal{O}(a^2)$ scaling.

In order to compute κ_c we followed the strategy introduced in [120]. In this way we compute κ_c for different values of the quark mass $a\mu$ and finally extrapolate to the chiral limit. We then use the chirally extrapolated value as our κ_c to perform our calculations, since it has been proven to reduce the discretization effects [120].

In order to tune κ to its critical value we use m_{pcac} which was defined in Eq. (2.42). Thus we tune κ for each quark mass $a\mu$ to a value which gives a $m_{\text{pcac}} < 0.1 a\mu$.

To compute m_{pcac} we first need to compute the correlators $\langle PP \rangle$ and $\langle PA \rangle$ where

$$P^a = \overline{\chi}\gamma_5\tau^a\chi, \qquad A^a_\mu = \overline{\chi}\gamma_5\gamma_5\tau^a\chi. \tag{D.7}$$

We performed all this calculations offline. However it is very common that this information is directly computed online for each configuration.

Once we have the offline measurements we computed the m_{pcac} using the publicly available *hadron* R package [121] which contains special routines to fit quantities related to latticeQCD.

We finally obtained the values of κ which give a vanishing m_{pcac} for different values of $a\mu$. We then could perform a chiral extrapolation linear in the quark mass for each β value and obtain κ_c^χ. In Fig. D.5 we show an example which corresponds to $\beta = 2.48$ of κ_c for several $a\mu$, we perform the chiral fit considering only the lowest masses $a\mu < 0.01$ since the larger masses deviates from the linear behavior. Notice that the data is highly correlated and therefore it is very important to consider the correlation to compute the errors. All the results are provided in Tab. D.3.

APPENDIX E

Notes on the mode number

E.1. Raw data

	A30.32		A40.32		A50.32	
M_R	ν	τ_{int}	ν	τ_{int}	ν	τ_{int}
57.6	89.8(1.0)	0.6(2)	91.2(8)	0.7(2)	27.0(4)	0.48(8)
76.8	127.4(2.1)	1.3(5)	130.0(1.2)	1.0(3)	40.1(6)	0.6(2)
96.0	165.4(3.5)	8.8(4.2)	170.6(1.2)	2.2(8)	55.4(7)	0.7(2)
115.2	210.2(2.4)	1.9(7)	215.6(1.4)	0.7(2)	68.6(1.3)	1.5(5)
M_R	$\partial\nu/\partial M_R$	$a^3\Sigma_{\text{eff}}$	$\partial\nu/\partial M_R$	$a^3\Sigma_{\text{eff}}$	$\partial\nu/\partial M_R$	$a^3\Sigma_{\text{eff}}$
90.9	4680(120)	0.003466 (89)(33)	4873(59)	0.003576 (44)(34)	5154(57)	0.003738 (42)(35)

	A60.24		A80.24	
M_R [MeV]	ν	τ_{int}	ν	τ_{int}
57.6	27.04(44)	0.48(8)	24.2(4)	0.7(2)
76.8	40.11(56)	0.58(16)	39.7(5)	0.5(1)
96.0	55.37(74)	0.66(17)	54.0(5)	0.6(1)
115.2	68.65(1.35)	1.53(54)	70.1(7)	0.7(2)
M_R [MeV]	$\partial\nu/\partial M_R$	$a^3\Sigma_{\text{eff}}$	$\partial\nu/\partial M_R$	$a^3\Sigma_{\text{eff}}$
90.9	1662(40)	0.003754 (91)(36)	1806(29)	0.003917 (63)(37)

Table E.1.: Mode number using spectral projectors for $N_f = 2+1+1$ $\beta = 1.90$. $a^3\Sigma_{\text{eff}}$ and $\partial\nu/\partial M_R$ at M_R are also included. The errors quoted are statistical; in the case of $a^3\Sigma_{\text{eff}}$ the second error corresponds to Z_P.

	B25.32		B35.32		B55.32	
M_R	ν	τ_{int}	ν	τ_{int}	ν	τ_{int}
53.5	48.3(7)	0.7(2)	51.1(5)	0.44(6)	47.3(6)	0.42(9)
71.4	69.1(7)	0.49(7)	73.7(6)	0.45(7)	71.6(6)	0.48(7)
89.4	91.8(1.1)	1.3(3)	95.0(9)	1.4(4)	94.5(4)	0.73(9)
107.1	114.5(1.6)	1.2(3)	119.6(1.6)	1.7(6)	120.3(1.0)	0.7(2)
M_R	$\partial\nu/\partial M_R$	$a^3\Sigma_{\text{eff}}$	$\partial\nu/\partial M_R$	$a^3\Sigma_{\text{eff}}$	$\partial\nu/\partial M_R$	$a^3\Sigma_{\text{eff}}$
80.3	3094(67)	0.002289 (49)(23)	3163(58)	0.002311 (42)(23)	3380(45)	0.00238 (32)(24)

	B75.32		B85.24	
M_R [MeV]	ν	τ_{int}	ν	τ_{int}
53.5	38.8(4)	0.59(14)	9.8(2)	0.44(7)
71.4	67.0(9)	0.6(2)	19.4(3)	0.38(6)
89.4	92.4(9)	0.8(2)	31.0(5)	0.7(2)
107.1	118.0(9)	0.50(7)	37.3(5)	0.48(7)
M_R [MeV]	$\partial\nu/\partial M_R$	$a^3\Sigma_{\text{eff}}$	$\partial\nu/\partial M_R$	$a^3\Sigma_{\text{eff}}$
80.3	3757(43)	0.00249 (29)(25)	1319(16)	0.00264 (32)(26)

Table E.2.: Mode number using spectral projectors for $N_f = 2+1+1$ $\beta = 1.95$. The result of $a^3\Sigma_{\text{eff}}$ and $\partial\nu/\partial M_R$ at M_R are also included. The errors quoted are statistical; in the case of $a^3\Sigma_{\text{eff}}$ the second error corresponds to Z_P.

	D15.48		D20.48		D30.48		D45.32	
M_R [MeV]	ν	τ_{int}	ν	τ_{int}	ν	τ_{int}	ν	τ_{int}
53.7	87.2(68)	0.5(1)	85.8(7)	0.41(6)	14.4(3)	0.4(7)	15.0(3)	0.49(7)
71.6	121.9(1.10)	0.7(2)	121.0(7)	0.49(7)	21.4(5)	0.7(2)	22.3(3)	0.43(6)
89.3	155.7(1.32)	1.1(3)	155.9(1.6)	0.6(1)	29.9(5)	0.6(1)	29.0(4)	0.50(7)
106.7	195.1(1.30)	0.7(2)	194.6(1.0)	0.44(7)	35.2(6)	0.6(1)	37.3(5)	0.7(2)
M_R [MeV]	$\partial\nu/\partial M_R$	$a^3\Sigma_{\text{eff}}$	$\partial\nu/\partial M_R$	$a^3\Sigma_{\text{eff}}$	$\partial\nu/\partial M_R$	$a^3\Sigma_{\text{eff}}$	$\partial\nu/\partial M_R$	$a^3\Sigma_{\text{eff}}$
80.2	6502(79)	0.000950 (12)(55)	6581(83)	0.000946 (12)(55)	1300(34)	0.000911 (24)(5)	1337(33)	0.000936 (23)(55)

Table E.3.: Mode number using spectral projectors for $N_f = 2+1+1$ $\beta = 2.1$. The result of $a^3\Sigma_{\text{eff}}$ and $\partial\nu/\partial M_R$ at M_R are also included. The errors quoted are statistical; in the case of $a^3\Sigma_{\text{eff}}$ the second error corresponds to Z_P.

	b30.32		b40.32		b64.24		b85.24	
M_R [MeV]	ν	τ_{int}	ν	τ_{int}	ν	τ_{int}	ν	τ_{int}
52.3	54.3(60)	0.37(7)	52.41(43)	0.42(8)	13.86(21)	0.45(6)	9.07(21)	-
69.7	76.26(89)	0.58(14)	76.80(66)	0.58(10)	22.44(29)	0.67(14)	19.99(21)	-
87.1	101.00(86)	0.47(8)	101.29(71)	0.51(7)	30.89(35)	0.46(6)	29.30(24)	-
104.5	127.52(1.17)	0.57(17)	125.94(69)	0.47(6)	39.56(54)	0.82(19)	37.93(40)	-
122.0	151.02(1.50)	0.85(28)	151.91(86)	0.49(6)	48.07(55)	0.76(18)	47.42(47)	-
M_R [MeV]	$\partial\nu/\partial M_R$	$a^3\Sigma_{\text{eff}}$	$\partial\nu/\partial M_R$	$a^3\Sigma_{\text{eff}}$	$\partial\nu/\partial M_R$	$a^3\Sigma_{\text{eff}}$	$\partial\nu/\partial M_R$	$a^3\Sigma_{\text{eff}}$
87.1	3217(41)	0.002369 (30)(38)	3291(26)	0.002391 (19)(38)	1138(15)	0.002482 (34)(40)	1285(13)	0.002602 (27)(42)

Table E.4.: Mode number using spectral projectors for $N_f = 2$ $\beta = 3.9$. The result of $a^3\Sigma_{\text{eff}}$ and $\partial\nu/\partial M_R$ at M_R are also included. The errors quoted are statistical; in the case of $a^3\Sigma_{\text{eff}}$ the second error corresponds to Z_P.

	c30.32		c60.32		c80.32	
M_R [MeV]	ν	τ_{int}	ν	τ_{int}	ν	τ_{int}
54.5	23.79(34)	0.47(7)	18.95(43)	0.44(8)	11.17(22)	0.46(7)
72.7	34.08(44)	0.51(8)	31.10(62)	0.71(22)	26.82(47)	0.86(23)
90.8	44.20(88)	1.38(47)	43.34(99)	1.27(47)	39.14(55)	0.63(15)
109.0	54.40(85)	1.09(35)	53.59(75)	0.83(29)	50.15(67)	0.76(18)
127.2	65.85(1.18)	1.56(52)	66.61(79)	0.49(9)	63.05(69)	0.75(18)
M_R [MeV]	$\partial\nu/\partial M_R$	$a^3\Sigma_{\text{eff}}$	$\partial\nu/\partial M_R$	$a^3\Sigma_{\text{eff}}$	$\partial\nu/\partial M_R$	$a^3\Sigma_{\text{eff}}$
90.8	1676(35)	0.001229 (26)(15)	1912(31)	0.001308 (21)(16)	3137(23)	0.001343 (14)(17)

Table E.5.: Mode number using spectral projectors for $N_f = 2$ $\beta = 4.05$. The result of $a^3\Sigma_{\text{eff}}$ and $\partial\nu/\partial M_R$ at M_R are also included. The errors quoted are statistical; in the case of $a^3\Sigma_{\text{eff}}$ the second error corresponds to Z_P.

	d20.48		d64.32	
M_R [MeV]	ν	τ_{int}	ν	τ_{int}
54.4	52.39(87)	0.46(11)	5.29(16)	0.43(6)
72.8	69.38(1.37)	0.98(42)	11.79(39)	1.12(33)
90.9	90.15(1.14)	0.59(19)	16.24(36)	0.71(17)
109.1	111.80(1.24)	0.49(11)	21.99(30)	0.43(6)
127.3	133.94(1.48)	0.55(18)	26.56(57)	0.96(26)
M_R [MeV]	$\partial\nu/\partial M_R$	$a^3\Sigma_{\text{eff}}$	$\partial\nu/\partial M_R$	$a^3\Sigma_{\text{eff}}$
90.9	4053(73)	0.0005920 (110)(150)	1098(18)	0.0007017 (117)(182)

Table E.6.: Mode number using spectral projectors for $N_f = 2$ $\beta = 4.2$. The result of $a^3\Sigma_{\text{eff}}$ and $\partial\nu/\partial M_R$ at M_R are also included. The errors quoted are statistical; in the case of $a^3\Sigma_{\text{eff}}$ the second error corresponds to Z_P.

	b40.16		b40.20		b40.24		b40.32	
M_R [MeV]	ν	τ_{int}	ν	τ_{int}	ν	τ_{int}	ν	τ_{int}
52.3	2.37(7)	0.50(4)	7.0(2)	0.7(1)	22.6(7)	2.1(6)	52.4(4)	0.4(1)
69.7	3.92(11)	0.7(1)	10.8(3)	0.7(1)	23.4(1.0)	1.8(7)	76.8(7)	0.6(1)
87.1	5.29(14)	1.9(6)	14.6(4)	3.5(1.3)	32.5(3)	1.4(5)	101.3(7)	0.5(1)
104.5	7.03(21)	1.4(3)	18.5(5)	1.2(3)	39.9(1.4)	1.9(7)	125.9(7)	0.5(1)
122.0	8.66(27)	1.8(4)	22.6(7)	2.1(6)	48.5(1.6)	1.7(6)	151.7(10)	0.5(1)
M_R [MeV]	$\partial\nu/\partial M_R$	$a^3\Sigma_{\text{eff}}$	$\partial\nu/\partial M_R$	$a^3\Sigma_{\text{eff}}$	$\partial\nu/\partial M_R$	$a^3\Sigma_{\text{eff}}$	$\partial\nu/\partial M_R$	$a^3\Sigma_{\text{eff}}$
87.1	204(5)	0.002368 (63)(38)	515(16)	0.002451 (75)(39)	1082(17)	0.002484 (40)(40)	3292(26)	0.002391 (19)(38)

Table E.7.: Finite volume effects of the Mode number using spectral projectors for $N_f = 2$ at $\beta = 3.9$ and $a\mu = 0.004$. The result of $a^3\Sigma_{\text{eff}}$ and $\partial\nu/\partial M_R$ at M_R are also included. The errors quoted are statistical; in the case of $a^3\Sigma_{\text{eff}}$ the second error corresponds to Z_P.

	A40.20		A40.24		A40.32	
M_R [MeV]	ν	τ_{int}	ν	τ_{int}	ν	τ_{int}
57.6	15.3(4)	0.9(2)	28.3(4)	2.9(1.1)	91.2(8)	0.7(2)
76.8	22.3(5)	0.9(2)	40.8(8)	2.2(0.8)	130.0(1.2)	1.0(3)
96.0	30.5(6)	0.09(2)	53.4(1.0)	1.3(4)	170.6(1.2)	2.2(8)
115.2	38.1(7)	0.9(3)	67.8(1.4)	1.2(4)	215.6(1.4)	0.7(2)
M_R [MeV]	$\partial\nu/\partial M_R$	$a^3\Sigma_{\text{eff}}$	$\partial\nu/\partial M_R$	$a^3\Sigma_{\text{eff}}$	$\partial\nu/\partial M_R$	$a^3\Sigma_{\text{eff}}$
86.4	905(30)	0.004342 (143)(74)	1530(45)	0.003549 (106)(60)	4873(59)	0.003576 (44)(61)

Table E.8.: Finite volume effects of the Mode number using spectral projectors for $N_f = 2+1+1$ at $\beta = 1.90$ and $a\mu = 0.004$. The result of $a^3\Sigma_{\text{eff}}$ and $\partial\nu/\partial M_R$ at M_R are also included. The errors quoted are statistical; in the case of $a^3\Sigma_{\text{eff}}$ the second error corresponds to Z_P.

All the errors statistical errors quoted in the present section were computed using the method described in [80]. In addition all the results were cross-checked through an independent analysis using the bootstrap method. Both set all results were perfectly compatible within errors in all the cases.

E.2. Analysis of the NLO effects of χPT for the chiral extrapolation of Σ

In addition to the careful study of systematic errors that we presented in Chap.4, and motivated by the work presented in [79] we decided to follow a different strategy to confirm that we are not sensitive to the NLO effects present in Eq. (4.2) and that a linear interpolation is therefore completely justified.

We chose a particular $\beta = 4.05$ to perform this exercise, however, we are confident, due to the randomness in the choice, that the same conclusions will be reached through a different set of ensembles.

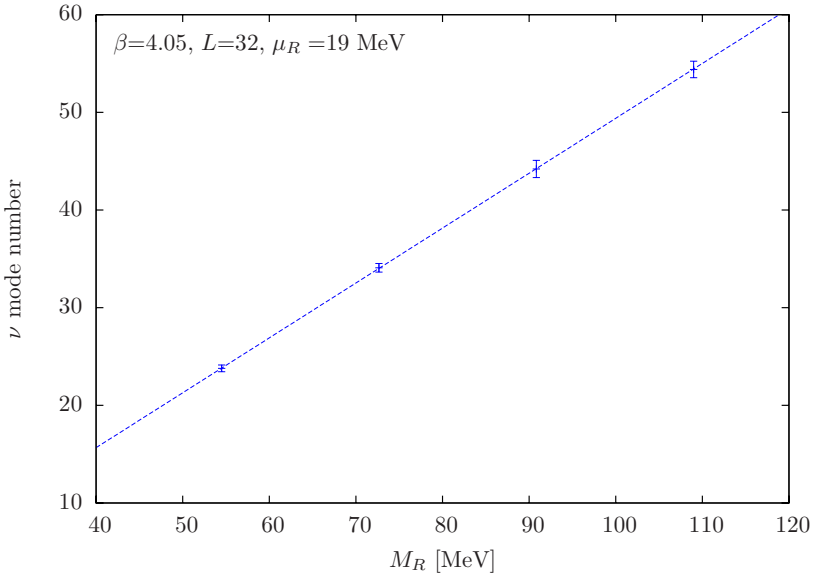

Figure E.1.: Mode number as a function of M_R for the ensemble $\beta = 4.05$, $L = 32$ and $a\mu = 19$ MeV. The line corresponds to a linear fit which contains all points. The corresponding errors of the mode number are not plotted.

Fig. E.1 shows the linear dependence of the mode number and the threshold parameter M for one of the analyzed ensembles. The basic idea behind this new strategy is to perform a chiral extrapolation for different values of M, since, in principle, the chiral value should be independent of M according to χPT. To do so we perform a linear fit of the mode number for different intervals of M, each of which contains two points. From each linear fit we can extract Σ_{eff}. We perform this analysis for three different masses and three different values of M.

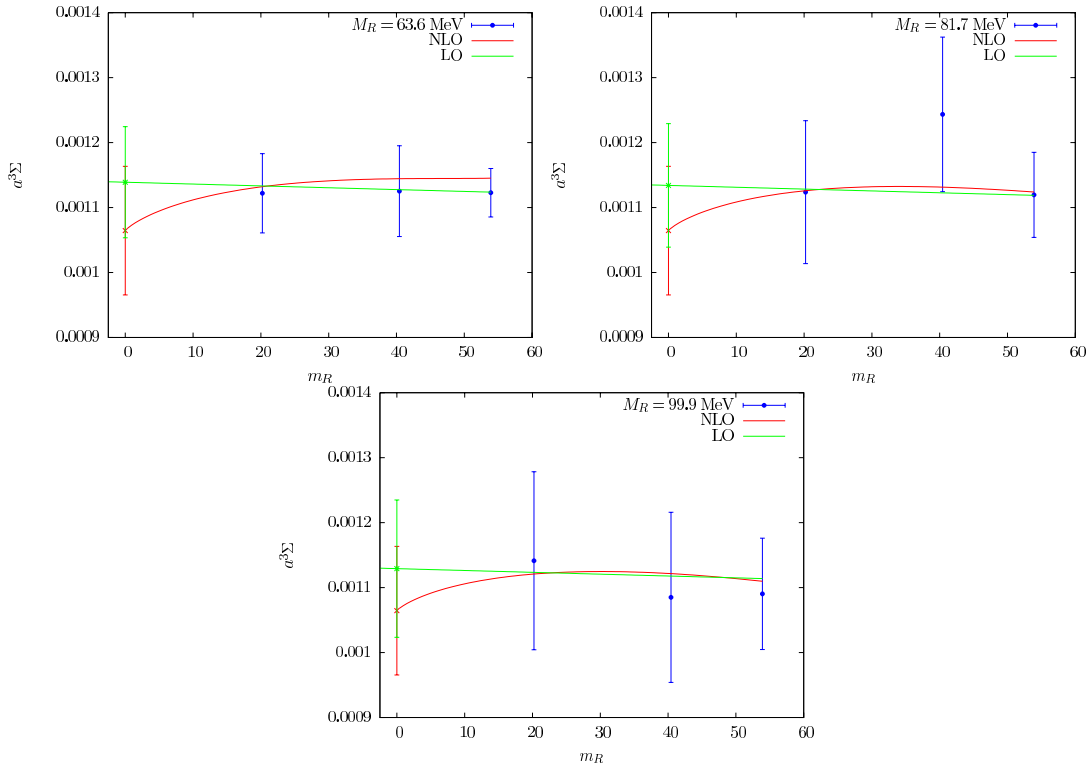

Figure E.2.: Chiral extrapolation of the chiral condensate at three different values of M. The lines correspond to a LO (green) and NLO (red) fit of χPT respectively. The corresponding value of M is shown in each plot.

fit	interval M_R [MeV]	central M_R [MeV]	$a^3\Sigma_\chi \cdot 10^{-3}$
LO	[54-109]	81.7	1.145(49)
NLO	global fit	-	1.064(99)
LO	global fit	-	1.156(68)
LO	[54-73]	63.6	1.139(86)
LO	[73-91]	81.7	1.134(95)
LO	[91-109]	99.9	1.129(106)

Table E.9.: Results of chirally extrapolated values of the chiral condensate for $\beta = 4.05$ at different values of M using LO and NLO fits of χPT.

In order to extrapolate to the chiral limit we use two approaches, a simple linear extrapolation and the NLO χPT formula given in Eq. (4.2). More concretely we performed a global fit to the equation suggested in [79] including the data for all the masses and all M. Fig. E.2 shows the individual extrapolations for each fixed M through a LO and a NLO global fit of χPT. Our data shows that we are not sensitive to the NLO effects, conclusion that supports our choice to perform a linear extrapolation. Moreover we confirm that the chirally extrapolated chiral condensate is independent of M as expected. In Tab. E.9 all the results are displayed to facilitate the comparison.

E.3. Relation of mode number, spectral sums and density chains

In this section we present the details in the calculation which leads to relate both definitions of the spectral sums given in Chap.3.

For simplicity we present again both equations. First we define the spectral sum as

$$\sigma_k(\mu, m) = \left\langle Tr\{(D_m^\dagger D_m + \mu^2)^{-k}\} \right\rangle = \sum_\lambda \frac{1}{(\lambda^2 + m_v^2)^k}, \tag{E.1}$$

where we have applied the spectral decomposition in the second equality.

On the other hand we have the relation between the spectral sum and the mode number, which is given by

$$\sigma_k(\mu, m_q) = \int_0^\infty dM \nu(M, m_q) \frac{2kM}{(M^2 + \mu^2)^{k+1}}. \tag{E.2}$$

Our goal is to relate Eq. (E.2) to Eq. (E.1). To this end we first insert the definition of the mode number, Eq. (3.3), in Eq. (E.2)

$$\sigma_k(\mu, m_q) = \int_0^\infty dM \frac{2kM}{(M^2 + \mu^2)^{k+1}} 2V \int_0^\Lambda d\lambda \rho(\lambda), \tag{E.3}$$

and then integrate by parts

$$\begin{cases} dv = \frac{2kM}{(M^2+\mu^2)^{k+1}} dM, & v = \frac{1}{(M^2+\mu^2)^{k+1}} \\ u = \int_0^\Lambda d\lambda \rho(\lambda), & du = 2V\rho(\lambda) \end{cases} d\lambda$$

where $v = v(M)$ and $u = u(\lambda)$.

$$\sigma_k(\mu, m_q) = \frac{2V \int_0^\Lambda d\lambda \rho(\lambda)}{(M^2 + \mu^2)^k} - \int_0^\infty dM \frac{2V\rho(\lambda)}{(M^2 + \mu^2)^k}. \tag{E.4}$$

The first term in Eq. (E.4) vanishes for $k \leq 3$ since we know that $\rho \sim \lambda^k$ for $M \to \infty$.

For convenience we make a change of variables to integrate over Λ instead of over M

$$\begin{array}{ll} \Lambda = \sqrt{M^2 - m^2}, & M = \sqrt{\Lambda^2 + m^2} \\ \frac{d\Lambda}{dM} = \frac{2M}{\sqrt{M^2-m^2}} = \frac{M}{\Lambda}, & dM = \frac{\Lambda}{M} d\Lambda \end{array}$$

, and we obtain

$$\begin{aligned} \sigma_k(\mu, m_q) &= \int_0^\infty d\Lambda \frac{\Lambda}{M} \frac{2V\rho(\lambda)}{(\Lambda^2 + m^2 + \mu^2)^k} = & \text{(E.5)} \\ &= 2V \int_0^\infty d\Lambda \sqrt{1 - \frac{m^2}{M^2}} \frac{\rho(\lambda)}{(\Lambda^2 + m_v^2)^k} = & \text{(E.6)} \\ &= V\sqrt{1 - \frac{m^2}{M^2}} \int_{-\infty}^\infty d\Lambda \frac{\rho(\lambda)}{(\Lambda^2 + m_v^2)^k}, & \text{(E.7)} \end{aligned}$$

where $m_v^2 = m^2 + \mu^2$ and $\frac{\Lambda}{M} = \sqrt{\frac{M^2-m^2}{m^2}} = \sqrt{1 - \frac{m^2}{M^2}}$.

If now we apply the definition of the spectral density

$$\rho(\lambda) = \frac{1}{V} \sum_{k=1}^\infty \langle \delta(\lambda - \lambda_k) \rangle \,, \tag{E.8}$$

and the definition of the δ function

$$\int dx \delta(x - x_0) f(x) = f(x_0), \tag{E.9}$$

we finally obtain

$$\begin{aligned} \sigma_k(\lambda, m) &= V \int_{-\infty}^\infty \frac{\frac{1}{V}\sum_{k=1}^\infty \langle \delta(\lambda - \lambda_k) \rangle}{(\Lambda^2 + m_v^2)^k} = & \text{(E.10)} \\ &= \frac{1}{V} \sum_{k=1}^\infty \int_{-\infty}^\infty \frac{\delta(\lambda - \lambda_k)}{(\Lambda^2 + m_v^2)} = & \text{(E.11)} \\ &= \sum_{k=1}^\infty \frac{1}{(\lambda_k^2 + m_v^2)^k}. & \text{(E.12)} \end{aligned}$$

We thus recover the expression given Eq. (E.1) and therefore we show that both definitions of the spectral sums are equivalent.

APPENDIX F

Notes on Z_P/Z_S

F.1. Raw data

$M_\star^2$	M_R	M_R [MeV]	$\langle\mathcal{A}\rangle$	τ_{int}	$\langle\mathcal{B}\rangle$	τ_{int}	Z_P/Z_S
0.001	0.2166	502	1.95(12)	0.7(2)	0.57(4)	0.7(2)	0.539(25)
0.002	0.3064	710	6.29(15)	0.6(2)	2.09(5)	0.6(1)	0.576(10)
0.003	0.3752	870	11.2(2)	0.5(1)	3.97(7)	0.6(2)	0.596(7)
0.004	0.4333	1006	16.9(2)	0.6(2)	6.24(9)	0.8(2)	0.608(6)
0.006	0.5306	1232	29.7(3)	0.7(2)	11.6(11)	0.7(2)	0.625(4)
0.007	0.5732	1330	36.7(2)	0.5(1)	14.6(9)	0.5(1)	0.631(3)
0.008	0.6128	1422	44.5(3)	0.6(2)	18(1)	0.6(2)	0.637(3)
0.009	0.6500	1508	52.2(3)	0.5(1)	21.4(1)	0.4(1)	0.64(2)
0.011	0.7186	1667	69(3)	0.5(1)	28.9(1)	0.4(1)	0.647(2)
0.012	0.7506	1741	77.8(4)	0.8(2)	33(1)	0.7(2)	0.651(2)
0.013	0.7811	1813	87.5(3)	0.4(1)	37.5(1)	0.4(1)	0.654(2)
0.014	0.8107	1881	96.9(4)	0.5(1)	41.8(2)	0.6(1)	0.657(2)
0.015	0.8391	1947	106(4)	0.7(2)	46.2(2)	0.6(1)	0.659(2)
0.01	0.6852	1589	60.5(3)	0.7(2)	25(1)	0.4(1)	0.643(2)
0.02	0.9690	2248	160.0(4)	0.5(1)	72.1(2)	0.4(1)	0.671(1)
0.03	1.187	2754	287(1)	0.5(1)	137(3)	0.5(1)	0.69(1)
0.04	1.370	3180	438(1)	0.5(1)	218(4)	0.6(1)	0.706(1)
0.05	1.532	3556	612(1)	0.5(1)	317(5)	0.5(1)	0.720(1)
0.1	2.167	5029	1741(1)	0.5(1)	1044(1)	0.6(1)	0.774(1)

Table F.1.: Observables $\langle\mathcal{A}\rangle$, $\langle\mathcal{B}\rangle$ for different values of M_R and their corresponding integrated autocorrelation time τ_{int} for $N_f = 2$, $\beta = 3.9$, $a\mu = 0.004$ and $L = 8$. Also the result Z_P/Z_S is included in the table.

$M_\star^2$	M_R	M_R [MeV]	$\langle\mathcal{A}\rangle$	τ_{int}	$\langle\mathcal{B}\rangle$	τ_{int}	Z_P/Z_S
0.0001	0.0131	159	12.3(3)	1.1(4)	2.81(8)	1.1(3)	0.479(9))
0.0003	0.0226	275	26.5(4)	0.5(1)	7.42(12)	0.51(09)	0.529(6)
0.0005	0.0292	355	38.8(7)	1.4(6)	11.7(2)	1.0(4)	0.55(7)
0.0007	0.0346	420	51.1(8)	0.9(3)	16.1(2)	0.9(3)	0.562(6)
0.0017	0.0414	502	70.4(1.0)	1.2(4)	23.2(3)	1.0(3)	0.574(5)
0.0015	0.0507	615	286(2)	1.6(8)	109(1)	1.3(6)	0.62(3)
0.002	0.0585	710	138(1)	1.1(4)	49.2(3)	0.8(2)	0.597(3)
0.003	0.0716	870	217(1)	1.5(6)	80.2(4)	1.0(3)	0.609(3)
0.004	0.0827	1006	302(2)	1.6(6)	115(1)	1.2(4)	0.617(2)
0.005	0.0925	1123	378(22)	4.7(2.3)	147(8)	4.7(2.3)	0.623(3)
0.007	0.1095	1330	610(2)	1.1(3)	244(1)	0.7(2)	0.633(1)
0.008	0.1170	1422	726(2)	0.7(2)	294(1)	0.7(2)	0.637(1)
0.009	0.1241	1508	848(2)	0.8(2)	349(1)	0.6(2)	0.641(1)
0.01	0.1308	1589	980(2)	1.3(4)	407(1)	1.0(3)	0.644(1)

Table F.2.: Observables $\langle\mathcal{A}\rangle$, $\langle\mathcal{B}\rangle$ for different values of M_R and their corresponding integrated autocorrelation time τ_{int} for $N_f = 2$, $\beta = 3.9$, $a\mu = 0.004$ and $L = 16$. Also the result Z_P/Z_S is included in the table.

$M_\star^2$	M_R	M_R [MeV]	$\langle\mathcal{A}\rangle$	τ_{int}	$\langle\mathcal{B}\rangle$	τ_{int}	Z_P/Z_S
0.0000317	0.0385	89	33.1(4)	0.9(3)	5.9(1)	0.7(3)	0.424(5)
0.00004	0.0433	100	37.9(4)	0.6(2)	7.2(1)	0.6(2)	0.435(4)
0.00005	0.0483	112	44(4)	0.8(3)	8.8(1)	0.6(2)	0.447(4)
0.00006	0.0530	132	48.9(7)	0.8(3)	10.2(2)	0.9(3)	0.456(5)
0.00007	0.0572	133	53.3(5)	0.6(2	11.6(1)	0.5(2)	0.466(3)
0.0001	0.0685	159	66.8(7)	0.9(3)	15.4(2)	0.7(3)	0.481(3)
0.0003	0.1186	275	138(1)	0.8(3)	38.8(3)	0.9(3)	0.53(3)
0.0004	0.1370	317	169(1)	0.9(3)	49.6(3)	0.7(3)	0.541(3)
0.00057	0.1532	355	201(1)	0.8(3)	60.6(4)	0.7(3)	0.549(3)
0.0007	0.1811	420	262(1)	0.7(3)	82.8(4)	0.6(2)	0.562(2)
0.001	0.2166	502	359(2)	0.8(3)	118(1)	0.8(3)	0.574(2)
0.002	0.3064	710	704(3)	0.9(3)	250(1)	0.8(3)	0.596(1)
0.003	0.3752	870	1099(3)	0.8(3)	406(1)	0.8(3)	0.608(1)
0.004	0.4333	1006	1538(4)	1.0(4)	584(1)	1.1(5)	0.616(1)
0.005	0.4844	1123	2019(3)	0.6(3)	782(1)	0.9(4)	0.623(1)
0.007	0.5732	1330	3092(4)	0.9(3)	1237(2)	0.9(4)	0.633(1)
0.01	0.6852	1590	4952(5)	1.0(3)	2054(2)	1.1(5)	0.644(1)

Table F.3.: Observables $\langle\mathcal{A}\rangle$, $\langle\mathcal{B}\rangle$ for different values of M_R and their corresponding integrated autocorrelation time τ_{int} for $N_f = 2$, $\beta = 3.9$, $a\mu = 0.004$ and $L = 24$. Also the result Z_P/Z_S is included in the table.

$M_\star^2$	M_R	M_R [MeV]	$\langle\mathcal{A}\rangle$	τ_{int}	$\langle\mathcal{B}\rangle$	τ_{int}	Z_P/Z_S
0.00007	0.0518	152	10.5(4)	0.5(1)	3.4(1)	0.5(1)	0.569(15)
0.0005	0.1385	407	50.8(9)	0.8(3)	20.7(4)	0.8(3)	0.638(8)
0.0007	0.1639	482	70.2(9)	0.5(1)	29.2(4)	0.5(1)	0.645(6)
0.001	0.1959	576	101(1)	0.5(1)	42.8(5)	0.5(1)	0.652(5)
0.003	0.3393	998	365(2)	0.6(2)	164(1)	0.5(1)	0.670(3)
0.005	0.4381	1289	713(3)	0.6(2)	329(1)	0.5(1)	0.678(2)
0.0077	0.5184	1525	1132(4)	0.6(2)	529(2)	0.6(2)	0.684(2)
0.01	0.6196	1824	1878(4)	0.4(1)	896(2)	0.4(1)	0.691(1)

Table F.4.: Observables $\langle\mathcal{A}\rangle$, $\langle\mathcal{B}\rangle$ for different values of M_R and their corresponding integrated autocorrelation time τ_{int} for $N_f = 2$, $\beta = 4.05$, $a\mu = 0.003$ and $L = 20$. Also the result Z_P/Z_S is included in the table.

$M_\star^2$	M_R	M_R [MeV]	$\langle\mathcal{A}\rangle$	τ_{int}	$\langle\mathcal{B}\rangle$	τ_{int}	Z_P/Z_S
0.00003	0.0328	118	7.5(4)	0.8(3)	2.9(2)	0.5(1)	0.622(24)
0.00005	0.0424	154	10.6(4)	0.8(3)	4.4(2)	0.7(2)	0.641(18)
0.00007	0.0501	183	12.8(5)	0.9(3)	5.5(2)	0.8(3)	0.655(19)
0.0001	0.0600	218	16.5(6)	1.0(4)	7.3(2)	0.8(3)	0.665(17)
0.0003	0.1041	380	41.5(7)	0.5(1)	19.6(3)	0.5(1)	0.687(8)
0.0005	0.1344	491	68.9(9)	0.8(3)	33.4(4)	0.5(1)	0.697(6)
0.0007	0.1590	580	99(1)	0.6(2)	48.6(7)	0.9(3)	0.702(7)
0.001	0.1900	694	144(1)	0.8(3)	71.7(8)	0.7(2)	0.706(5)
0.003	0.3292	1202	575(3)	0.6(2)	293.5(1.6)	0.8(3)	0.714(3)
0.005	0.4249	1552	1175(4)	0.5(1)	606.8(2.0)	0.6(2)	0.718(2)
0.007	0.5027	1837	1909(4)	0.5(1)	994.2(2.0)	0.5(1)	0.722(1)
0.01	0.6010	2196	3251(6)	0.4(1)	1711.9(3.2)	0.5(1)	0.726(1)

Table F.5.: Observables $\langle\mathcal{A}\rangle$, $\langle\mathcal{B}\rangle$ for different values of M_R and their corresponding integrated autocorrelation time τ_{int} for $N_f = 2$, $\beta = 4.2$, $a\mu = 0.002$ and $L = 24$. Also the result Z_P/Z_S is included in the table.

$M_\star^2$	M_R	M_R [MeV]	$\langle\mathcal{A}\rangle$	τ_{int}	$\langle\mathcal{B}\rangle$	τ_{int}	Z_P/Z_S
0.0003	0.0959	411	85(1)	1.1(4)	46(1)	1.0(4)	0.7381(87)
0.0005	0.1238	530	214(1)	0.4(1)	118(7)	0.4(1)	0.7438(32)
0.0007	0.1465	628	1449(6)	0.6(2)	808(4)	0.6(2)	0.7468(26)
0.003	0.3034	1300	3062(8)	0.5(1)	1715(5)	0.5(1)	0.7485(15)
0.005	0.3916	1678	5090(14)	0.5(1)	2862(10)	0.5(1)	0.7500(17)
0.007	0.4633	1987	8786(25)	0.5(1)	4978(17)	0.5(1)	0.7527(17)

Table F.6.: Observables $\langle\mathcal{A}\rangle$, $\langle\mathcal{B}\rangle$ for different values of M_R and their corresponding integrated autocorrelation time τ_{int} for $N_f = 2$, $\beta = 4.35$, $a\mu = 0.00175$ and $L = 32$. Also the result Z_P/Z_S is included in the table.

$M_\star^2$	$r_0 M$	M [MeV]	$\langle \mathcal{A} \rangle$	τ_{int}	$\langle \mathcal{B} \rangle$	τ_{int}	Z_P/Z_S
0.0002	0.1526	61	115(1)	0.5(1)	29.9(3)	0.4(1)	0.509(3)
0.0004	0.2181	86	171(2)	1.0(3)	50.9(4)	0.6(2)	0.546(4)
0.0008	0.3079	122	260(1)	0.4(1)	86.3(4)	0.3(1)	0.576(2)
0.001	0.3451	136	297(2)	0.6(1)	102(1)	0.5(1)	0.585(2)
0.003	0.5961	236	682(2)	0.5(1)	264(1)	0.5(1)	0.622(1)
0.005	0.7709	305	1112(2)	0.4(1)	451(1)	0.4(1)	0.637(1)
0.007	0.9131	361	159(4)	0.5(1)	6672)	0.6(1)	0.646(1)
0.009	1.035	409	2137(4)	0.5(1)	913(2)	0.5(1)	0.653(1)
0.012	1.195	472	3036(5)	0.7(2)	1331(2)	0.5(1)	0.662(1)
0.014	1.291	510	3703(5)	0.5(1)	1648(2)	0.5(1)	0.667(1)
0.016	1.381	545	4408(5)	0.4(1)	1987(3)	0.4(1)	0.671(1)
0.018	1.463	578	5164(6)	0.5(1)	2360(3)	0.4(1)	0.676(1)
0.01	1.092	431	2433(5)	0.6(2)	1048(2)	0.7(2)	0.656(1)
0.02	1.544	609	5949(7)	0.6(1)	2751(3)	0.5(1)	0.68(1)
0.025	1.726	681	8081(7)	0.5(1)	3837(4)	0.5(1)	0.689(1)
0.03	1.892	746	10449(9)	0.6(2)	5083(4)	0.6(2)	0.697(1)
0.035	2.043	806	13020(9)	0.6(1)	6475(4)	0.5(1)	0.705(1)
0.04	2.184	862	15792(10)	0.5(1)	8017(5)	0.5(1)	0.712(1)
0.045	2.316	914	18768(10)	0.5(1)	9710(6)	0.6(1)	0.719(1)
0.05	2.442	964	21923(12)	0.6(1)	11542(7)	0.6(1)	0.726(1)
0.055	2.560	1011	25239(11)	0.4(1)	13519(6)	0.4(1)	0.732(1)
0.07	2.888	1140	36195(14)	0.5(1)	20308(8)	0.4(1)	0.749(1)

Table F.7.: Observables $\langle \mathcal{A} \rangle$, $\langle \mathcal{B} \rangle$ for different values of M_R and their corresponding integrated autocorrelation time τ_{int} for quenched ensembles $\beta = 2.37$, $a\mu = 0.0087$ and $L = 20$. Also the result Z_P/Z_S is included in the table.

$M_\star^2$	$r_0 M$	M [MeV]	$\langle \mathcal{A} \rangle$	τ_{int}	$\langle \mathcal{B} \rangle$	τ_{int}	Z_P/Z_S
0.0005	0.2917	116	236(1)	0.4(1)	93.8(5)	0.5(1)	0.630(2)
0.0007	0.3471	137	294(1)	0.5(1)	121(1)	0.5(1)	0.642(2)
0.0009	0.3944	156	349(1)	0.5(1)	147(1)	0.5(1)	0.649(2)
0.001	0.4152	164	374(2)	0.5(1)	159(1)	0.4(1)	0.653(2)
0.003	0.7180	284	963(2)	0.5(1)	444(1)	0.4(1)	0.679(2)
0.005	0.9282	367	1668(4)	0.6(2)	790(2)	0.6(2)	0.688(1)
0.007	1.099	434	2497(4)	0.5(1)	1204(2)	0.5(1)	0.694(1)
0.01	1.315	519	3939(5)	0.5(1)	1938(3)	0.6(2)	0.701(1)
0.013	1.499	592	5598(6)	0.6(2)	2798(3)	0.6(2)	0.707(1)
0.015	1.609	635	6833(8)	0.7(2)	3452(4)	0.7(2)	0.711(1)
0.017	1.712	677	8141(7)	0.6(2)	4149(4)	0.5(1)	0.714(0)
0.02	1.859	734	10265(9)	0.6(2)	5299(5)	0.6(1)	0.718(0)
0.025	2.078	820	14188(8)	0.7(1)	7469(5)	0.5(1)	0.726(0)
0.03	2.277	899	18562(10)	0.5(1)	9948(6)	0.5(1)	0.732(0)
0.035	2.459	971	23337(13)	0.5(1)	12717(7)	0.5(1)	0.738(0)
0.04	2.630	1038	28520(12)	0.5(1)	15790(7)	0.5(1)	0.744(0)

Table F.8.: Observables $\langle \mathcal{A} \rangle$, $\langle \mathcal{B} \rangle$ for different values of M_R and their corresponding integrated autocorrelation time τ_{int} for quenched ensembles $\beta = 2.48$, $a\mu = 0.0074$ and $L = 24$. Also the result Z_P/Z_S is included in the table.

$M_\star^2$	$r_0 M$	M [MeV]	$\langle \mathcal{A} \rangle$	τ_{int}	$\langle \mathcal{B} \rangle$	τ_{int}	Z_P/Z_S
0.00001	0.0544	23	28.6(6)	0.4(1)	6.9(2)	0.5(1)	0.493(8)
0.00003	0.0984	39	68(1)	0.9(4)	24.6(4)	0.6(2)	0.599(8)
0.00005	0.1276	51	92(1)	0.7(3)	36.2(6)	0.9(3)	0.629(6)
0.00007	0.1496	60	112(1)	0.5(1)	47.1(4)	0.3(1)	0.649(4)
0.0003	0.3146	125	248(2)	0.5(1)	125(1)	0.5(1)	0.708(4)
0.0005	0.4059	161	348(2)	0.4(1)	181(1)	0.5(1)	0.721(3)
0.0007	0.4830	191	446(2)	0.4(1)	236(1)	0.5(1)	0.728(3)
0.001	0.5781	228	594(3)	0.4(1)	319(2)	0.4(1)	0.733(3)
0.003	0.9989	395	1849(4)	0.4(1)	1024(2)	0.4(1)	0.744(1)
0.005	1.292	510	3524(7)	0.6(2)	1978(4)	0.6(2)	0.749(1)
0.007	1.530	604	5544(6)	0.4(1)	3134(3)	0.4(1)	0.752(1)
0.009	1.735	685	7928(9)	0.5(1)	4513(6)	0.5(1)	0.754(1)
0.01	1.830	722	9223(10)	0.5(1)	5266(6)	0.5(1)	0.756(1)
0.011	1.918	757	10555(12)	0.4(1)	6045(7)	0.4(1)	0.757(1)
0.013	2.086	823	13528(9)	0.4(1)	7791(5)	0.3(1)	0.759(0)
0.015	2.240	884	16717(13)	0.5(1)	9681(8)	0.5(1)	0.761(0)
0.02	2.587	1021	25828(17)	0.3(1)	15141(11)	0.4(1)	0.766(0)

Table F.9.: Observables $\langle \mathcal{A} \rangle$, $\langle \mathcal{B} \rangle$ for different values of M_R and their corresponding integrated autocorrelation time τ_{int} for quenched ensembles $\beta = 2.67$, $a\mu = 0.0055$ and $L = 32$. Also the result Z_P/Z_S is included in the table.

$M_\star^2$	$r_0 M$	M [MeV]	$\langle \mathcal{A} \rangle$	τ_{int}	$\langle \mathcal{B} \rangle$	τ_{int}	Z_P/Z_S
0.0001	0.2377	94	161(1)	0.5(1)	88.8(6)	0.5(1)	0.743(3)
0.0005	0.5287	210	462(2)	0.7(2)	278(1)	0.7(2)	0.775(3)
0.001	0.7525	297	876(3)	0.5(1)	533(2)	0.5(1)	0.780(2)
0.002	1.062	420	1927(3)	0.4(1)	1184(2)	0.4(1)	0.784(1)
0.003	1.300	515	3251(4)	0.5(1)	2005(3)	0.5(1)	0.785(1)
0.004	1.506	595	4797(6)	0.6(1)	2969(4)	0.5(1)	0.787(1)
0.005	1.682	665	6563(6)	0.4(1)	4066(4)	0.4(1)	0.787(1)
0.006	1.844	728	8555(8)	0.6(1)	5310(5)	0.6(1)	0.788(0)
0.007	1.992	786	10719(8)	0.5(1)	6666(5)	0.5(1)	0.789(0)
0.008	2.130	841	13096(8)	0.4(1)	8158(5)	0.4(1)	0.789(0)
0.009	2.258	892	15633(9)	0.5(1)	9756(6)	0.5(1)	0.79(0)
0.01	2.382	940	18344(11)	0.5(1)	11466(7)	0.5(1)	0.791(0)

Table F.10.: Observables $\langle \mathcal{A} \rangle$, $\langle \mathcal{B} \rangle$ for different values of M_R and their corresponding integrated autocorrelation time τ_{int} for quenched ensembles $\beta = 2.85$, $a\mu = 0.0043$ and $L = 40$. Also the result Z_P/Z_S is included in the table.

All the errors quoted in the present section are statistical and were computed using the method described in [80]. In addition all the results were cross-checked through an independent analysis using the bootstrap method. Both set all results were perfectly compatible within errors in all the cases.

APPENDIX G

Notes on the topological susceptibility

G.1. Analogous representation of $\chi_{\rm top}$ for spectral projectors and twisted mass

In this section we will partly follow the steps introduced in [106] where a definition of the continuum topological susceptibility which is free of short distance singularities was introduced.

We start from an expression analogous to the index theorem

$$\mathrm{Tr}\{\gamma_5 f(D)\} = f(0)Q \tag{G.1}$$

where Q is the topological charge and D is the Dirac operator.

From Eq. (G.1) the topological charge can be defined in many different ways. In particular, in Ref. [106] the following was proposed

$$\begin{aligned} a^{4r} \sum_{x_1 \ldots x_r} \langle P_{r1}(x_1) S_{12}(x_2) \ldots S_{r-1\, r}(x_r) \rangle_F = \\ - \mathrm{Tr}\{\gamma_5 (D_{m_1})^{-1} (D_{m_2})^{-1} \ldots (D_{m_r})^{-1}\} \end{aligned} \tag{G.2}$$

where in this case we have applied a Wilson-type Dirac operator and the $\langle\rangle_F$ represents the fermion expectation value, i.e. Wick contractions.

Following a particular example we can easily show the intermediate steps which lead to Eq. (G.2)

$$\begin{aligned} a^{16} \sum_{x_1 \ldots x_4} \langle P_{41}(x_1) S_{12}(x_2) S_{23}(x_3) S_{34}(x_4) \rangle_F \\ = a^{16} \sum_{x_1 \ldots x_4} \left\langle \overline{\psi}_4 \gamma_5 \psi_1 \; \overline{\psi}_1 \psi_2 \; \overline{\psi}_2 \psi_3 \; \overline{\psi}_3 \; \psi_4 \right\rangle_F \end{aligned} \tag{G.3}$$

where for simplicity we ignore the space-time dependency. If we now apply Wick con-

tractions

$$a^{16}\sum_{x_1\ldots x_4}\left\langle \overline{\psi}_4\gamma_5\overbrace{\psi_1\overline{\psi}_1}\overbrace{\psi_2\overline{\psi}_2}\overbrace{\psi_3\overline{\psi}_3}\psi_4\right\rangle = \mathrm{Tr}\{\gamma_5\ S_1\ S_2\ S_3\ S_4\} \tag{G.4}$$

$$= \mathrm{Tr}\left\{\gamma_5 (D_{m_1})^{-1}(D_{m_2})^{-1}(D_{m_3})^{-1}(D_{m_4})^{-1}\right\} \tag{G.5}$$

where S denotes the propagators.

After the previous steps the topological charge is defined as

$$Q = -m_1\ldots m_4\ a^{16}\sum_{x_1,\ldots,x_4}\langle P_{41}(x_1)S_{12}(x_2)S_{23}(x_3)S_{34}(x_4)\rangle_F \tag{G.6}$$

Notice that the mass terms come from the evaluation at zero of $f(D) = (D+m_i)^{-1}$ which appears in Eq. (G.1).

We are ultimately interested in the application of the spectral projectors, and therefore we are interested in a definition of the topological charge in terms of $D^\dagger D$. Eq. (G.1) is generic enough to include the following function

$$\mathrm{Tr}\left\{\gamma_5 (D_{m_1})^{-1}(D^\dagger_{m_2})^{-1}(D_{m_3})^{-1}(D^\dagger_{m_4})^{-1}\right\}, \tag{G.7}$$

where we again continue with a concrete example, although the generalization is straightforward.

The corresponding density chain correlation function in this case would be

$$\mathrm{Tr}\{\gamma_5 (D_{m_1})^{-1}(D^\dagger_{m_2})^{-1}(D_{m_3})^{-1}(D^\dagger_{m_4})^{-1}\} = \mathrm{Tr}\{\gamma_5\ S_1\ S_2^\dagger\ S_3\ S_4^\dagger\} \tag{G.8}$$

$$= \mathrm{Tr}\{\gamma_5\ S_1\ \gamma_5 S_2\gamma_5\ S_3\ \gamma_5 S_4\gamma_5\} \tag{G.9}$$

$$= a^{16}\sum_{x_1\ldots x_5}\left\langle\ \overline{\psi}_4\ \psi_1\overline{\psi}_1\ \gamma_5\ \psi_2\overline{\psi}_2\ \gamma_5\ \psi_3\overline{\psi}_3\ \gamma_5\ \psi_4\right\rangle_F \tag{G.10}$$

$$= a^{16}\sum_{x_1\ldots x_5}\langle S_{41}(x_1)\ P_{12}(x_2)\ P_{23}(x_3)\ P_{34}(x_4)\rangle_F \tag{G.11}$$

We have now a definition of the topological charge which is completely analogous to Eq. (G.2) and therefore leads to a definition of the topological susceptibility which is free of divergences and regularization independent.

In addition, we are interested in the twisted mass formalism, and therefore, following the strategy presented for the mode number, we need to introduce doublets of flavors, whose components are differently discretized . Consequently, the number of flavors which we had in the case above will correspond to the number of doublets and the subindex a, b corresponds to each doublet which contains two flavors u, d in the following way

$$\psi_a = \begin{pmatrix} u_a \\ d_a \end{pmatrix}, \qquad \overline{\psi}_a = (\overline{u}_a, \overline{d}_a), \tag{G.12}$$

Thus, in order to obtain the same density chain, our correlator takes the following

form

$$a^{16}\sum_{x_1\ldots x_5}\left\langle S^+_{41}(x_1)\ P^-_{12}(x_2)\ P^+_{23}(x_3)\ P^-_{34}(x_4)\right\rangle_F, \tag{G.13}$$

where the densities are defined as

$$S^+_{ab}=\overline{\psi}_a\tau^+\psi_b=\overline{u}_a d_b \tag{G.14}$$
$$S^-_{ab}=\overline{\psi}_a\tau^-\psi_b=\overline{d}_a u_b \tag{G.15}$$
$$P^+_{ab}=\overline{\psi}_a\tau^+\gamma_5\psi_b=\overline{u}_a\gamma_5 d_b \tag{G.16}$$
$$P^-_{ab}=\overline{\psi}_a\tau^-\gamma_5\psi_b=\overline{d}_a\gamma_5 u_b \tag{G.17}$$

Again we emphasize that the components of the doublet u,d are discretized differently in the twisted mass formulation, and therefore it is important to differentiate them from the beginning.

All these singularities lead to the following result

$$a^{16}\sum_{x_1\ldots x_5}\left\langle S^+_{41}(x_1)\ P^-_{12}(x_2)\ P^+_{23}(x_3)\ P^-_{34}(x_4)\right\rangle = \tag{G.18}$$
$$= a^{16}\sum_{x_1\ldots x_5}\left\langle \overline{u}_4 d_1\ \overline{d}_1\gamma_5 u_2\ \overline{u}_2\gamma_5 d_3\ \overline{d}_3\gamma_5 u_4\right\rangle \tag{G.19}$$
$$= a^{16}\sum_{x_1\ldots x_5}\left\langle \overline{u}_4\overbrace{d_1\ \overline{d}_1}\gamma_5\overbrace{u_2\ \overline{u}_2}\gamma_5\overbrace{d_3\ \overline{d}_3}\gamma_5 u_4\right\rangle \tag{G.20}$$
$$= \mathrm{Tr}\{S_{d1}\ \gamma_5 S_{u2}\gamma_5\ S_{d3}\ \gamma_5 S_{u4}\gamma_5\gamma_5\} = \mathrm{Tr}\{\gamma_5\ S_{d1}S^\dagger_{d2}\ S_{d3}\ S^\dagger_{d4}\} \tag{G.21}$$
$$= \mathrm{Tr}\left\{\gamma_5\left(D^\dagger D+\mu^2\right)^{-2}\right\} = \sigma_2'(\mu) \tag{G.22}$$

Since all the additional flavors are degenerate in mass, we can write the density chain correlation function in terms of the spectral sum σ_2'. Thus we arrive at a completely analogous expression to what we found in the case of the mode number (Eq. (3.10)) and therefore the application of spectral projectors should follow the same principles.

G.2. $\mathcal{O}(a^2)$ scaling and short distance singularities

The present section is devoted to the study of the scaling towards the continuum limit of the topological susceptibility χ_{top}. To this end we report on the short distance singularities and prove that they vanish in the continuum limit and therefore the automatic $O(a)$ improvement still holds for this case.

The indispensable property that any operator needs to hold in order to guarantee the automatic $O(a)$ improvement given by the maximally twisted mass fermions is that it remains invariant under the $\mathcal{R}^1_5$ transformations, which written by components are

$$\begin{cases} u\to i\gamma_5 d, & \overline{u}\to i\overline{d}\gamma_5 \\ d\to i\gamma_5 u, & \overline{d}\to i\overline{u}\gamma_5. \end{cases} \tag{G.23}$$

These transformations are equivalent to the transformations to the spinor fields given by Eq. (2.33).

If we apply Eq. (G.23) to Eq. (G.13) we obtain the following expression:

$$S^+_{41}(x_1)\ P^-_{12}(x_2)\ P^+_{23}(x_3)\ P^-_{34}(x_4) = [\overline{u}_4 d_1\ \overline{d}_1\gamma_5 u_2\ \overline{u}_2\gamma_5 d_3\ \overline{d}_3\gamma_5 u_4] \xrightarrow{\mathcal{R}^1_5} (-1)^4[\overline{d}_4 u_1\ \overline{u}_1\gamma_5 d_2\ \overline{d}_2\gamma_5 u_3\ \overline{u}_3\gamma_5 d_4]. \tag{G.24}$$

As we can see recovering the original expression is not as trivial as in the case of the mode number. In this case, we need to apply an additional symmetry: charge conjugation. After this, a simple relabeling of the flavors gives us the original expression.

Following the steps described above it can be shown that Eq. (G.13) remains invariant under $\mathcal{R}^1_5$ transformations. Moreover, we can also extend the discussion and conclude for a generic, but even, number of densities, that the observable is always $\mathcal{R}^{1,2}_5$ even.

Analogously to App.C, we are now ready to show that the short distance singularities do not spoil the automatic $O(a)$ improvement, which is otherwise guaranteed for this observable, as we just explained.

In order to prove that all the contact terms that appear in the Symanzik expansion vanish at maximal twist we will follow a different strategy than the one we used in the case of the chiral condensate described in Sec.4.2. We will show that all the contact terms that arise because of the short distance singularities are $\mathcal{R}^1_5$ odd, and therefore vanish in the continuum limit. Moreover this alternative method based on symmetry properties can be equally applied to the mode number with the same results.

In this particular case, the Symanzik expansion of the observable takes the following form

$$\int d^4x_1 \dots d^4x_5 \left\langle S^+_{41}(x_1)P^-_{12}(x_2)P^+_{23}(x_3)P^-_{34}(x_4)S^+_{56}(x_5)P^-_{65}(0)\right\rangle_l \tag{G.25a}$$

$$= \int d^4x_1 \dots d^4x_5 \left\langle S^+_{41}(x_1)P^-_{12}(x_2)P^+_{23}(x_3)P^-_{34}(x_4)S^+_{56}(x_5)P^-_{65}(0)\right\rangle_0 \tag{G.25b}$$

$$+ ac_1 \int d^4x_2 d^4x_3 d^4x_4 d^4x_5 \left\langle P^\uparrow_{42}(x_2)P^+_{23}(x_3)P^-_{34}(x_4)S^+_{56}(x_5)P^-_{65}(0)\right\rangle_0 \tag{G.25c}$$

$$+ ac_2 \int d^4x_1 d^4x_2 d^4x_3 d^4x_5 \left\langle P^\downarrow_{31}(x_1)P^-_{12}(x_2)P^+_{23}(x_3)S^+_{56}(x_5)P^-_{65}(0)\right\rangle_0 \tag{G.25d}$$

$$- iac_3 \int d^4x_1 d^4x_3 d^4x_4 d^4x_5 \left\langle S^+_{41}(x_1)S^\downarrow_{13}(x_3)P^-_{34}(x_4)S^+_{56}(x_5)P^-_{65}(0)\right\rangle_0 \tag{G.25e}$$

$$- iac_4 \int d^4x_1 d^4x_2 d^4x_4 d^4x_5 \left\langle S^+_{41}(x_1)P^-_{12}(x_2)S^\uparrow_{24}(x_4)S^+_{56}(x_5)P^-_{65}(0)\right\rangle_0 \tag{G.25f}$$

$$+ ac_5 \int d^4x_1 d^4x_2 d^4x_3 d^4x_4 \left\langle S^+_{41}(x_1)P^-_{12}(x_2)P^+_{23}(x_3)P^-_{34}(x_4)P^\uparrow_{55}(0)\right\rangle_0, \tag{G.25g}$$

$$+ ac_5 \int d^4x_1 d^4x_2 d^4x_3 d^4x_4 \left\langle S^+_{41}(x_1)P^-_{12}(x_2)P^+_{23}(x_3)P^-_{34}(x_4)P^\downarrow_{66}(0)\right\rangle_0, \tag{G.25h}$$

where the subindex $\langle\rangle_0$ indicates expectation value in the continuum[1].

We have applied the operator product expansion OPE to all pairs of consecutive densities which have a common flavor structure. These cases lead to the only relevant short distance singularities, since they correspond to $O(a)$ terms in the Symanzik expansion. When three or more densities seat at the same point the arisen term is $\mathcal{O}(a^2)$ or even higher power. The results of the OPE which were used to derive Eq. (G.25) correspond to

$$P^+(x)S^-(0) \overset{x\to 0}{\sim} C_1(x)P^\uparrow(0) \tag{G.26}$$

$$P^+(x)P^-(0) \overset{x\to 0}{\sim} C_2(x)S^\uparrow(0). \tag{G.27}$$

In the following lines we are going to prove that all the contact terms that appear in Eq. (G.25) are $\mathcal{R}_5^1$ odd and therefore vanish in the continuum.

We then just apply the argument of automatic $O(a)$ improvement [38] which is based on the symmetries of the twisted mass lattice action.

The combined symmetry $\mathcal{R}_5^1 \times \mathcal{D} \times [\mu \to -\mu]$ is a symmetry of the action if we are at maximal twist. If our original operator is $\mathcal{R}_5^{1,2}$ even and even/odd $\mathcal{D}$, then an operator whose $\mathcal{D}$ is odd/even, i.e. the opposite, will have to be $\mathcal{R}_5^{1,2}$ odd to still be symmetric under $\mathcal{R}_5^1 \times \mathcal{D} \times [\mu \to -\mu]$. These already tells us that our operator has the desired automatic $O(a)$ improvement. However we are going to prove it term by term.

One important step that has to be considered is that the contact terms vanish in pairs. Individually the contact terms do not have a define $\mathcal{R}_5^{1,2}$ symmetry, whereas in pairs it can be proven that are odd under $\mathcal{R}_5^{1,2}$ transformations, and therefore vanish in the continuum limit.

We start with the first two contact terms G.25c and G.25d

$$\begin{aligned}&\left\langle P_{42}^\uparrow(x_2)P_{23}^+(x_3)P_{34}^-(x_4)S_{56}^+(x_5)P_{65}^-(0)\right\rangle_0 + \left\langle P_{31}^\downarrow(x_1)P_{12}^-(x_2)P_{23}^+(x_3)S_{56}^+(x_5)P_{65}^-(0)\right\rangle_0 \\ &= \left\langle \overline{u}_4\gamma_5 u_2\overline{u}_2\gamma_5 d_3\overline{d}_3\gamma_5 u_4\overline{u}_5 d_6\overline{d}_6\gamma_5 u_5\right\rangle_0 + \left\langle \overline{d}_3\gamma_5 d_1\overline{d}_1\gamma_5 u_2\overline{u}_2\gamma_5 d_3\overline{u}_5 d_6\overline{d}_6\gamma_5 u_5\right\rangle_0 .\end{aligned} \tag{G.28}$$

If we now apply the $\mathcal{R}_5^{1,2}$ transformations we obtain

$$-\left\langle \overline{d}_4\gamma_5 d_2\overline{d}_2\gamma_5 u_3\overline{u}_3\gamma_5 d_4\overline{d}_5 u_6\overline{u}_6\gamma_5 d_5\right\rangle - \left\langle \overline{u}_3\gamma_5 u_1\overline{u}_1\gamma_5 d_2\overline{d}_2\gamma_5 u_3\overline{d}_5 u_6\overline{u}_6\gamma_5 d_5\right\rangle \tag{G.29}$$

Just by relabeling the flavors in Eq. (G.29) we recover the original expression given in Eq. (G.28) except for a global minus sign. We have thus shown that the first two contact terms, taken in pairs, are $\mathcal{R}_5^{1,2}$ odd and therefore vanish in the continuum limit.

Completely equivalent is the calculation for the terms G.25g and G.25h. A bit more difficult is to prove that the terms G.25e and G.25f are $\mathcal{R}_5^{1,2}$ odd, since we need to apply charge conjugation to recover the original expression. However the calculation remains as simple as in the case illustrated by Eq. (G.24).

[1]Notice that in the case $S_{56}^+P_{65}^-$ the mixing with the identity, even though it would be allowed from the point of view of its trivial flavor structure, but it is actually forbidden because of parity reasons, since the product is odd and the identity by construction is parity even.

We can then conclude that whereas the original expression, in this particular case given by Eq. (G.25b), has an even number of densities and therefore is even under $\mathcal{R}_5^{1,2}$, the $O(a)$ contact terms which always correspond to two consecutive densities placed at the same point, contain an odd number of densities and therefore are $\mathcal{R}_5^{1,2}$ odd. Since all the $\mathcal{R}_5^{1,2}$ objects vanish in the continuum, none of the contact terms contribute to the expansion if we are at maximal twist, as it is in our case.

This study can be easily expanded to a generic number of densities. However, due to the fact that we are interested in a representation which can be written in terms of $D^\dagger D$, in any case the chain will contain an even number of densities, which guarantees that the contact terms will contain an odd number of operators and therefore will be odd under $\mathcal{R}_5^{1,2}$ transformation, vanishing in the continuum.

G.3. Stochastic Estimate of the Topological Susceptibility

In order to compute the observable

$$\chi_{\text{top}} = \left\langle \text{Tr}\{\gamma_5 \mathbb{R}_M^2\} \text{Tr}\{\gamma_5 \mathbb{R}_M^2\} \right\rangle \tag{G.30}$$

we need to compute $\text{Tr}\{\gamma_5 \mathbb{R}_M^2\}$ for two different sets of stochastic sources and then multiply them.

We start with the observable $\mathcal{C}$, that was defined as

$$\mathcal{C} = \frac{1}{N} \sum_{k=1}^{N} (\mathbb{R}_M \eta_k,\ \gamma_5 \mathbb{R}_M \eta_k) \tag{G.31}$$

In particular we are interested in the expectation value of the square $\left\langle \mathcal{C}^2 \right\rangle$ more explicitly $\langle \mathcal{C} * \mathcal{C}' \rangle$ where the prime indicates that both terms are computed using completely different sets of stochastic sources

$$\mathcal{C} = \frac{1}{N} \sum_{i=1}^{N} (\mathbb{R}_M \eta_i,\ \gamma_5 \mathbb{R}_M \eta_i), \qquad \mathcal{C}' = \frac{1}{N} \sum_{j=1}^{N} (\mathbb{R}_M \eta_j,\ \gamma_5 \mathbb{R}_M \eta_j) \tag{G.32}$$

In this way we can compute

$$\mathcal{C}^2 = \mathcal{C} * \mathcal{C}' = \frac{1}{N} \sum_{i=1}^{N} (\mathbb{R}_M \eta_i,\ \gamma_5 \mathbb{R}_M \eta_i) \frac{1}{N} \sum_{j=N+1}^{2N} (\mathbb{R}_M \eta_j,\ \gamma_5 \mathbb{R}_M \eta_j) \tag{G.33}$$

$$= \frac{1}{N^2} \sum_{i=1}^{N} \sum_{j=N+1}^{2N} (\mathbb{R}_M^*)^{ab} (\eta_i^*)^b \gamma_5^{ac} \mathbb{R}_M^{cd} \eta_i^d (\mathbb{R}_M^*)^{ef} (\eta_j^*)^f \gamma_5^{eg} \mathbb{R}_M^{gh} \eta_j^h \tag{G.34}$$

We apply now that $\mathbb{R}_M$ is hermitian and therefore the elements $(\mathbb{R}_M)_{ij} = (R_M^*)^{ji}$, we

can thus rewrite Eq. (G.33)

$$\mathcal{C}^2 = \frac{1}{N^2}\sum_{i=1}^{N}\sum_{j=N+1}^{2N} \mathbb{R}_M^{ba}\gamma_5^{ac}\mathbb{R}_M^{cd}\mathbb{R}_M^{fe}\gamma_5^{eg}\mathbb{R}_M^{gh}(\eta_i^*)^b\eta_i^d(\eta_j^*)^f\eta_j^h \tag{G.35}$$

Now we need to contract the stochastic sources. In this case there is only one possibility $(\overbrace{\eta_i^*)^b\eta_i^d}(\eta_j^*)^f\eta_j^h}$ which gives us the following expression

$$\mathcal{C}^2 = \frac{1}{N^2}\sum_{i=1}^{N}\sum_{j=N+1}^{2N} \mathbb{R}_M^{ba}\gamma_5^{ac}\mathbb{R}_M^{cd}\mathbb{R}_M^{fe}\gamma_5^{eg}\mathbb{R}_M^{gh}(\delta^{bd}\delta_{ii}\delta^{fh}\delta_{jj}) \tag{G.36}$$

if we apply

$$\sum_{i=1}^{N}\delta_{ii} = N, \qquad \sum_{j=N+1}^{2N}\delta_{jj} = N \tag{G.37}$$

the N terms that appeared in front of the expression cancel

$$\mathcal{C}^2 = \sum_{i=1}^{N}\sum_{j=N+1}^{2N} \mathbb{R}_M^{ba}\gamma_5^{ac}\mathbb{R}_M^{cb}\mathbb{R}_M^{fe}\gamma_5^{eg}\mathbb{R}_M^{gf} \tag{G.38}$$

$$= \sum_{i=1}^{N}\sum_{j=N+1}^{2N} \gamma_5^{ac}\mathbb{R}_M^{cb}\mathbb{R}_M^{ba}\gamma_5^{eg}\mathbb{R}_M^{gf}\mathbb{R}_M^{fe}. \tag{G.39}$$

At this point it is important to remember that we are working with elements of matrices and therefore the order is not important anymore. We can rewrite it in term of traces

$$\left\langle \mathcal{C}^2 \right\rangle = \left\langle \mathrm{Tr}\{\gamma_5\mathbb{R}_M^2\}\mathrm{Tr}\{\gamma_5\mathbb{R}_M^2\}\right\rangle. \tag{G.40}$$

The above equation tells us that we just need to compute the expectation value of $\mathcal{C}^2$ to obtain the topological susceptibility. However using two different sets of stochastic sources can be a expensive procedure, since it would mean effectively to double the effort.

If instead of using two sets, we use only one and then square the result, we expect that some correction would have to be added to the formula above. This correction will depend on the number of stochastic sources, since we expect that the correction will vanish in the limit of infinite sources. In the following lines we compute explicitly this correction by inserting twice the element $\mathcal{C}$ evaluated using the same set of sources.

$$\left\langle \mathcal{C}^2 \right\rangle = \frac{1}{N}\sum_{i=1}^{N}(\mathbb{R}_M\eta_i,\ \gamma_5\mathbb{R}_M\eta_i)\frac{1}{N}\sum_{j=1}^{N}(\mathbb{R}_M\eta_j,\ \gamma_5\mathbb{R}_M\eta_j) \tag{G.41}$$

$$= \frac{1}{N}\left[\frac{1}{N}\sum_{i=j}(\mathbb{R}_M\eta_i,\ \gamma_5\mathbb{R}_M\eta_i)(\mathbb{R}_M\eta_j,\ \gamma_5\mathbb{R}_M\eta_j)\right. \tag{G.42}$$

$$+\frac{1}{N}\sum_{i\neq j}(\mathbb{R}_M\eta_i,\ \gamma_5\mathbb{R}_M\eta_i)(\mathbb{R}_M\eta_j,\ \gamma_5\mathbb{R}_M\eta_j)\Bigg]. = \frac{1}{N}\left[T_1+T_2\right]$$

For simplicity we analyze each term individually starting with the first one T_1

$$T_1 = \frac{1}{N}\sum_i(\mathbb{R}_M\eta_i,\ \gamma_5\mathbb{R}_M\eta_i)(\mathbb{R}_M\eta_i,\ \gamma_5\mathbb{R}_M\eta_i) \tag{G.43}$$

$$= \frac{1}{N}\sum_i(\mathbb{R}^*_M)^{ab}(\eta^*_i)^b\gamma_5^{ac}\mathbb{R}^{cd}_M\eta^d_i(\mathbb{R}^*_M)^{ef}(\eta^*_i)^f\gamma_5^{eg}\mathbb{R}^{gh}_M\eta^h_i. \tag{G.44}$$

Applying again that $\mathbb{R}_M$ is hermitian and therefore $(\mathbb{R}_M)_{ij} = (R^*_M)^{ji}$ we obtain

$$T_1 = \frac{1}{N}\sum_i \mathbb{R}^{ba}_M\gamma_5^{ac}\mathbb{R}^{cd}_M\mathbb{R}^{fe}_M\gamma_5^{eg}\mathbb{R}^{gh}_M(\eta^*_i)^b\eta^d_i(\eta^*_i)^f\eta^h_i. \tag{G.45}$$

Now if we apply the contractions of the pseudo-fermions η_i we see that in this case we have more options

$$\eta^*_i\eta_i\eta^*_i\eta_i = \overbrace{\eta^*_i\eta_i}\overbrace{\eta^*_i\eta_i} + \overbrace{\eta^*_i\eta_i\eta^*_i}\eta_i, \tag{G.46}$$

since by construction $\eta^*\eta = 1$.

$$T_1 = \frac{1}{N}\sum_i \mathbb{R}^{ba}_M\gamma_5^{ac}\mathbb{R}^{cd}_M\mathbb{R}^{fe}_M\gamma_5^{eg}\mathbb{R}^{gh}_M\left[\delta^{bd}\delta_{ii}\delta^{fh}\delta_{ii} + \delta^{bh}\delta_{ii}\delta^{df}\delta_i i\right]. \tag{G.47}$$

If we apply $\sum_i \delta_{ii}\delta_{ii} = N$ we cancel the$N$ factor that appears in front of the expression and we finally get

$$T_1 = \mathbb{R}^{ba}_M\gamma_5^{ac}\mathbb{R}^{cb}_M\mathbb{R}^{fe}_M\gamma_5^{eg}\mathbb{R}^{gf}_M + \mathbb{R}^{ba}_M\gamma_5^{ac}\mathbb{R}^{cd}_M\mathbb{R}^{de}_M\gamma_5^{eg}\mathbb{R}^{gb}_M \tag{G.48}$$

$$= \gamma_5^{ac}\mathbb{R}^{cb}_M\mathbb{R}^{ba}_M\gamma_5^{eg}\mathbb{R}^{gf}_M\mathbb{R}^{fe}_M + \gamma_5^{ac}\mathbb{R}^{cd}_M\mathbb{R}^{de}_M\gamma_5^{eg}\mathbb{R}^{gb}_M\mathbb{R}^{ba}_M \tag{G.49}$$

$$= \mathrm{Tr}\{\gamma_5\mathbb{R}^2_M\}\mathrm{Tr}\{\gamma_5\mathbb{R}^2_M\} + \mathrm{Tr}\{\gamma_5\mathbb{R}^2_M\gamma_5\mathbb{R}^2_M\}. \tag{G.50}$$

We still have to analyze the second term T_2

$$T_2 = \frac{1}{N}\sum_{i\neq j}^{N-1}\sum_j^N(\mathbb{R}_M\eta_i,\ \gamma_5\mathbb{R}_M\eta_i)(\mathbb{R}_M\eta_j,\ \gamma_5\mathbb{R}_M\eta_j) \tag{G.51}$$

$$= \frac{1}{N}\sum_{i\neq j}\sum_j(\mathbb{R}^*_M)^{ab}(\eta^*_i)^b\gamma_5^{ac}\mathbb{R}^{cd}_M\eta^d_i(\mathbb{R}^*_M)^{ef}(\eta^*_j)^f\gamma_5^{eg}\mathbb{R}^{gh}_M\eta^h_j \tag{G.52}$$

$$= \frac{1}{N}\sum_{i\neq j}^{N-1}\sum_j^N \mathbb{R}^{ba}_M\gamma_5^{ac}\mathbb{R}^{cd}_M\mathbb{R}^{fe}_M\gamma_5^{eg}\mathbb{R}^{gh}_M\overbrace{(\eta^*_i)^b\eta^d_i}\overbrace{(\eta^*_j)^f\eta^h_j} \tag{G.53}$$

$$= \frac{1}{N}\sum_{i\neq j}^{N-1}\sum_{j}^{N}\mathbb{R}_M^{ba}\gamma_5^{ac}\mathbb{R}_M^{cd}\mathbb{R}_M^{fe}\gamma_5^{eg}\mathbb{R}_M^{gh}(\delta^{ab}\delta_{ii}\delta^{fh}\delta_{jj}). \tag{G.54}$$

Now we sum up the δ's and we get $\sum_i^{N-1}\delta_{ii} = N-1$ and $\sum_j^N \delta_{jj} = N$ and we finally obtain

$$T_2 = (N-1)\mathbb{R}_M^{ba}\gamma_5^{ac}\mathbb{R}_M^{cb}\mathbb{R}_M^{fe}\gamma_5^{eg}\mathbb{R}_M^{gf} \tag{G.55}$$
$$= (N-1)\gamma_5^{ac}\mathbb{R}_M^{cb}\mathbb{R}_M^{ba}\gamma_5^{eg}\mathbb{R}_M^{gf}\mathbb{R}_M^{fe} \tag{G.56}$$
$$= (N-1)\mathrm{Tr}\{\gamma_5\mathbb{R}_M^2\}\mathrm{Tr}\{\gamma_5\mathbb{R}_M^2\}. \tag{G.57}$$

Now we have to insert the above results into Eq. (G.42)

$$\mathcal{C}^2 = \frac{1}{N}\left[T_1 + T_2\right] \tag{G.58}$$
$$= \frac{1}{N}\Big[\mathrm{Tr}\{\gamma_5\mathbb{R}_M^2\}\mathrm{Tr}\{\gamma_5\mathbb{R}_M^2\} + \mathrm{Tr}\{\gamma_5\mathbb{R}_M^2\gamma_5\mathbb{R}_M^2\} \tag{G.59}$$
$$+ (N-1)\mathrm{Tr}\{\gamma_5\mathbb{R}_M^2\}\mathrm{Tr}\{\gamma_5\mathbb{R}_M^2\}\Big]. \tag{G.60}$$

Finally we obtain

$$\mathcal{C}^2 = \mathrm{Tr}\{\gamma_5\mathbb{R}_M^2\}\mathrm{Tr}\{\gamma_5\mathbb{R}_M^2\} + \frac{1}{N}\mathrm{Tr}\{\gamma_5\mathbb{R}_M^2\gamma_5\mathbb{R}_M^2\}, \tag{G.61}$$

and therefore

$$\left\langle \mathrm{Tr}\{\gamma_5\mathbb{R}_M^2\}\mathrm{Tr}\{\gamma_5\mathbb{R}_M^2\}\right\rangle = \left\langle\mathcal{C}^2\right\rangle - \frac{1}{N}\left\langle\mathrm{Tr}\{\gamma_5\mathbb{R}_M^2\gamma_5\mathbb{R}_M^2\}\right\rangle$$
$$= \left\langle\mathcal{C}^2\right\rangle - \frac{\langle\mathcal{B}\rangle}{N}. \tag{G.62}$$

We can see that the correction depends directly on the number of sources, as expected, and therefore in the limit where $N\to\infty$ we recover the original expression (Eq. (G.40)) obtained when two different sets of stochastic sources are used.

G.3.1. Numerical test

In order to test numerically the theoretical proof given above we compare both results $\left\langle\mathcal{C}^2\right\rangle - \langle\mathcal{B}\rangle/V$ and $\langle\mathcal{C}_1\mathcal{C}_2\rangle$ for the $N_f = 2$ ensemble b40.32, for which we computed 12 sources.

On the one hand, we computed $\mathcal{C}_1$ and $\mathcal{C}_2$ using 2 different sets of 6 sources and build the product $\mathcal{C}_1\mathcal{C}_2$ for each configuration. On the other hand we computed $\mathcal{C}$ using 12 sources and squared the result to obtain $\mathcal{C}^2$.

Tab. G.1 shows the results obtained for $\langle\mathcal{A}\rangle$, $\langle\mathcal{B}\rangle$, $\langle\mathcal{C}\rangle$, $\langle\mathcal{C}_1\rangle$ and $\langle C_2\rangle$. However the

$\langle A \rangle$	$\langle B \rangle$	$\langle \mathcal{C} \rangle$	$\langle \mathcal{C}_1 \rangle$	$\langle \mathcal{C}_2 \rangle$
100.5(5)	17.8(1)	-0.37(37)	-0.45(41)	-0.31(36)

Table G.1.: Numerical test of the stochastic correction to $\mathcal{C}$. The $N_f = 2$ ensemble corresponds to a $32^3 \times 64$ lattice at $\beta = 3.9$ and $a\mu = 0.004$.

$\langle \mathcal{C}^2 \rangle$	$\langle \mathcal{C}'^2 \rangle$	$\langle \mathcal{C}_1 \mathcal{C}_2 \rangle$
10.0(1.3)	8.56(1.31)	8.54(1.29)

Table G.2.: Numerical test of the stochastic correction to $\mathcal{C}$. The $N_f = 2$ ensemble corresponds to a $32^3 \times 64$ lattice at $\beta = 3.9$ and $a\mu = 0.004$. $\langle \mathcal{C}_1 \rangle$ and $\langle \mathcal{C}_2 \rangle$ were computed using 2 different sets of 6 sources, whereas $\langle \mathcal{C}^2 \rangle$ was computed for 12 sources. $\langle C'^2 \rangle$ corresponds to the *corrected* $\langle \mathcal{C}^2 \rangle$

most relevant information is displayed in Tab. G.2 where one can find $\langle \mathcal{C}^2 \rangle$, $\langle \mathcal{C}_1 \mathcal{C}_2 \rangle$ and the *corrected* $\langle \mathcal{C}^2 \rangle$ denoted by $\langle \mathcal{C}'^2 \rangle$ and given by

$$\langle \mathcal{C}'^2 \rangle = \langle \mathcal{C}^2 \rangle - \frac{\langle \mathcal{B} \rangle}{V}, \tag{G.63}$$

where V is the volume.

The results confirm that the corrected result corresponds to the value obtained using two separated sets of stochastic sources, as expected.

Bibliography

[1] M. E. Peskin and D. V. Schroeder, *An Introduction to Quantum Field Theory*. 1995.

[2] M. Srednicki, *Quantum Field Theory*. 2007.

[3] M. Gell-Mann, "A Schematic Model of Baryons and Mesons," *Phys.Lett.* **8** (1964) 214–215.

[4] G. Zweig, "An SU(3) Model for Strong Interaction Symmetry and its Breaking. Pt. 1,".

[5] T. Feldmann, "Quark Structure of Pseudoscalar Mesons," *Int.J.Mod.Phys.* **A15** (2000) 159–207.

[6] C.-N. Yang and R. L. Mills, "Conservation of Isotopic Spin and Isotopic Gauge Invariance," *Phys.Rev.* **96** (1954) 191–195.

[7] K. G. Wilson, "Confinement of Quarks," *Phys.Rev.* **D10** (1974) 2445–2459.

[8] D. Gross and F. Wilczek, "Ultraviolet Behavior of Nonabelian Gauge Theories," *Phys.Rev.Lett.* **30** (1973) 1343–1346.

[9] H. D. Politzer, "Reliable Perturbative Results for Strong Interactions?," *Phys.Rev.Lett.* **30** (1973) 1346–1349.

[10] D. B. Kaplan, "Chiral Symmetry and Lattice Fermions," `arXiv:0912.2560 [hep-lat]`.

[11] M. Creutz, "Confinement, Chiral Symmetry, and the Lattice," *Acta Phys.Slov.* **61** (2011) 1–127, `arXiv:1103.3304 [hep-lat]`.

[12] S. L. Adler, "Axial Vector Vertex in Spinor Electrodynamics," *Phys.Rev.* **177** (1969) 2426–2438.

[13] J. Bell and R. Jackiw, "A PCAC Puzzle: pi0 –> gamma gamma in the sigma Model," *Nuovo Cim.* **A60** (1969) 47–61.

[14] K. Fujikawa, "Path Integral Measure for Gauge Invariant Fermion Theories," *Phys.Rev.Lett.* **42** (1979) 1195.

[15] M. Atiyah and I. Singer, "The Index of Elliptic Operators. 5.," *Annals Math.* **93** (1971) 139–149.

[16] E. Witten, "Current Algebra Theorems for the U(1) Goldstone Boson," *Nucl.Phys.* **B156** (1979) 269.

[17] G. Veneziano, "U(1) Without Instantons," *Nucl.Phys.* **B159** (1979) 213–224.

[18] L. Giusti, G. Rossi, M. Testa, and G. Veneziano, "The U(A)(1) Problem on the Lattice with Ginsparg-Wilson Fermions," *Nucl.Phys.* **B628** (2002) 234–252.

[19] L. Giusti, G. Rossi, M. Testa, and G. Veneziano, "The U(A)(1) Problem on the Lattice," *Nucl.Phys.Proc.Suppl.* **106** (2002) 1001–1003.

[20] C. Gattringer and C. B. Lang, "Quantum Chromodynamics on the Lattice," *Lect.Notes Phys.* **788** (2010) 1–211.

[21] H. Rothe, "Lattice Gauge Theories: An Introduction," *World Sci.Lect.Notes Phys.* **43** (1992) 1–381.

[22] R. Gupta, "Introduction to Lattice QCD: Course," `arXiv:hep-lat/9807028 [hep-lat]`.

[23] S. Elitzur, "Impossibility of Spontaneously Breaking Local Symmetries," *Phys.Rev.* **D12** (1975) 3978–3982.

[24] R. Sommer, "A New Way to Set the Energy Scale in Lattice Gauge Theories and its Applications to the Static Force and alpha-s in SU(2) Yang-Mills Theory," *Nucl.Phys.* **B411** (1994) 839–854.

[25] P. Weisz, "Continuum Limit Improved Lattice Action for Pure Yang-Mills Theory. 1.," *Nucl.Phys.* **B212** (1983) 1.

[26] M. Lüscher and P. Weisz, "On-Shell Improved Lattice Gauge Theories," *Commun.Math.Phys.* **97** (1985) 59.

[27] Y. Iwasaki, "Renormalization Group Analysis of Lattice Theories and Improved Lattice Action: Two-Dimensional Nonlinear O(N) Sigma Model," *Nucl.Phys.* **B258** (1985) 141–156.

[28] Y. Iwasaki, K. Kanaya, T. Kaneko, and T. Yoshie, "Scaling in SU(3) Pure Gauge Theory with a Renormalization Group Improved Action," *Phys.Rev.* **D56** (1997) 151–160.

[29] K. G. Wilson, "Quarks and Strings on a Lattice,".

[30] M. Lüscher, S. Sint, R. Sommer, and P. Weisz, "Chiral Symmetry and O(a) Improvement in Lattice QCD," *Nucl.Phys.* **B478** (1996) 365–400.

[31] B. Sheikholeslami and R. Wohlert, "Improved Continuum Limit Lattice Action for QCD with Wilson Fermions," *Nucl.Phys.* **B259** (1985) 572.

[32] P. Fritzsch *et al.*, "The Strange Quark Mass and Lambda Parameter of Two Flavor QCD," *Nucl.Phys.* **B865** (2012) 397–429.

[33] S. Sint, "Lattice QCD with a Chiral Twist," `arXiv:hep-lat/0702008 [HEP-LAT]`.

[34] A. Shindler, "Twisted Mass Lattice QCD," *Phys.Rept.* **461** (2008) 37–110.

[35] R. Frezzotti, P. A. Grassi, S. Sint, and P. Weisz, "A Local Formulation of Lattice QCD Without Unphysical Fermion Zero Modes," *Nucl.Phys.Proc.Suppl.* **83** (2000) 941–946.

[36] **Alpha** Collaboration, R. Frezzotti, P. A. Grassi, S. Sint, and P. Weisz, "Lattice QCD with a Chirally Twisted Mass Term," *JHEP* **0108** (2001) 058.

[37] **ALPHA** Collaboration, R. Frezzotti, S. Sint, and P. Weisz, "O(a) Improved Twisted Mass Lattice QCD," *JHEP* **0107** (2001) 048.

[38] R. Frezzotti and G. Rossi, "Chirally Improving Wilson Fermions. 1. O(a) Improvement," *JHEP* **0408** (2004) 007.

[39] R. Frezzotti, G. Martinelli, M. Papinutto, and G. Rossi, "Reducing Cutoff Effects in Maximally Twisted Lattice QCD Close to the Chiral Limit," *JHEP* **0604** (2006) 038.

[40] **ETM** Collaboration, R. Baron *et al.*, "Light Meson Physics from Maximally Twisted Mass Lattice QCD," *JHEP* **1008** (2010) 097.

[41] **ETM** Collaboration, P. Boucaud *et al.*, "Dynamical Twisted Mass Fermions with Light Quarks," *Phys.Lett.* **B650** (2007) 304–311.

[42] **ETM collaboration** Collaboration, P. Boucaud *et al.*, "Dynamical Twisted Mass Fermions with Light Quarks: Simulation and Analysis Details," *Comput.Phys.Commun.* **179** (2008) 695–715, `arXiv:0803.0224 [hep-lat]`.

[43] R. Baron *et al.*, "Light Hadrons from Lattice QCD with Light (u,d), Strange and Charm Dynamical Quarks," *JHEP* **1006** (2010) 111.

[44] **ETM** Collaboration, R. Baron *et al.*, "Computing K and D Meson Masses with $N_f = 2+1+1$ Twisted Mass Lattice QCD," *Comput.Phys.Commun.* **182** (2011) 299–316.

[45] **ETM** Collaboration, R. Baron *et al.*, "Light Hadrons from Nf=2+1+1 Dynamical Twisted Mass Fermions," *PoS* **LATTICE2010** (2010) 123.

[46] H. B. Nielsen and M. Ninomiya, "No Go Theorem for Regularizing Chiral Fermions," *Phys.Lett.* **B105** (1981) 219.

[47] P. H. Ginsparg and K. G. Wilson, "A Remnant of Chiral Symmetry on the Lattice," *Phys.Rev.* **D25** (1982) 2649.

[48] H. Neuberger, "Exactly Massless Quarks on the Lattice," *Phys.Lett.* **B417** (1998) 141–144.

[49] H. Neuberger, "More About Exactly Massless Quarks on the Lattice," *Phys.Lett.* **B427** (1998) 353–355.

[50] M. Lüscher, "Exact Chiral Symmetry on the Lattice and the Ginsparg-Wilson Relation," *Phys.Lett.* **B428** (1998) 342–345.

[51] P. Hasenfratz, V. Laliena, and F. Niedermayer, "The Index Theorem in QCD with a Finite Cutoff," *Phys.Lett.* **B427** (1998) 125–131.

[52] K. Fujikawa, "A Continuum Limit of the Chiral Jacobian in Lattice Gauge Theory," *Nucl.Phys.* **B546** (1999) 480–494.

[53] K. Cichy, G. Herdoíza, and K. Jansen, "Continuum Limit of Overlap Valence Quarks on a Twisted Mass Sea," *Nucl.Phys.* **B847** (2011) 179–196.

[54] K. Cichy, V. Drach, E. García-Ramos, G. Herdoíza, and K. Jansen, "Overlap Valence Quarks on a Twisted Mass Sea: a Case Study for Mixed Action Lattice QCD," *Nucl.Phys.* **B869** (2013) 131–163.

[55] N. Metropolis, A. Rosenbluth, M. Rosenbluth, A. Teller, and E. Teller, "Equation of State Calculations by Fast Computing Machines," *J.Chem.Phys.* **21** (1953) 1087–1092.

[56] M. Creutz, "Monte Carlo Study of Quantized SU(2) Gauge Theory," *Phys.Rev.* **D21** (1980) 2308–2315.

[57] S. Duane, A. Kennedy, B. Pendleton, and D. Roweth, "Hybrid Monte Carlo," *Phys.Lett.* **B195** (1987) 216–222.

[58] M. Lüscher, "Computational Strategies in Lattice QCD," `arXiv:1002.4232 [hep-lat]`.

[59] L. Giusti and M. Lüscher, "Chiral Symmetry Breaking and the Banks-Casher Relation in Lattice QCD with Wilson quarks," *JHEP* **0903** (2009) 013.

[60] T. Banks and A. Casher, "Chiral Symmetry Breaking in Confining Theories," *Nucl.Phys.* **B169** (1980) 103.

[61] H. Leutwyler and A. V. Smilga, "Spectrum of Dirac Operator and Role of Winding Number in QCD," *Phys.Rev.* **D46** (1992) 5607–5632.

[62] P. Damgaard, K. Splittorff, and J. Verbaarschot, "Microscopic Spectrum of the Wilson Dirac Operator," *Phys.Rev.Lett.* **105** (2010) 162002.

[63] G. Akemann, P. Damgaard, K. Splittorff, and J. Verbaarschot, "Spectrum of the Wilson Dirac Operator at Finite Lattice Spacings," *Phys.Rev.* **D83** (2011) 085014.

[64] K. Splittorff and J. Verbaarschot, "The Microscopic Twisted Mass Dirac Spectrum," *Phys.Rev.* **D85** (2012) 105008.

[65] J. Gasser and H. Leutwyler, "Spontaneously Broken Symmetries: Effective Lagrangians at Finite Volume," *Nucl.Phys.* **B307** (1988) 763.

[66] J. Gasser and H. Leutwyler, "Thermodynamics of Chiral Symmetry," *Phys.Lett.* **B188** (1987) 477.

[67] J. Gasser and H. Leutwyler, "Light Quarks at Low Temperatures," *Phys.Lett.* **B184** (1987) 83.

[68] J. Osborn, D. Toublan, and J. Verbaarschot, "From Chiral Random Matrix Theory to Chiral Perturbation Theory," *Nucl.Phys.* **B540** (1999) 317–344.

[69] P. Damgaard, J. Osborn, D. Toublan, and J. Verbaarschot, "The Microscopic Spectral Density of the QCD Dirac Operator," *Nucl.Phys.* **B547** (1999) 305–328.

[70] S. Necco and A. Shindler, "Spectral Density of the Hermitean Wilson Dirac operator: a NLO Computation in Chiral Perturbation Theory," *JHEP* **1104** (2011) 031.

[71] P. Weisz, "Renormalization and Lattice Artifacts," `arXiv:1004.3462 [hep-lat]`.

[72] A. Vladikas, "Three Topics in Renormalization and Improvement," `arXiv:1103.1323 [hep-lat]`.

[73] G. Martinelli, C. Pittori, C. T. Sachrajda, M. Testa, and A. Vladikas, "A General Method for Nonperturbative Renormalization of Lattice Operators," *Nucl.Phys.* **B445** (1995) 81–108.

[74] L. Del Debbio, L. Giusti, M. Lüscher, R. Petronzio, and N. Tantalo, "Stability of Lattice QCD Simulations and the Thermodynamic Limit," *JHEP* **0602** (2006) 011.

[75] L. Giusti, C. Hoelbling, M. Lüscher, and H. Wittig, "Numerical Techniques for Lattice QCD in the Epsilon Regime," *Comput.Phys.Commun.* **153** (2003) 31–51.

[76] W. H. Press, S. A. Teukolsky, W. T. Vetterling, and B. P. Flannery, *Numerical Recipes in FORTRAN: The Art of Scientific Computing*. 1992.

[77] J. Stoer, R. Bulirsch, R. Bartels, W. Gautschi, and C. Witzgall, *Introduction to Numerical Analysis*, vol. 2. Springer New York, 1993.

[78] K. Jansen and C. Urbach, "tmLQCD: A Program Suite to Simulate Wilson Twisted Mass Lattice QCD," *Comput.Phys.Commun.* **180** (2009) 2717–2738.

[79] G. P. Engel, L. Giusti, S. Lottini, and R. Sommer, "Chiral Condensate from the Banks-Casher Relation," `arXiv:1309.4537 [hep-lat]`.

[80] **ALPHA** Collaboration, U. Wolff, "Monte Carlo Errors with Less Errors," *Comput.Phys.Commun.* **156** (2004) 143–153.

[81] K. Cichy, E. García-Ramos, and K. Jansen, "Chiral Condensate from the Twisted Mass Dirac operator Spectrum," `arXiv:1303.1954 [hep-lat]`.

[82] **ETM** Collaboration, M. Constantinou *et al.*, "Non-Perturbative Renormalization of Quark Bilinear Operators with $N_f = 2$ (tmQCD) Wilson fermions and the Tree-Level Improved Gauge Action," *JHEP* **1008** (2010) 068.

[83] C. Alexandrou, M. Constantinou, T. Korzec, H. Panagopoulos, and F. Stylianou, "Renormalization Constants of Local Operators for Wilson type Improved Fermions," *Phys.Rev.* **D86** (2012) 014505.

[84] **ETM** Collaboration, Private communication with D. Palao, "Preliminary results for $N_f = 4$ renormalization constants.".

[85] **ETM** Collaboration, B. Blossier *et al.*, "Average Up/Down, Strange and Charm Quark Masses with Nf=2 Twisted Mass Lattice QCD," *Phys.Rev.* **D82** (2010) 114513.

[86] **ETM** Collaboration, C. Alexandrou *et al.*, "Light Baryon Masses with Dynamical Twisted Mass Fermions," *Phys.Rev.* **D78** (2008) 014509.

[87] G. Colangelo *et al.*, "Review of Lattice Results Concerning Low Energy Particle Physics," *Eur.Phys.J.* **C71** (2011) 1695.

[88] **RBC , UKQCD** Collaboration, Y. Aoki *et al.*, "Continuum Limit Physics from 2+1 Flavor Domain Wall QCD," *Phys.Rev.* **D83** (2011) 074508.

[89] A. Bazavov *et al.*, "Nonperturbative QCD Simulations with 2+1 Flavors of Improved Staggered Quarks," *Rev.Mod.Phys.* **82** (2010) 1349–1417.

[90] A. Bazavov *et al.*, "Staggered Chiral Perturbation Theory in the Two-Flavor Case and SU(2) Analysis of the MILC Data," *PoS* **LATTICE2010** (2010) 083.

[91] S. Borsanyi *et al.*, "SU(2) Chiral Perturbation Theory Low-Energy Constants from 2+1 Flavor Staggered Lattice Simulations," `arXiv:1205.0788 [hep-lat]`.

[92] Y. Aoki *et al.*, "The QCD Transition Temperature: Results with Physical Masses in the Continuum Limit II.," *JHEP* **0906** (2009) 088.

[93] F. Burger, V. Lubicz, M. Müller-Preußker, S. Simula, and C. Urbach, "Quark Mass and Chiral Condensate from the Wilson Twisted Mass Lattice Quark Propagator," *Phys.Rev.* **D87** (2013) 034514.

[94] C. McNeile *et al.*, "Direct Determination of the Strange and Light Quark Condensates from Full Lattice QCD," *Phys.Rev.* **D87** no. 3, (2013) 034503.

[95] C. Bernard *et al.*, "Status of the MILC Light Pseudoscalar Meson Project," *PoS* **LAT2007** (2007) 090.

[96] **HPQCD** Collaboration, R. Dowdall *et al.*, "The Upsilon Spectrum and the Determination of the Lattice Spacing from Lattice QCD Including Charm Quarks in the Sea," *Phys.Rev.* **D85** (2012) 054509.

[97] K. Cichy, K. Jansen, and P. Korcyl, "Non-Perturbative Renormalization in Coordinate Space for $N_f = 2$ Maximally Twisted Mass Fermions with Tree-Level Symanzik Improved Gauge Action," *Nucl.Phys.* **B865** (2012) 268–290.

[98] M. Lüscher, "Topology of Lattice Gauge Fields," *Commun.Math.Phys.* **85** (1982) 39.

[99] N. Makhaldiani and M. Müller-Preussker, "The Topological Susceptibility From SU(3) Lattice Gauge Theory," *JETP Lett.* **37** (1983) 523.

[100] M. Campostrini, A. Di Giacomo, and H. Panagopoulos, "The Topological Susceptibility on the Lattice," *Phys.Lett.* **B212** (1988) 206.

[101] A. Phillips and D. Stone, "Lattice Gauge Fields, Principal Bundles and the Calculation of Topological Charge," *Commun.Math.Phys.* **103** (1986) 599–636.

[102] A. S. Kronfeld, M. Laursen, G. Schierholz, and U. Wiese, "High Statistics Computation of the Topological Susceptibility of SU(2) Gauge Theory," *Nucl.Phys.* **B292** (1987) 330.

[103] B. Alles, A. Di Giacomo, and M. Giannetti, "Topological Susceptibility from Different Definitions of Topological Charge in Lattice QCD," *Phys.Lett.* **B249** (1990) 490–494.

[104] F. Bruckmann *et al.*, "Comparing Topological Charge Definitions Using Topology Fixing Actions," *Eur.Phys.J.* **A43** (2010) 303–311.

[105] L. Giusti, G. Rossi, and M. Testa, "Topological Susceptibility in Full QCD with Ginsparg-Wilson Fermions," *Phys.Lett.* **B587** (2004) 157–166.

[106] M. Lüscher, "Topological Effects in QCD and the Problem of Short Distance Singularities," *Phys.Lett.* **B593** (2004) 296–301.

[107] M. Lüscher and F. Palombi, "Universality of the Topological Susceptibility in the SU(3) Gauge Theory," *JHEP* **1009** (2010) 110.

[108] L. Giusti, M. Lüscher, P. Weisz, and H. Wittig, "Lattice QCD in the Epsilon Regime and Random Matrix Theory," *JHEP* **0311** (2003) 023.

[109] S. Schäfer and F. Virotta, "Autocorrelations in Hybrid Monte Carlo Simulations," *PoS* **LATTICE2010** (2010) 042.

[110] **ALPHA** Collaboration, S. Schäfer, R. Sommer, and F. Virotta, "Critical Slowing Down and Error Analysis in Lattice QCD Simulations," *Nucl.Phys.* **B845** (2011) 93–119.

[111] M. Lüscher and S. Schäfer, "Lattice QCD Without Topology Barriers," *JHEP* **1107** (2011) 036.

[112] L. Del Debbio, L. Giusti, and C. Pica, "Topological Susceptibility in the SU(3) Gauge Theory," *Phys.Rev.Lett.* **94** (2005) 032003.

[113] **TWQCD** Collaboration, Y.-Y. Mao and T.-W. Chiu, "Topological Susceptibility to the One-Loop Order in Chiral Perturbation Theory," *Phys.Rev.* **D80** (2009) 034502.

[114] S. Durr *et al.*, "Lattice QCD at the Physical Point: Simulation and Analysis Details," *JHEP* **1108** (2011) 148.

[115] **ETM** Collaboration, K. Ottnad *et al.*, "η and η' Mesons from Nf=2+1+1 Twisted Mass Lattice QCD," *JHEP* **1211** (2012) 048.

[116] Beringer, J. *et al* (Particle Data Group), "The Review of Particle Physics," *Phys.Rev.* **D86** (2012) .

[117] P. Hernández, K. Jansen, and M. Lüscher, "Locality Properties of Neuberger's Lattice Dirac Operator," *Nucl.Phys.* **B552** (1999) 363–378.

[118] A. Vladikas and G. Herdoíza, "School on non-perturbative renormalization on the lattice.," 2012.

[119] **ETM** Collaboration, K. Jansen, F. Karbstein, A. Nagy, and M. Wagner, "$\Lambda_{\bar{M}S}$ from the Static Potential for QCD with $n_f = 2$ Dynamical Quark Flavors," *JHEP* **1201** (2012) 025.

[120] **XLF** Collaboration, K. Jansen, M. Papinutto, A. Shindler, C. Urbach, and I. Wetzorke, "Light Quarks with Twisted Mass Fermions," *Phys.Lett.* **B619** (2005) 184–191.

[121] C. Urbach., "http://www.itkp.uni-bonn.de/ urbach/software.html. Hadron *R package*.".

[122] A. S. Schwarz, "On Regular Solutions of Euclidean Yang-Mills Equations," *Phys.Lett.* **B67** (1977) 172–174.